

NEW DIRECTIONS FOR CANCER DRUG RESEARCH OF RUTHENIUM AND  
RHODIUM COMPOUNDS: INVESTIGATION OF CYTOTOXICITIES,  
MECHANISMS OF CANCER CELL DEATH, AND CELLULAR TARGETS

A Dissertation

by

BRUNO PENA MACEDA

Submitted to the Office of Graduate and Professional Studies of  
Texas A&M University  
in partial fulfillment of the requirements for the degree of

DOCTOR OF PHILOSOPHY

Chair of Committee,	Kim R. Dunbar
Committee Members,	Marcetta Y. Darensbourg
	Oleg V. Ozerov
	Robert C. Burghardt
Head of Department,	David H. Russell

August 2014

Major Subject: Chemistry

Copyright 2014 Bruno Pena Maceda

## ABSTRACT

The discovery of the antitumor properties of cisplatin revolutionized the field of medicinal inorganic chemistry and fostered the development of metal-based anticancer drugs, a topic that continues to play a prominent role in chemotherapy. Ruthenium (Ru) compounds are a promising class of anticancer compounds that display improved therapeutic activities, different mechanisms of action, and reduced side-effects as compared to cisplatin. Two ruthenium compounds are being tested in clinical trials for the treatment of cancer malignancies for which platinum drugs are inactive and several other transition metal complexes are in preclinical studies.

In an effort to expand the current state-of-the art in cancer metallotherapeutics, two new classes of ruthenium compounds were synthesized and fully characterized. The first class of complexes is based on Ru(II) coordination compounds of general formula  $[\text{Ru}(\text{N}^{\wedge}\text{N})_2(\text{N}^{\wedge}\text{O}^-)][\text{PF}_6]$ , where  $\text{N}^{\wedge}\text{N}$  is a bidentate polypyridyl ligand (bpy = 2,2'-bipyridine; phen = 1,10-phenanthroline) and  $\text{N}^{\wedge}\text{O}^-$  is a bidentate nitrogen/oxygen-donor anionic ligand (dphol = dibenzo[*a,c*]phenazin-10-olate; hbtz = 2-(benzo[*d*]thiazol-2-yl)phenolate). These molecules exhibit cytotoxic properties that are comparable or more effective than cisplatin against lung cancer cells and were found to induce cellular death through the intrinsic pathway of apoptosis.

The second class of molecules consist of organometallic Ru(II) compounds of formula  $[\text{Ru}(\text{phpy})(\text{N}^{\wedge}\text{N}_1)(\text{N}^{\wedge}\text{N}_2)][\text{PF}_6]$ , where phpy is cyclometallated 2-phenylpyridine and  $\text{N}^{\wedge}\text{N}$  are bidentate polypyridyl ligands. The compounds  $[\text{Ru}(\text{phpy})(\text{bpy})(\text{dppn})][\text{PF}_6]$

and  $[\text{Ru}(\text{phpy})(\text{pap})(\text{dppn})][\text{PF}_6]$  (dppn = benzo[*i*]dipyrido[3,2-*a*:2',3'-*c*]phenazine; pap = 2-(phenylazo)pyridine) are the most potent members of the series against cervical and ovarian cancer cells and are also active in the multidrug resistant NCI/ADR-RES ovarian cancer cell line. In addition, the compound  $[\text{Ru}(\text{phpy})(\text{biq})_2][\text{PF}_6]$  (biq = 2,2'-biquinoline) was shown to exhibit an enhancement of its cytotoxicity when irradiated with red light, results that poise Ru(II) cyclometallated compounds as promising candidates for further development in cancer chemotherapy and photochemotherapy.

Finally, an unprecedented fluorophore-labeled metal-metal bonded dirhodium compound was synthesized and characterized, and its cellular distribution and subcellular localization were studied in living cancer cells by using confocal fluorescence microscopy. This fluorescent compound traverses the cellular membrane of lung cancer cells and localizes in lysosomes and mitochondria. In contrast to previous reports of dirhodium anticancer compounds, it does not target the cell nucleus, supporting the contention that other cellular targets can be reached by tuning the ligand environment around the dirhodium core, opening new avenues for drug design.

*To Astrid and Andrea,  
thanks for accompanying me throughout this winding but successful journey.*

*To my parents, Pilar and Luis,  
thanks for all your support and encouragement.*

*To my cousin Johann, my uncle Pepe Floro and my grandmother Efigenia,  
you are now angels in the sky.*

## ACKNOWLEDGEMENTS

The support and friendship of several people along these five years have been indispensable for the research work that is presented in this dissertation. I am truly grateful to my advisor, Prof. Kim R. Dunbar who mentored and guided me throughout these years. The passion, love and excitement for chemistry that you constantly transmitted was a catalyst that helped me push the limits of knowledge every time I sought for your advice. Thanks for trusting in me when I joined your group and thanks for the freedom you gave me to explore different areas of chemistry; the tools and scientific knowledge I gained from my research projects will be invaluable to continue my career as an independent scientist.

I want to thank Prof. Claudia Turro for giving me the opportunity to collaborate with her group, for her friendship, for her endless willingness to help me and vital advice in different topics of inorganic photochemistry. I am also thankful to Prof. Rola Barhoumi and Prof. Robert C. Burghardt for their advice in microscopy and live cell imaging and for their constant motivation and valuable insight when discussing my research projects. I also want to thank my committee members Prof. Marcetta Y. Darensbourg and Oleg V. Ozerov.

Thanks also go to my friends from the Dunbar group, Amanda David, Andrew Brown, Maryfer Ballesteros, Codi Sanders, Zhanyong Li, Mohamed Saber, Jill Frank, Toby Woods, Xuan Zhang, David Kempe, Francisco Birk, Charles “Carlitos” Culberston, Sayan Saha, Bianca Ramirez, Mayela Canales, Helen Chifotides, Hanhua

Zhao, Ian Giles, Heather Southerland and Zhongyue Zhang, who made my time in College Station special.

I would like to thank Prof. Alfredo Angeles-Boza, Dr. J. Dafhne Aguirre and Dr. Carolina Avendano for their generous help and friendship during my first semester at Texas A&M University. In particular, I want to thank Alfredo for his invaluable advice and for sharing his expertise in dirhodium chemistry along these years. I also want to thank Dr. Sara Goberna-Ferron and Prof. Jose Ramon Galan-Mascaros for their fantastic friendship and for taking me in a challenging water oxidation catalysis adventure. Thanks Sara for being a wonderful friend and for teaching me several electrochemical techniques.

Finally, I want to thank my parents, Luis and Pilar, for all the sacrifices you made to help me during my career and for the support and encouragement you gave me throughout these years. And I want to thank you, Andrea, for your infinite love and patience, for risking everything to be with me, for spending long hours at night accompanying me and for giving me the greatest gift, our beautiful daughter, Astrid.

## TABLE OF CONTENTS

	Page
ABSTRACT .....	ii
DEDICATION .....	iv
ACKNOWLEDGEMENTS .....	v
TABLE OF CONTENTS .....	vii
LIST OF FIGURES.....	x
LIST OF TABLES .....	xx
CHAPTER I INTRODUCTION .....	1
Motivation: Worldwide and United States Cancer Statistics.....	1
Platinum Compounds in Cancer Drug Research.....	5
Cisplatin, The Landmark Story of an Inorganic Compound.....	5
Mechanism of Action .....	9
Tumor Resistance .....	12
Intrinsic Pathway of Apoptosis .....	17
The Emergence of Ruthenium Anticancer Drugs .....	20
Ruthenium(III) Drugs in Clinical Trials for Cancer Chemotherapy .....	20
Ruthenium(II) Organometallic Compounds as Anticancer Agents .....	23
Ruthenium(II) Polypyridyl Anticancer Compounds .....	28
Early Reports of Biological Activity.....	28
Cellular Uptake .....	30
Cytotoxicity and Mechanism of Cancer Cell Death.....	33
Dissertation Objectives and Outline.....	44
CHAPTER II CYTOTOXICITY STUDIES OF RUTHENIUM COMPOUNDS AND AN IRIDIUM ANALOG WITH N <sup>+</sup> O <sup>-</sup> ANCILLARY LIGANDS .....	46
Introduction .....	46
Experimental Section .....	57
General Methods .....	57
Instrumentation.....	58
Synthetic Details.....	59
X-Ray Crystallography.....	63

Cell Culture Experiments .....	64
In vitro Cytotoxicity .....	64
JC-1 Assay.....	65
Calcein AM Assay.....	65
Caspase Glo Assay .....	66
Results and Discussion.....	67
Synthesis and Characterization .....	67
X-ray Structures of Compounds 1, 3, 4 and 6.....	71
Electrochemical Properties.....	85
Optical Properties.....	93
Cytotoxic Properties.....	99
Investigation of the Mechanism of Cancer Cell Death .....	102
Conclusions .....	115
CHAPTER III RUTHENIUM CYCLOMETALLATED DYES AS A NEW CLASS OF ORGANOMETALLIC ANTICANCER DRUGS.....	117
Introduction .....	117
Experimental Section .....	125
General Methods .....	125
Instrumentation.....	126
Synthetic Details.....	127
X-Ray Crystallography.....	136
Cell Culture Details.....	137
In Vitro Cytotoxicity, SYTOX® Green and MitoProbe® JC-1 Assay.....	137
Phototoxicity of Complex 5 .....	138
Theoretical Calculations.....	139
Results and Discussion.....	140
Synthesis and Characterization of Compounds 1–5.....	140
Synthesis and Characterization of Compounds 6–8.....	149
Electrochemistry.....	162
Electronic Absorption Spectroscopy Studies .....	168
Electronic Structure Calculations.....	175
Cytotoxicity Studies .....	194
Conclusions .....	200
CHAPTER IV LIVE CELL IMAGING STUDIES OF A FLUOROPHORE- LABELED METAL-METAL BONDED DIRHODIUM COMPOUND .....	202
Multiple Bonds Between Metal Atoms.....	202
Anticancer Active Dirhodium Compounds.....	205
Dirhodium Tetraacetate and its Derivatives.....	205
Interactions of Dirhodium Compounds with DNA .....	210
Interactions with DNA Base Models and Dinucleotides .....	210



Interactions with Single-stranded and Double-stranded DNA.....	215
Dirhodium Anticancer Drugs Containing Polypyridyl Ligands.....	216
Ubiquitin-Proteasome System as a Potential Target.....	219
Other M–M Bonded Anticancer Compounds.....	222
Intracellular Distribution of Metal-Based Drugs.....	224
Experimental Section.....	228
General Methods.....	228
Instrumentation.....	229
Synthetic Procedures.....	230
Cell Culture.....	233
In vitro Cytotoxicity.....	233
Confocal Fluorescence Microscopy Studies.....	234
Results and Discussion.....	236
Synthesis and Characterization.....	236
Electronic Absorption Spectroscopy and Fluorescence Spectroscopy Studies.....	243
Laser Scanning Confocal Fluorescence Microscopy Studies.....	246
Conclusions.....	257
CHAPTER V CONCLUSIONS AND FUTURE OUTLOOK.....	259
REFERENCES.....	265

## LIST OF FIGURES

	Page
Figure 1. 1 Estimated number of cancer deaths in the United States for 2014. Data obtained from the National Cancer Institute, reference 3. ....	4
Figure 1. 2 Molecular structures of (a) Pt(IV) and (b) Pt(II) antitumor compounds reported by Rosenberg in 1969 and (c) carboplatin.....	7
Figure 1. 3 Cellular uptake and mechanism of action of cisplatin. ....	10
Figure 1. 4 X-ray structure of duplex DNA containing a cisplatin 1,2-d(GpG) intrastrand cross-links (left) and space filling model of the same structure (right). The platinum ion is depicted in gray color. Adapted with permission from reference 31. Copyright 2007 American Chemical Society. ....	11
Figure 1. 5 Molecular structures of oxaliplatin and other Pt drugs. ....	15
Figure 1. 6 Molecular structures of Ru drugs in clinical trials. ....	21
Figure 1. 7 Molecular structures of (a) Ru(II) organometallic anticancer compounds from Sadler's laboratories, (b) RM175 and HC11. ....	24
Figure 1. 8 Molecular structure of (a) RAPTA-T and RAPTA-C, (b) Ru( $\eta^6$ - phenylethacrylate)(pta)Cl <sub>2</sub> and (c) a Ru-based kinase inhibitor. ....	26
Figure 1. 9 Molecular structures of the cationic complexes [Ru(phen) <sub>3</sub> ] <sup>2+</sup> , [Ru(bpy) <sub>3</sub> ] <sup>2+</sup> , [Ru(tmphen) <sub>3</sub> ] <sup>2+</sup> and [Ru(tmphen) <sub>2</sub> (acac)] <sup>+</sup> .....	30
Figure 1. 10 Molecular structure of [Ru(DIP) <sub>2</sub> (dppz)] <sup>2+</sup> and confocal image of HeLa cells incubated with 5 $\mu$ M [Ru(DIP) <sub>2</sub> (dppz)] <sup>2+</sup> for 4 h. Scale bar is 10 $\mu$ m. Adapted with permission from reference 12. Copyright 2008 American Chemical Society. ....	32
Figure 1. 11 Molecular structures of [Ru(bpy) <sub>2</sub> (L)] <sup>2+</sup> complexes. ....	34
Figure 1. 12 (a) Molecular structures of Ru polypyridyl complexes with phenylimidazo- phenanthroline ligands and (b) molecular structure of RuPOP. ....	35

Figure 1. 13 Molecular structures Ru polypyridyl (a) bpy-norharman and (b) norharman complexes.....	37
Figure 1. 14 (a) Molecular structure of $[\text{Ru}(\text{dppz})_2(\text{CppH})]^{2+}$ . Fluorescence confocal microscopy images of HeLa cells incubated with $[\text{Ru}(\text{dppz})_2(\text{CppH})]^{2+}$ (20 $\mu\text{M}$ ) for 2 h: (a) nuclear staining, (b) cellular staining of $[\text{Ru}(\text{dppz})_2(\text{CppH})]^{2+}$ , (c) mitochondrial staining, and (d) the overlay image. Adapted with permission from reference 127. Copyright 2012 American Chemical Society.....	39
Figure 1. 15 Molecular structure of Ru polypyridyl complexes containing the anthracenyl chelating ligand PAIH.....	41
Figure 1. 16 Molecular structures of (a) $[\text{Ru}(\text{bpy})_2(\text{thppz})]^{2+}$ , (b) $[\text{Ru}(\text{phen})_2(\text{thppz})]^{2+}$ and (c) $[(\text{Ru}(\text{DIP})_2)_2(\mu\text{-tpphz})]^{4+}$ .....	42
Figure 2. 1 Location of the platinum group metals in the Periodic Table. Ru = ruthenium, Os = osmium, Rh = rhodium, Ir = iridium, Pd = palladium, Pt = platinum.....	47
Figure 2. 2 (a) Schematic representation Ru polypyridyl complexes on (a) $[\text{Ru}^{\text{II}}\text{N}_6]^{2+}$ and (b) $[\text{Ru}^{\text{II}}\text{N}_5\text{O}]^+$ coordination environments. (c) Molecular structures of phox and quo ligands.....	48
Figure 2. 3 Molecular structures of (a,b) monocationic Ru compounds incorporating $\text{N}^+\text{O}^-$ -ligands and (c) dicationic Ru polypyridyl compounds related to those shown in (a,b). $\text{IC}_{50}$ values ( $\mu\text{M}$ ) are shown in parenthesis.....	50
Figure 2. 4 (a) Schematic representation of Ir(III) cyclopentadienyl complexes. (b) Monocationic $\text{Cp}^*\text{Ir}(\text{III})$ compounds. $\text{IC}_{50}$ values ( $\mu\text{M}$ ) are shown in parenthesis. (c) Dual DNA binding mode of $\text{Irphen}^{\text{biph}}$ .....	52
Figure 2. 5 (a) Cyclometallated piano-stool Ir cytotoxic compounds. $\text{IC}_{50}$ values ( $\mu\text{M}$ ) are shown in parenthesis. (b) Octahedral Ir(III) molecules with anticancer activity.....	54
Figure 2. 6 Molecular structures of (a) Ru(II) and (b) Ir(III) compounds containing $\text{N}^+\text{O}^-$ -bidentate ligands in this study.....	56
Figure 2. 7 Reaction scheme for the syntheses of 1–5.....	68
Figure 2. 8 $^1\text{H}$ NMR spectra ( $(\text{CD}_3)_2\text{CO}$ , 500 MHz) of compounds (a) 1, (b) 2 and (c) 5.....	69

Figure 2. 9 <sup>1</sup> H NMR spectra (500 MHz) of compounds (a) 3 (CD <sub>3</sub> CN), (b) 4 (CD <sub>3</sub> CN) and (c) 6 (CDCl <sub>3</sub> ). .....	70
Figure 2. 10 (Top) Thermal ellipsoid plots at the 50% probability level of the X-ray structure of [Ru(bpy) <sub>2</sub> (dphol)][PF <sub>6</sub> ] (1). The [PF <sub>6</sub> ] <sup>-</sup> anion and H atoms have been omitted for the sake of clarity. (Bottom) Distortion of the dphol ligand in compound 1. ....	72
Figure 2. 11 Thermal ellipsoid plots at the 50% probability level of the X-ray structures of [Ru(bpy) <sub>2</sub> (hbtz)][PF <sub>6</sub> ] (3), [Ru(phen) <sub>2</sub> (hbtz)][PF <sub>6</sub> ] (4) and Ir(phpy) <sub>2</sub> (hbtz) (6). The [PF <sub>6</sub> ] <sup>-</sup> anion (in the case of 3 and 4) and H atoms have been omitted for the sake of clarity. ....	73
Figure 2. 12 Space filling models highlighting intermolecular π-π stacking interactions between phenanthrene moieties of dphol ligands in the crystal packing of compound 1. ....	80
Figure 2. 13 Space filling models highlighting intermolecular π-π stacking interactions between bpy ligands in the crystal packing of compound 1. ....	81
Figure 2. 14 Intermolecular π-π stacking interactions in the crystal packing of compound 3. Space filling models highlighting the interactions between (a) bpy ligands and (b) hbtz ligands. ....	82
Figure 2. 15 Intermolecular π-π stacking interactions in the crystal packing of compound 4. Space filling models highlighting the interactions between (a) phen ligands and (b) hbtz ligands. ....	83
Figure 2. 16 Intermolecular π-π stacking interactions in the crystal packing of compound 6. Space filling models highlighting the interactions between (a) phpy ligands and (b) hbtz ligands. ....	84
Figure 2. 17 Cyclic voltammograms (vs Ag/AgCl) of compounds 1, 2 and 5 in acetonitrile (0.1 M [ <sup>n</sup> Bu <sub>4</sub> N][PF <sub>6</sub> ], 100 mV/s scan rate). <i>i<sub>c</sub></i> = cathodic current, <i>i<sub>a</sub></i> = anodic current, ox. = oxidation, red. = reduction. The black arrows indicate the direction of the scan. ....	86
Figure 2. 18 Cyclic voltammograms (vs Ag/AgCl) of compounds 3–5 in acetonitrile (0.1 M [ <sup>n</sup> Bu <sub>4</sub> N][PF <sub>6</sub> ], 100 mV/s scan rate). <i>i<sub>c</sub></i> = cathodic current, <i>i<sub>a</sub></i> = anodic current, ox. = oxidation, red. = reduction. The black arrows indicate the direction of the scan. ....	87
Figure 2. 19 Cyclic voltammogram (vs Ag/AgCl) of compound 6 in acetonitrile (0.1 M [ <sup>n</sup> Bu <sub>4</sub> N][PF <sub>6</sub> ], 100 mV/s scan rate). <i>i<sub>c</sub></i> = cathodic current,	

$i_a$ = anodic current, ox. = oxidation, red. = reduction. The black arrows indicate the direction of the scan. ....	89
Figure 2. 20 Schematic representation of the destabilization of the occupied Ru(4d $\pi$ ) orbitals in 1–5 with respect to [Ru(bpy) <sub>3</sub> ] <sup>2+</sup> . E <sub>MCLT</sub> = energy of the MCLT transition. ....	90
Figure 2. 21 Schematic representation of the relative energies of Ru(4d $\pi$ ) and Ir(5d $\pi$ ) orbitals. E <sub>MCLT</sub> = energy of the metal-to-ligand charge transfer transition. ....	91
Figure 2. 22 Electronic absorption spectra of 1, 2 and 5 in acetonitrile. ....	94
Figure 2. 23 Electronic absorption spectra of 3–5 in acetonitrile. ....	95
Figure 2. 24 Electronic absorption spectra of free ligands in acetonitrile. The concentrations of the compounds were adjusted to have comparable intensities. ....	95
Figure 2. 25 Photograph showing the solid state colors of compounds 4 and 6. ....	97
Figure 2. 26 (a) Emission spectrum of an aerated solution of compound 6 in CH <sub>2</sub> Cl <sub>2</sub> ( $\lambda_{ex}$ = 350 nm). (b) Photographs showing phosphorescence from a solution of 6 (~10 <sup>-5</sup> M) in CH <sub>2</sub> Cl <sub>2</sub> ( $\lambda_{ex}$ = 254 nm from a hand-held UV lamp). ....	98
Figure 2. 27 Molecular structures of (a) Janus Green B and (b) JC-1. ....	100
Figure 2. 28 <i>R</i> values from JC-1 when A549 cells are exposed after 48 h of incubation to different concentrations of compounds (a) 1, (b) 2, (c) 3 and (d) 4. The graphs represent means with standard deviation. Control experiments (no metal complex) are depicted in gray color. ....	104
Figure 2. 29 <i>R</i> values from JC-1 when A549 cells are exposed after 48 h of incubation to different concentrations of cisplatin and compound 4. The graphs represent means with standard deviation. ....	105
Figure 2. 30 Confocal fluorescence images of JC-1 in A549 cells in the absence of compound 4. (a) Green and (b) red fluorescence from JC-1. (c) Overlay of (a,b) images. Field of view = 75 × 75 $\mu$ m. Images were collected after 48 h of incubation. ....	106
Figure 2. 31 Confocal red fluorescence images of JC-1 in A549 cells incubated with (a) 0 $\mu$ M 4, (b) 500 nM 4 and (c) 1 $\mu$ M 4. Field of view = 75 × 75 $\mu$ m. Images were collected after 48 h of incubation. ....	107

Figure 2. 32 Molecular structure of calcein AM.....	108
Figure 2. 33 Confocal fluorescence images of A549 cells coincubated with Calcein AM and Mitotracker in the absence of compound 4. (a) Green fluorescence from Calcein (+CoCl <sub>2</sub> ), (b) red fluorescence from Mitotracker and (c) overlay of (a,b) images. Field of view = 75 × 75 μm. Images were collected after 48 h of incubation.....	110
Figure 2. 34 Confocal fluorescence images of A549 cells coincubated with compound 4 (1 μM), Calcein AM and Mitotracker. (a) Green fluorescence from Calcein AM (+CoCl <sub>2</sub> ), (b) red fluorescence from Mitotracker and (c) overlay of (a,b) images. Field of view = 75 × 75 μm. Images were collected after 48 h of incubation.....	111
Figure 2. 35 Reaction pathway that leads to oxyluciferin fluorescence during the measurement of caspase-3/7 activity. ATP = adenosine triphosphate. AMP = Adenosine monophosphate. PP <sub>i</sub> = pyrophosphate.....	113
Figure 2. 36 Caspase-3/7 activity measurements when A549 cells are exposed to compound 4 and cisplatin (48 h of incubation). The graphs represent means with standard deviation.....	114
Figure 3. 1 Schematic representations of the molecular structures of (a) (η <sup>6</sup> -arene)Ru and (b) Ru(phpy) scaffolds.....	118
Figure 3. 2 Molecular structures of (a) RDC9, (b) RDC11, (c) [Ru(phpy)(phen) <sub>2</sub> ][PF <sub>6</sub> ], and (d) an example of a Ru(II) anticancer compound incorporating both arene and phpy-type ligands.....	122
Figure 3. 3 Molecular structures of Ru(II) cyclometallated complexes in this study.....	124
Figure 3. 4 Numbering scheme used to assign the <sup>1</sup> H NMR spectra of selected Ru complexes.....	135
Figure 3. 5 Reaction scheme for the synthesis of 2–5.....	140
Figure 3. 6 Thermal ellipsoid plots at the 50% probability level of the X-ray structures of [Ru(phpy)(biq) <sub>2</sub> ][PF <sub>6</sub> ] (5, top) and [Ru(phpy)(bpy)(NCCH <sub>3</sub> ) <sub>2</sub> ][PF <sub>6</sub> ] (9, bottom). The [PF <sub>6</sub> ] <sup>-</sup> anions and H atoms have been omitted for the sake of clarity.....	143
Figure 3. 7 Intermolecular π-π stacking interactions in the crystal packing of compound 5. (a) Shortest centroid-centroid distance and slippage angle	

and (b) space filling model highlighting the stacking of $\pi$ -systems of biquinolime moieties. ....	147
Figure 3. 8 Space filling model highlighting intermolecular $\pi$ - $\pi$ interactions in the crystal packing of compound 9. ....	148
Figure 3. 9 Possible geometric isomers of compound 6 with <i>cis</i> arrangement of acetonitrile ligands. ....	150
Figure 3. 10 Comparison of the proton resonances in the aromatic region of $[\text{Ru}(\text{phpy})(\text{NCCH}_3)_4]^+$ and $[\text{Ru}(\text{phpy})(\text{pap})(\text{NCCH}_3)_2]$ (6). ....	151
Figure 3. 11 Thermal ellipsoid plots at the 50% probability level of the X-ray structures of compounds $[\text{Ru}(\text{phpy})(\text{pap})(\text{NCCH}_3)_2][\text{PF}_6]$ (6, top) and $[\text{Ru}(\text{phpy})(\text{pap})(\text{dcm})][\text{PF}_6]$ (7, bottom). The $[\text{PF}_6]^-$ anions and H atoms have been omitted for the sake of clarity. ....	153
Figure 3. 12 Centroid-to-centroid distances in compounds 6 (left) and 7 (right). ....	156
Figure 3. 13 $^1\text{H}$ NMR (500 MHz) spectra of 6 in $\text{CD}_3\text{CN}$ at $21^\circ\text{C}$ : (a) 0 d, (b) 1 d, (c) 3 d, (d) 7 d. ....	158
Figure 3. 14 Aromatic region of the $^1\text{H}$ NMR (500 MHz) spectra of 6 in $\text{CD}_3\text{CN}$ at $70^\circ\text{C}$ : (a) 0 h, (b) 1 h, (c) 2 h, (d) 4 h, (e) 6 h. ....	160
Figure 3. 15 Comparison of the aromatic region of the $^1\text{H}$ NMR spectra (500 MHz, $\text{CD}_3\text{CN}$ ) of compounds 6, 6a, 7 and 8. ....	161
Figure 3. 16 Cyclic voltammograms ( <i>vs</i> Ag/AgCl) of compounds 1–3 in acetonitrile (0.1 M $[\text{nBu}_4\text{N}][\text{PF}_6]$ , 100 mV/s scan rate). $i_c$ = cathodic current, $i_a$ = anodic current, ox. = oxidation, red. = reduction. The black arrows indicate the direction of the scan. ....	164
Figure 3. 17 Cyclic voltammograms ( <i>vs</i> Ag/AgCl) of compounds 4–5 in acetonitrile (0.1 M $[\text{nBu}_4\text{N}][\text{PF}_6]$ , 100 mV/s scan rate). $i_c$ = cathodic current, $i_a$ = anodic current, ox. = oxidation, red. = reduction. The black arrows indicate the direction of the scan. ....	165
Figure 3. 18 Cyclic voltammogram ( <i>vs</i> Ag/AgCl) of compound 8 in acetonitrile (0.1 M $[\text{nBu}_4\text{N}][\text{PF}_6]$ , 100 mV/s scan rate). $i_c$ = cathodic current, $i_a$ = anodic current, ox. = oxidation, red. = reduction. The black arrows indicate the direction of the scan. ....	167

Figure 3. 19 Solid state colors of selected Ru cyclometallated compounds. Compounds 2–4 display the same color of 1 in the solid state; compound 7 displays the same color of 6 in the solid state.....	169
Figure 3. 20 Solution colors of selected Ru cyclometallated compounds in acetonitrile (100 $\mu$ M). Compounds 2 and 4 display the same color of 3 in solution; compound 7 displays the same color of 8 in solution.....	169
Figure 3. 21 Electronic absorption spectra of 1–3 in acetonitrile. ....	171
Figure 3. 22 Electronic absorption spectra of 1, 4 and 5. Inset: red and near-IR absorption of 4 and 5. ....	173
Figure 3. 23 Electronic absorption spectra of 6–8. Inset: red and near-IR absorption of the three complexes. ....	174
Figure 3. 24 Molecular orbital diagrams (HOMO-2 to LUMO+3) of 1, 2, 4–6 and 8.....	176
Figure 3. 25 Ru( $d\sigma$ ) “ $e_g^*$ -type” MOs of $[\text{Ru}(\text{bpy})_3]^{2+}$ and 1 (isovalue = 0.04).....	183
Figure 3. 26 Correlation between (a) $E_{1/2} [\text{Ru}^{3+/2+}]$ vs $E_{\text{HOMO}}$ and (b) $E_{1/2 \text{ red1}}$ vs $E_{\text{LUMO}}$ .....	186
Figure 3. 27 Experimental (solid lines) and calculated (dotted lines) electronic absorption spectra of 1, 2, 4–6 in acetonitrile.....	187
Figure 3. 28 Reduction of MTT. ....	194
Figure 3. 29 JC-1 fluorescence (overlay of green and red channels) images of HeLa cells treated with 2 (7 $\mu$ M) at (a) 0 h, (b) 30 min, (c) 1 h and (d) 2 h.....	197
Figure 4. 1 Schematic representation of the molecular structure of the $[\text{Re}_2\text{Cl}_8]^{2-}$ anion. Distances are indicated in $\text{\AA}$ . ....	203
Figure 4. 2 Qualitative molecular orbital diagram in M–M bonded compounds.....	204
Figure 4. 3 Molecular structures of cisplatin and compound 1. One of the equatorial carboxylate ligands in 1 is highlighted in red. ....	206
Figure 4. 4 Molecular structures of compounds 2–4. One of the equatorial carboxylate ligands is highlighted in red. ....	208



Figure 4. 5 Molecular structures of cytotoxic dirhodium compounds developed during the 1990–2001 period. The axial ligands have been omitted for the sake of clarity. ....	209
Figure 4. 6 Axial interactions of the Rh <sub>2</sub> <sup>4+</sup> core with purines. Adapted with permission from reference 218. Copyright 2005 American Chemical Society. ....	211
Figure 4. 7 Equatorial binding of guanine and adenine base models to the Rh <sub>2</sub> <sup>4+</sup> core. Adapted with permission from reference 218. Copyright 2005 American Chemical Society. ....	213
Figure 4. 8 Molecular structures of (a) d(GpG) and d(pGpG) and (b) H–H conformation of Rh <sub>2</sub> (μ-O <sub>2</sub> CCH <sub>3</sub> ) <sub>2</sub> (deoxydinucleotide). ....	214
Figure 4. 9 Dirhodium compounds with one polypyridyl bidentate ligand (N^N) in the equatorial position. L denotes an equatorially bound methanol ligand; the axial methanol ligands have been omitted for the sake of clarity. ....	217
Figure 4. 10 Rh <sub>2</sub> <sup>4+</sup> compounds with two polypyridyl bidentate ligand (N^N) in the equatorial position. L denotes an equatorially bound methanol ligand; the axial methanol ligands have been omitted for the sake of clarity. ....	218
Figure 4. 11 Molecular structures of (a) MG-262, (b) dirhodium tetracarboxylate compounds that behave as UPS inhibitors, and (c) dirhodium tetrapyrrolidinonato (14). The axial ligands have been omitted for the sake of clarity. ....	220
Figure 4. 12 Molecular structures of antitumor diruthenium and dirhenium compounds. The axial solvent molecules have been omitted for the sake of clarity. ....	223
Figure 4. 13 Molecular structures of fluorophore-labeled metal complexes. ....	225
Figure 4. 14 (a) Schematic representation of a dirhodium compound tagged with a fluorophore in the equatorial position. Molecular structures of (b) phenbodipy and (c) Rh <sub>2</sub> phenbodipy. ....	227
Figure 4. 15 Numbering scheme used to describe the <sup>1</sup> H NMR spectra of 20 and phenbodipy. ....	233
Figure 4. 16 Synthesis of phenbodipy. ....	237

Figure 4. 17 ESI(+) mass spectrum of Rh <sub>2</sub> phenbodipy in methanol.....	239
Figure 4. 18 Portion of the spectra of (a) Rh <sub>2</sub> phenbodipy, (b) Rh <sub>2</sub> phen and (c) Rh <sub>2</sub> bpy (500 MHz, CD <sub>3</sub> OD). The proton resonances marked with (*) correspond to the methyl groups of bound phenbodipy.....	240
Figure 4. 19 Molecular structures of the two geometric isomers of Rh <sub>2</sub> phenbobipy. L denotes a solvent molecule.....	241
Figure 4. 20 <sup>1</sup> H NMR spectrum of Rh <sub>2</sub> phenbodipy (500 MHz, CD <sub>3</sub> OD). See experimental section for complete proton assignments.....	242
Figure 4. 21 Electronic absorption spectrum of phenbodipy and dirhodium compounds in methanol. Inset: absorption maxima in the 500–700 nm region corresponding to the MC Rh <sub>2</sub> (π*) → Rh <sub>2</sub> (σ*) transition. ....	244
Figure 4. 22 (a) Absorption (blue) and normalized emission (green, λ <sub>ex</sub> = 496 nm) spectra of Rh <sub>2</sub> phenbodipy in methanol. (b) Photograph depicting green fluorescence (λ <sub>ex</sub> = 254 nm from a hand-held UV lamp) of a 1 μM solution of phenbodipy in methanol. ....	245
Figure 4. 23 Microscopy images of (a) phenbodipy (1 μM) and (b) Rh <sub>2</sub> phenbodipy (1 μM) after 2 h of incubation. DIC = differential interference contrast. Field of view = 143 μm × 143 μm.....	247
Figure 4. 24 Microscopy images of (a) phenbodipy (1 μM) and (b) Rh <sub>2</sub> phenbodipy (1 μM) after 24 h of incubation. DIC = differential interference contrast. Field of view = 143 μm × 143 μm.....	248
Figure 4. 25 Molecular structures of organic fluorescent dyes used on the colocalization experiments. ....	250
Figure 4. 26 Confocal fluorescence images of 10 μM Rh <sub>2</sub> phenbodipy (left), Lyotracker (middle), and overlay (right) after 5 h incubation. Field of view = 105 × 105 μm.....	251
Figure 4. 27 Confocal fluorescence images of 10 μM Rh <sub>2</sub> phenbodipy (left) Mitotracker (middle), and overlay (right) after 5 h incubation. Field of view = 105 × 105 μm.....	252
Figure 4. 28 Mander's colocalization coefficients of (a) Rh <sub>2</sub> phenbodipy over Lyotracker signals and (b) Rh <sub>2</sub> phenbodipy over Mitotracker signals. The graphs represent means with standard deviation. The asterisk (*) indicates significant difference (at <i>p</i> < 0.05) between the colocalization coefficients at 5 and 24 h for 100 μM Rh <sub>2</sub> phenbodipy.....	253

Figure 4. 29 Confocal fluorescence images of Hoechst 33258 dye (nuclear stain, left), 10 $\mu$ M Rh <sub>2</sub> phenbodipy (middle), and overlay of images (right) after 24 h of incubation in A549 cells. Field of view = 75 $\mu$ m $\times$ 75 $\mu$ m.....	255
Figure 4. 30 Fluorescence mean intensity of Rh <sub>2</sub> phenbodipy in A549 cancer cells measured after 24 h incubation. The graphs represent means with standard deviation. The asterisk (*) indicates significant difference compared to the 10 $\mu$ M concentration at $p < 0.05$ .....	256
Figure 5. 1 Molecular structures of monocationic Ru compounds containing the DIP ligand.....	261
Figure 5. 2 Schematic representation of the (a) equatorial and (b) axial positions from which a fluorophore can be attached to the dirhodium core.....	263

## LIST OF TABLES

	Page
Table 2. 1 Crystal Structural Data and Refinement Parameters for the compounds [Ru(bpy) <sub>2</sub> (dphol)][PF <sub>6</sub> ]·(CH <sub>3</sub> ) <sub>2</sub> CO (1) and [Ru(bpy) <sub>2</sub> (hbtz)][PF <sub>6</sub> ]·(CH <sub>3</sub> ) <sub>2</sub> CO (3).....	74
Table 2. 2 Crystal Structural Data and Refinement Parameters for the compounds [Ru(phen) <sub>2</sub> (hbtz)][PF <sub>6</sub> ] (4) and Ir(phpy) <sub>2</sub> (hbtz) (6). ....	75
Table 2. 3 Selected bond distances and angles for [Ru(bpy) <sub>2</sub> (dphol)][PF <sub>6</sub> ]·(CH <sub>3</sub> ) <sub>2</sub> CO (1). ....	76
Table 2. 4 Selected bond distances and angles for [Ru(bpy) <sub>2</sub> (hbtz)][PF <sub>6</sub> ]·(CH <sub>3</sub> ) <sub>2</sub> CO (3).....	76
Table 2. 5 Selected bond distances and angles for [Ru(phen) <sub>2</sub> (hbtz)][PF <sub>6</sub> ] (4). ....	77
Table 2. 6 Selected bond distances and angles for Ir(phpy) <sub>2</sub> (hbtz) (6). ....	77
Table 2. 7 Distances and angles associated with the π-π stacking interaction of polypyridyl ligands in compounds 1, 3 and 4.....	79
Table 2. 8 Half wave redox potentials ( <i>E</i> <sub>1/2</sub> ) of 1–6 recorded in acetonitrile.....	85
Table 2. 9 Electronic absorption data for 1–6 recorded in acetonitrile. ....	94
Table 2. 10 Cytotoxicity data for Ru and Ir complexes against A549 cells.....	100
Table 3. 1 Crystal Structural Data and Refinement Parameters for the compounds [Ru(phpy)(biq) <sub>2</sub> ][PF <sub>6</sub> ]·2CH <sub>2</sub> Cl <sub>2</sub> (5) and [Ru(phpy)(bpy)(NCCH <sub>3</sub> ) <sub>2</sub> ][PF <sub>6</sub> ]·NCCH <sub>3</sub> (9). ....	144
Table 3. 2 Selected bond distances and angles for [Ru(phpy)(biq) <sub>2</sub> ][PF <sub>6</sub> ]·2CH <sub>2</sub> Cl <sub>2</sub> (5).....	145
Table 3. 3 Selected bond distances and angles for Ru((phpy)(bpy)(NCCH <sub>3</sub> ) <sub>2</sub> )[PF <sub>6</sub> ]·NCCH <sub>3</sub> (9). ....	145
Table 3. 4 Crystal Structural Data and Refinement Parameters for the compounds [Ru(phpy)(pap)(NCCH <sub>3</sub> ) <sub>2</sub> ][PF <sub>6</sub> ] (6) and [Ru(phpy)(pap)(dcmb)][PF <sub>6</sub> ] (7). ....	154

Table 3. 5 Selected bond distances and angles for [Ru(phpy)(pap)(NCCH <sub>3</sub> ) <sub>2</sub> ][PF <sub>6</sub> ] (6). .....	155
Table 3. 6 Selected bond distances and angles for [Ru((phpy)(pap)(dcmb))][PF <sub>6</sub> ] (7). .....	155
Table 3. 7 Half wave redox potentials ( $E_{1/2}$ ) of 1–8 recorded in acetonitrile.....	163
Table 3. 8 Absorption maxima of 1–8 recorded in acetonitrile.....	168
Table 3. 9 Energies ( $E_{MO}$ ) and percent contributions of selected MOs of [Ru(bpy) <sub>3</sub> ] <sup>2+</sup> , 1 and 2 and 4.....	177
Table 3. 10 Energies ( $E_{MO}$ ) and percent contributions of selected MOs of 4–6 and 8.....	178
Table 3. 11 Frontier orbitals (HOMO-2 to LUMO) for [Ru(bpy) <sub>3</sub> ] <sup>2+</sup> , 1, 2 and 4 (isovalue = 0.04). .....	179
Table 3. 12 Frontier orbitals (LUMO+1 to LUMO+4) for [Ru(bpy) <sub>3</sub> ] <sup>2+</sup> , 1, 2 and 4 (isovalue = 0.04). .....	180
Table 3. 13 Frontier orbitals (HOMO-2 to LUMO) for 5, 6 and 8 (isovalue = 0.04). .....	181
Table 3. 14 Frontier orbitals (LUMO+1 to LUMO+4) for 5, 6 and 8 (isovalue = 0.04). .....	182
Table 3. 15 TDDFT data of [Ru(bpy) <sub>3</sub> ] <sup>2+</sup> .....	189
Table 3. 16 TDDFT data of 1.....	189
Table 3. 17 TDDFT data of 2.....	190
Table 3. 18 TDDFT data of 4.....	191
Table 3. 19 TDDFT data of 5.....	193
Table 3. 20 TDDFT data of 6.....	193
Table 3. 21 Cytotoxicity data of Ru complexes against HeLa cells. ....	195
Table 3. 22 Cytotoxicity data of compounds 2 and 8 against ovarian cancer cells.....	198

# CHAPTER I

## INTRODUCTION

### **Motivation: Worldwide and United States Cancer Statistics**

Cancer is a complex family of more than one hundred diseases characterized by the uncontrolled growth of cells produced by multiple alterations at the genomic level.<sup>1,2</sup> It is caused by both internal factors (inherited DNA mutations, hormones, immune system defects) and external factors (tobacco consumption, passive smoking, infectious organisms, environmental chemicals and radiation).<sup>3,4</sup> The abnormal gene expression that occurs in cancer causes an imbalance between cell proliferation and cell death and evolves into a population of cells (tumor or neoplasm) that can invade other tissues by spreading through the blood and lymph systems often interrupting vital functions, causing significant disease and, if untreated, death of the host.<sup>1,2</sup> In contrast, benign tumors grow by expansion, are encapsulated and do not invade surrounding tissue, but they may become life threatening if they press on nerves or blood vessels.<sup>1</sup>

According to the World Health Organization and the American Cancer Society, cancer is the leading cause of death worldwide in developed countries and the second leading cause of death in developing countries following heart disease.<sup>5</sup> In 2008, 12.7 million new cancer cases were diagnosed, from which 5.6 million and 7.1 million cases occurred in economically developed and economically developing countries, respectively, and 7.6 million deaths were estimated the same year (2.8 million and 4.8

million deaths in economically developed and economically developing countries, respectively).<sup>5</sup> Lung and bronchial cancer (~0.95 million deaths) and breast cancer (~0.46 million deaths) were the most common cancer types in men and women worldwide, respectively, in 2008.<sup>5</sup> The World Cancer Research Fund has estimated that overweight or obesity, physical inactivity, and/or poor nutrition cause up to one third of the cancer cases in developed countries.<sup>3</sup>

Cancer is the second leading cause of death in the United States after heart disease.<sup>6,7</sup> Lung cancer remains the most common cancer that leads to death in men since the 1950s.<sup>3</sup> Although the mortality rates of this type of cancer in men have decreased gradually since 1990,<sup>1,3</sup> data indicate that it still has one of the lowest 5-year percent survival rates (16.8% for both sexes the 2004–2010 period).<sup>8</sup> Breast cancer has been the leading cause of death among cancer types in women since the 1950s and was later overtaken by lung cancer since the 1985–1990 period.<sup>3</sup>

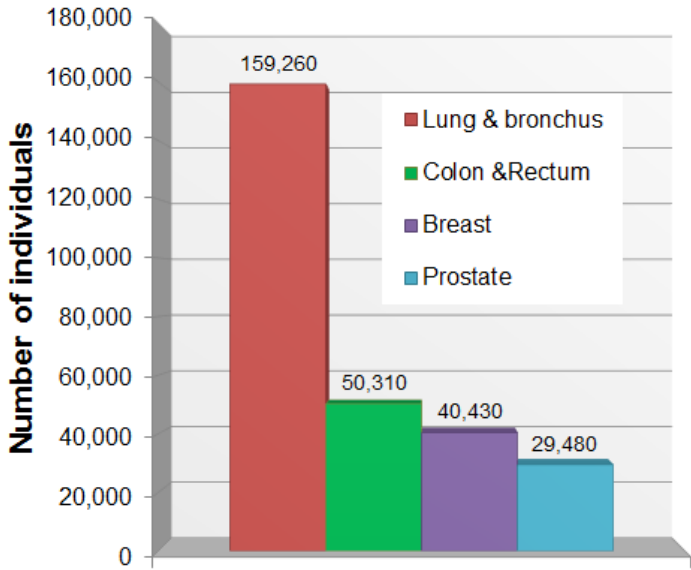
In the year 2014, the American Cancer Society has estimated that ~1.67 million new cancer cases will be diagnosed and ~0.58 million deaths will occur (~1 600 deaths per day!).<sup>3</sup> The cancer types with the highest mortality (both sexes) continue to be lung and bronchial, colorectal, breast and prostate cancers (Figure 1.1) and account for almost half (~0.28 million) of the estimated deaths in the present year.<sup>3</sup> The prevalence of lung cancer as the first cause of death in the United States has been attributed to cigarette smoking, pollution, diet and lifestyle changes, and the American Cancer Society has estimated that almost 176,000 of the estimated deaths in 2014 could have been prevented by stopping cigarette smoking and the heavy use of alcohol.<sup>3</sup> Although there has been a

steady rise in cancer death rates during the past >75 years (in part because more people live long enough to acquire this disease), a greater amount of people are cured from cancer today. For example, only 25% of people diagnosed with cancer lived at least 5 years after treatment in the 1940s and that figure rose to 40% in the 1990s.<sup>1</sup>

The aforementioned cancer statistics underscores the fact that cancer is a worldwide problem and a major health issue in the United States. Such statistics continue to prompt enormous global research efforts across several disciplines to gain a better understanding of cancer biology with the aims of providing faster and more accurate cancer diagnosis, improved treatments and better health care for cancer patients. Chemistry is the scientific discipline that is at the forefront of cancer drug research and continuously provides solutions for the treatment of cancer through the development of more effective and safer chemotherapy drugs.



**Estimated Number of Deaths  
by Cancer Type - US, 2014**



Total estimated number of deaths for 2014: 585,720

**Figure 1. 1** Estimated number of cancer deaths in the United States for 2014. Data obtained from the National Cancer Institute, reference 3.

## Platinum Compounds in Cancer Drug Research

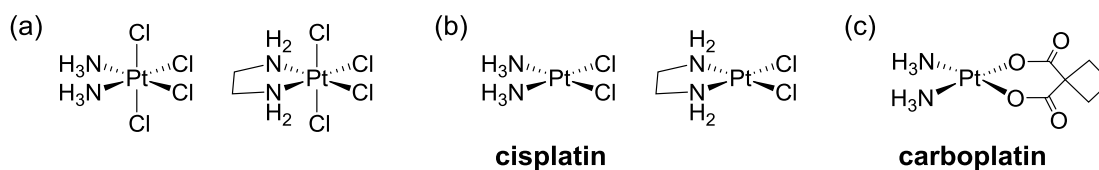
### *Cisplatin, The Landmark Story of an Inorganic Compound*

Bioinorganic chemistry is a research area that focuses on the role of metal ions in biological processes including the transport, storage and function of metal ions in living systems, the structure and activity of metalloproteins, the impact of metals in natural environments and the application of metals in medicine.<sup>9,10</sup> The latter field is known as medicinal inorganic chemistry, where the unique properties of metal ions are exploited in the rational design of metallodrugs for the diagnosis and therapy of diseases and metabolic disorders.<sup>11,12,13,14</sup> The great variety of coordination numbers and molecular geometries of transition metal complexes, which are not readily available to organic-based drugs, the possibility to access different redox states and fine-tune ligand substitution kinetics, as well as the intrinsic properties of the metal ion and the ligand environment, constitute a rich platform to tailor the medicinal properties of a drug.<sup>14,15,16</sup>

A revolution on this field occurred in the 1960's, when Barnet Rosenberg, Loretta VanCamp and Thomas Krigas at Michigan State University serendipitously discovered the antiproliferative properties of platinum (Pt) compounds while studying the effects of an electric field on the cell growth of *Escherichia coli* bacteria. In their seminal paper published in 1965,<sup>17</sup> the authors reported filamentous bacterial growth and inhibition of cell division a few hours after turning on the electric field. The observed antiproliferative activity was not due to the generated electric current, but by a Pt compound that was formed by oxidation of the Pt mesh electrodes that were included in the growth chamber that also contained ammonium chloride (NH<sub>4</sub>Cl) buffer. Further studies suggested that an octahedral Pt(IV) species such as [NH<sub>4</sub>]<sub>2</sub>[PtCl<sub>6</sub>] or *cis*-Pt(NH<sub>3</sub>)<sub>2</sub>Cl<sub>4</sub> was responsible of bacterial growth inhibition.<sup>17</sup>

In 1969, Rosenberg and coworkers reported that two Pt(IV) compounds *cis*-Pt(NH<sub>3</sub>)<sub>2</sub>Cl<sub>4</sub> and Pt(NH<sub>2</sub>CH<sub>2</sub>CH<sub>2</sub>NH<sub>2</sub>)Cl<sub>4</sub> (Figure 1.2a), and two Pt(II) compounds, *cis*-Pt(NH<sub>3</sub>)<sub>2</sub>Cl<sub>2</sub> and Pt(NH<sub>2</sub>CH<sub>2</sub>CH<sub>2</sub>NH<sub>2</sub>)Cl<sub>2</sub> (Figure 1.2b), decreased the tumor size and increased the survival time of mice bearing sarcoma 180 and leukemia L1210 tumors. The Pt(II) compound *cis*-Pt(NH<sub>3</sub>)<sub>2</sub>Cl<sub>2</sub> (cisplatin) was the most active and led to the realization “that inorganic platinum metal compounds form a new class of antitumor agents”.<sup>18</sup> Such a discovery represents a milestone in Inorganic Chemistry and has profoundly influenced the design of anticancer drugs and cancer research. Later, cisplatin (Platinol®, Bristol Myers Squibb) was approved by the Food and Drug administration (FDA, 1978) to treat metastatic ovarian and testicular cancers. In 1993, its approval to treat cell bladder cancer was quickly granted.<sup>9,19</sup> Other cancers that are

treated with cisplatin include cervical, head and neck, esophageal, non-small cell lung cancer (NSCLC) and small-cell lung cancer (SCLC).<sup>20,21</sup> Since the discovery of its antitumor properties, cisplatin has become a benchmark in the field, a front-line anticancer agent and one of the most effective chemotherapeutic agents in clinical use, achieving impressive cure rates of 90% for testicular cancer.<sup>22,23</sup>



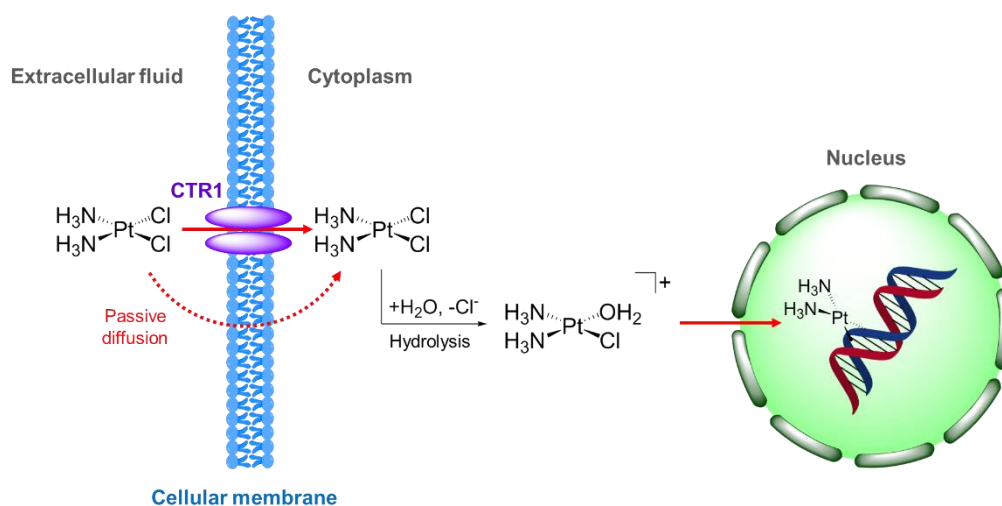
**Figure 1. 2** Molecular structures of (a) Pt(IV) and (b) Pt(II) antitumor compounds reported by Rosenberg in 1969 and (c) carboplatin.

The clinical use of cisplatin is, unfortunately, accompanied by detrimental dose-limiting side effects such as neurotoxicity (nervous system damage), hepatotoxicity (liver damage), ototoxicity (hearing loss), nephrotoxicity (kidney damage), gastrointestinal tract toxicity, nausea and vomiting, because of its indiscriminate uptake by normal healthy cells as well as rapidly dividing tumor cells.<sup>19,21</sup> These side effects are due to cisplatin binding to proteins present in the bloodstream, particularly those containing thiol groups such as human serum albumin: it has been reported that one day after cisplatin administration, ~90% of the platinum in blood plasma is protein bound.<sup>24,25</sup> Inherent resistance (observed in patients with colorectal, prostate, breast and NSCLC) or acquired resistance (as occurs in patients with ovarian cancer) during cycles of therapy is the second major problem associated with Pt drugs.<sup>19,26,27</sup>

Carboplatin (Paraplatin®, Bristol Myers Squibb, Figure 1.2c), a second generation Pt(II) compound, was developed to lower the systemic toxicity of cisplatin and it was approved by the FDA in 1989 to treat ovarian cancer.<sup>9,19</sup> This drug has similar efficacy profile to cisplatin, but with the advantage that it does not exhibit nephrotoxicity and provokes lower neurotoxicity and gastrointestinal toxicity than cisplatin. However, myelosuppression (decreased bone marrow activity that leads to low levels of red blood cells, white blood cells and platelets) is dose-limiting for this drug.<sup>19</sup> Carboplatin is currently undergoing clinical trials for the treatment of salivary gland cancer and advanced mullerian cancer (a type of ovarian cancer).<sup>21</sup>

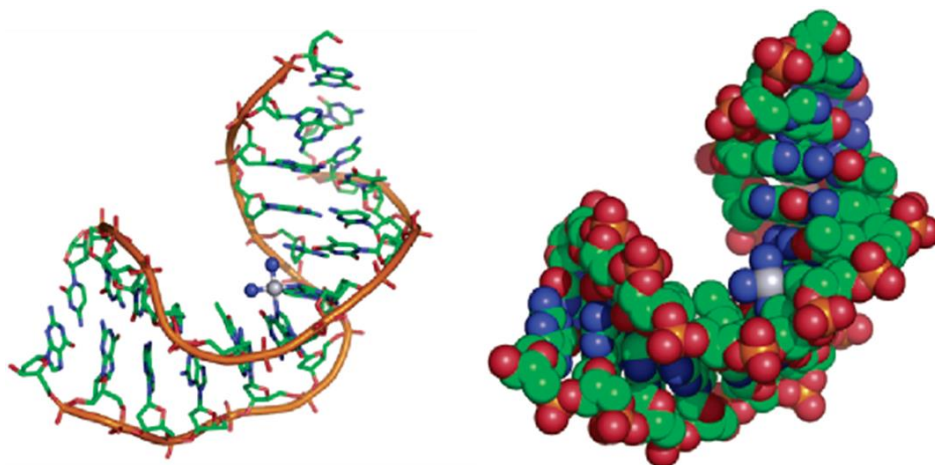
### *Mechanism of Action*

Upon administration via intravenous injection, the high chloride ( $\text{Cl}^-$ ) concentration in the bloodstream ( $\sim 100$  mM) prevents hydrolysis of the Pt–Cl bonds.<sup>19,20,22</sup> Cisplatin then traverses the cellular membrane of cancer and healthy cells via passive diffusion,<sup>28,29,30,31</sup> facilitated diffusion through the copper transporter-1 protein (CTR1), a transmembrane plasma protein that mediates copper homeostasis, has also been reported to play an important role in the cellular uptake of this drug.<sup>19,31,32,33,34,35,36</sup> Cisplatin is then thermally activated intracellularly by hydrolysis (aquation) of one of the Pt–Cl bonds ( $\text{Pt}^{\text{II}}\text{--Cl} + \text{H}_2\text{O} \rightarrow \text{Pt}^{\text{II}}\text{--OH}_2 + \text{Cl}^-$ , Figure 1.3) forming the reactive cationic mono-aqua species  $\text{cis-}[\text{Pt}(\text{NH}_3)_2(\text{H}_2\text{O})\text{Cl}]^+$ ,<sup>37,38,39</sup> which is able to react more readily with cellular targets. The lower cytoplasmic chloride concentration ( $\sim 4$  mM) facilitates the hydrolysis reaction.<sup>19,22,31</sup> Cisplatin can be therefore regarded as a prodrug since it needs to be activated by hydrolysis before it binds to DNA.<sup>40</sup>



**Figure 1. 3** Cellular uptake and mechanism of action of cisplatin.

Although many cellular components (RNA, proteins, membrane phospholipids, and microfilaments that make up the cytoskeleton) react with  $\text{cis-}[\text{Pt}(\text{NH}_3)_2(\text{H}_2\text{O})\text{Cl}]^+$ , it is well-accepted that the antitumor activity of cisplatin derives from its ability to form bifunctional DNA crosslinks.<sup>20</sup> Different types of DNA adducts can be formed, with 1,2-intrastrand  $\text{cis-}[\text{Pt}(\text{NH}_3)_2(\text{dGpG})]$  (*cis*-GG) and  $\text{cis-}[\text{Pt}(\text{NH}_3)_2(\text{dApG})]$  (*cis*-AG) crosslinks being the major adducts (65% and 25%, respectively), in which the Pt center is bound to the N7 positions of the two adjacent purine bases.<sup>20,41,42</sup> Figure 1.4 depicts the 2.6 Å resolution X-ray crystal structure of a DNA dodecamer containing a 1,2-intrastrand  $\text{cis-}[\text{Pt}(\text{NH}_3)_2(\text{dGpG})]$  reported by Stephen J. Lippard in 1995, in which the helix unwinds and bends by  $\sim 50^\circ$  toward the major groove.<sup>20,42</sup>



**Figure 1. 4** X-ray structure of duplex DNA containing a cisplatin 1,2-d(GpG) intrastrand cross-links (left) and space filling model of the same structure (right). The platinum ion is depicted in gray color. Adapted with permission from reference 31. Copyright 2007 American Chemical Society.

Cisplatin binding to DNA is kinetically controlled and the rate limiting step for DNA binding is the aquation reaction mentioned above, with a half-life ( $t_{1/2}$ ) of  $\sim 2$  h that is in the same order of magnitude as cellular division processes,<sup>20,22,43</sup> explaining the success of this type of Pt(II) compound as an anticancer drug since rapid ligand substitution kinetics would prevent it from reaching its biological target. The DNA distortions caused by cisplatin impede replication and transcription and eventually lead to apoptotic cell death or cell cycle arrest.<sup>19,20,31</sup>

Carboplatin forms the same type of DNA adducts like cisplatin, but hydrolysis and Pt-DNA adduct formation rates are slower for carboplatin because the



cyclobutanediendicarboxylato ligand is not a good leaving group compared to the chloride ligands of cisplatin. For example, the rate constants for the aquation of cisplatin and carboplatin at 37°C in free Cl<sup>-</sup> phosphate buffer (pH = 7) are  $8 \times 10^{-5} \text{ s}^{-1}$  ( $t_{1/2} = 2.4 \text{ h}$ ) and  $7.2 \times 10^{-7} \text{ s}^{-1}$  ( $t_{1/2} = 267 \text{ h}$ ), respectively.<sup>44</sup> In addition, higher doses of carboplatin (20–40-fold) with respect to that of cisplatin are needed to produce the same amount of bound Pt-DNA lesions *in vivo* due to the much faster rate of aquation of cisplatin.<sup>44</sup> The slower ligand substitution kinetics of carboplatin also explains the reduced side effects in cancer patients with respect to cisplatin.

### *Tumor Resistance*

Cisplatin and carboplatin resistance can occur from (i) reduced platinum accumulation by decreased influx or increased efflux of the Pt drugs, (ii) increased production of intracellular thiol-containing molecules, (iii) increased ability to repair Pt-DNA lesions and (iv) increased ability to tolerate Pt-DNA lesion thereby failing to induce cell death.<sup>19,20,27,45,46</sup>

Down-regulation of CTR-1 and overexpression of proteins that are involved in copper intracellular transport and efflux (copper export pump proteins ATP7A ATP7B) have been implicated in cisplatin and carboplatin resistance.<sup>34,35,47</sup> High intracellular levels of thiol-containing species such as glutathione (GSH) and metallothioneins (a detoxification protein rich in cysteine and methionine amino acids) have been also found in Pt-resistant cancer cells, which are able to deactivate and facilitate the efflux of Pt

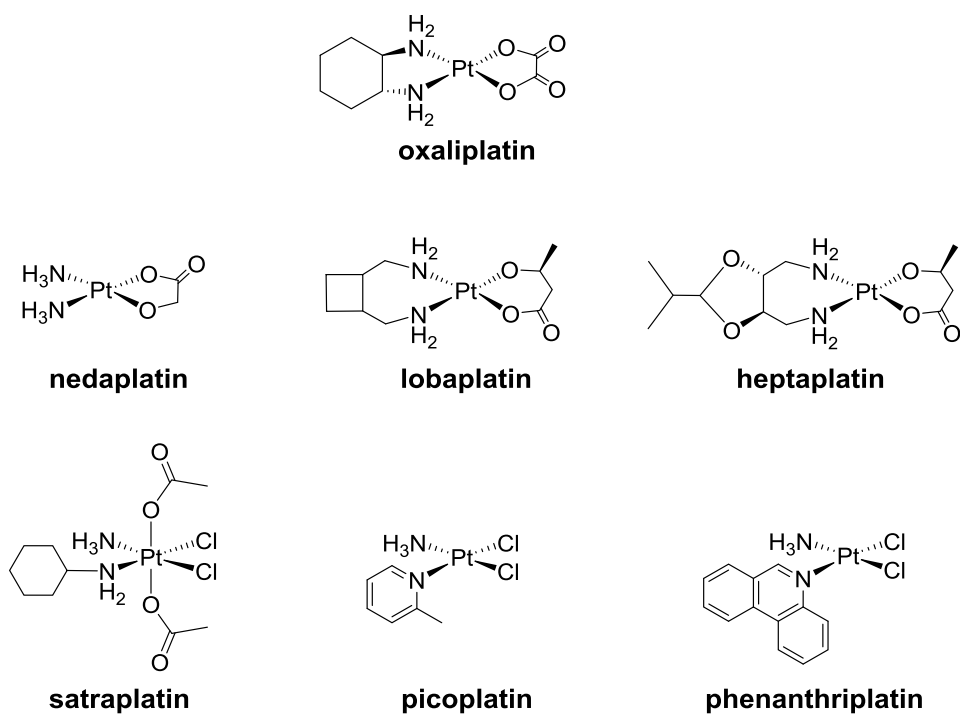
drugs.<sup>19,45</sup> For example, the cisplatin-GSH conjugate is readily exported from cells by the ATP-dependent glutathione *S*-conjugate export pump (GS-X pump, also known as MRP2 or ABCC2), decreasing the intracellular accumulation of cisplatin.<sup>48,49</sup>

Increased DNA-repair capacity has been observed in Pt-resistant cancer cells, in which nucleotide excision repair (NER) is one of the major pathways for the removal of DNA lesions.<sup>19,31,45</sup> In contrast, low NER capacity in testicular tumors explains the high cure rates observed for this cancer type.<sup>19</sup> The mismatch repair (MMR) system also plays an important role in cisplatin resistance.<sup>45,50</sup> When this pathway is active, MMR proteins are unable to repair DNA lesions at the platination site and trigger an apoptotic signal to destroy the cell; this death signal, however, is reduced by MMR deficiency in cisplatin- and carboplatin-resistant cancer cells.<sup>50</sup> Increased ability of DNA polymerases (such as Pol  $\beta$  and Pol  $\eta$ ) to bypass cisplatin-DNA lesions during DNA replication (a process called translesion synthesis)<sup>51,52</sup> and decreased expression of apoptotic signaling pathways (*e.g.* mutations on the tumor suppression protein p53, down-regulation of Bax, overexpression of Bcl-2)<sup>45</sup> have also been involved in cell resistance to cisplatin and carboplatin.

The development of Pt compounds that circumvent cancer cell resistance continued during the 1900's and several drugs entered clinical trials. Armed with a better understanding of the mechanism of action of Pt drugs, a third Pt(II) drug which is called oxaliplatin (Eloxatin®, Sanofi-Aventis, Figure 1.5) was discovered and received accelerated FDA approval in 2002 for the treatment of metastatic colorectal cancer in combination with 5-fluorouracil and leukovorin, for which both cisplatin and

carboplatin are clinically inactive due to cell resistance to these two drugs.<sup>9,19,53</sup> Studies have revealed that up-regulation of organic cation transporters (OCTs) in cancer cells increase the cellular uptake of oxaliplatin; the propensity of colorectal cancer cells to overexpress OCTs in the plasma membrane may explain the efficacy of oxaliplatin for the treatment of metastatic colorectal cancer.<sup>54</sup> It has been also hypothesized that the ability of oxaliplatin to overcome resistance relies on the bulkiness of the cyclohexane moiety around the Pt-DNA lesion that prevents the recognition and binding of DNA repairing proteins, inducing cell death more efficiently.<sup>21,32,53</sup> Neuropathy (nerve toxicity) is one of the side effects reported for oxaliplatin.<sup>9,19,53</sup>

The design and development of new antitumor Pt compounds (Figure 1.5), such as nedaplatin (approved in Japan in 1995 for the treatment of NSCLC and SCLC, head, neck and esophageal cancers), lobaplatin (approved in China for the treatment of chronic myelogenous leukemia, inoperable metastatic breast cancer and SCLC), heptaplatin (approved in South Korea for the treatment of gastric cancer), satraplatin (phase III clinical trials; orally active; treatment of hormone-refractory prostate cancer), picoplatin (phase III clinical trials; treatment of SCLC, colorectal and ovarian cancer, hormone-refractory prostate cancer) and phenanthriplatin (developed by Stephen J. Lippard, MIT; preclinical trials), among others, as well as the strategies that are currently being followed to improve the delivery of Pt drugs to tumors (Prolindac<sup>TM</sup> and Lipoplatin<sup>TM</sup>) and overcome cell resistance will not be further addressed since thorough reviews have been published in the literature.<sup>14,19,21,55,56,57,58</sup>



**Figure 1. 5** Molecular structures of oxaliplatin and other Pt drugs.

The development of cisplatin as an antitumor drug is considered the most successful example of an inorganic compound in medicinal chemistry and it is often referred as the “gold standard” or “prototype” inorganic drug, because it gave birth to modern medicinal inorganic chemistry and started a new area of anticancer research based on metallopharmaceuticals. Numerous studies to understand the activation, mechanism of action, toxicity, cell resistance and cellular processing of cisplatin both *in vitro* and *in vivo* have been fundamental for the successful development of new

generations of Pt-based antitumor drugs (carboplatin and oxaliplatin) which are widely used in cancer treatment today worldwide. Considering that approximately half of all cancer patients are currently treated with a platinum drug,<sup>57</sup> and that the worldwide annual sales of platinum anticancer drugs in 2011 were \$2.062 billion in the United States<sup>59</sup> with Eloxatin® alone occupying the fifth place among the leading cancer drugs (~\$1.3 billion in revenue),<sup>60</sup> reflects the importance of metal based-drugs on the treatment of the second cause of death in the United States.

Several strategies are currently under investigation to improve the activity, reduce systemic toxicity, overcome cellular resistance and develop vehicles for targeted chemotherapy of Pt compounds with the ultimate goal of improving cancer patient care. The success of Pt compounds in the clinic has also stimulated the exploration of the antitumor properties of several other transition metals including ruthenium, osmium, rhodium, iridium, gold and titanium, among which ruthenium has emerged as a particularly attractive alternative to platinum in cancer therapeutics. This topic will be discussed after providing an overview of one of the main mechanisms of cell death that is relevant to metal-based cancer drugs, namely apoptosis.

## **Intrinsic Pathway of Apoptosis**

Apoptosis, also known as programmed cell death, is a tightly regulated and ordered process wherein cells that are no longer needed, or that are a threat to the integrity of an organism, are induced to commit “suicide”.<sup>61,62,63</sup> Since most chemotherapeutic drugs act through induction of apoptosis,<sup>64</sup> the topic will be briefly described.

The intrinsic pathway is one of the two most characterized (the other one being the extrinsic pathway) and prominent mechanisms that leads to apoptosis; most apoptosis in mammals occurs through this mechanism.<sup>61,64,65</sup> The intrinsic pathway is also known as mitochondrial pathway since mitochondria, the powerhouse of the cell, play a crucial role in this route to cell death. The outer mitochondrial membrane contains anti-apoptotic (also called pro-survival) proteins of the Bcl-2 family such as Bcl-2 and Bcl-xL that maintain the integrity of the outer mitochondrial membrane and promote cell survival by preventing the release of cytochrome *c* and other pro-apoptotic proteins from the mitochondria to the cytosol and the nucleus.<sup>61,64,65</sup>

When internal cell stress occurs, such as DNA damage, mitochondria damage, endoplasmic reticulum stress, formation of reactive oxygen species (ROS), pro-apoptotic proteins from the Bcl-2 family such as Bax and Bak migrate to the outer mitochondrial membrane and oligomerize which inhibits Bcl-2 proteins and creates supramolecular openings (pores) on the surface of the mitochondrion. As a consequence, outer mitochondrial membrane permeabilization (MMP) takes place and proteins located in the intermembrane space (*e.g.* cytochrome *c*) are able to diffuse into the cytosol.<sup>61,64,65,66</sup> Cytochrome *c* translocates to the endoplasmic reticulum where it binds the inositol (1,4,5) trisphosphate receptor (InsP<sub>3</sub>R), triggering Ca<sup>2+</sup> release and an increase in the concentration of this cation in the cytosol.<sup>67</sup>

MPP is accompanied by the long-lasting opening of the mitochondrial permeability transition pore (MPTP, which is a protein complex that forms a channel and allows the exchange of metabolites between the cytosol and the mitochondrial matrix), allowing the entrance of Ca<sup>2+</sup> into the mitochondrial matrix and causing permanent dissipation of the inner mitochondrial transmembrane potential ( $\Delta\Psi_m$ ), permeabilization of the inner mitochondrial membrane and decreased ATP production.<sup>61,67</sup> As a consequence, an augmented release of cytochrome *c* is produced.<sup>67</sup> In addition, swelling of the mitochondria is observed due to the massive entry of solutes and water.

After these initial events, cytosolic cytochrome *c* is recruited by the apoptotic protease activating factor-1 (Apaf-1), along with the cofactors dATP/ATP (deoxyadenosine triphosphate/adenosine triphosphate), and forms a wheel-shaped

multiprotein complex known as apoptosome. The apoptosome binds and activates caspase-9 (caspase = cysteine-dependent aspartate specific proteinase). This initiator caspase then activates the executioner (effector) caspases -3, -6 and -7, which digest structural proteins in the cytoplasm and degrades chromosomal DNA during the demolition phase of apoptosis.<sup>68</sup> Other morphology changes that are observed during apoptosis are: cell shrinkage, plasma membrane blebbing, chromatin condensation, nuclear fragmentation, chromosomal DNA degradation and phosphatidylserine exposure on the surface of the plasma membrane.<sup>61,62,63</sup> The downstream cascade of proteolytic activity dismantles the cell; the cell breaks apart and forms membrane-bound vesicles called apoptotic bodies that are phagocytized and digested by macrophages or neighboring cells without activating immune response.<sup>62,63,65,68</sup>

Necrosis is a different mechanism of cancer cell death that is characterized by gain of cell volume that leads to rupture of the plasma membrane, along with an unorganized dismantling of organelles.<sup>62,63</sup> Necrosis is considered to be harmful because necrotic cells burst, damage neighboring healthy cells and promote a local inflammation response that may support tumor growth.<sup>61,62,63</sup> For this reason, harmless removal of tumor cells through apoptosis is a desirable feature for cancer chemotherapy.



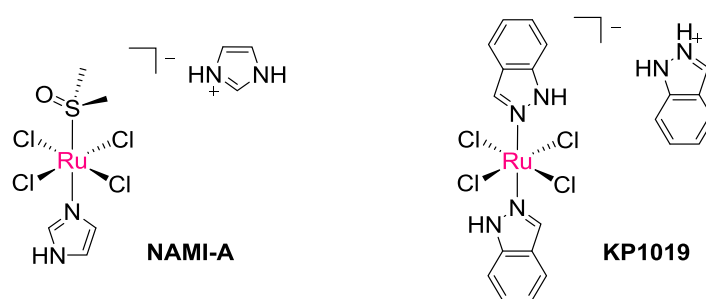
## The Emergence of Ruthenium Anticancer Drugs

### *Ruthenium(III) Drugs in Clinical Trials for Cancer Chemotherapy*

Ruthenium (Ru) is a second row transition metal that belongs to the so-called platinum group elements. The investigation of Ru complexes as metallopharmaceuticals for the treatment of cancer disease has been fuelled by the success of Pt drugs in the clinic and is now a fruitful and mature field that has successfully led to the investigation of two drugs in clinical trials.<sup>16,69,70</sup>

The Ru compounds that are in phase II clinical trials are  $[\text{H}_2\text{im}][\text{trans-RuCl}_4(\text{S-dmso})(\text{Him})]$  (NAMI-A; Him = imidazole, dmso = dimethylsulfoxide, Figure 1.6) and  $[\text{H}_2\text{ind}][\text{trans-RuCl}_4(\text{Hind})_2]$  (KP1019; Hind = indazole, Figure 1.6).<sup>70,71</sup> Although the structures of these drugs are quite similar, they exhibit contrasting anticancer properties. NAMI-A was developed by Enzo Alessio, Gianni Sava and coworkers in Italy, it does not exhibit appreciable cytotoxicity in cancer cell cultures, but it has an impressive efficacy for stopping solid tumor metastases, such as lung metastases. The drug entered clinical trials in 1999.<sup>71</sup> This Ru compound induces caspase activation, inhibits matrix metalloproteinases (Zn-containing proteolytic enzymes that degrade the extracellular matrix that surrounds tumors and facilitate tumor migration), promotes tumor adhesion and decreases angiogenic activity, preventing tumor invasion to healthy tissue.<sup>69,71,72,73,74</sup> The drug KP1019 was developed by Bernhard K. Keppler and coworkers in Germany and is superbly active against platinum-resistant colorectal tumors and kills tumors cells

via the intrinsic pathway of apoptosis (induces depolarization of inner mitochondrial membrane, activation of caspase-3 and down-regulation of Bcl-2);<sup>70</sup> this drug entered clinical trials in 2003.<sup>75,76,77</sup> Both Ru drugs display low general toxicity toward healthy tissues because the Ru(III) ion is capable of mimicking iron (Fe(III)) in binding to important carrier proteins, such as transferrin.<sup>74,78</sup> In fact, X-ray crystallographic studies have demonstrated that KP1019 binds to apo-lactoferrin via a histidine residue and the indazole ligands remain bound to the Ru center.<sup>75,78,79</sup> Since cancer cells overexpress transferrin receptors to satisfy their increased demand for iron,<sup>71,76,80</sup> NAMI-A and KP1019 may be delivered more efficiently and selectively to cancer cells, explaining their lower systemic toxicity.<sup>71</sup>



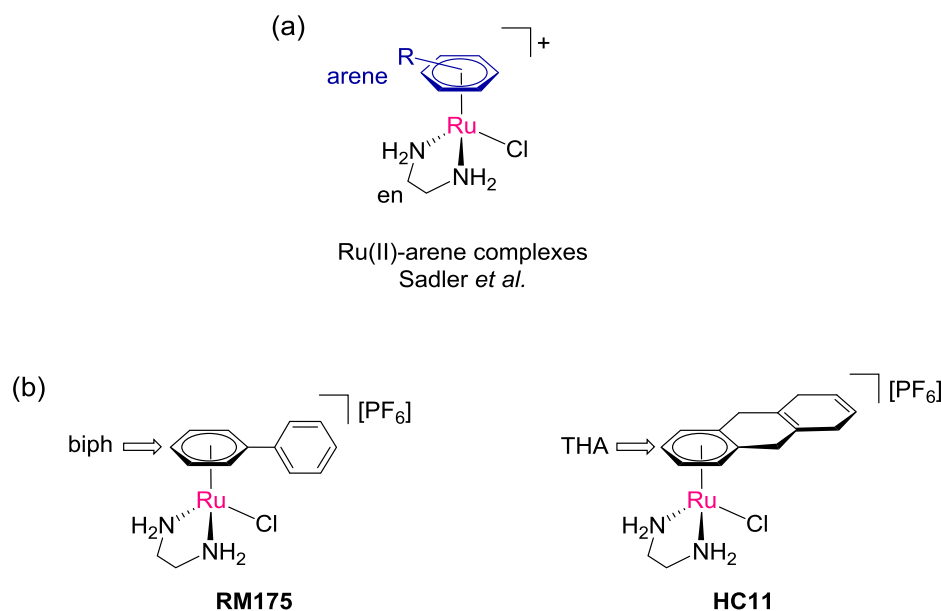
**Figure 1. 6** Molecular structures of Ru drugs in clinical trials.

KP1019 and NAMI-A contain a Ru(III) center and it has been hypothesized by Clarke and coworkers that these two drugs are activated by intracellular reduction (promoted by glutathione) of the metal center to Ru(II), followed by hydrolysis and binding to biological targets.<sup>74</sup> This type of activation may confer selectivity towards solid tumors because they are more hypoxic due to insufficient vascularization and provide a more reducing environment than normal tissues facilitating the metal-based reduction.<sup>71,81</sup> The ligand exchange kinetics of coordination compounds of Pt(II) and Ru(II) with chloride and N-donor ligands is similar, and within the timescale of cellular division processes, which could explain in part the applicability of Ru(II) compounds as chemotherapy drugs.<sup>22,43,82</sup> However, this “activation by reduction” mechanism still remains only a hypothesis.<sup>69</sup> Although numerous *in vitro* and *in vivo* investigations have been performed, the mechanism of action of NAMI-A and KP1019 is still poorly understood, biological targets *in vivo* have not been conclusively determined and their identification remains a challenging task that requires the collective knowledge from many different fields, including chemistry, pharmacology, molecular biology, physiology and medicine, requiring an interdisciplinary approach.<sup>40,69,75</sup>

## *Ruthenium(II) Organometallic Compounds as Anticancer Agents*

The impressive antitumor properties of NAMI-A and KP1019 and their evaluation in human clinical trials sparked interest in the exploration of the biological activities of Ru compounds across different research areas leading to the development of novel classes of Ru(II) antitumor compounds, among which organometallic complexes reported by Peter J. Sadler (United Kingdom) and Paul J. Dyson (Switzerland) hold great potential and are currently in preclinical trials.<sup>70,82,83,84,85,86</sup> These organometallic anticancer drugs belong to an emerging and exciting field known as bioorganometallic chemistry, which will be further discussed in Chapter II.

Organometallic Ru(II)-arene compounds of the type  $[(\eta^6\text{-arene})\text{RuCl}(\text{en})]^+$  (en = ethylenediamine, Figure 1.7a), developed by Sadler and coworkers, were reported to exhibit cytotoxic properties against a variety of cancer cell lines.<sup>87,88,89</sup> In these complexes, the arene ligand stabilizes the Ru(II) oxidation state and occupies three coordination sites of the pseudo-octahedral geometry.<sup>40</sup> The bidentate en ligand provides relatively good water solubility and recognition sites since its NH groups can engage in hydrogen-bonding interactions, and the chloride ligand endows these complexes with a reactive site.<sup>40</sup> In particular,  $[(\eta^6\text{-biph})\text{RuCl}(\text{en})][\text{X}]$  (RM175; biph = biphenyl, X = Cl<sup>-</sup> or PF<sub>6</sub><sup>-</sup>, Figure 1.7b) and  $[(\eta^6\text{-THA})\text{RuCl}(\text{en})][\text{X}]$  (HC11; THA = 5,8,9,10-tetrahydroanthracene, X = Cl<sup>-</sup> or PF<sub>6</sub><sup>-</sup>, Figure 1.7b) are two of the most active compounds and exhibit high anticancer activity in A2780 human ovarian cancer xenografts, with activities comparable to cisplatin and carboplatin.<sup>87,88,89</sup>



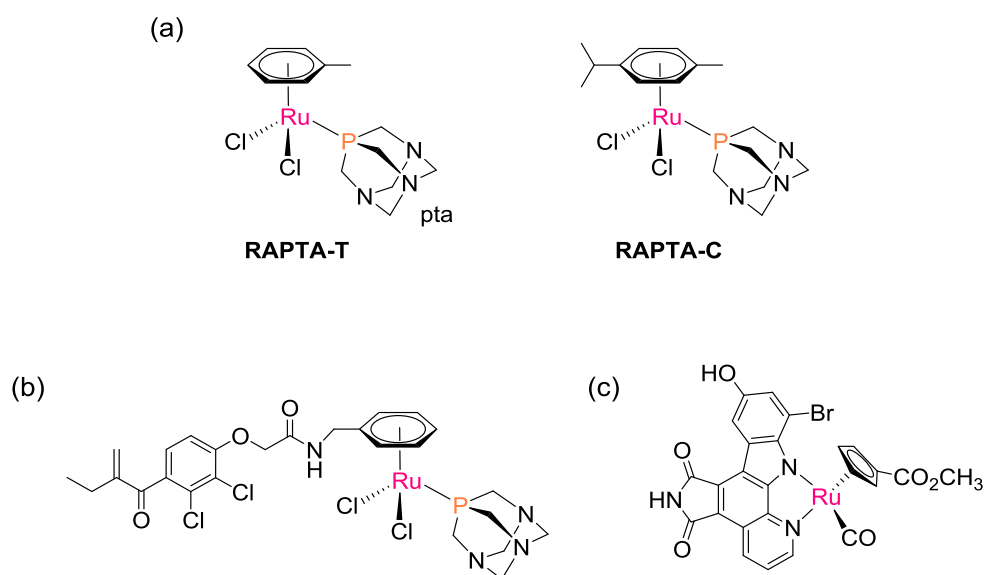
**Figure 1. 7** Molecular structures of (a) Ru(II) organometallic anticancer compounds from Sadler's laboratories, (b) RM175 and HC11.

The main reaction that is important for these compounds is aquation of the Ru–Cl bond to afford the more reactive aqua complex  $[(\eta^6\text{-arene})\text{Ru}(\text{OH}_2)(\text{en})]^+$ .<sup>40,90</sup> The rate of hydrolysis is faster ( $\sim 5 \times 10^{-3} \text{ s}^{-1}$  at  $37^\circ\text{C}$  in  $0.1 \text{ M NaClO}_4$  (aq)) as compared to cisplatin, with  $t_{1/2}$  values ( $\sim 2.5 \text{ min}$ ) that are  $\sim 50$ -times shorter than that of the Pt drug.<sup>91</sup> Although it has not yet been established unequivocally, the primary cellular target for these compounds is thought to be nuclear DNA.<sup>40,90</sup> It has been shown that after hydrolysis,  $[(\eta^6\text{-arene})\text{Ru}(\text{OH}_2)(\text{en})]^{2+}$  is able to form monofunctional Ru-DNA adducts by substitution of the aqua ligand with the N7 atom of guanine preferentially,<sup>92</sup> a process

that is enhanced by hydrogen-bonding between the NH group of the en ligand and the O6 atom of guanine.<sup>92,93,94</sup> Interestingly, it was shown that  $[(\eta^6\text{-biph})\text{Ru}(\text{OH}_2)(\text{en})]^+$  binds covalently to the 14-mer DNA duplex d(5'-ATACATGGTACATA-3')/(3'-TATGTACCATGTAT-5') and that it also intercalates its biphenyl moiety between DNA bases and engages in  $\pi$ - $\pi$  stacking interactions, thereby increasing DNA affinity. Such a dual DNA binding mode represents a new structural feature in metal-DNA adducts.<sup>92,93,94,95</sup> The coordinated water molecules of  $[(\eta^6\text{-biph})\text{Ru}(\text{OH}_2)(\text{en})]^{2+}$  and  $[(\eta^6\text{-THA})\text{Ru}(\text{OH}_2)(\text{en})]^{2+}$  have  $\text{p}K_a$  values of 7.71 and 8.01, respectively, in water at 37°C, indicating a low acidity for the water ligand which means that only small amounts of the hydroxo species  $[(\eta^6\text{-arene})\text{Ru}(\text{OH})(\text{en})]^+$  will be present in physiological media.<sup>91</sup> This is an important factor for this class of anticancer compounds because the hydroxo species is less susceptible to DNA binding.<sup>40,92</sup>

Paul J. Dyson and coworkers developed a closely related series of neutral Ru(II)-arene compounds of formula  $\text{Ru}(\eta^6\text{-arene})(\text{pta})\text{Cl}_2$ , where pta is the amphiphilic phosphine 1,3,5-triaza-7-phosphatricyclo[3.3.1.1]decane.<sup>84</sup> This family of compounds are known in the literature as RAPTA compounds. For example,  $\text{Ru}(\eta^6\text{-toluene})(\text{pta})\text{Cl}_2$  (RAPTA-T; Figure 1.8a) and  $\text{Ru}(\eta^6\text{-}p\text{-cymene})(\text{pta})\text{Cl}_2$  (RAPTA-C; Figure 1.8b) are not cytotoxic *in vitro*, but display selective activity for metastatic tumors *in vivo*, similar to NAMI-A.<sup>96,97</sup> The RAPTA compounds have a strong preference for protein binding over DNA,<sup>98</sup> and are devoid of toxicity to healthy cells even with prolonged exposure at millimolar concentrations.<sup>70</sup> Part of their mode of action involves the inhibition of detachment of tumor cells from the primary tumor, inhibition of re-adhesion to a new

growth substrate and down-regulation of matrix metalloproteinases.<sup>84,97</sup> Although the RAPTA compounds are still under development,<sup>84</sup> it is remarkable that a second type of metal-based drugs that prevents tumor invasion and formation of metastases has been discovered.



**Figure 1. 8** Molecular structure of (a) RAPTA-T and RAPTA-C, (b) Ru( $\eta^6$ -phenylethacrylate)(pta)Cl<sub>2</sub> and (c) a Ru-based kinase inhibitor.

The design of hybrid compounds containing an organometallic Ru(II)-arene moiety and an enzyme inhibitor has been a successful approach for targeted therapies in this field.<sup>82,83,84,85</sup> For example, Ru( $\eta^6$ -phenylethacrylate)(pta)Cl<sub>2</sub> (Figure 1.8b) is a potent inhibitor of glutathione-S-transferase (GST), which is a detoxification enzyme that catalyzes nucleophilic attack of GSH with electrophilic molecules (such as anticancer drugs) and facilitates expulsion of the molecule-GSH conjugates through the glutathione *S*-conjugate efflux pump.<sup>99</sup> The GST enzyme is overexpressed in primary and metastatic tumors<sup>99</sup> and inhibition of GST will play an important role in overcoming cancer cell resistance. The compound Ru( $\eta^6$ -phenylethacrylate)(pta)Cl<sub>2</sub> inhibits GSTP1-1 by accommodation of the ethacrinic acid moiety in a hydrophobic pocket within the enzyme active site (H-site) and by covalent binding of a cysteine residue (Cys101) to the Ru center by displacement of the chloride ligands at the G-site (which is the binding motif for GSH). Therefore, the inhibitory ability of ethacrinic acid is enhanced by providing an additional binding mode at the active site.<sup>100</sup> Kinetically inert Ru(II) organometallic compounds that act as highly selective enzyme inhibitors (*e.g.* cyclopentadienyl Ru(II) compounds as protein kinase inhibitors) have been reported by Eric Meggers (Germany) and have been found to be highly toxic toward human melanoma cells. Although such work will not be discussed herein, the interested reader is encouraged to read the articles published in this vibrant area.<sup>101,102,103,104,105,106</sup>



## *Ruthenium(II) Polypyridyl Anticancer Compounds*

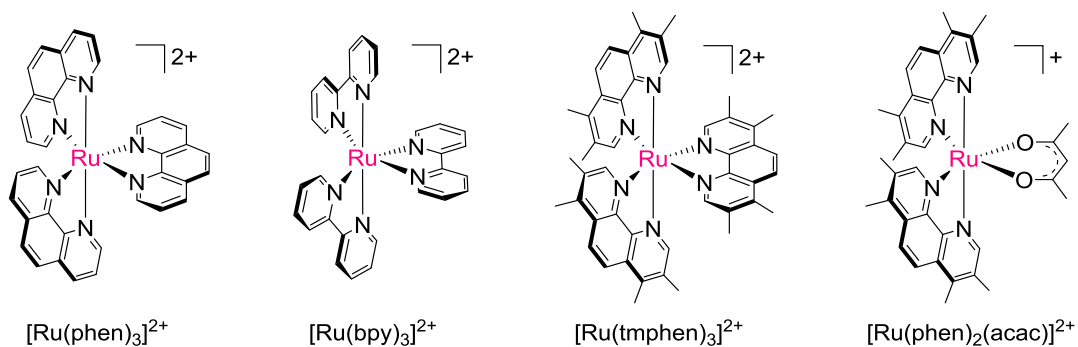
Coordinatively saturated and kinetically inert Ru coordination compounds have also been studied in cancer drug research. The structure of this class of molecules departs from the paradigm of using the inherent reactivity of the transition metal to exert a therapeutic effect by DNA binding, because there are no labile positions at the metal center in these compounds. Numerous examples of Ru(II) polypyridyl complexes that display promising anticancer properties have been reported. More interestingly, new cellular targets, such as mitochondria and endoplasmic reticulum, have been recognized. Due to the relevance of this field to my research work, this topic will be discussed more in detail to continuation.

### **Early Reports of Biological Activity**

The first report of the biological activity of Ru(II) polypyridyl complexes appeared in 1952.<sup>102,107</sup> Dwyer and coworkers determined that the LD<sub>50</sub> (dose required to kill half a cell population after a specified test duration) of the dicationic compounds [Ru(phen)<sub>3</sub>]<sup>2+</sup> (phen = 1,10-phenanthroline, Figure 1.9) and [Ru(bpy)<sub>3</sub>]<sup>2+</sup> (bpy = 2,2'-bipyridine, Figure 1.9) are ~10–15 mg/kg when administered to mice via intraperitoneal (IP) injection.<sup>107</sup> For comparison sake, the oral and intravenous LD<sub>50</sub> values of cisplatin in mice are 32.7 and 11 kg/mg, respectively.<sup>108</sup> Exposure of mice with a dose equal to the LD<sub>50</sub> of the Ru compounds resulted in paralysis and respiratory failure due to direct

inhibition of acetylcholinesterase.<sup>107,109</sup> The two Ru compounds were reported to be chemically highly stable as they are not attacked by concentrated acids or bases and dissociation of the complexes is considered extremely minimal in biological systems.<sup>107</sup> In fact, it was shown that  $[\text{Ru}(\text{phen})_3]^{2+}$  is not metabolized and is excreted essentially in an unaltered state in the urine after IP injection in mice.<sup>110</sup>

In 1965, the same year when the antiproliferative properties of cisplatin were discovered, the antitumor properties of  $[\text{Ru}(\text{tmphen})_3]^{2+}$  (tmphem = 3,4,7,8-tetramethyl-1,10-phenanthroline, Figure 1.9) and  $[\text{Ru}(\text{tmphen})_2(\text{acac})]^+$  (acac = acetylacetonate, Figure 1.9) were studied in mice bearing Landschütz ascites tumors (a transplantable highly virulent tumor that can be grown in any strain of mice).<sup>111</sup> Significant inhibition of tumor growth without substantial weight loss of the animals was observed after administration of the compounds, with the monocationic compound exhibiting more pronounced tumor growth inhibition. Such a finding represents an early example of the effectiveness of reducing the positive charge of Ru(II) polypyridyl complexes from 2+ to 1+ by coordination of a monoanionic chelating ligand (such as acac) for increasing the cellular accumulation of the metal compound. It was also reported that  $[\text{Ru}(\text{tmphen})_2(\text{acac})]^+$  localizes in the mitochondria of Landschütz ascites tumor cells.<sup>110</sup>



**Figure 1. 9** Molecular structures of the cationic complexes  $[\text{Ru}(\text{phen})_3]^{2+}$ ,  $[\text{Ru}(\text{bpy})_3]^{2+}$ ,  $[\text{Ru}(\text{tmphen})_3]^{2+}$  and  $[\text{Ru}(\text{phen})_2(\text{acac})]^{2+}$ .

## Cellular Uptake

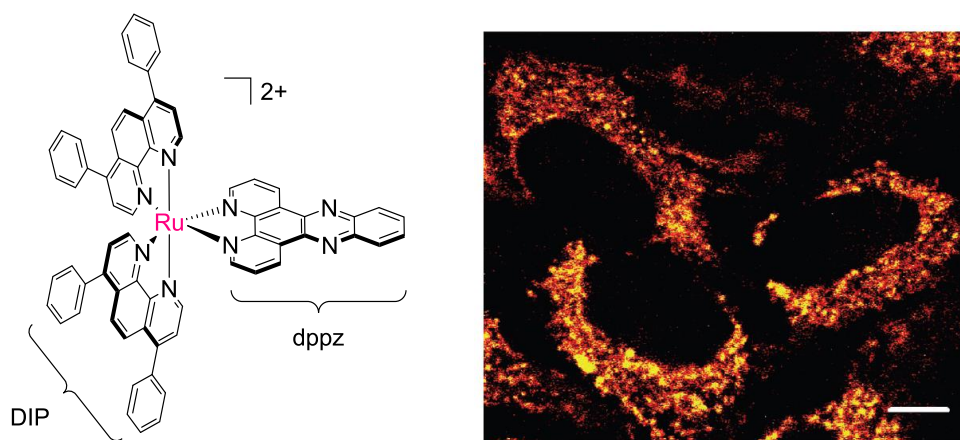
The mechanisms by which this class of molecules traverse the plasma membrane of cells has been thoroughly studied by Barton and coworkers.<sup>112,113,114,115</sup> The cellular uptake of the lipophilic cationic compound  $[\text{Ru}(\text{DIP})_2(\text{dppz})]^{2+}$  (DIP = 4,7-diphenyl-1,10-phenanthroline, dppz = dipyrido[3,2-*a*:2',3'-*c*]phenazine, Figure 1.10) was studied in human cervical (HeLa) cancer cells using confocal fluorescence microscopy, inductively coupled plasma mass spectrometry (ICP-MS) and flow cytometry.

Confocal imaging revealed that emission from  $[\text{Ru}(\text{DIP})_2(\text{dppz})]^{2+}$  is observed throughout the cytosol and very weak emission is observed in the nucleus (Figure 1.10), indicating that  $[\text{Ru}(\text{DIP})_2(\text{dppz})]^{2+}$  does not target specific cellular compartments in this cancer cell line. There is substantial cellular uptake of the complex after 1 h of

incubation (37°C) which reaches a concentration of 16  $\mu\text{M}$  and 398  $\mu\text{M}$  inside the cells when incubated in serum and serum-free medium, respectively, as determined by ICP-MS. No uptake preference was observed when the  $\Delta$ - and  $\Lambda$ -isomers of  $[\text{Ru}(\text{DIP})_2(\text{dppz})]^{2+}$  were incubated with the cells separately.<sup>112</sup>

Cellular uptake of small molecules occurs through energy-dependent (endocytosis, active protein transport) and energy independent (facilitated diffusion, passive diffusion) processes. In order to deplete the cells of energy, HeLa cells were incubated with  $[\text{Ru}(\text{DIP})_2(\text{dppz})]^{2+}$  at low temperature (4°C) or in the presence of metabolic inhibitors, such as deoxyglucose (a glucose analogue that inhibits glycolysis) and oligomycin (an inhibitor of oxidative phosphorylation). Energy depletion did not decrease the uptake of  $[\text{Ru}(\text{DIP})_2(\text{dppz})]^{2+}$ , ruling out the energy-dependent pathways endocytosis and active protein transport as mechanisms of cellular uptake.<sup>112</sup> Organic cation transporters (OCTs) are polyspecific transporters that facilitate the cellular uptake/efflux of organic cations.<sup>116</sup> Incubation of HeLa cells with  $[\text{Ru}(\text{DIP})_2(\text{dppz})]^{2+}$  in the presence of OCTs inhibitors (*e.g.* procainamide, tetraalkylammonium salts) also did not have a negative impact on the uptake of the metal complex either. In contrast, decreasing the potential of the plasma membrane to close to zero (membrane potential of cells is  $-50$  to  $-70$  mV; inside of the cell is negative with respect to the outside)<sup>112,117</sup> by incubation in buffer with  $\text{K}^+$  concentration similar to that found in the cytosol of HeLa cells ( $\sim 170$  mM)<sup>118</sup> produced a 66% decrease of uptake of  $[\text{Ru}(\text{DIP})_2(\text{dppz})]^{2+}$ , indicating that the potential difference across the cellular membrane drives the cellular internalization of this Ru complex and that  $[\text{Ru}(\text{DIP})_2(\text{dppz})]^{2+}$  enters HeLa cancer cells

by passive diffusion.<sup>112</sup> This study is very important for the field of anticancer Ru(II) polypyridyl drugs because it paved the road for the design of other lipophilic Ru compounds. Moreover, since passive diffusion is a mechanism of cellular uptake that does not rely on specific transporters, lipophilic Ru compounds could potentially exhibit cytotoxicity against a broad panel of cancer cells, even against those that are cisplatin-resistant.

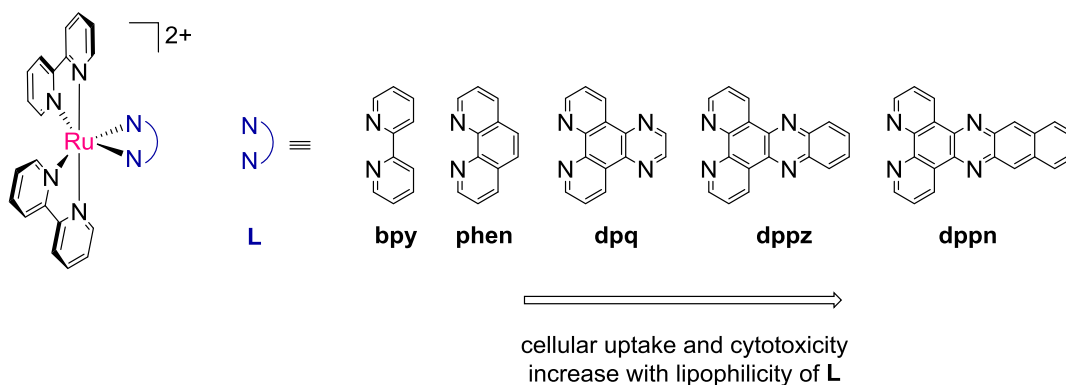


**Figure 1. 10** Molecular structure of  $[\text{Ru}(\text{DIP})_2(\text{dppz})]^{2+}$  and confocal image of HeLa cells incubated with  $5 \mu\text{M}$   $[\text{Ru}(\text{DIP})_2(\text{dppz})]^{2+}$  for 4 h. Scale bar is  $10 \mu\text{m}$ . Adapted with permission from reference 112. Copyright 2008 American Chemical Society.

## Cytotoxicity and Mechanism of Cancer Cell Death

Lipophilicity and cellular uptake play a crucial role on the cytotoxicity of Ru(II) polypyridyl complexes. Several studies in this vein, as well as the elucidation of the mechanism of cancer cell death induced by this type of complexes, have been published over past few years and several reviews have appeared on the topic.<sup>114,115,119</sup> Selected examples are discussed below.

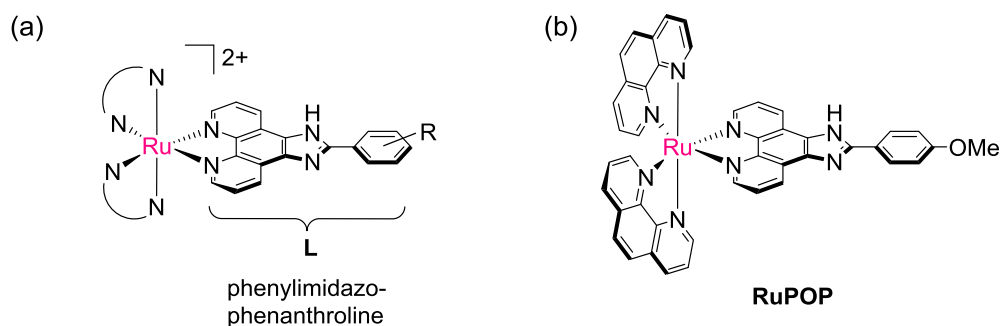
Schatzschneider and coworkers studied the cellular uptake of polypyridyl complexes of the type  $[\text{Ru}(\text{bpy})_2(\text{L})]^{2+}$ , where L = bpy, phen, dpq, dppz, dppn (Figure 1.11).<sup>120</sup> The cellular uptake (measured by atomic absorption spectrometry (AAS)) of these compounds in human colon (HT-29) and breast (MCF-7) cancer cells was related to the lipophilicity (or size) of the L ligand, suggesting that more lipophilic Ru compounds are able to traverse the plasma membrane more easily than less lipophilic compounds. Moreover, their cytotoxicity increases with cellular uptake, indicating that ligands with extended aromatic systems may improve the cellular accumulation of Ru polypyridyl compounds inside the cells leading to higher cytotoxicities. The most potent compound was found to be  $[\text{Ru}(\text{bpy})_2(\text{dppn})]^{2+}$  (dppn = benzo[*i*]dipyrido[3,2-*a*:2',3'-*c*]phenazine) and is as cytotoxic as cisplatin against both cancer cell lines (96 h of treatment).<sup>120</sup> Analogous results have been reported for other Ru(II) and Ir(III) compounds with a similar series of L ligands including dppn.<sup>121</sup>



**Figure 1.11** Molecular structures of  $[Ru(bpy)_2(L)]^{2+}$  complexes.

Liu, Wong and coworkers studied the anticancer activity of several compounds of general type  $[Ru(N^N)_2(L)]^{2+}$ , where  $N^N$  is a bpy-type ligand and L is a phenylimidazo-phenanthroline ligand (Figure 1.12a).<sup>122,123</sup> It was found that RuPOP (Figure 1.12b) is the most cytotoxic of the series in melanoma (A375), hepatocellular carcinoma (HepG2) and colorectal adenocarcinoma (SW620) cancer cells (48 h of treatment), and that RuPOP is ~2-fold more cytotoxic than cisplatin. RuPOP exhibits lower cytotoxicities towards normal cells (fibroblast (Hs68) and kidney cells (HK-2)), a highly desirable feature for cancer drug design. In contrast, cisplatin did not show any selectivity towards either normal or cancer cells under the same experimental conditions. RuPOP induces apoptosis, in which DNA fragmentation, nuclear condensation and cytoplasmic shrinkage were observed. This compound also induces mitochondrial fragmentation and loss of  $\Delta\Psi_m$ , confirming cell death via the intrinsic pathway of

apoptosis. Further biological analyses revealed that RuPOP suppresses the expression of the Bcl-2 anti-apoptotic protein, upregulates the expression of the pro-apoptotic protein Bad and activates caspase-9, concluding that RuPOP induces mitochondria-mediated and caspase-dependent apoptosis in human cancer cells.<sup>122</sup>



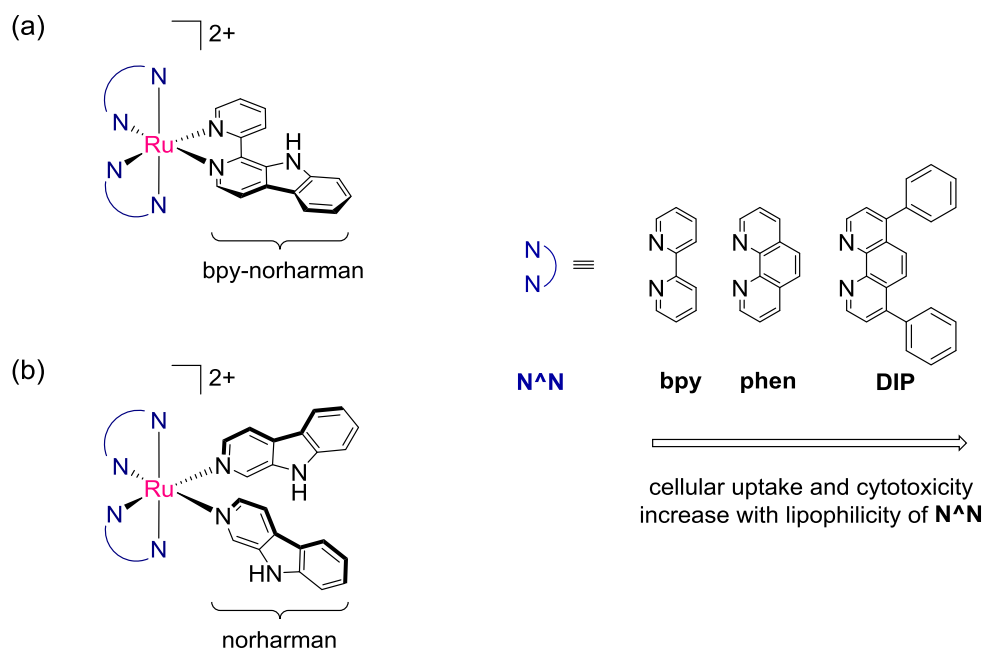
**Figure 1. 12** (a) Molecular structures of Ru polypyridyl complexes with phenylimidazo-phenanthroline ligands and (b) molecular structure of RuPOP.

Xu and coworkers conducted biological studies on three polypyridyl complexes of the type  $[\text{Ru}(\text{N}^{\wedge}\text{N})_2(\text{bpy-norharman})]^{2+}$  (Figure 1.13a), where  $\text{N}^{\wedge}\text{N} = \text{bpy}$ , phen and DIP; bpy-norharman is a chelating ligand derived from the norharman  $\beta$ -carboline alkaloid.<sup>124</sup> The three complexes exhibit greater cytotoxicities than  $[\text{Ru}(\text{bpy})_2(\text{dppz})]^{2+}$  (which is practically inactive) against three types of tumor cells (HeLa, HepG2, MCF-7;



48 h of treatment). As expected, their cytotoxicities increased with their lipophilicity and cellular uptake:  $[\text{Ru}(\text{bpy})_2(\text{bpy-norharman})]^{2+} < [\text{Ru}(\text{phen})_2(\text{bpy-norharman})]^{2+} < [\text{Ru}(\text{DIP})_2(\text{bpy-norharman})]^{2+}$ . Increasing the lipophilicity enhances the rate of cellular uptake and, consequently, the cytotoxic activity increases, as observed in previous studies. The bpy-norharman ligand alone was inactive against all the cells tested. The most active compound,  $[\text{Ru}(\text{DIP})_2(\text{bpy-norharman})]^{2+}$ , was found to be ~6-fold more cytotoxic than cisplatin in the three cell lines tested and the three complexes were found to traverse the cellular membrane by an energy-independent process (passive diffusion) as proposed for  $[\text{Ru}(\text{DIP})_2(\text{dppz})]^{2+}$ .<sup>112,124</sup>

The three compounds induced apoptosis via the intrinsic pathway: increased percentage of sub-G1 phase cells, cell shrinkage, membrane blebbing, chromatin condensation, nuclear fragmentation, depletion of  $\Delta\Psi_m$  and promotion of caspase-3/7 activity were observed. Autophagy, a self-digestion process in which parts of the cytosol are sequestered within acidic vesicular organelles and are degraded by lysosomal hydrolytic enzymes,<sup>61,125</sup> was observed simultaneously with apoptosis in HeLa cells and both processes seemed to be triggered by production of ROS. Suppression of autophagy using autophagy inhibitors enhanced apoptotic cell death, suggesting that autophagy had a protective role.<sup>124</sup> This family of complexes represents the first example of dual apoptosis- and autophagy-inducing Ru compounds.



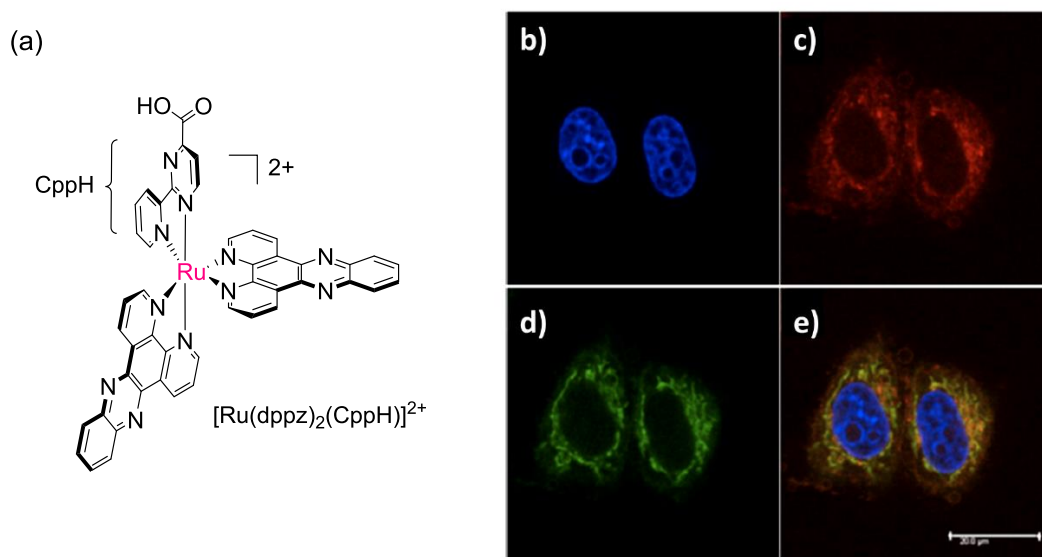
**Figure 1.13** Molecular structures Ru polypyridyl (a) bpy-norharman and (b) norharman complexes.

Confocal microscopy studies revealed that red emission from  $[Ru(N^N)_2(bpy-norharman)]^{2+}$  ( $N^N = phen, DIP$ ) is observed in the cytosol and increases gradually inside the nucleus of HeLa cells over time. In contrast,  $[Ru(bpy)_2(dppz)]^{2+}$  and  $[Ru(DIP)_2(dppz)]^{2+}$  localizes mainly in the cytosol,<sup>112,113,124</sup> indicating that bpy-norharman influences the cellular localization of these Ru complexes. The *in vitro* DNA binding ability of the three Ru bpy-norharman complexes increases in the following order:  $[Ru(bpy)_2(bpy-norharman)]^{2+} < [Ru(phen)_2(bpy-norharman)]^{2+} < [Ru(DIP)_2(bpy-norharman)]^{2+}$ , which when correlated with their cytotoxicities suggests that DNA

intercalation may be triggering the apoptotic response.<sup>124</sup> The same authors reported that Ru complexes of formula  $[\text{Ru}(\text{N}^{\wedge}\text{N})_2(\text{norharman})]^{2+}$  ( $\text{N}^{\wedge}\text{N}$  = bpy, phen and DIP), featuring norharman as a monodentate ligand (Figure 1.13b), induce cancer cell death via the intrinsic pathway.<sup>126</sup> Similar to the previous series of compounds, the most cytotoxic molecule is  $[\text{Ru}(\text{DIP})_2(\text{norharman})]^{2+}$ , and it is ~20-fold more cytotoxic than cisplatin (Hela, HepG2, MCF-7 cancer cells; 48 h of treatment) and targets the nucleus of HeLa cells.<sup>126</sup>

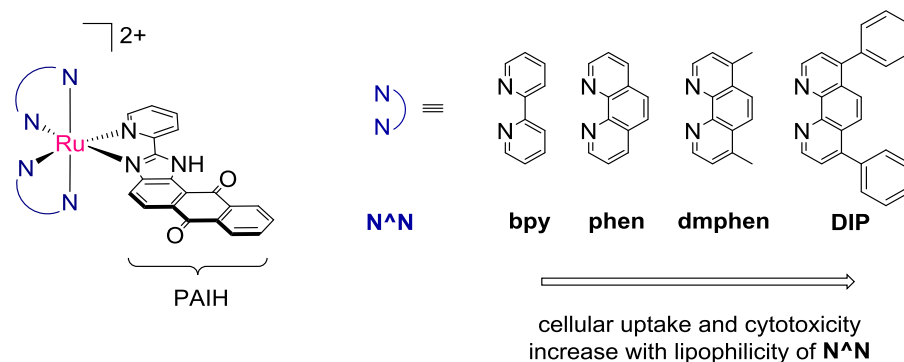
Gasser and coworkers documented the biological effects of a photoluminescent Ru(II) compound,  $[\text{Ru}(\text{dppz})_2(\text{CppH})]^{2+}$  (CppH = 2-(2'-pyridyl)pyrimidine-4-carboxylic acid, Figure 1.14a).<sup>127</sup> This compound exhibits cytotoxic properties (48 h treatment) comparable to cisplatin in HeLa, MCF-7, human ovarian carcinoma (A2780) and osteosarcoma (U2OS) cancer cells, and is three times more cytotoxic than cisplatin in the cisplatin-resistant A2780-CP70 cell line. It binds DNA by intercalation *in vitro* but does not target DNA *in cellulo*. Confocal microscopy studies indicate that the primary target of  $[\text{Ru}(\text{dppz})_2(\text{CppH})]^{2+}$  is mitochondria: Figures 1.14b-e shows that the orange emission of  $[\text{Ru}(\text{dppz})_2(\text{CppH})]^{2+}$  colocalizes with the green emission of Mitotracker green (a mitochondria-specific fluorescent dye), indicating that the Ru complex localizes in mitochondria. Quantification of the ruthenium content by using AAS in mitochondria of HeLa cells exposed to this compound supported the microscopy results and it was found that 68% of the total uptake of  $[\text{Ru}(\text{dppz})_2(\text{CppH})]^{2+}$  localizes in mitochondria. These findings underscores the contention that if a Ru complex binds DNA through intercalation *in vitro*, it does not necessary imply that nuclear DNA will be the target *in*

*cellulo* (or *in vivo*). The mechanism of cell death was investigated in HeLa cells and it was shown that  $[\text{Ru}(\text{dppz})_2(\text{CppH})]^{2+}$  impairs the  $\Delta\Psi_m$  and induces apoptosis via the intrinsic pathway. In addition,  $\text{Ru}(\text{dppz})_2(\text{CppH})^{2+}$  enters HeLa cells through an energy-dependent mechanism.<sup>127</sup>



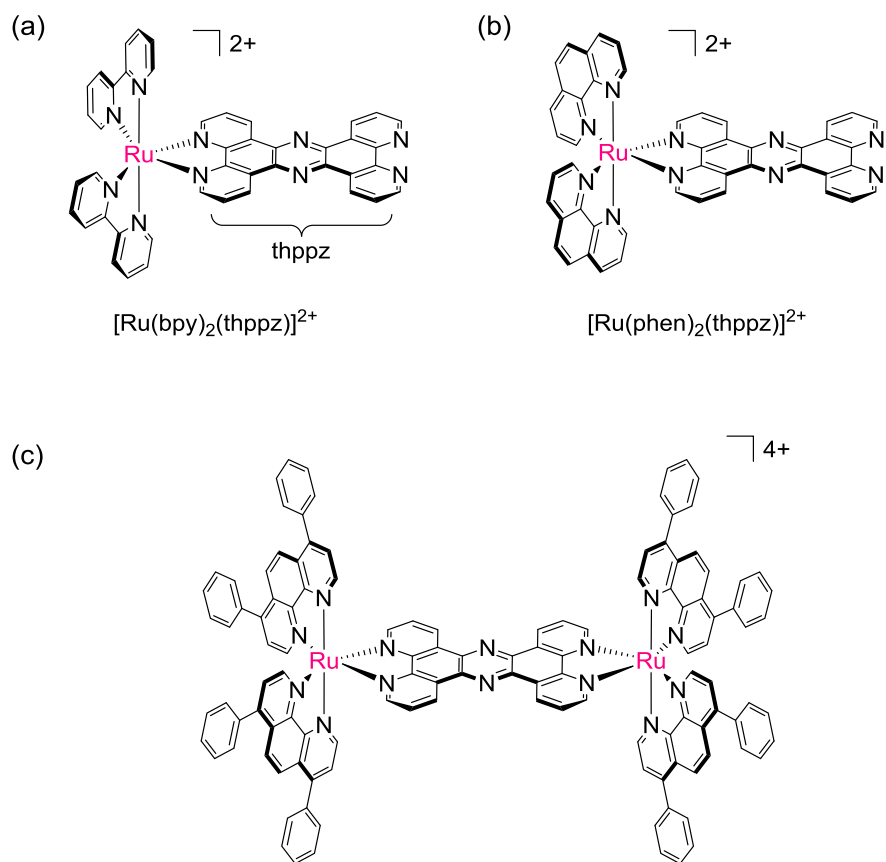
**Figure 1. 14** (a) Molecular structure of  $[\text{Ru}(\text{dppz})_2(\text{CppH})]^{2+}$ . Fluorescence confocal microscopy images of HeLa cells incubated with  $[\text{Ru}(\text{dppz})_2(\text{CppH})]^{2+}$  (20  $\mu\text{M}$ ) for 2 h: (a) nuclear staining, (b) cellular staining of  $[\text{Ru}(\text{dppz})_2(\text{CppH})]^{2+}$ , (c) mitochondrial staining, and (d) the overlay image. Adapted with permission from reference 127. Copyright 2012 American Chemical Society.

More recently, Ji, Chao and coworkers showed that polypyridyl complexes of the type  $[\text{Ru}(\text{N}^{\wedge}\text{N})_2(\text{PAIH})]^{2+}$  ( $\text{N}^{\wedge}\text{N}$  = bpy, phen, dmphen, DIP), where PAIH is an anthracenyl chelating ligand (2-Pyridyl-1*H*-anthra[1,2-*d*]imidazole-6,11-dione, Figure 1.15), are cytotoxic against various cancer cell lines, such as HeLa, HepG2, human hepatocellular carcinoma (BEL-7402) and lung carcinoma (A549).<sup>128</sup> The compound with the greatest lipophilicity,  $[\text{Ru}(\text{DIP})_2(\text{PAIH})]^{2+}$ , is the most cytotoxic and its  $\text{IC}_{50}$  values (48 h treatment) are comparable to those of cisplatin in all the cell lines tested but less cytotoxic than cisplatin against normal cells (hepatic cells (LO2)). The PAIH ligand alone is inactive. As documented in previous studies, the cellular uptake (measured by ICP-MS) and cytotoxicities of the compounds correlates with the lipophilicity of the complex. HeLa cells incubated with  $[\text{Ru}(\text{DIP})_2(\text{PAIH})]^{2+}$  showed nuclear fragmentation, chromatin condensation, externalization of phosphatidylserine, and an increased number of cells in the subG1 phase, suggesting apoptosis as the mechanism of cancer cell death. Additionally this Ru compound accumulates preferentially in mitochondria, induces production of ROS in a dose-dependent fashion, disrupts the  $\Delta\Psi_m$ , suppresses the expression of the anti-apoptotic proteins Bcl-2 and Bcl-xL, increases the expression level of the pro-apoptotic protein Bax, induces the release of cytochrome-*c* and promotes the activation of the initiator caspase-9 and the downstream effectors caspase-3 and caspase-7. These collective findings indicate that the intrinsic pathway is operating during cancer cell death.<sup>128</sup>



**Figure 1. 15** Molecular structure of Ru polypyridyl complexes containing the anthracenyl chelating ligand PAIH

Thomas and coworkers studied the antitumor properties of two Ru complexes containing the lipophilic thppz ligand (tetrapyrido[3,2-*a*:2',3'-*c*:3'',2''-*h*:2''',3'''-*j*]phenazine):  $[\text{Ru}(\text{bpy})_2(\text{tpphz})]^{2+}$  (Figure 1.16a) and  $[\text{Ru}(\text{phen})_2(\text{tpphz})]^{2+}$  (Figure 1.16b).<sup>129</sup> Both compounds show strong DNA binding through intercalation *in vitro*, exhibit comparable cytotoxicity to cisplatin against MCF-7 and A2780 cancer cells and are active in the A2780-CP70 cisplatin-resistant cell line. Confocal fluorescence studies revealed that these photoluminescent compounds target the nucleus of MCF-7 cancer cells and are remarkable DNA stains, and that both compounds traverse the cellular membrane by an active transport mechanism.<sup>129</sup>



**Figure 1.16** Molecular structures of (a)  $[\text{Ru}(\text{bpy})_2(\text{thppz})]^{2+}$ , (b)  $[\text{Ru}(\text{phen})_2(\text{thppz})]^{2+}$  and (c)  $[(\text{Ru}(\text{DIP})_2)_2(\mu\text{-tpphz})]^{4+}$ .

The Thomas group later studied the cytotoxic properties and subcellular localization of the homodinuclear polypyridyl compound  $[(\text{Ru}(\text{DIP})_2)_2(\mu\text{-tpphz})]^{4+}$ .<sup>130</sup> In contrast to their previous studies on mononuclear complexes,<sup>129</sup> this photoluminescent compound was found to localize in the endoplasmic reticulum of MCF-7 cancer cells, which was attributed to its great lipophilicity and affinity for hydrophobic membranes.

In fact, this is the first example of a Ru compound that targets this cellular organelle, extending the scope of biological activities exhibited by Ru polypyridyl complexes.<sup>130</sup> The dinuclear complex is three times more cytotoxic than cisplatin in HeLa and MCF-7 cells (24 h treatment) and cell swelling, cellular debris and evidence of intracellular vacuolization were apparent in these two cell lines, suggesting that the cells died by necrosis. Its cellular uptake in MCF-7 cells is temperature-dependent, indicating that  $[(\text{Ru}(\text{DIP})_2)_2(\mu\text{-tpphz})]^{4+}$  traverses the cellular membrane by an active transport mechanism. The analogous compound  $[(\text{Ru}(\text{phen})_2)_2(\mu\text{-tpphz})]^{4+}$  is inactive against the cancer cells tested and was found to target nuclear DNA.<sup>130,131</sup>

In summary, the biological studies discussed herein reveal that the lipophilicity of the ancillary ligands of Ru polypyridyl compounds with a  $[\text{Ru}^{\text{II}}\text{N}_6]^{2+}$  coordination environment plays an important role on their cellular accumulation and cytotoxicity. The Ru polypyridyl compounds are now considered as promising new candidates in cancer drug research, exhibiting antitumor properties comparable or superior to the benchmark drug cisplatin. Moreover, their photoluminescent properties facilitate the study of their subcellular localization, allowing for straightforward identification of cellular targets by using confocal fluorescence microscopy. Since this class of complexes is coordinatively saturated and kinetically inert, they do not bind covalently to nuclear DNA as in the case of cisplatin; in fact, they exhibit very different mechanisms of action and are able to target other organelles such as mitochondria and endoplasmic reticulum, which is a desirable feature for overcoming tumor resistance in cancer chemotherapy.



## Dissertation Objectives and Outline

The research conducted to date in the field of medicinal inorganic chemistry has led to the conclusion that Ru-based anticancer drugs are a very promising generation of metallopharmaceuticals for cancer chemotherapy. Two Ru compounds are currently in human clinical trials and several more are being evaluated in preclinical studies. The structural diversity, reactivities, and rich redox and photophysical properties of Ru complexes lead to a wide array of possibilities for the rational design of anticancer drugs.

The research on Ru-based metallopharmaceuticals, however, has focused mainly on Ru(II) polypyridyl compounds with a  $[\text{Ru}^{\text{II}}\text{N}_6]^+$  pseudo-octahedral coordination environment and organometallic Ru(II)-arene piano-stool complexes, with almost no attention focused on the other scaffolds that are accessible in Ru(II) chemistry. The primary objective of this work, therefore, was to design, synthesize and characterize two novel Ru(II) architectures that have not been well-developed in the field and to evaluate their potential use in cancer drug research by studying their cytotoxic properties in cancer cell lines. In the case of those found to be anticancer active the goal is to determine the mechanism(s) of cancer cell death. In addition, albeit not discussed in this introductory chapter due to a need for brevity, a fluorescent metal-metal bonded dirhodium compound, the first of its kind, has been used as a model compound to gain a better understanding of the cellular distribution of metal-metal bonded compounds in

cancer cells and to discover new cellular targets in order to guide the research of this class metal compounds in cancer therapeutics.

Chapter II is a thorough investigation of the mechanism of cell death in human lung adenocarcinoma (A549) cells induced by Ru(II) polypyridyl compounds that possess a  $[\text{Ru}^{\text{II}}\text{N}_5\text{O}]^+$  pseudo-octahedral coordination environment. This study expands the diversity of Ru(II) polypyridyl drugs and demonstrates that compounds of this type are capable of inducing apoptosis. A discussion of the cytotoxicity of an iridium analog is also included.

In Chapter III, the cytotoxic properties of a group of coordinatively saturated organometallic Ru(II) compounds whose structure, redox and optical properties are similar to those of Ru cyclometallated dyes used in dye-sensitized solar cells, are explored in human cervical (HeLa) and ovarian (OVCAR-8 and NCI/ADR-RES) cancer cells and a commentary on the suitability of Ru organometallic dyes as anticancer agents is provided.

Chapter IV describes a study aimed at determining new cellular targets for anticancer metal-metal bonded dirhodium compounds. A literature review of the anticancer properties of dirhodium drugs is provided and the synthesis, characterization, subcellular distribution and localization of a fluorophore-labeled dirhodium compound in human lung adenocarcinoma (A549) cells are discussed.

Overall conclusions and future research work are found in Chapter V.

CHAPTER II  
CYTOTOXICITY STUDIES OF RUTHENIUM COMPOUNDS AND AN  
IRIDIUM ANALOG WITH N<sup>+</sup>O<sup>-</sup> ANCILLARY LIGANDS

**Introduction**

Cisplatin (*cis*-Pt(NH<sub>3</sub>)<sub>2</sub>Cl<sub>2</sub>) is the most successful example of a metal-based drug in the history of cancer therapeutics.<sup>19</sup> The compound was approved by the Food and Drug Administration (FDA) in 1978 to treat metastatic testicular and ovarian cancers, with high curing rates (80–90%) being standard for cisplatin-treated testicular cancer.<sup>23</sup> The early success of cisplatin notwithstanding, the severe side effects and cancer cell resistance observed during the treatment of cancer patients with this drug led to intense exploration of the antitumor properties of other platinum (Pt) compounds<sup>19,55</sup> and complexes with different transition metal ions.<sup>15,16,85,132</sup> The search for metal anticancer drugs with (i) greater antiproliferative activity, (ii) lower side effects experienced by patients and (iii) different mechanism of action to overcome cell resistance, continues to be an active and important research area within the field of medicinal chemistry for providing safe and effective drugs for the treatment and cure of cancers, the second cause of death in the United States.

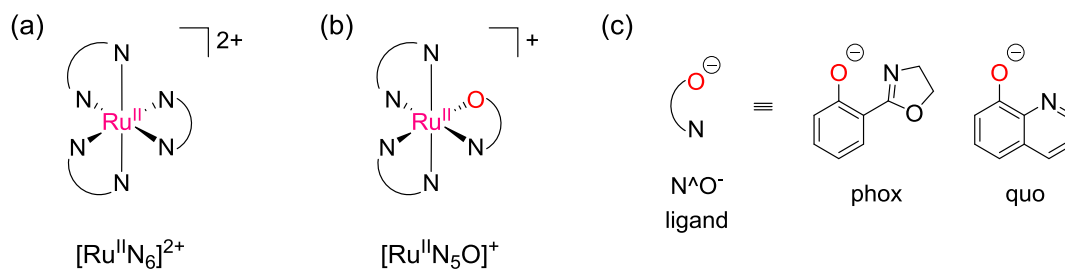
H	<u>Platinum Group Metals</u>																He
Li	Be											B	C	N	O	F	Ne
Na	Mg											Al	Si	P	S	Cl	Ar
K	Ca	Sc	Ti	V	Cr	Mn	Fe	Co	Ni	Cu	Zn	Ga	Ge	As	Se	Br	Kr
Rb	Sr	Y	Zr	Nb	Mo	Tc	<b>Ru</b>	<b>Rh</b>	<b>Pd</b>	Ag	Cd	In	Sn	Sb	Te	I	Xe
Cs	Ba	La <sup>(1)</sup>	Hf	Ta	W	Re	<b>Os</b>	<b>Ir</b>	<b>Pt</b>	Au	Hg	Tl	Pb	Bi	Po	At	Rn
Fr	Ra	Ac <sup>(2)</sup>	Rf	Db	Sg	Bh	Hs	Mt	Ds	Rg	Cn	Uut	Fl	Uup	Lv	Uus	Uuo
			(1)Ce Pr Nd Pm Sm Eu Gd Tb Dy Ho Er Tm Yb Lu														
			(2)Th Pa U Np Pu Am Cm Bk Cf Es Fm Md No Lr														

**Figure 2. 1** Location of the platinum group metals in the Periodic Table. Ru = ruthenium, Os = osmium, Rh = rhodium, Ir = iridium, Pd = palladium, Pt = platinum.

As has been discussed in Chapter I, ruthenium (Ru) pharmaceuticals are the second most explored metal compounds in cancer therapeutics among the platinum group elements (Figure 2.1).<sup>70,83,133</sup> Although there is great interest in developing Ru complexes as an alternative to Pt drugs in cancer chemotherapy, it is surprising that most of the reports on the biological activity of octahedral Ru(II) polypyridyl molecules have focused mainly on substitutionally inert complexes that possess an “all nitrogen” coordination environment<sup>115,119,127</sup> ( $[\text{Ru}^{\text{II}}\text{N}_6]^{2+}$ , Figure 2.2a), with no attention paid to donor atoms such as oxygen (O), sulfur (S) and phosphorus (P). The rich photophysical properties of octahedral  $[\text{Ru}^{\text{II}}\text{N}_6]^{2+}$  polypyridyl compounds may be one of the reasons for this tendency, since their intrinsic relatively intense phosphorescence facilitates

tremendously the study of the cellular distribution, subcellular localization and cellular uptake using confocal fluorescence microscopy, as described in Chapter I.<sup>119,134</sup>

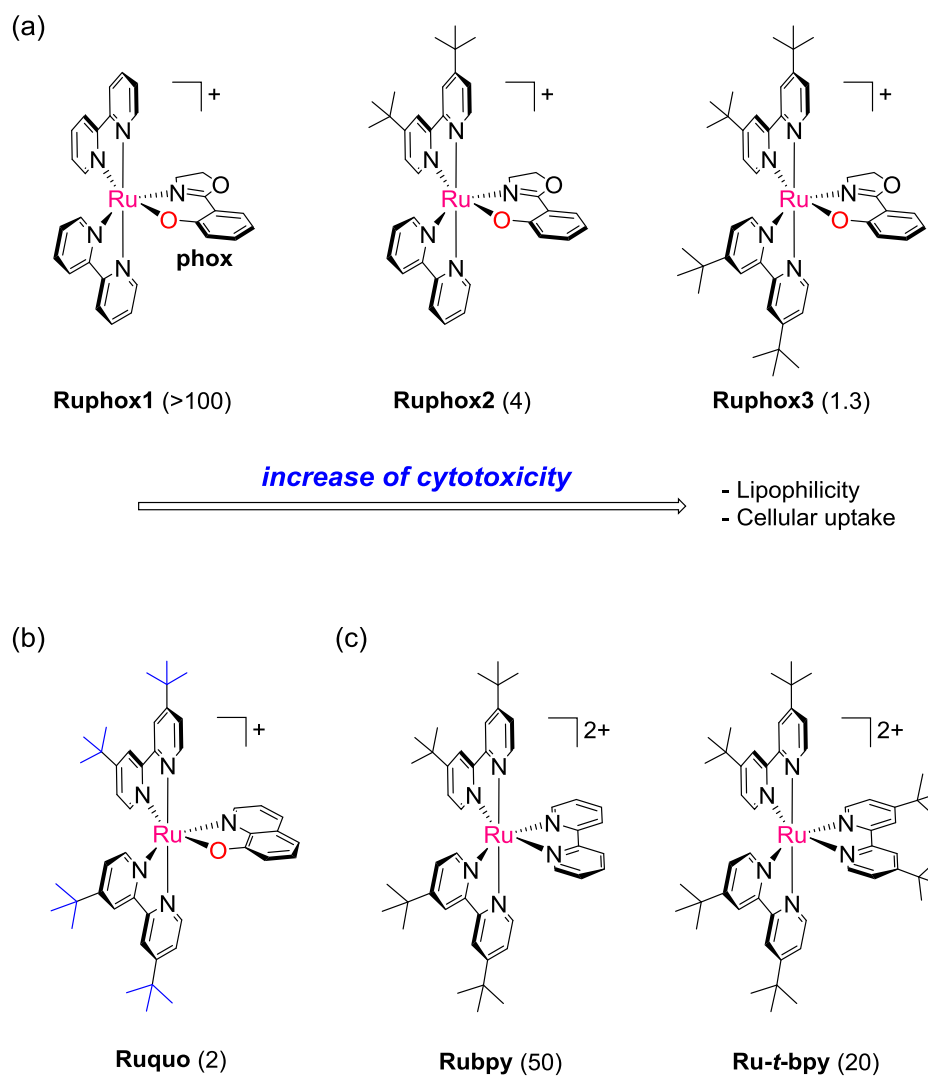
There is one main study on the cytotoxicity of Ru complexes on a  $[\text{Ru}^{\text{II}}\text{N}_5\text{O}]^+$  coordination environment (Figure 2.2b). In this report, Meggers and coworkers used a combinatorial, high throughput screening approach that led to the discovery of the first examples of cytotoxic octahedral Ru(II) polypyridyl compounds with  $\text{N}^-\text{O}^-$  bidentate ligands (Figure 2.2c).<sup>135</sup>



**Figure 2. 2** (a) Schematic representation Ru polypyridyl complexes on (a)  $[\text{Ru}^{\text{II}}\text{N}_6]^{2+}$  and (b)  $[\text{Ru}^{\text{II}}\text{N}_5\text{O}]^+$  coordination environments. (c) Molecular structures of phox and quo ligands.

The most active drugs in this series of compounds, **Ruphox3** and **Ruquo** (Figures 2.3a and 2.3b, respectively), exhibit low micromolar  $\text{IC}_{50}$  values (which is the

concentration of compound required to inhibit 50% of cell survival) in HeLa cervical cancer cells and **Ruphox3** was found to decrease the mitochondrial membrane potential of Burkitt-like lymphoma (BJAB) cells, suggesting the involvement of the intrinsic pathway of apoptosis.<sup>135</sup> Interestingly a decrease in the lipophilicity of the Ruphox-type compounds (**Ruphox3** > **Ruphox2** > **Ruphox1**, Figure 2.3a) is correlated with a decrease in the cytotoxicity of these compounds, stressing the importance of including hydrophobic moieties to improve the cellular uptake and activity of metal compounds. The lipophilicity of these compounds is due to the incorporation of *tert*-butyl groups on the 4,4'-positions of the bipyridine ligands (highlighted in blue color for **Ruquo** in Figure 2.3b). The authors also investigated the cytotoxicity of the 2+ charged analogs, **Rubpy** and **Ru'Buzbpy** (Figure 2.3c), and found that they were less active than the monocationic compounds. For example, **Ru'Buzbpy** is ~15 times less cytotoxic than **Ruphox3**.<sup>135</sup> It is worth noting that the increase in positive charge from **Ruphox3** (or **Ruquo**) to **Rubpy** decreases the activity of these structurally related molecules, hinting that a decrease in lipophilicity (or increase in hydrophilic character) leads to a reduced ability to traverse the cellular membrane for **Rubpy**.<sup>135</sup> Confocal fluorescence studies using the compounds with N<sup>+</sup>O<sup>-</sup> bidentate ligands were not possible to be performed because Ru complexes with a [Ru<sup>II</sup>N<sub>5</sub>O]<sup>+</sup> coordination environment are either non-emissive or display very weak phosphorescence at room temperature.<sup>136,137</sup>

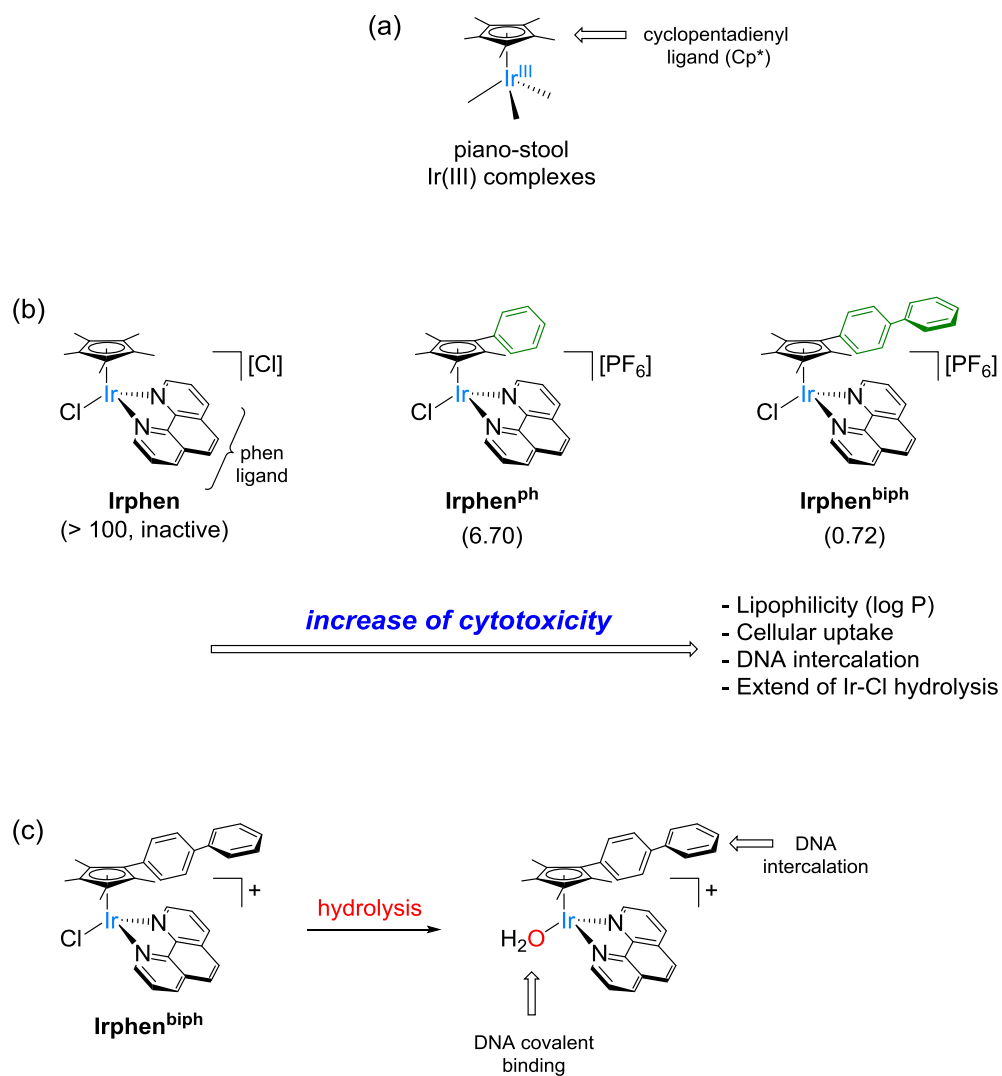


**Figure 2. 3** Molecular structures of (a,b) monocationic Ru compounds incorporating  $N^{\wedge}O^{-}$ -ligands and (c) dicationic Ru polypyridyl compounds related to those shown in (a,b).  $IC_{50}$  values ( $\mu M$ ) are shown in parenthesis.

A platinum group element that has gained momentum in cancer drug research in the past five years is iridium (Ir), a third-row (5d) transition metal element. The current state-of-the-art of Ir compounds as anticancer agents has been recently reviewed by Peter J. Sadler, a main contributor to this field,<sup>138</sup> and quite a few compounds have been shown to exhibit promising antitumor activity. Some examples and structure-activity relationship studies are highlighted in the passages below.

Three piano-stool Ir(III) compounds (Figure 2.4a) of the type  $[\text{Cp}^*\text{Ir}(\text{N}^{\wedge}\text{N})\text{Cl}]^+$  ( $\text{Cp}^*$  = pentamethylcyclopentadienyl,  $\text{N}^{\wedge}\text{N}$  = 1,10-phenanthroline (phen)) are shown in Figure 2.4b. It was found that their cytotoxicity against human ovarian carcinoma (A2780) cells increases by addition of phenyl substituents on the  $\text{Cp}^*$  ring (highlighted in green color in Figure 2.4b).<sup>139</sup> The trend in the anticancer activity of these compounds correlates with an increase of their lipophilicity (quantified by the  $\log(P)$  value;  $P$  = partition coefficient in *n*-octanol/water) and cellular uptake, indicating that the hydrophobicity of the  $\text{Cp}^*$  ring facilitates the passage of these compounds through the cellular membrane. The most active compound, **Irphen<sup>biph</sup>**, is two-fold more cytotoxic than cisplatin in A2780 cells. In addition, it was found that the three complexes undergo hydrolysis of the Ir–Cl bond forming Ir–OH<sub>2</sub> species (Figure 2.4c) that can bind covalently to DNA bases (guanine). These compounds are also able to modify DNA by intercalation of their  $\text{Cp}^*$ -arene moieties. In fact, this series of drugs were found to access the nucleus of A2780 cells, suggesting that DNA binding is one of their mechanisms of action.<sup>139</sup>



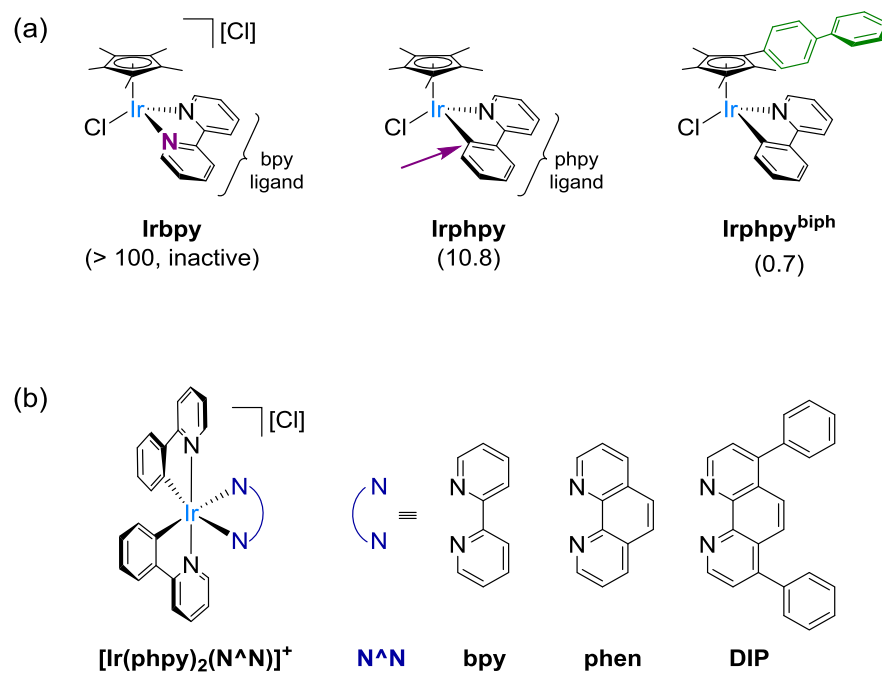


**Figure 2. 4** (a) Schematic representation of Ir(III) cyclopentadienyl complexes. (b) Monocationic Cp\*Ir(III) compounds. IC<sub>50</sub> values (μM) are shown in parenthesis. (c) Dual DNA binding mode of **Irphen<sup>biph</sup>**.

A closely related series of compounds is illustrated in Figure 2.5a. First, substitution of a N atom donor by isoelectronic C<sup>-</sup> (indicated in purple color in Figure 2.5a) decreases the overall charge of the compound, thereby increasing the hydrophobicity, cellular uptake and cytotoxicity against A2780 cells (compare **Ir**bp**y** vs **Ir**ph**py**).<sup>140</sup> Increasing the hydrophobicity of the Cp\* moiety in **Ir**ph**py<sup>biph</sup>** (highlighted in green in Figure 2.5a) further improves the cellular uptake and anticancer activity (2-fold more cytotoxic than cisplatin).<sup>139,140,141</sup>

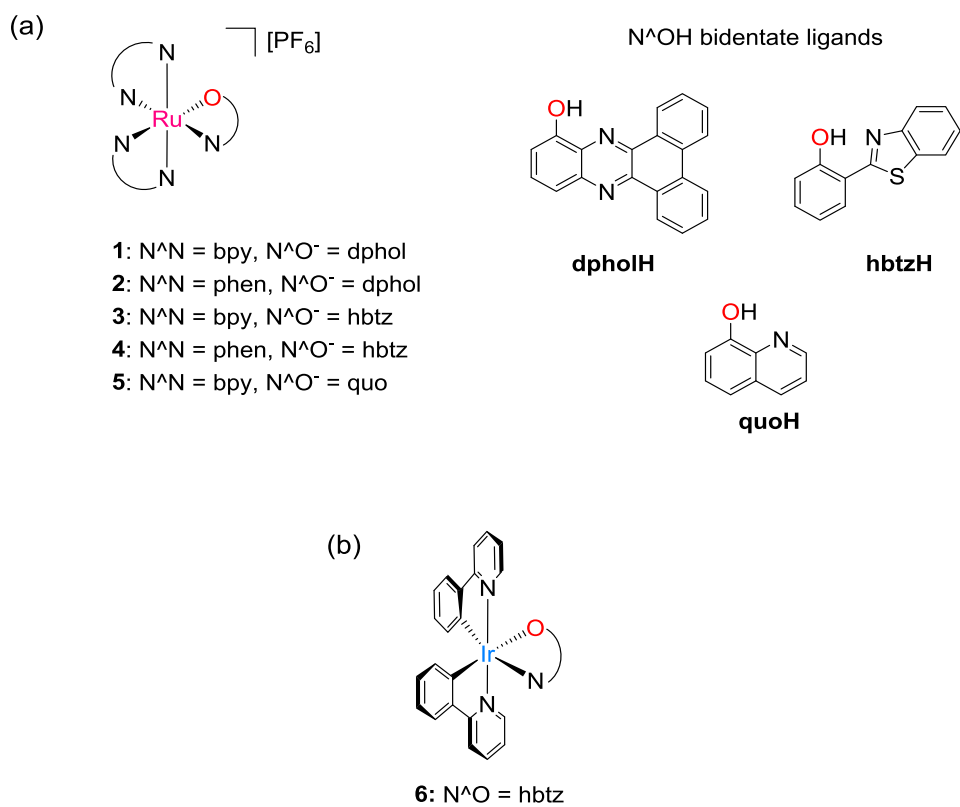
Increasing the hydrophobicity of the ancillary bidentate ligands is also a strategy that has been used to design anticancer active Ir(III) compounds in an octahedral geometry.<sup>142,143</sup> For example, the cytotoxicity of compounds of the type [Ir(phpy)<sub>2</sub>(N<sup>^</sup>N)]<sup>+</sup> increases when expanding the π-system of the chelating polypyridyl N<sup>^</sup>N ligand (Figure 2.5b).<sup>142</sup> The compound [**Ir(phpy)<sub>2</sub>(DIP)**]<sup>+</sup> exhibits the highest cellular uptake and was the most active of the series. This monocationic compound is 6-fold, 20-fold and 10-fold more cytotoxic than cisplatin against cervical (HeLa), lung (A549) and breast (MCF-7) cancer cells, respectively.<sup>142</sup> [**Ir(phpy)<sub>2</sub>(DIP)**]<sup>+</sup> was shown to localize in the endoplasmic reticulum (ER), induce ER stress and release of ER stored Ca<sup>2+</sup> into the cytoplasm. The authors found that rapid accumulation of Ca<sup>2+</sup> in the matrix of mitochondria led to swelling and fragmentation of these organelles. Moreover, increase of cytoplasmic cytochrome c levels and induction of the activity of caspase 3, along with chromatin condensation and blebbing of the plasma membrane, was observed when HeLa cells were treated with [**Ir(phpy)<sub>2</sub>(DIP)**]<sup>+</sup>. These series of events clearly

demonstrate that the intrinsic pathway of apoptosis was the mechanism of cancer cell death.<sup>142</sup>



**Figure 2. 5** (a) Cyclometallated piano-stool Ir cytotoxic compounds. IC<sub>50</sub> values (μM) are shown in parenthesis. (b) Octahedral Ir(III) molecules wit anticancer activity.

To further explore the cytotoxic properties of Ru polypyridyl complexes in an  $[\text{Ru}^{\text{II}}\text{N}_5\text{O}]^+$  pseudo-octahedral coordination environment and taking into account the direct relation between hydrophobicity, cellular uptake and cytotoxic activity, the synthesis of Ru(II) monocationic compounds with  $\text{N}^+\text{O}^-$ -donor ligands possessing  $\pi$ -extended systems was pursued. It was hypothesized that introducing lipophilic  $\text{N}^+\text{O}^-$  bidentate ligands will provide a new family of cytotoxic Ru complexes. Four new Ru complexes (Figure 2.6a),  $[\text{Ru}(\text{bpy})_2(\text{dphol})][\text{PF}_6]$  (**1**; bpy = 2,2'-bipyridine, dphol = dibenzo[*a,c*]phenazin-10-olate),  $[\text{Ru}(\text{phen})_2(\text{dphol})][\text{PF}_6]$  (**2**; phen = 1,10-phenanthroline),  $[\text{Ru}(\text{bpy})_2(\text{hbtz})][\text{PF}_6]$  (**3**; hbtz = 2-(benzo[*d*]thiazol-2-yl)phenolate) and  $[\text{Ru}(\text{phen})_2(\text{hbtz})][\text{PF}_6]$  (**4**) and the known compound  $[\text{Ru}(\text{bpy})_2(\text{quo})][\text{PF}_6]$  (**5**; quo = quinolin-8-olate), were synthesized and characterized and their cytotoxicity against human lung adenocarcinoma (A549) cells was tested. The mechanism of cancer cell death was also investigated using two different biological assays. Additionally, due to the current interest on the antitumor properties of Ir compounds, preliminary results on the anticancer properties of an octahedral Ir(III) complex with the hbtz ligand,  $\text{Ir}(\text{phpy})_2(\text{hbtz})$  (**6**; Figure 2.6b) will be discussed.



**Figure 2. 6** Molecular structures of (a) Ru(II) and (b) Ir(III) compounds containing N<sup>O</sup>-bidentate ligands in this study.

## Experimental Section

### *General Methods*

Standard Schlenk-line techniques ( $N_2$  atmosphere) were used to maintain anaerobic conditions during the preparation of the compounds. The solvents used were of reagent grade quality. Ethanol (KORTEP, 200 proof), acetone (EMD Chemicals), dichloromethane (EMD Chemicals), diethyl ether (EMD Chemicals) and glacial acetic acid (EMD Chemicals) were used as received without further purification.  $RuCl_3 \cdot xH_2O$  (Pressure Chemicals Co.),  $IrCl_3 \cdot xH_2O$  (Pressure Chemicals Co.), 2,2'-bipyridine (bpy, Alfa Aesar), 1,10-phenanthroline (phen, Alfa Aesar), 8-hydroxyquinoline (quoH, Acros Organics), 2-(2-hydroxyphenyl)benzothiazole (hbtzH, Sigma Aldrich), 2,3-diaminophenol (Sigma Aldrich), 9,10-phenanthrenequinone (Sigma Aldrich),  $NH_4PF_6$  (Sigma Aldrich),  $NaHCO_3$  (Mallinckrodt) and  $K_2CO_3$  (Spectrum) were purchased and used as received. The compounds *cis*- $RuCl_2(N^{\wedge}N)_2 \cdot 2H_2O$  ( $N^{\wedge}N =$  bpy, phen),<sup>144</sup>  $[Ir(pphpy)Cl]_2$ <sup>145,146</sup> and  $Ir(phpy)_2(hbtz)$  (**6**)<sup>147</sup> were prepared following reported procedures.

## *Instrumentation*

The  $^1\text{H}$  NMR spectra were recorded on an Inova 500 MHz spectrometer. Chemical shifts are reported in  $\delta$  (ppm) and coupling constants ( $J$ ) in hertz (Hz). The residual solvent peak was used as an internal reference ( $\delta$  1.94 for  $\text{CD}_3\text{CN}$ , 2.05 for  $(\text{CD}_3)_2\text{CO}_2$ ). Electrospray ionization (ESI) mass spectra were acquired on an Applied Biosystems PE SCIEX QSTAR mass spectrometer (MDS Sciex). Elemental analyses were performed by Atlantic Microlab, Inc. (Norcross, GA). Absorption spectra were recorded on a Shimadzu UVPC-3001 spectrophotometer. Electrochemical measurements were performed under anaerobic conditions ( $\text{N}_2$  atmosphere) with a HCH Electrochemical Analyzer model CH 1620A using a BAS Pt disk working electrode, Pt wire auxiliary electrode, Ag/AgCl (3M  $\text{KCl}_{(\text{aq})}$ ) reference electrode and 0.1 M tetra-*n*-butylammonium hexafluorophosphate ( $[\text{nBu}_4\text{N}][\text{PF}_6]$ ) in dry acetonitrile as a supporting electrolyte and 0.1 V/s scan rate. The concentration of the Ru complexes for the electrochemical experiments was  $\sim 1$  mM. Ferrocene was used as an internal standard and exhibited a  $E_{1/2} = 0.44$  V vs Ag/AgCl for the  $\text{Fc}^+/\text{Fc}$  couple under the same experimental conditions. The  $E_{1/2}$  of the Ru complexes were referenced vs NHE using the following expression:  $E_{1/2}$  vs NHE =  $[(E_{1/2}$  vs Ag/AgCl of Ru complex) + (0.64 – 0.44)] V, where 0.64 V =  $E_{1/2}$  [ $\text{Fc}^+/\text{Fc}$ ] vs NHE and 0.44 V =  $E_{1/2}$  [ $\text{Fc}^+/\text{Fc}$ ] vs Ag/AgCl.

### *Synthetic Details*

**Dibenzo[*a,c*]phenazin-10-ol (dpholH).** A mixture of 2,3-diaminophenol (210 mg, 1.69 mmol) and 9,10-phenanthrenequinone (336 mg, 1.61 mmol) in 20 mL of ethanol/acetic acid (1:1) was heated to reflux for 2 h. The yellow precipitate was collected by filtration, dissolved in hot dichloromethane (100 mL) and filtered through a short plug of SiO<sub>2</sub>. A yellow band was eluted with dichloromethane and the combined fractions were reduced to *ca.* 25 mL. After keeping the yellow solution in an ice bath for 30 min, the light yellow precipitated was collected and washed with cold dichloromethane. Yield: 208 mg (44%). <sup>1</sup>H NMR (500 MHz, CDCl<sub>3</sub>): δ 9.39 (dd, 1H, <sup>3</sup>*J* = 8.0, <sup>4</sup>*J* = 1.5), 9.29 (dd, 1H, <sup>3</sup>*J* = 8.0, <sup>4</sup>*J* = 1.0), 8.57 (m, 2H), 8.15 (s, 1H), 7.87 (dd, 1H, <sup>3</sup>*J* = 8.5, <sup>4</sup>*J* = 1.0), 7.84-7.72 (m, 5H), 7.31 (dd, 1H, <sup>3</sup>*J* = 7.5, <sup>4</sup>*J* = 1.5). HRMS (ESI+): Calcd. for [C<sub>20</sub>H<sub>13</sub>N<sub>2</sub>O]<sup>+</sup> ([M + H]<sup>+</sup>), 297.1028. Found: 297.1026.

**[Ru(bpy)<sub>2</sub>(dphol)][PF<sub>6</sub>] (1).** *cis*-RuCl<sub>2</sub>(bpy)<sub>2</sub>•2H<sub>2</sub>O (150 mg, 0.29 mmol), dpholH (95 mg, 0.32 mmol) and NaHCO<sub>3</sub> (74 mg, 0.88 mmol) were suspended in ethanol (70 mL) and were heated to reflux for 8 h. The resulting dark red solution was cooled to room temperature and filtered. NH<sub>4</sub>PF<sub>6(aq)</sub> (5 eq dissolved in 2 mL of water) was added to the filtrate and a dark red solid precipitated. The solid was dissolved in dichloromethane (50 mL) and washed with water (3 x 30 mL). The organic layer was dried with MgSO<sub>4</sub> and reduced to dryness. The residue was dissolved in acetone (10 mL), diethyl ether was added slowly until solid started precipitating and the mixture was kept at 0°C overnight.



A dark red microcrystalline solid was collected by filtration and was washed with diethyl ether (25 mL). Yield: 195 mg (79%).  $^1\text{H}$  NMR (500 MHz,  $(\text{CD}_3)_2\text{CO}$ ):  $\delta$  9.01 (m, 2H), 8.94 (d, 1H,  $^3J = 5.0$ ), 8.86 (d, 1H,  $^3J = 8.5$ ), 8.75 (d, 1H,  $^3J = 8.5$ ), 8.51 (d, 1H,  $^3J = 5.5$ ), 8.47 (d, 1H,  $^3J = 8.0$ ), 8.33 (m, 3H), 8.25 (ddd, 1H,  $^3J = 8.0$ ,  $^3J = 8.0$ ,  $^4J = 1.5$ ), 8.16 (d, 1H,  $^3J = 8.0$ ), 8.03 (ddd, 1H,  $^3J = 8.0$ ,  $^3J = 8.0$ ,  $^4J = 1.5$ ), 7.87 (ddd, 1H,  $^3J = 8.0$ ,  $^3J = 8.0$ ,  $^4J = 1.5$ ), 7.77 (ddd, 1H,  $^3J = 8.5$ ,  $^3J = 7.0$ ,  $^4J = 1.5$ ), 7.70 (ddd, 1H,  $^3J = 8.0$ ,  $^3J = 7.0$ ,  $^4J = 1.0$ ), 7.66 (m, 2H), 7.61 (ddd, 1H,  $^3J = 7.5$ ,  $^3J = 5.5$ ,  $^4J = 1.5$ ), 7.59 (d, 1H,  $^3J = 5.5$ ), 7.41-7.35 (m, 2H), 7.29 (ddd, 1H,  $^3J = 7.5$ ,  $^3J = 5.5$ ,  $^4J = 1.5$ ), 7.24 (dd, 1H,  $^3J = 8.0$ ,  $^4J = 1.0$ ), 7.18 (ddd, 1H,  $^3J = 7.5$ ,  $^3J = 5.5$ ,  $^4J = 1.5$ ), 7.13 (ddd, 1H,  $^3J = 8.5$ ,  $^3J = 7.5$ ,  $^4J = 1.0$ ), 6.94 (dd, 1H,  $^3J = 8.0$ ,  $^4J = 1.5$ ). HRMS (ESI+): Calcd. for  $[\text{C}_{40}\text{H}_{27}\text{N}_6\text{ORu}]^+$  ( $[\text{M} - \text{PF}_6]^+$ ), 709.1290. Found: 709.1287. Anal. Calcd. for  $\text{C}_{40}\text{H}_{27}\text{N}_6\text{OF}_6\text{PRu} \cdot 1.05(\text{CH}_3)_2\text{CO}$ : C, 56.66; H, 3.67; N, 9.19. Found: C, 56.84; H, 3.82; N, 9.36.

**[Ru(phen)<sub>2</sub>(dphol)][PF<sub>6</sub>] (2).** The compound was prepared in a similar fashion to that described for **1** using *cis*-RuCl<sub>2</sub>(phen)<sub>2</sub>•2H<sub>2</sub>O (151 mg, 0.27 mmol), dpholH (87 mg, 0.19 mmol), NaHCO<sub>3</sub> (69 mg, 0.82 mmol) and ethanol (70 mL) as solvent. A dark red microcrystalline solid was obtained. Yield: 185 mg (77%).  $^1\text{H}$  NMR (500 MHz,  $(\text{CD}_3)_2\text{CO}$ ):  $\delta$  9.18 (dd, 1H,  $^3J = 5.5$ ,  $^4J = 1.0$ ), 9.05 (dd, 1H,  $^3J = 8.0$ ,  $^4J = 1.0$ ), 8.75 (m, 2H), 8.70 (dd, 1H,  $^3J = 8.0$ ,  $^4J = 1.0$ ), 8.66 (d, 1H,  $^3J = 8.0$ ), 8.49 (dd, 1H,  $^3J = 8.0$ ,  $^4J = 1.0$ ), 8.41 (dd, 1H,  $^3J = 5.5$ ,  $^4J = 1.0$ ), 8.36 (d, 2H,  $^3J = 8.0$ ), 8.28-8.19 (m, 3H), 8.18 (d, 1H,  $^3J = 8.0$ ), 8.11 (d, 1H,  $^3J = 9.0$ ), 8.01 (dd, 1H,  $^3J = 8.0$ ,  $^3J = 5.5$ ), 7.88 (dd, 1H,  $^3J =$

8.0,  $^3J = 5.5$ ), 7.75-7.66 (m, 2H), 7.63 (t, 1H,  $^3J = 8.0$ ), 7.56 (dd, 1H,  $^3J = 5.5$ ,  $^4J = 1.0$ ), 7.46 (dd, 1H,  $^3J = 8.0$ ,  $^3J = 8.0$ ), 7.29-7.22 (m, 2H), 7.21 (ddd, 1H,  $^3J = 8.0$ ,  $^3J = 7.0$ ,  $^4J = 1.0$ ), 6.87 (dd, 1H,  $^3J = 8.0$ ,  $^4J = 1.0$ ), 6.44 (t, 1H,  $^3J = 7.5$ ). HRMS (ESI+): Calcd. for  $[\text{C}_{44}\text{H}_{27}\text{N}_6\text{ORu}]^+$  ( $[\text{M} - \text{PF}_6]^+$ ), 757.1290. Found: 757.1284. Anal. Calcd. for  $\text{C}_{44}\text{H}_{27}\text{N}_6\text{OF}_6\text{PRu}$ : C, 58.61; H, 3.02; N, 9.32. Found: C, 58.60; H, 3.06; N, 9.30.

**[Ru(bpy)<sub>2</sub>(hbtz)][PF<sub>6</sub>] (3).** The compound was prepared in a similar fashion to that described for **1** using RuCl<sub>2</sub>(bpy)<sub>2</sub>·2H<sub>2</sub>O (158 mg, 0.30 mmol), hbtzH (77 mg, 0.34 mmol), K<sub>2</sub>CO<sub>3</sub> (88 mg, 0.64 mmol) and ethanol/water 1:1 (30 mL) as solvent. A dark red microcrystalline solid was obtained. Yield: 175 mg (73%). <sup>1</sup>H NMR (500 MHz, CD<sub>3</sub>CN):  $\delta$  8.94 (d, 1H,  $^3J = 5.5$ ), 8.61 (d, 1H,  $^3J = 5.5$ ), 8.43 (d, 1H,  $^3J = 8.0$ ), 8.40 (d, 1H,  $^3J = 8.0$ ), 8.34 (m, 2H), 8.06 (d, 1H,  $^3J = 5.5$ ), 8.01-7.94 (m, 2H), 7.85 (ddd, 1H,  $^3J = 8.0$ ,  $^3J = 7.5$ ,  $^4J = 1.5$ ), 7.82 (d, 1H,  $^3J = 8.0$ ), 7.76 (ddd, 1H,  $^3J = 8.0$ ,  $^3J = 7.5$ ,  $^4J = 1.5$ ), 7.57 (dd, 1H,  $^3J = 8.0$ ,  $^4J = 1.5$ ), 7.47 (ddd, 1H,  $^3J = 7.5$ ,  $^3J = 5.5$ ,  $^4J = 1.5$ ), 7.40 (d, 1H,  $^3J = 5.5$ ), 7.34 (ddd, 1H,  $^3J = 7.5$ ,  $^3J = 5.5$ ,  $^4J = 1.5$ ), 7.20-7.11 (m, 3H), 7.02 (ddd, 1H,  $^3J = 8.5$ ,  $^3J = 7.0$ ,  $^4J = 1.5$ ), 6.90 (ddd, 1H,  $^3J = 8.5$ ,  $^3J = 7.0$ ,  $^4J = 1.5$ ), 6.45 (ddd, 1H,  $^3J = 8.5$ ,  $^3J = 7.0$ ,  $^4J = 1.5$ ), 6.40 (d, 1H,  $^3J = 8.5$ ), 6.37 (dd, 1H,  $^3J = 8.5$ ,  $^4J = 1.0$ ). HRMS (ESI+): Calcd. for  $[\text{C}_{33}\text{H}_{24}\text{N}_5\text{OSRu}]^+$  ( $[\text{M} - \text{PF}_6]^+$ ), 640.0748. Found: 640.0752. Anal. Calcd. for  $\text{C}_{33}\text{H}_{24}\text{N}_5\text{OF}_6\text{PSRu} \cdot 0.95(\text{CH}_3)_2\text{CO}$ : C, 51.27; H, 3.56; N, 8.34. Found: C, 51.36; H, 3.55; N, 8.42.

**[Ru(phen)<sub>2</sub>(hbtz)][PF<sub>6</sub>] (4).** The compound was prepared in a similar fashion to that described for **1** using RuCl<sub>2</sub>(phen)<sub>2</sub>•2H<sub>2</sub>O (177 mg, 0.31 mmol), hbtzH (81 mg, 0.36 mmol), K<sub>2</sub>CO<sub>3</sub> (86 mg, 0.62 mmol) and ethanol/water 1:1 (30 mL) as solvent. A dark red-green microcrystalline solid was obtained. Yield: 156 mg (60%). <sup>1</sup>H NMR (500 MHz, CD<sub>3</sub>CN): δ 9.27 (dd, 1H, <sup>3</sup>J = 5.0, <sup>4</sup>J = 1.0), 9.03 (dd, 1H, <sup>3</sup>J = 5.0, <sup>4</sup>J = 1.0), 8.56 (m, 2H), 8.32 (dd, 1H, <sup>3</sup>J = 8.0, <sup>4</sup>J = 1.0), 8.25-8.18 (m, 3H), 8.15 (d, 1H, <sup>3</sup>J = 9.0), 8.11 (d, 1H, <sup>3</sup>J = 9.0), 8.06 (d, 1H, <sup>3</sup>J = 8.5), 7.88 (dd, 1H, <sup>3</sup>J = 8.5, <sup>3</sup>J = 5.0), 7.78-7.73 (m, 2H), 7.62 (dd, 1H, <sup>3</sup>J = 8.0, <sup>4</sup>J = 1.5), 7.46 (dd, 1H, <sup>3</sup>J = 5.5, <sup>3</sup>J = 1.5), 7.34-7.28 (m, 2H), 7.08 (ddd, 1H, <sup>3</sup>J = 8.0, <sup>3</sup>J = 7.0, <sup>4</sup>J = 1.0), 7.00 (ddd, 1H, <sup>3</sup>J = 8.5, <sup>3</sup>J = 7.0, <sup>4</sup>J = 1.5), 6.72 (ddd, 1H, <sup>3</sup>J = 8.5, <sup>3</sup>J = 7.5, <sup>4</sup>J = 1.5), 6.50-6.42 (m, 2H), 6.28 (dd, 1H, <sup>3</sup>J = 8.5, <sup>4</sup>J = 1.0). HRMS (ESI+): Calcd. for [C<sub>37</sub>H<sub>24</sub>N<sub>5</sub>OSRu]<sup>+</sup> ([M - PF<sub>6</sub>]<sup>+</sup>), 688.0745. Found: 688.0714. Calcd. for C<sub>37</sub>H<sub>24</sub>N<sub>5</sub>OF<sub>6</sub>PSRu·(CH<sub>3</sub>)<sub>2</sub>CO: C, 53.30; H, 3.44; N, 7.97. Found: C, 53.51; H, 3.58; N, 7.89.

**[Ru(bpy)<sub>2</sub>(quo)][PF<sub>6</sub>] (5).** The compound was prepared in a similar fashion to that described for **1** using *cis*-RuCl<sub>2</sub>(bpy)<sub>2</sub>•2H<sub>2</sub>O (121 mg, 0.23 mmol), quoH (41 mg, 0.28 mmol), K<sub>2</sub>CO<sub>3</sub> (65 mg, 0.47 mmol) in ethanol/water (1:1, 30 mL). A dark green-red microcrystalline solid was collected by filtration and was washed with diethyl ether (25 mL). Yield: 138 mg (85%). <sup>1</sup>H NMR (500 MHz, (CD<sub>3</sub>)<sub>2</sub>CO): δ 8.89 (d, 1H, <sup>3</sup>J = 5.5), 8.74-8.65 (m, 4H), 8.17 (d, 1H, <sup>3</sup>J = 6.0), 8.13-8.04 (m, 4H), 8.00 (m, 2H), 7.89 (d, 1H, <sup>3</sup>J = 5.0), 7.65 (ddd, 1H, <sup>3</sup>J = 7.5, <sup>3</sup>J = 6.0, <sup>4</sup>J = 1.5), 7.55 (dd, 1H, <sup>3</sup>J = 5.0, <sup>4</sup>J = 1.0), 7.46 (m, 1H), 7.40 (m, 2H), 7.32 (t, 1H, <sup>3</sup>J = 8.0), 7.20 (dd, 1H, <sup>3</sup>J = 8.5, <sup>3</sup>J = 5.0), 6.87

(dd, 1H,  $^3J = 8.0$ ,  $^4J = 1.0$ ), 6.79 (dd, 1H,  $^3J = 8.0$ ,  $^4J = 1.0$ ). HRMS (ESI+): Calcd. for  $[\text{C}_{29}\text{H}_{22}\text{N}_5\text{ORu}]^+$  ( $[\text{M} - \text{PF}_6]^+$ ), 558.0868. Found: 558.0866. Calcd. for  $\text{C}_{29}\text{H}_{22}\text{N}_5\text{OF}_6\text{PRu}\cdot 0.5(\text{CH}_3\text{CH}_2)_2\text{O}$ : C, 50.34; H, 3.68; N, 9.47. Found: C, 50.29; H, 3.79; N, 9.23.

### *X-Ray Crystallography*

Single crystals of compounds **1**, **3** and **4** were obtained by slow diffusion of diethyl ether into acetone solutions of the compounds at room temperature. Single crystals of compound **6** were grown from slow evaporation of an ethyl acetate solution of the compound at room temperature. X-ray data were collected at 110 K on a Bruker APEX II CCD X-ray diffractometer equipped with a graphite monochromated  $\text{MoK}\alpha$  radiation source ( $\lambda = 0.71073 \text{ \AA}$ ). The data sets were integrated with the Bruker SAINT software package.<sup>148</sup> The absorption correction (SADABS)<sup>149</sup> was based on fitting a function to the empirical transmission surface as sampled by multiple equivalent measurements. Solution and refinement of the crystal structures was carried out using the SHELX<sup>150</sup> (2013) suite of programs and the graphical interface *ShelXle*<sup>151</sup> was used during the refinement. The structures were solved by Patterson methods, all non-hydrogen atoms were refined with anisotropic displacement parameters using a full-matrix least-squares technique on  $F^2$ . Hydrogen atoms were fixed to parent atoms and refined using the riding model. PLATON/SQUEEZE was employed in the case of **4** after attempts to model a disordered diethyl ether solvent molecule failed. The solvent

molecules in the unit cell (one solvent molecule per asymmetric unit,  $Z = 4$ ) were determined to occupy  $642.9 \text{ \AA}^3$ . The number of electron counts in voids per unit cell was 159, which is close to that expected for four diethyl ether molecules (168 electrons).

### *Cell Culture Experiments*

The human lung adenocarcinoma A549 cell line, derived from type II pneumocytes (CCL 185), was obtained from American Type Culture Collection (Manassas, VA). Cells were cultured in DMEM-F12 medium (Dulbecco's Modified Eagle Medium: Nutrient Mixture F-12) with 10% FBS. Cell cultures were incubated in a humidified atmosphere containing 5% CO<sub>2</sub> at 37°C and were approximately 80% confluent at the time of analysis.

### *In vitro Cytotoxicity*

A549 cells were plated in a 96 well plate and were pre-incubated in a humidified atmosphere containing 5% CO<sub>2</sub> at 37°C for 24 h. Solutions of the metal complexes in DMEM/F12 medium were added at different concentration (final concentrations of compounds: 0–50  $\mu\text{M}$  range, 0.1 % DMSO) and the cells were incubated for another 48 h. Cells were then washed twice with PBS and fixed with methanol for 30 min. Following fixation, Janus green B (1 mg/mL, Alfa Aesar) was added to each well and incubated at room temperature for 5 min. Cells were again washed twice with PBS and

100  $\mu$ L of methanol was added to each well to extract the dye. Janus Green B signal was then measured using a BioTek Synergy 4 plate reader set to an absorbance of 630 nm.

#### *JC-1 Assay*

Live cell imaging studies were performed using a Zeiss 510 META NLO multiphoton system consisting of an Axiovert 200 MOT inverted laser scanning confocal microscope (Carl Zeiss Microimaging, Thornwood, NY). A Zeiss Plan-Neofluar 40x/NA=1.3 oil immersion objective was used to acquire the images.

Cells were plated in coverglass chamber slides for 24 h prior to treatment with compounds **1–4** and cisplatin for 48 h. Cells were then washed with PBS and labeled with JC-1 at a final concentration of 5  $\mu$ g/mL for 30 min at 37°C. Excitation of JC-1 (Invitrogen) was performed using an Ar-ion laser at 488 nm and emission data were collected using a dichroic 545 nm SP in combination with 2 filters 500–550 BP and 565–615 BP. At least eight areas per well were scanned. Two wells were analyzed per treatment. Two experiments were conducted on different days.

#### *Calcein AM Assay*

Cells were plated in coverglass chamber slides for 24 h prior to treatment with compound **4** and cisplatin for 48 h. Cells were then washed with PBS and incubated with 1  $\mu$ g/ml Hoeschst 33258 (Invitrogen) and 10  $\mu$ M acetoxymethyl ester of Calcein dye

(calcein AM, Invitrogen) for 30min, and with 50 nM Mitotracker Deep Red FM (Invitrogen) for 15 min. Following loading, cells were washed and 1 mM cobalt (II) chloride hexahydrate was added to the cells and images were acquired. To collect Hoechst 33258 (Invitrogen) fluorescence, cells were irradiated with the Chameleon tunable Ti:Sapphire laser (Coherent Inc., Santa Clara, CA) at an excitation wavelength of 740 nm (which is roughly equivalent to 370 nm in single photon excitation with a continuous wavelength laser system) and emission was collected at 430–480 nm. Calcein was excited with an Ar-ion laser at 458 nm and emission was monitored using a band pass 500–530 filter. Mitotracker Deep Red FM (Invitrogen) was excited with a He-Ne laser at 633 nm and emission was collected using a BP 650–710 filter. Image acquisition was performed sequentially to reduce the possibility of bleedthrough between channels. At least eight areas per well were scanned. Two wells were analyzed per treatment. Two experiments were conducted on different days.

#### *Caspase Glo Assay*

Cells were cultured for 24 h prior to addition of compound **4** or cisplatin for 48 h. Cells were then washed twice with PBS and 100  $\mu$ L of the Caspase-Glo® 3/7 reagent solution (Promega) was added to each well. Wells were then scanned every 10 min for 30 min and luminescence readings were recorded with Biotek Synergy plate reader. Four wells per concentration were recorded.

## Results and Discussion

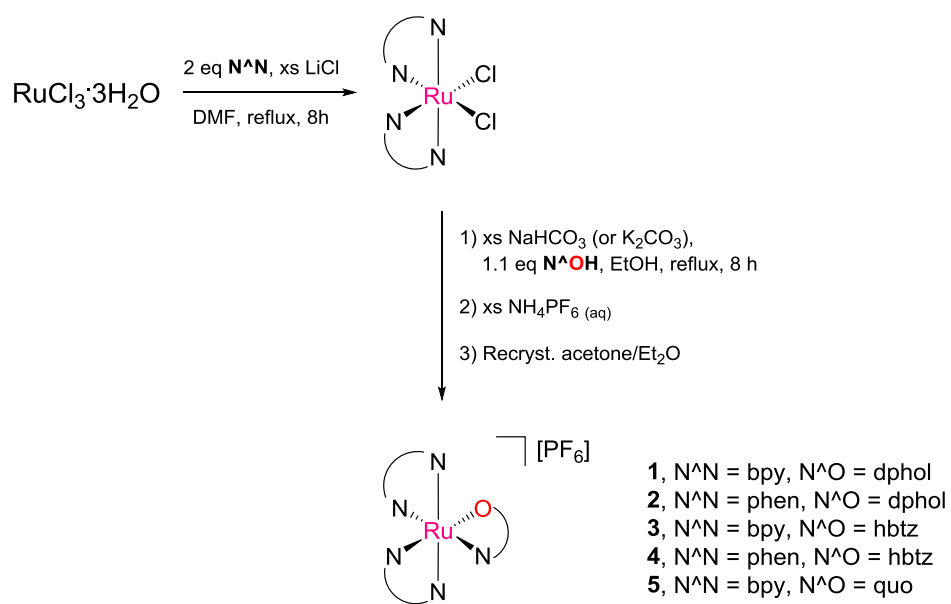
### *Synthesis and Characterization*

The precursor for the syntheses of **1–5** is *cis*-RuCl<sub>2</sub>(N<sup>^</sup>N)<sub>2</sub> (N<sup>^</sup>N = bpy, phen) that was prepared by reacting RuCl<sub>3</sub> with 2 eq of N<sup>^</sup>N in refluxing DMF and in the presence of LiCl (Figure 2.7).<sup>144</sup> The crude products [Ru(N<sup>^</sup>N)<sub>2</sub>(N<sup>^</sup>O<sup>-</sup>)]PF<sub>6</sub> were obtained by reacting *cis*-RuCl<sub>2</sub>(N<sup>^</sup>N)<sub>2</sub> with 1.1 eq of N<sup>^</sup>OH (dpholH, hbtzH and quoH) in refluxing ethanol (or aqueous ethanol) and in the presence of a base (NaHCO<sub>3</sub> or K<sub>2</sub>CO<sub>3</sub>) to deprotonate the phenol moiety of N<sup>^</sup>OH, followed by precipitation with NH<sub>4</sub>PF<sub>6(aq)</sub>. The five complexes were obtained as dark red microcrystalline solids after recrystallization from acetone/diethyl ether. Although hbtzH is a commercially available, there are no reports of Ru complexes with this ligand. Due to the C<sub>1</sub> symmetry of **1–5**, there are no magnetic equivalent protons in their <sup>1</sup>H NMR spectra (Figures 2.8 and 2.9); the integration of the signals match the expected number of protons for each complex (**1**, 27 H; **2**, 27 H; **3**, 24 H; **4**, 24 H; **5**, 22H). The identity and purity of the compounds were confirmed by elemental analyses and ESI-MS, where a single peak corresponding to the [M - PF<sub>6</sub>]<sup>+</sup> cations was observed for all of the complexes (**1**, *m/z* = 709.1287; **2**, *m/z* = 757.1284; **3**, 640.0752; **4**, *m/z* = 688.0714; **5**, 558.0866).

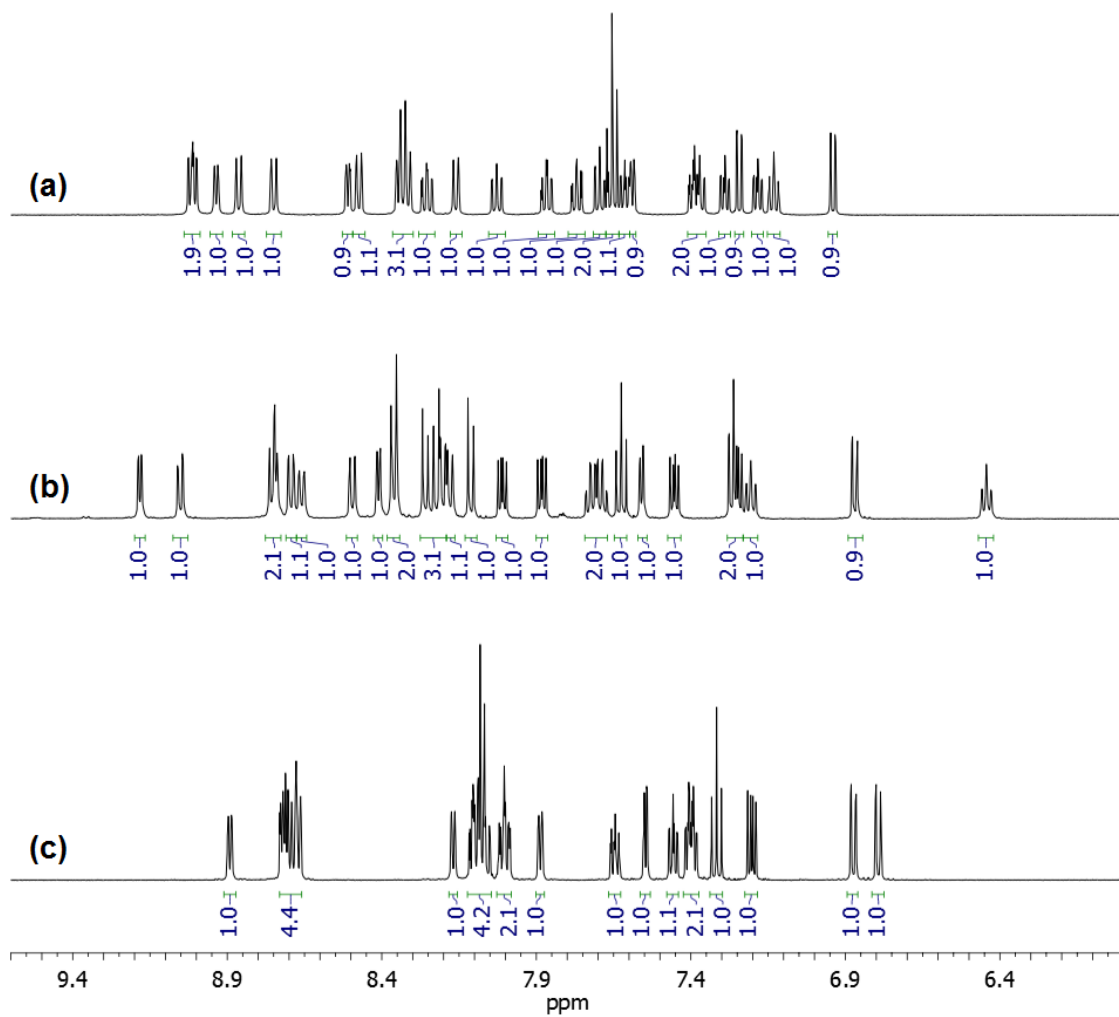
The Ir compound Ir(phpy)<sub>2</sub>(hbtz) (**6**), which can be considered an analog of [Ru(bpy)<sub>2</sub>(hbtz)]<sup>+</sup> (**3**) and [Ru(phen)<sub>2</sub>(hbtz)]<sup>+</sup> (**4**), was obtained as a yellow solid by reacting the μ-chloro Ir(III) dimer [Ir(phpy)Cl]<sub>2</sub> with 2 eq of hbtzH in the presence of a



base ( $[\text{tBu}_4\text{N}][\text{OH}]$  or  $[\text{Me}_4\text{N}][\text{OH}]$ ) in dichloromethane, as reported in the literature.<sup>147,152</sup> Compound **6** also possesses  $C_1$  symmetry and 24 H resonances were observed in its  $^1\text{H}$  NMR spectrum (Figure 2.9c).<sup>147,152</sup>



**Figure 2. 7** Reaction scheme for the syntheses of **1–5**.



**Figure 2. 8**  $^1\text{H}$  NMR spectra ( $(\text{CD}_3)_2\text{CO}$ , 500 MHz) of compounds (a) **1**, (b) **2** and (c) **5**.

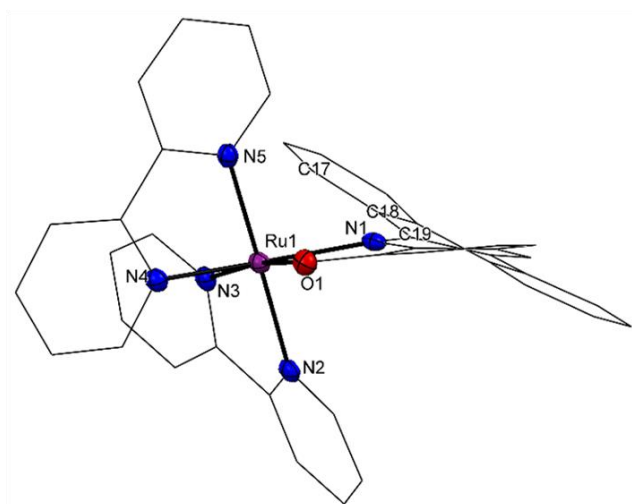
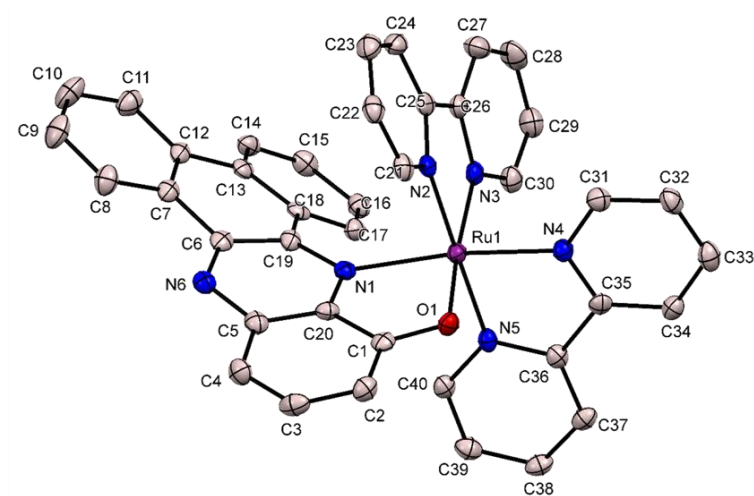


### *X-ray Structures of Compounds 1, 3, 4 and 6*

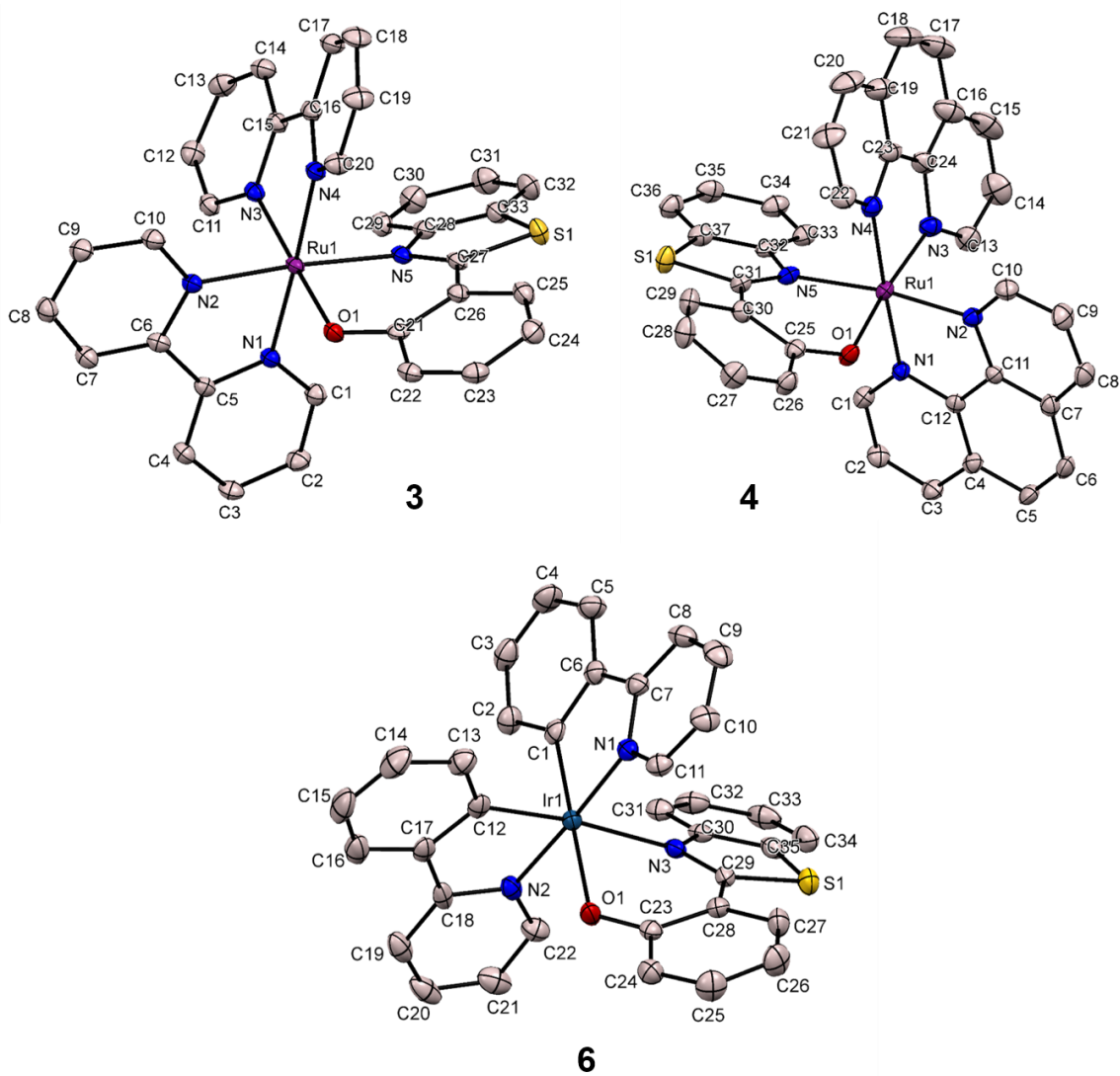
Single crystals of **1**, **3** and **4** were obtained by slow diffusion of diethyl ether into acetone solutions of the compounds at room temperature. Their X-ray structures are shown in Figures 2.10 and 2.11 and the crystallographic data are compiled in Tables 2.1–2.6. Compounds **1** and **3** crystallize in the triclinic space group  $P\bar{1}$ , whereas **4** crystallizes in the monoclinic space group  $P2/n$ . There is an interstitial acetone molecule in the asymmetric unit of **1** and **3**.

The coordination sphere of the metal center in the structures of the three ruthenium molecules consists of five N atoms and one O atom in a distorted octahedral environment. The Ru–O bond distances are  $\sim 2.060$  Å in the three compounds and are similar to that reported for  $[\text{Ru}(\text{bpy})_2(\text{quo})][\text{PF}_6]$  (**5**; 2.063(6) Å).<sup>153</sup> Their Ru–N bond distances to bpy and phen fall in the 2.019–2.079 Å range and are also in agreement with the respective distances in  $[\text{Ru}(\text{bpy})_2(\text{quo})][\text{PF}_6]$  and Ru(II) polypyridyl compounds in a  $[\text{RuN}_6]$  coordination environment. In contrast, the Ru–N bond distances to dphol in **1** (Ru–N1, 2.152(3) Å) and to hbtz in **3** (Ru–N5, 2.110(2) Å) and **4** (Ru–N5, 2.110(3) Å) are longer. The elongation of such Ru–N bonds is likely to be caused by steric repulsions between the bulky phenanthrene moiety of dphol and adjacent bpy ligand in the case of **1**, and between the benzothiazolyl moiety of hbtz and adjacent bpy and phen ligands in the case of **3** and **4**, respectively. The dphol ligand in **1** is twisted as depicted in Figure 2.10, displaying dihedral angles of  $-30.7(5)$  for Ru1–N1–C19–C18 and  $-19.3(6)$  for N1–C19–C18–C17. The hbtz ligands in **3** and **4** are twisted around the C–C bond that

connects the phenoxido and benzothiazolyl moieties, exhibiting dihedral angles of  $8.5(3)^\circ$  (N5–C27–C26–C21) and  $-16.3(5)^\circ$  (N5–C31–C30–C25), respectively



**Figure 2. 10** (Top) Thermal ellipsoid plots at the 50% probability level of the X-ray structure of  $[\text{Ru}(\text{bpy})_2(\text{dphol})][\text{PF}_6]$  (**1**). The  $[\text{PF}_6]^-$  anion and H atoms have been omitted for the sake of clarity. (Bottom) Distortion of the dphol ligand in compound **1**.



**Figure 2.11** Thermal ellipsoid plots at the 50% probability level of the X-ray structures of  $[\text{Ru}(\text{bpy})_2(\text{hbtz})][\text{PF}_6]$  (**3**),  $[\text{Ru}(\text{phen})_2(\text{hbtz})][\text{PF}_6]$  (**4**) and  $\text{Ir}(\text{phpy})_2(\text{hbtz})$  (**6**). The  $[\text{PF}_6]^-$  anion (in the case of **3** and **4**) and H atoms have been omitted for the sake of clarity.

**Table 2. 1** Crystal Structural Data and Refinement Parameters for the compounds [Ru(bpy)<sub>2</sub>(dphol)][PF<sub>6</sub>]·(CH<sub>3</sub>)<sub>2</sub>CO (**1**) and [Ru(bpy)<sub>2</sub>(hbtz)][PF<sub>6</sub>]·(CH<sub>3</sub>)<sub>2</sub>CO (**3**).

Compound	<b>1</b>	<b>3</b>
CCDC number	997833	997834
Empirical Formula	C <sub>43</sub> H <sub>33</sub> F <sub>6</sub> N <sub>6</sub> O <sub>2</sub> PRu	C <sub>36</sub> H <sub>30</sub> F <sub>6</sub> N <sub>5</sub> O <sub>2</sub> PRuS
Formula weight	911.79	842.75
Temperature, K	110(2)	110(2)
Crystal system	Triclinic	Triclinic
Space group	<i>P</i> -1	<i>P</i> -1
Unit cell dimensions	<i>a</i> = 9.894(2), $\alpha$ = 107.82(3) <i>b</i> = 11.556(2), $\beta$ = 91.60(3) <i>c</i> = 17.230(3), $\gamma$ = 96.54(3)	<i>a</i> = 9.3106(19), $\alpha$ = 66.68(3) <i>b</i> = 13.975(3), $\beta$ = 78.29(3) <i>c</i> = 14.581(3), $\gamma$ = 88.96(3)
Volume, Å <sup>3</sup>	1859.2(6)	1701.8(7)
Z	2	2
Density, g/cm <sup>3</sup>	1.629	1.645
Absorption coefficient, mm <sup>-1</sup>	0.544	0.645
<i>F</i> (000)	924	852
Crystal color, morphology	purple, block	purple, block
Crystal size, mm <sup>3</sup>	0.28 × 0.18 × 0.10	0.29 × 0.26 × 0.21
Reflections collected	15696	18194
Independent reflections	5493 [R <sub>int</sub> = 0.0349]	7156 [R <sub>int</sub> = 0.0178]
Data/restraints/parameters	5493 / 0 / 534	7156 / 0 / 471
Goodness-of-fit on F <sup>2</sup>	1.055	1.180
R indices [I > 2σ(I)]	R <sub>1</sub> = 0.0377 wR <sub>2</sub> = 0.0979	R <sub>1</sub> = 0.0247 wR <sub>2</sub> = 0.0696
R indices (all data)	R <sub>1</sub> = 0.0450 wR <sub>2</sub> = 0.1025	R <sub>1</sub> = 0.0278 wR <sub>2</sub> = 0.0805
Largest diff. peak, hole, e/Å <sup>3</sup>	0.911 / -0.441	0.803 / -0.704

**Table 2. 2** Crystal Structural Data and Refinement Parameters for the compounds [Ru(phen)<sub>2</sub>(hbtz)][PF<sub>6</sub>] (**4**) and Ir(phpy)<sub>2</sub>(hbtz) (**6**).

Compound	<b>4</b>	<b>6</b>
CCDC number	997835	997836
Empirical Formula	C <sub>37</sub> H <sub>24</sub> F <sub>6</sub> N <sub>5</sub> OPRuS	C <sub>35</sub> H <sub>24</sub> IrN <sub>3</sub> OS
Formula weight	832.71	726.83
Temperature, K	110(2)	110(2)
Crystal system	Monoclinic	Triclinic
Space group	<i>P2<sub>1</sub>/n</i>	<i>P-1</i>
Unit cell dimensions	<i>a</i> = 14.373(3), $\alpha$ = 90 <i>b</i> = 12.824(3), $\beta$ = 92.73(3) <i>c</i> = 20.057(4), $\gamma$ = 90	<i>a</i> = 10.912(2), $\alpha$ = 75.61(3) <i>b</i> = 11.655(2), $\beta$ = 68.71(3) <i>c</i> = 12.099(2), $\gamma$ = 71.55(3)
Volume, Å <sup>3</sup>	3692.6(13)	1344.4(6)
Z	4	2
Density, g/cm <sup>3</sup>	1.498	1.795
Absorption coefficient, mm <sup>-1</sup>	0.592	5.079
<i>F</i> (000)	1672	712
Crystal color, morphology	purple, block	orange, plate
Crystal size, mm <sup>3</sup>	0.24 × 0.17 × 0.11	0.12 × 0.09 × 0.04
Reflections collected	38831	15489
Independent reflections	7583 [R <sub>int</sub> = 0.0483]	5871 [R <sub>int</sub> = 0.0296]
Data/restraints/parameters	7583 / 0 / 470	5871 / 0 / 370
Goodness-of-fit on F <sup>2</sup>	1.049	1.049
R indices [I > 2σ(I)]	R <sub>1</sub> = 0.0419 wR <sub>2</sub> = 0.0942	R <sub>1</sub> = 0.0206 wR <sub>2</sub> = 0.0453
R indices (all data)	R <sub>1</sub> = 0.0528 wR <sub>2</sub> = 0.0991	R <sub>1</sub> = 0.0232 wR <sub>2</sub> = 0.0464
Largest diff. peak/hole, e/Å <sup>3</sup>	2.640 / -0.847	1.026 / -0.748



**Table 2. 3** Selected bond distances and angles for [Ru(bpy)<sub>2</sub>(dphol)][PF<sub>6</sub>] $\cdot$ (CH<sub>3</sub>)<sub>2</sub>CO (**1**).

Bond lengths (Å)		Bond angles (°)	
Ru1–O1	2.061(3)	N1–Ru1–O1	80.5(1)
Ru1–N1	2.152(3)	N2–Ru1–N3	78.4(1)
Ru1–N2	2.065(4)	N4–Ru1–N5	78.7(1)
Ru1–N3	2.052(3)	O1–Ru1–N4	89.9(1)
Ru1–N4	2.035(3)	N1–Ru1–N3	105.6(1)
Ru1–N5	2.060(4)	N3–Ru1–N4	84.1(1)
Dihedral angles (°)			
N1–Ru1–O1–C1		3.7(2)	
Ru1–N1–C19–C18		–30.7(5)	
N1–C19–C18–C17		–19.3(6)	
N6–C6–C7–C8		–10.8(5)	

**Table 2. 4** Selected bond distances and angles for [Ru(bpy)<sub>2</sub>(hbtz)][PF<sub>6</sub>] $\cdot$ (CH<sub>3</sub>)<sub>2</sub>CO (**3**).

Bond lengths (Å)		Bond angles (°)	
Ru1–O1	2.059(2)	O1–Ru1–N5	87.93(6)
Ru1–N1	2.047(2)	N1–Ru1–N2	78.75(7)
Ru1–N2	2.041(2)	N3–Ru1–N4	78.41(7)
Ru1–N3	2.019(2)	O1–Ru1–N2	90.27(6)
Ru1–N4	2.045(2)	N5–Ru1–N3	94.41(7)
Ru1–N5	2.110(2)	N2–Ru1–N3	87.78(7)
Dihedral angles (°)			
N3–Ru1–N4–C16		–16.4(1)	
N4–Ru1–N3–C15		17.1(1)	
N5–Ru1–O1–C21		27.6(2)	
O1–Ru1–N5–C27		–28.6(2)	
N5–C27–C26–C21		8.5(3)	
C25–C26–C27–S1		5.0(3)	

**Table 2. 5** Selected bond distances and angles for [Ru(phen)<sub>2</sub>(hbtz)][PF<sub>6</sub>] (**4**).

Bond lengths (Å)		Bond angles (°)	
Ru1–O1	2.060(2)	O1–Ru1–N5	87.18(9)
Ru1–N1	2.053(3)	N1–Ru1–N2	80.4(1)
Ru1–N2	2.035(3)	N3–Ru1–N4	80.0(1)
Ru1–N3	2.028(3)	O1–Ru1–N2	84.54(9)
Ru1–N4	2.079(3)	N5–Ru1–N3	100.0(1)
Ru1–N5	2.110(3)	N2–Ru1–N3	88.3(1)
Dihedral angles (°)			
N5–Ru1–O1–C25			–35.3(2)
O1–Ru1–N5–C31			27.8(2)
N5–C31–C30–C25			–16.3(5)
C29–C30–C31–S1			–17.3(4)

**Table 2. 6** Selected bond distances and angles for Ir(phpy)<sub>2</sub>(hbtz) (**6**).

Bond lengths (Å)		Bond angles (°)	
Ir1–O1	2.141(3)	O1–Ir1–N3	82.35(8)
Ir1–N1	2.049(2)	N1–Ir1–C1	79.9(1)
Ir1–N2	2.048(2)	N2–Ir1–C12	80.9(1)
Ir1–N3	2.205(2)	O1–Ir1–C12	90.5(1)
Ir1–C1	1.999(3)	N3–Ir1–C1	98.2(1)
Ir1–C12	1.995(4)	C1–Ru1–C12	89.0(1)
Dihedral angles (°)			
O1–Ir1–N3–C29			–36.2(2)
N3–Ir1–O1–C23			43.3(2)
C23–C28–C29–N3			18.7(5)
C27–C28–C29–S1			17.3(4)

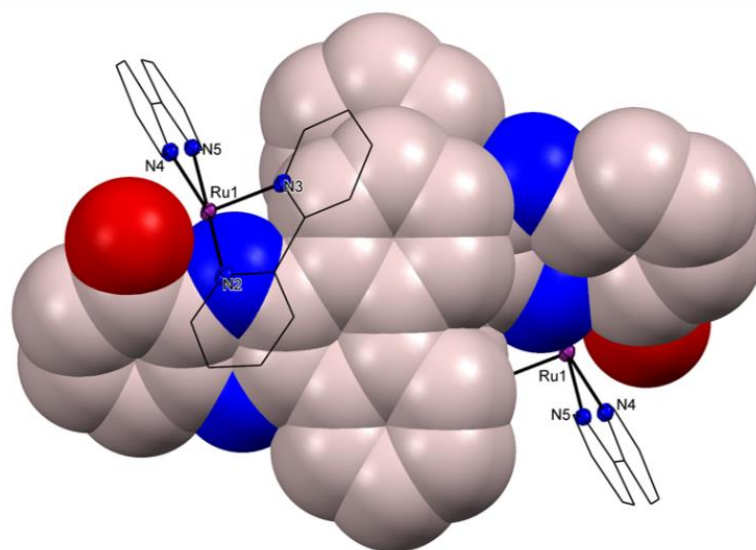
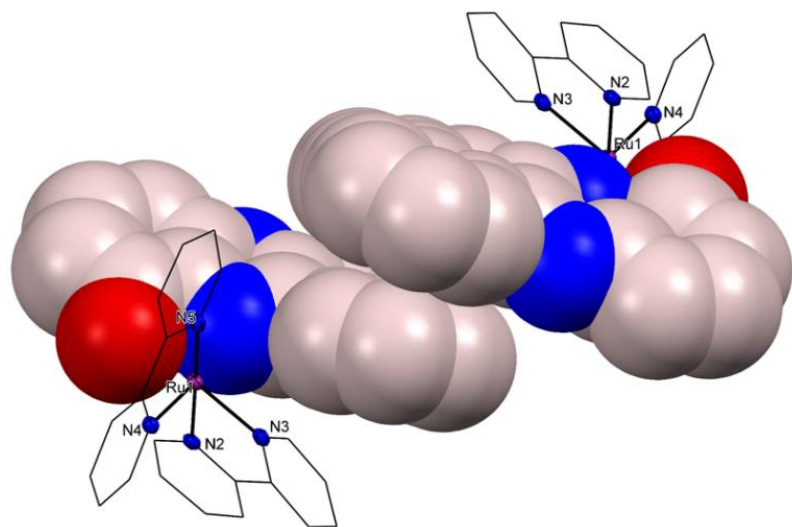
Although the synthesis, characterization and optical properties of the Ir compound **6** have been previously documented,<sup>152</sup> its X-ray structure was not previously reported. Single crystals of **6** were grown from slow evaporation of an ethyl acetate solution of the compound at room temperature. Compound **6** crystallizes in the triclinic space group  $P\bar{1}$ . The Ir center exhibits a distorted octahedral environment (Figure 2.11), the C<sup>-</sup> donors of each phpy ligand are *cis* to each other, whereas the N atom donors of both phpy ligands are *trans* to each other. Such an arrangement of phpy ligands is well-established in Ir(III) complexes possessing the “Ir(phpy)<sub>2</sub>” fragment. The reason for this disposition of C<sup>-</sup> and N donor atoms is the strong *trans* influence of the cyclometallating C<sup>-</sup> donor of phpy, avoiding the positioning the both C<sup>-</sup> strong donors in *trans* disposition.<sup>154,155</sup> The elongation of the Ir–N3 bond (2.205(2) Å) with respect to Ir1–N1 and Ir1–N2 bond distances (2.048(2) and 2.048(2) Å, respectively) is due to the strong donating properties (*trans* influence) of the C12 atom donor that is in *trans* position, as also observed in the Ru cyclometallated compounds that will be described in Chapter III. The Ir1–O1 bond (2.141(3) Å) is longer than the Ru–O bond in **3** and **4** (~2.06 Å) because of the *trans* influence of the C1 atom that is located in *trans* position to the Ir1–O1 bond in **6**. The bond distances and angles in compound **6** are also similar to those reported for the related compounds of formula Ir(phpy)<sub>2</sub>(quoR), where quoR = derivatives of 8-hydroxyquinolinolate.<sup>156</sup> The hbtz ligand is twisted around the C–C bond that connects the phenoxido and benzothiazolyl (C23–C28–C29–N3, 18.7(5)°), as observed in the Ru compounds **3** and **4**.

Intermolecular  $\pi$ - $\pi$  stacking interactions involving dphol ligands of different [Ru(bpy)<sub>2</sub>(dphol)]<sup>+</sup> cations are observed in the crystal packing of **1** (Figure 2.12), where the distance between the planes containing the phenanthrene moieties is 3.52 Å. The ancillary bpy ligands of **1** are also involved in intermolecular  $\pi$ - $\pi$  stacking interactions (Figure 2.13). Likewise, stacking interactions between polypyridyl ligands (bpy, phen, phpy) are observed in the crystal packing of **3**, **4** and **6** (Figures 2.14–2.16). A summary of centroid-centroid distances, interplanar distances and displacement angles is compiled in Table 2.7. These three parameters in complexes **1**, **3** and **4** and **6** are within the range observed for polypyridyl metal complexes reported in the literature.<sup>157,158</sup> In addition, the hbtz ligands in **3**, **4** and **6** exhibit stacking interactions in the crystal packing, with interplanar distances of 3.62, 3.92 and 3.43 Å, respectively (Figures 2.14–2.16).

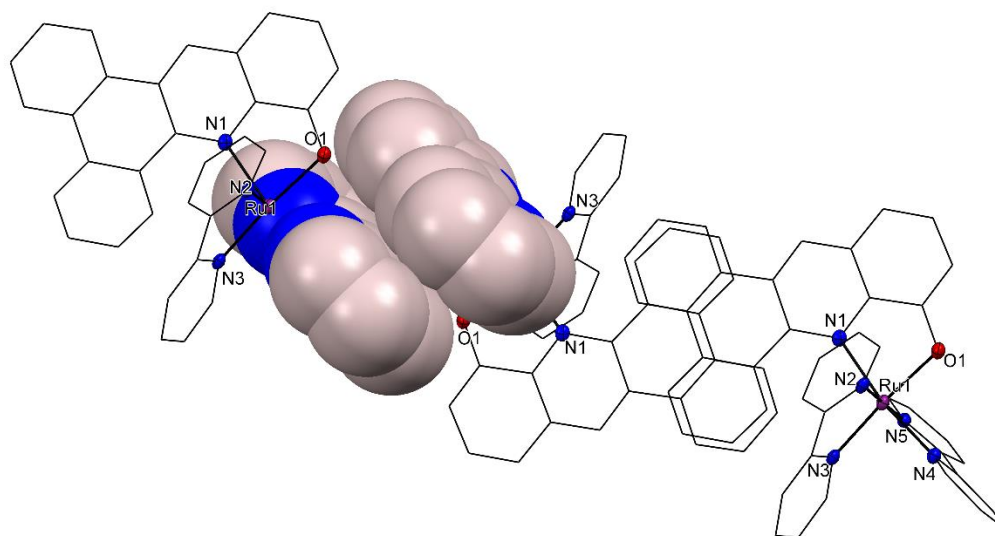
**Table 2. 7** Distances and angles associated with the  $\pi$ - $\pi$  stacking interaction of polypyridyl ligands in compounds **1**, **3** and **4**.

Compound	Ligands involved	Centroid-centroid distance (Å)	Interplanar Distance (Å)	Displacement angle (°)
<b>1</b>	bpy–bpy	3.63	3.28	28
<b>3</b>	bpy–bpy	3.69	3.38	24
<b>4</b>	phen–phen	4.09 <sup>a</sup>	3.50	31
<b>6</b>	phpy–phpy	4.66 <sup>b</sup>	3.40	43

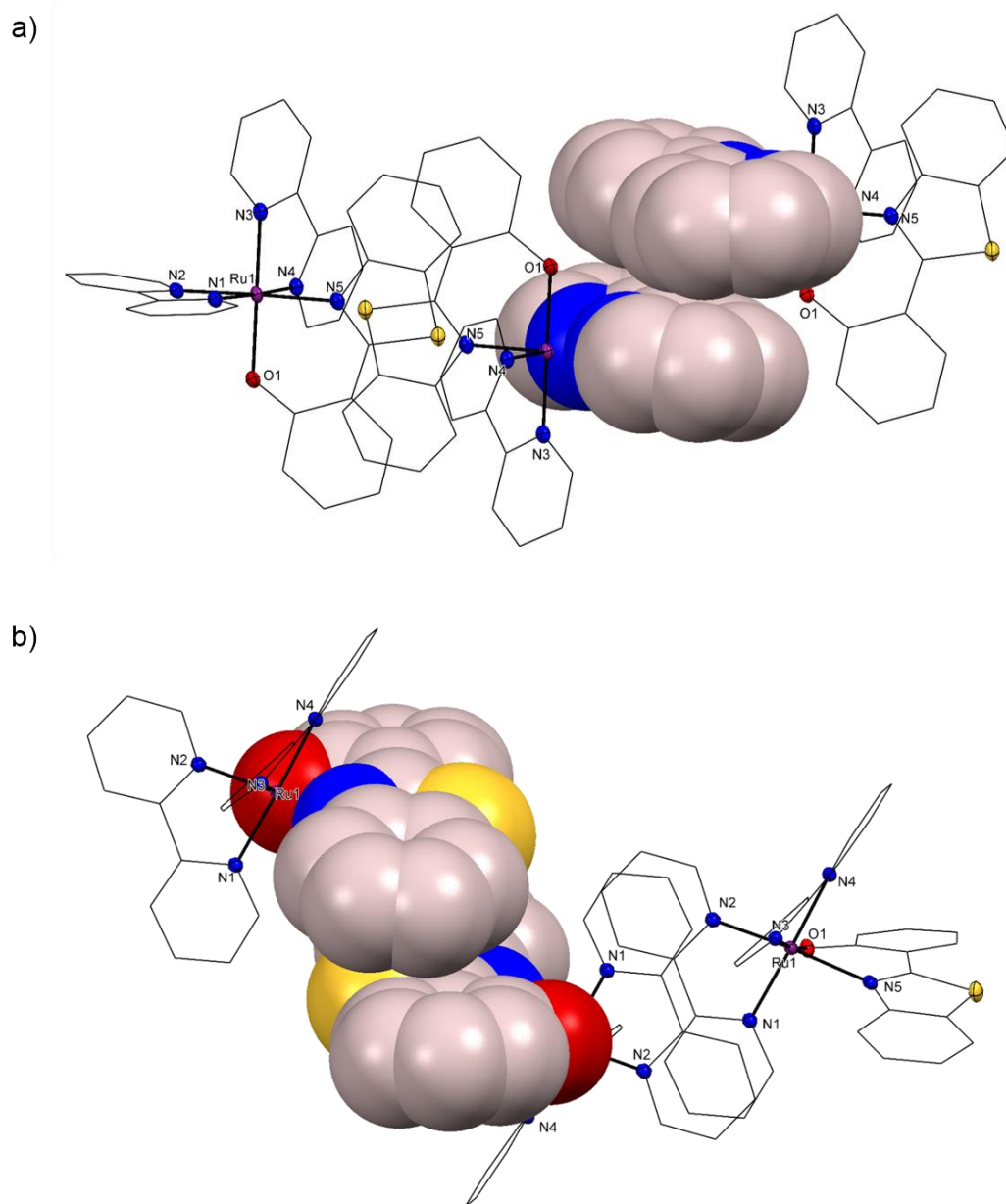
<sup>a</sup>Centroid of the central benzene ring of phen ligands. <sup>b</sup>Centroid of pyridyl ring to centroid phenyl ring of phpy ligands.



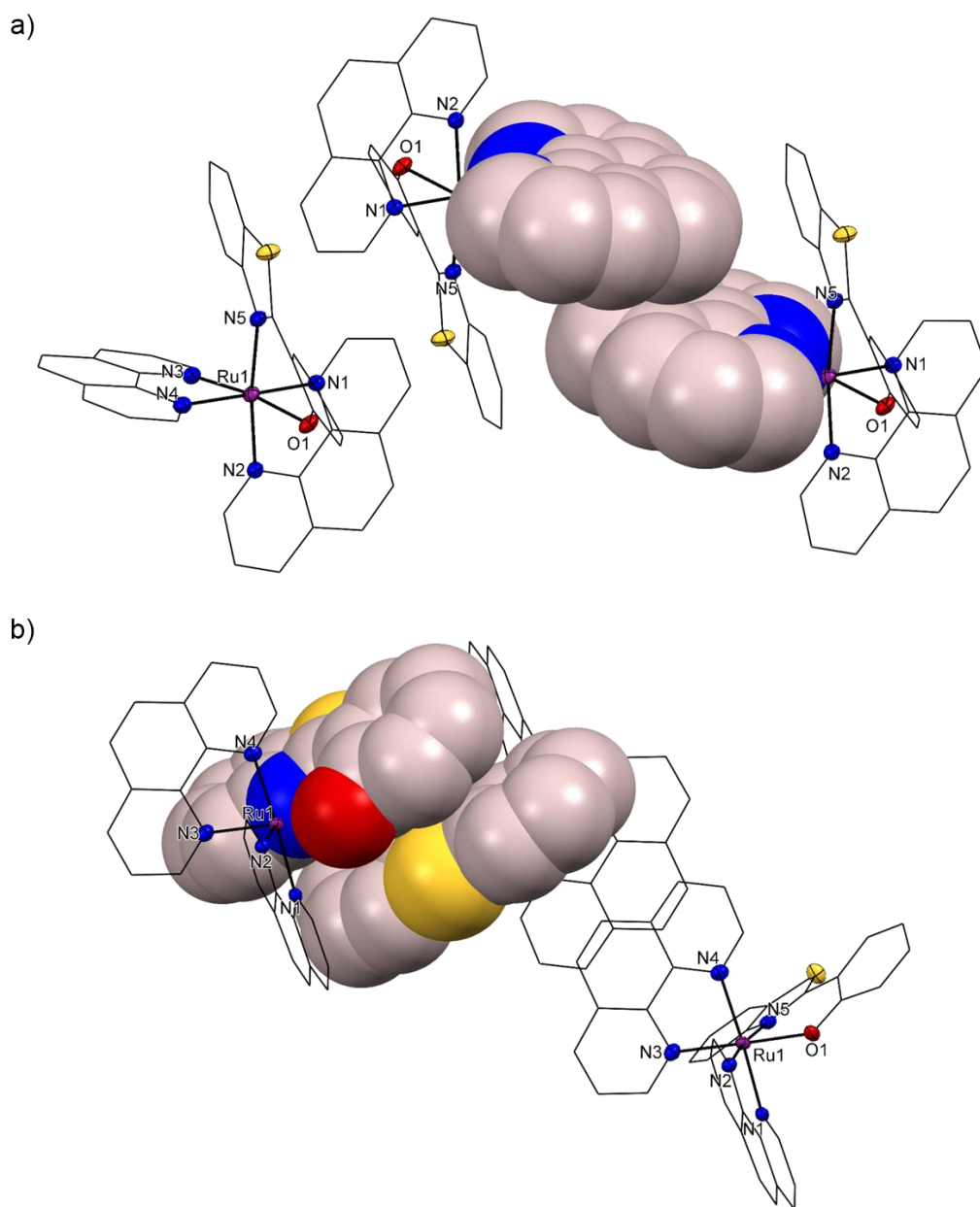
**Figure 2. 12** Space filling models highlighting intermolecular  $\pi$ - $\pi$  stacking interactions between phenanthrene moieties of dphol ligands in the crystal packing of compound **1**.



**Figure 2. 13** Space filling models highlighting intermolecular  $\pi$ - $\pi$  stacking interactions between bpy ligands in the crystal packing of compound **1**.

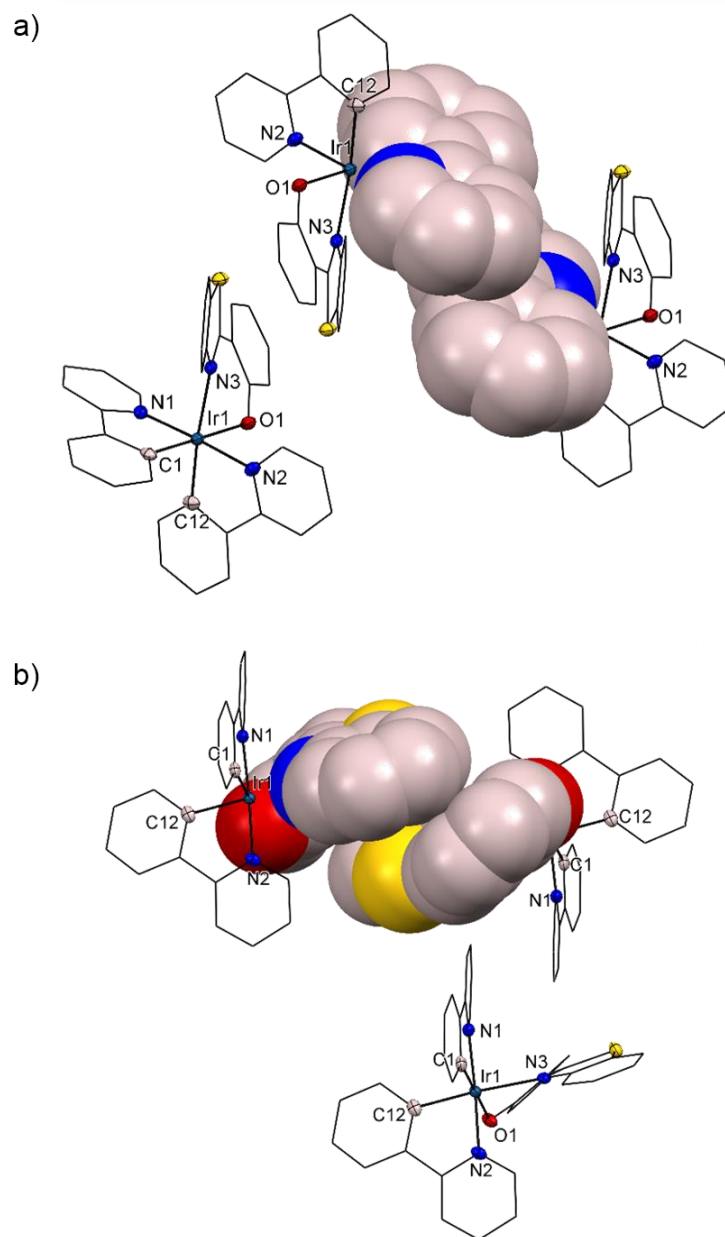


**Figure 2. 14** Intermolecular  $\pi$ - $\pi$  stacking interactions in the crystal packing of compound **3**. Space filling models highlighting the interactions between (a) bpy ligands and (b) hbtz ligands.



**Figure 2. 15** Intermolecular  $\pi$ - $\pi$  stacking interactions in the crystal packing of compound **4**. Space filling models highlighting the interactions between (a) phen ligands and (b) hbtz ligands.





**Figure 2. 16** Intermolecular  $\pi$ - $\pi$  stacking interactions in the crystal packing of compound 6. Space filling models highlighting the interactions between (a) phpy ligands and (b) hbtz ligands.

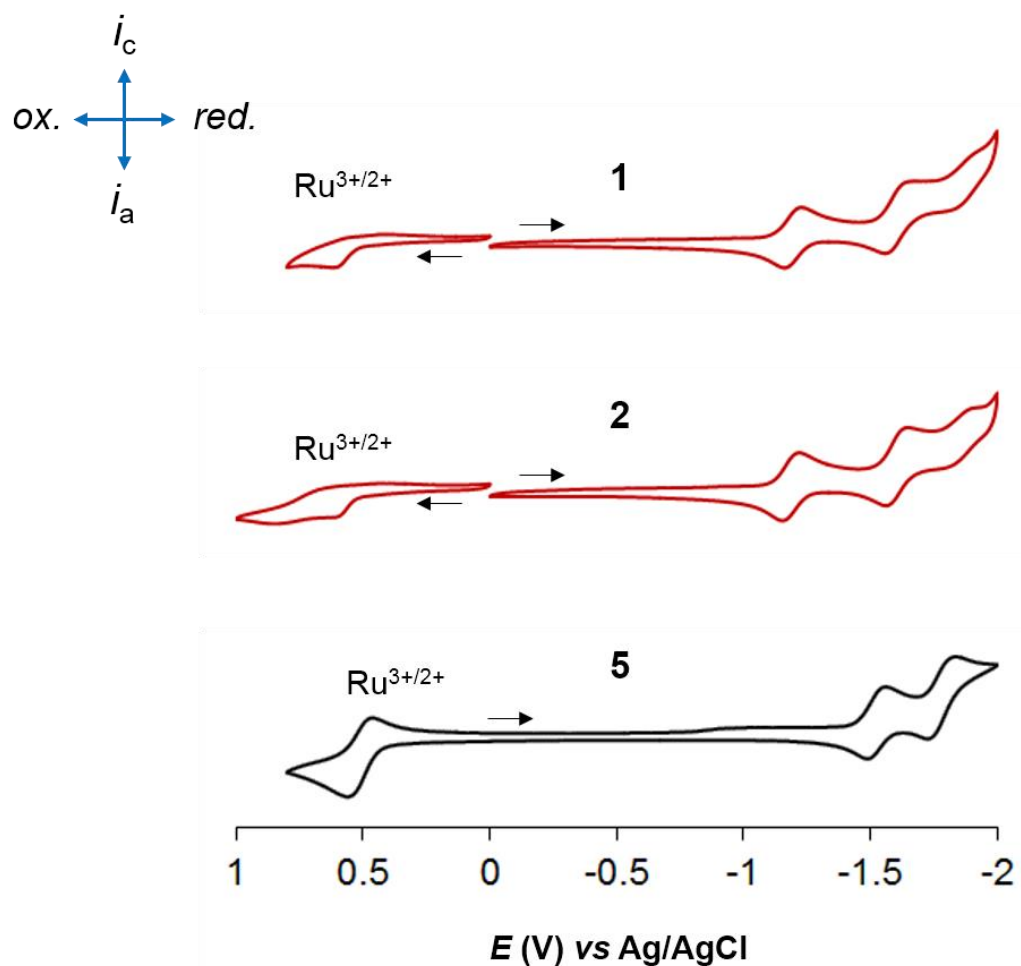
## Electrochemical Properties

The redox properties of complexes **1–6** were studied by cyclic voltammetry in acetonitrile. The half-wave potential values ( $E_{1/2}$ ) vs Ag/AgCl were obtained from the cyclic voltammograms of **1–6** and are provided in Figures 2.17–2.19. The  $E_{1/2}$  values have been referenced vs NHE for the discussion of the results (NHE = normal hydrogen electrode) as described in the Experimental Section and the values are presented in Table 2.8. The redox events observed in the cyclic voltammogram of **1–6** are quasi-reversible ( $i_{pa}/i_{pc} \approx 1$ ), except for the metal-based oxidation process of **1**, **2** and **6**, which are irreversible.

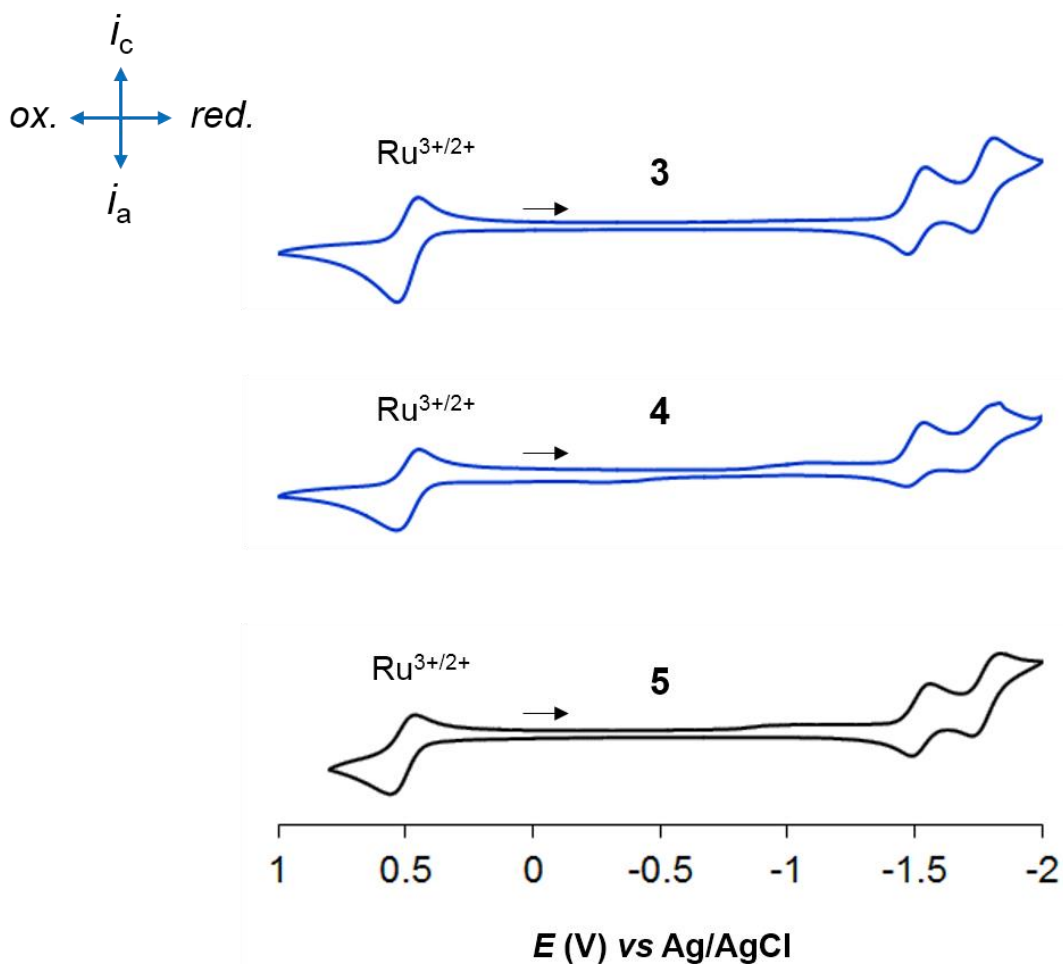
**Table 2. 8** Half wave redox potentials ( $E_{1/2}$ ) of **1–6** recorded in acetonitrile.

Compound	$E_{1/2}$ (V) vs NHE ( $\Delta E = E_{pa} - E_{pc}$ in mV)			
	$E_{1/2} [M^{(n+1)+/n+}]^a$	$E_{1/2,red1}$	$E_{1/2,red2}$	$E_{1/2,red3}$
[Ru(bpy) <sub>2</sub> (dphol)][PF <sub>6</sub> ] ( <b>1</b> )	0.86 <sup>b</sup>	-0.94 (66)	-1.35 (66)	-1.61 (88)
[Ru(phen) <sub>2</sub> (dphol)][PF <sub>6</sub> ] ( <b>2</b> )	0.85 <sup>b</sup>	-0.93 (64)	-1.36 (85)	-1.59 (80)
[Ru(bpy) <sub>2</sub> (hbtz)][PF <sub>6</sub> ] ( <b>3</b> )	0.74 (80)	-1.25 (60)	-1.52 (78)	-
[Ru(phen) <sub>2</sub> (hbtz)][PF <sub>6</sub> ] ( <b>4</b> )	0.74 (90)	-1.26 (65)	-1.54 (86)	-
[Ru(bpy) <sub>2</sub> (quo)][PF <sub>6</sub> ] ( <b>5</b> )	0.76 (95)	-1.28 (68)	-1.53 (94)	-
Ir(phpy) <sub>2</sub> (hbtz) ( <b>6</b> )	1.71 <sup>b</sup>	-	-	-

<sup>a</sup>Ru<sup>3+/2+</sup> couple for **1–5**; Ir<sup>4+/3+</sup> couple for **6**. <sup>b</sup>Irreversible; the anodic peak potential ( $E_{p,a}$ ) is reported.

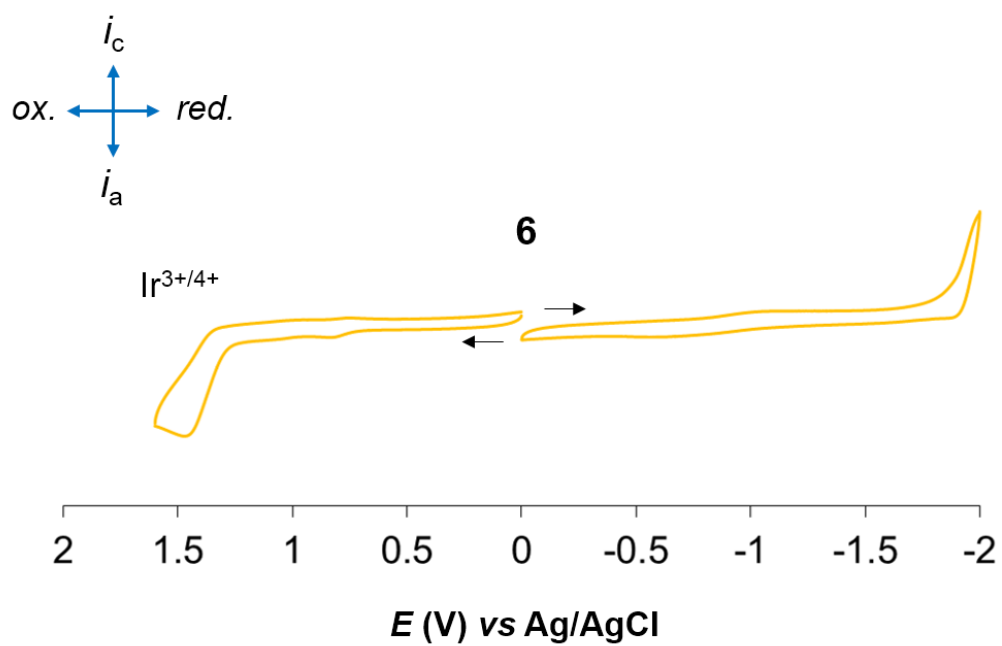


**Figure 2. 17** Cyclic voltammograms (vs Ag/AgCl) of compounds **1**, **2** and **5** in acetonitrile (0.1 M [ $n\text{Bu}_4\text{N}$ ][ $\text{PF}_6$ ], 100 mV/s scan rate).  $i_c$  = cathodic current,  $i_a$  = anodic current, ox. = oxidation, red. = reduction. The black arrows indicate the direction of the scan.

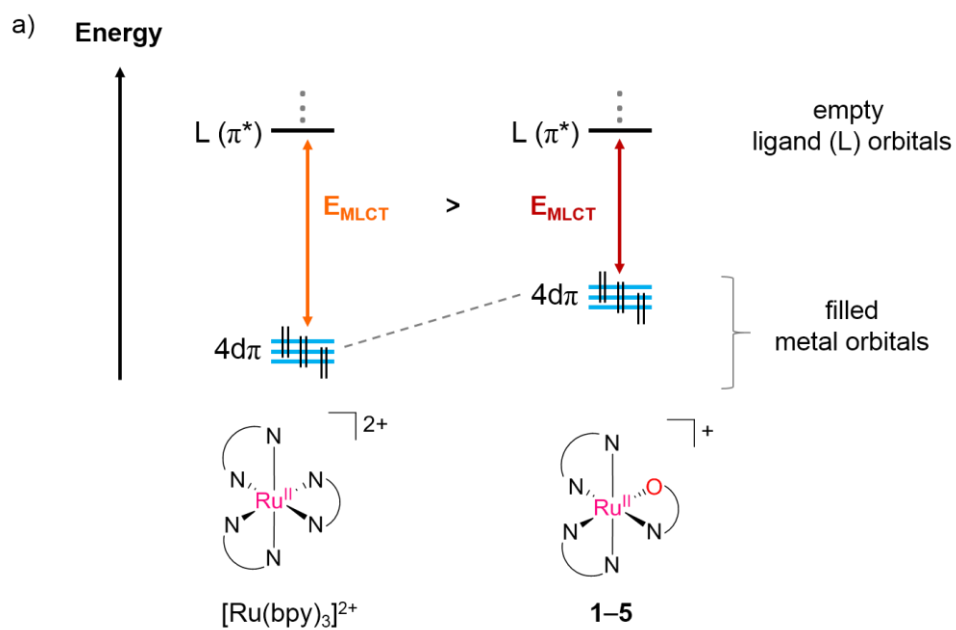


**Figure 2. 18** Cyclic voltammograms (vs Ag/AgCl) of compounds **3–5** in acetonitrile (0.1 M [ $n$ Bu<sub>4</sub>N][PF<sub>6</sub>], 100 mV/s scan rate).  $i_c$  = cathodic current,  $i_a$  = anodic current, ox. = oxidation, red. = reduction. The black arrows indicate the direction of the scan.

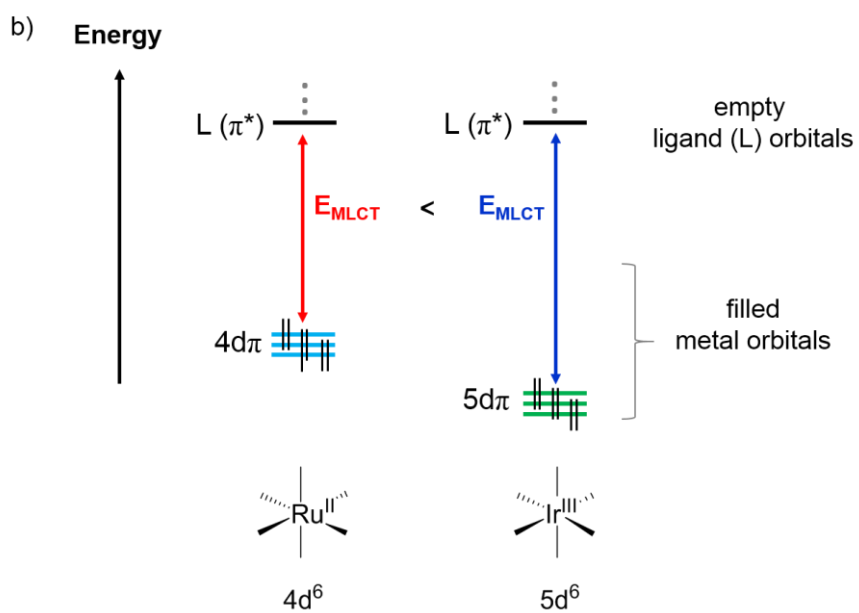
The Ru<sup>3+/2+</sup> redox couples of **1–5** ( $E_{1/2} [\text{Ru}^{3+/2+}] = 0.86$  to  $0.74$  V range) occur at less positive potentials with respect to  $[\text{Ru}(\text{bpy})_3]^{2+}$  ( $E_{1/2} [\text{Ru}]^{3+/2+} = 1.54$  V<sup>159</sup>). The anionic character and  $\pi$ -donating ability of the O-atom donor of the N<sup>-</sup>O<sup>-</sup> ligands destabilizes the Ru( $d\pi$ ) “ $t_{2g}$ -type” orbitals (Figure 2.20) and facilitates metal oxidation. This destabilization effect was verified by DFT calculations reported for the known compound **5**,<sup>160</sup> where the HOMO has contributions from both the Ru( $d\pi$ ) and O( $p\pi$ ) orbitals and the HOMO-1 and HOMO-2 are mainly metal-based. In contrast, the Ir<sup>4+/3+</sup> redox couple of **6** occurs at a more positive potential ( $E_{1/2} [\text{Ru}^{4+/3+}] = 1.71$  V). The stronger ligand field splitting for third-row (5d) transition metal ions with respect to second-row (4d) transition metal ions, as well as the more positive charge of the metal center in **6** (Ir<sup>3+</sup> vs Ru<sup>2+</sup>), results in a greater stabilization of the occupied “ $t_{2g}$ -type” Ir( $5d\pi$ ) orbitals as schematically shown in Figure 2.21,<sup>154,155</sup> explaining why **6** is more difficult to oxidize than **1–5** and  $[\text{Ru}(\text{bpy})_3]^{2+}$ .



**Figure 2. 19** Cyclic voltammogram (vs Ag/AgCl) of compound **6** in acetonitrile (0.1 M  $[\text{Bu}_4\text{N}][\text{PF}_6]$ , 100 mV/s scan rate).  $i_c$  = cathodic current,  $i_a$  = anodic current, ox. = oxidation, red. = reduction. The black arrows indicate the direction of the scan.



**Figure 2. 20** Schematic representation of the destabilization of the occupied Ru( $4d\pi$ ) orbitals in **1-5** with respect to  $[Ru(bpy)_3]^{2+}$ .  $E_{MLCT}$  = energy of the MCLT transition.



**Figure 2. 21** Schematic representation of the relative energies of Ru( $4d\pi$ ) and Ir( $5d\pi$ ) orbitals.  $E_{MLCT}$  = energy of the metal-to-ligand charge transfer transition.



The redox events observed for **5** are in agreement with previous reports.<sup>160,161,162</sup> The metal-based redox couple at  $E_{1/2} = 0.76$  V corresponds to the  $\text{Ru}^{3+/2+}$  oxidation couple, whereas those at  $E_{1/2} = -1.28$  and  $-1.53$  V correspond to consecutive  $1e^-$  reductions of the bpy ligands. Reduction of quo is not observed in the  $1.8$  to  $-1.8$  V range of potentials. The  $\text{Ru}^{3+/2+}$  redox events for **1** and **2** are irreversible and are shifted anodically by  $\sim 100$  mV with respect to **5** (Figure 2.17), that is, compounds **1** and **2** are more difficult to oxidize than **5**.

The first reduction waves of **1** and **2** ( $E_{1/2,\text{red1}} \sim -0.94$  V) occur at less negative potentials than that of **5** ( $E_{1/2,\text{red1}} = -1.28$  V, bpy-based reduction) and are assigned as reduction of the dphol ligand:  $\text{dphol} + e^- \rightarrow \text{dphol}^-$ . The dphol ligand is easier to reduce than bpy (or quo) due to its more delocalized  $\pi$ -system and it is likely that the electron is delocalized in the phenanthrene moiety of dphol. The other two ligand-based reduction waves at  $\sim -1.35$  and  $\sim -1.60$  V are assigned as consecutive  $1e^-$  reductions of bpy in the case of **1**, and phen in the case of **2**.

Compounds **3** and **4** display metal-based and ligand-based redox processes at very similar  $E_{1/2}$  values to those of **5** (Figure 2.18). Therefore, it can be concluded that the  $E_{1/2} [\text{Ru}^{3+/2+}]$  of **3** and **4** occurs at  $E_{1/2} = 0.74$  V and that the ligand-based redox events at  $E_{1/2} -1.25$  and  $-1.52$  V for **3**, and  $E_{1/2} -1.26$  and  $-1.54$  V for **4**, correspond to consecutive  $1e^-$  reductions of bpy and phen ligands, respectively. The reduction of the hbtz ligand is likely to occur at more negative potentials and is not observed in the potential window of the cyclic voltammogram experiments. Compound **6** does not exhibit any reversible event in the  $0$  to  $-1.8$  V range of potentials (Figure 2.19).

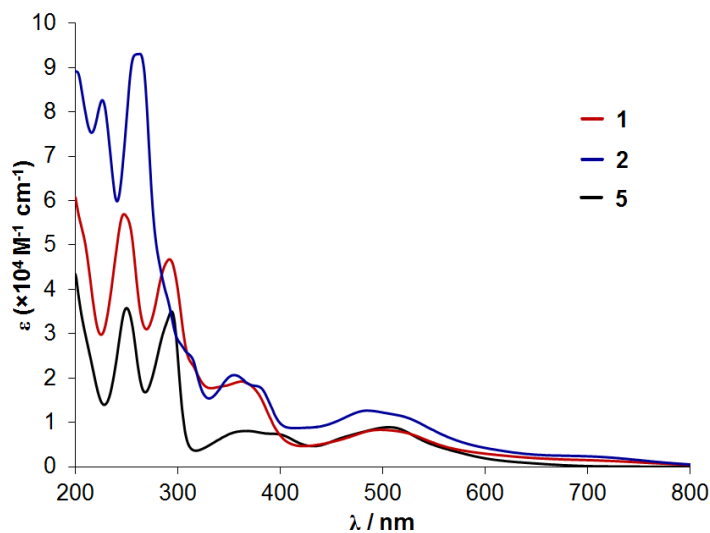
## *Optical Properties*

The absorption maxima ( $\lambda_{\text{abs}}$ ) and molar extinction coefficients ( $\epsilon$ ) for **1–6** in acetonitrile are listed in Table 2.9 and their electronic absorption spectra in acetonitrile are shown in Figures 2.22–2.24. The Ru compounds with phen as an ancillary ligand (**2** and **4**) exhibits slightly higher molar absorptivity coefficients in the visible region than those with bpy ligands (**1**, **3** and **5**). The absorption maxima at ~500 nm for **1**, **3** and **5** are assigned as singlet metal-to-ligand charge transfer ( $^1\text{MLCT}$ ) transitions ( $\text{Ru}(d\pi) \rightarrow \text{bpy}(\pi^*)$ ). Similarly, broad  $^1\text{MLCT}$  bands centered in the 480–500 nm interval are observed for **2** and **4**, which arise from  $\text{Ru}(d\pi) \rightarrow \text{phen}(\pi^*)$  transitions. Such  $^1\text{MLCT}$  bands for **1–5** are red-shifted with respect to the prototype Ru(II) complex  $[\text{Ru}(\text{bpy})_3]^{2+}$  ( $^1\text{MLCT}$  at 450 nm<sup>159</sup>) due to the destabilization of the Ru-HOMOs (occupied “ $t_{2g}$ -type” orbitals), which in turn decreases the HOMO-LUMO gap and the energy of the MLCT transition as illustrated in Figure 2.20. Compounds **1** and **2** exhibit additional absorption features in the 650–800 nm region that are assigned as  $\text{Ru}(d\pi) \rightarrow \text{dphol}(\pi^*)$   $^1\text{MLCT}$  transitions. These low energy transitions are in agreement with the less negative reduction potential of coordinated dphol with respect to quo or hbtz, indicating that the  $\pi^*$  MOs of dphol are lower in energy.

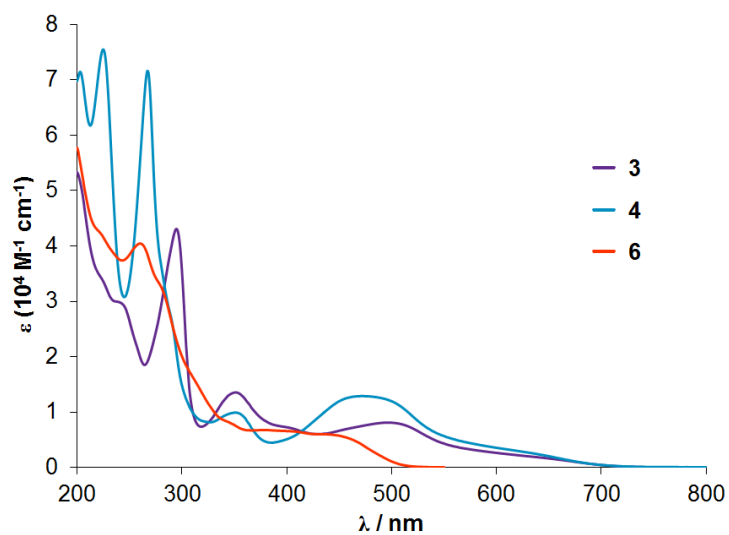
**Table 2. 9** Electronic absorption data for **1–6** recorded in acetonitrile.

Compound	$\lambda_{\text{max}}$ , nm ( $\epsilon \times 10^4 \text{ M}^{-1} \text{ cm}^{-1}$ )
[Ru(bpy) <sub>2</sub> (dphol)][PF <sub>6</sub> ] ( <b>1</b> )	710 (0.14), 500 (0.83), 363 (1.92), 292 (4.67), 246 (5.65)
[Ru(phen) <sub>2</sub> (dphol)][PF <sub>6</sub> ] ( <b>2</b> )	710 (0.23), 525 <sup>a</sup> (1.10), 485 (1.26), 380 (1.80), 355 (2.07), 263 (9.30), 226 (8.26)
[Ru(bpy) <sub>2</sub> (hbtz)][PF <sub>6</sub> ] ( <b>3</b> )	652 (0.16), 496 (0.81), 351 (1.35), 292 (4.29)
[Ru(phen) <sub>2</sub> (hbtz)][PF <sub>6</sub> ] ( <b>4</b> )	650 (0.20), 480 (1.28), 351 (1.00), 267 (7.14), 225 (7.53)
[Ru(bpy) <sub>2</sub> (quo)][PF <sub>6</sub> ] ( <b>5</b> )	506 (0.89), 460 (0.65), 394 (0.74), 368 (0.80), 295 (3.47), 252 (3.52)
Ir(phpy) <sub>2</sub> (hbtz) ( <b>6</b> )	450 (0.57), 404 (0.65), 382 (0.67), 345 (0.81), 260 (4.05)

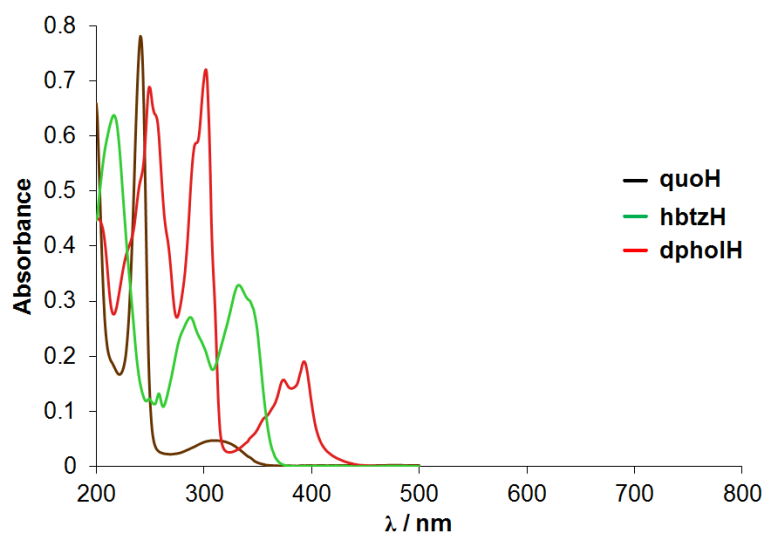
<sup>a</sup>Shoulder.



**Figure 2. 22** Electronic absorption spectra of **1**, **2** and **5** in acetonitrile.



**Figure 2. 23** Electronic absorption spectra of **3–5** in acetonitrile.

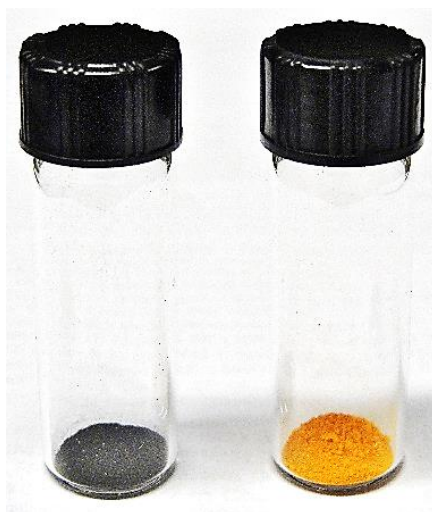


**Figure 2. 24** Electronic absorption spectra of free ligands in acetonitrile. The concentrations of the compounds were adjusted to have comparable intensities.

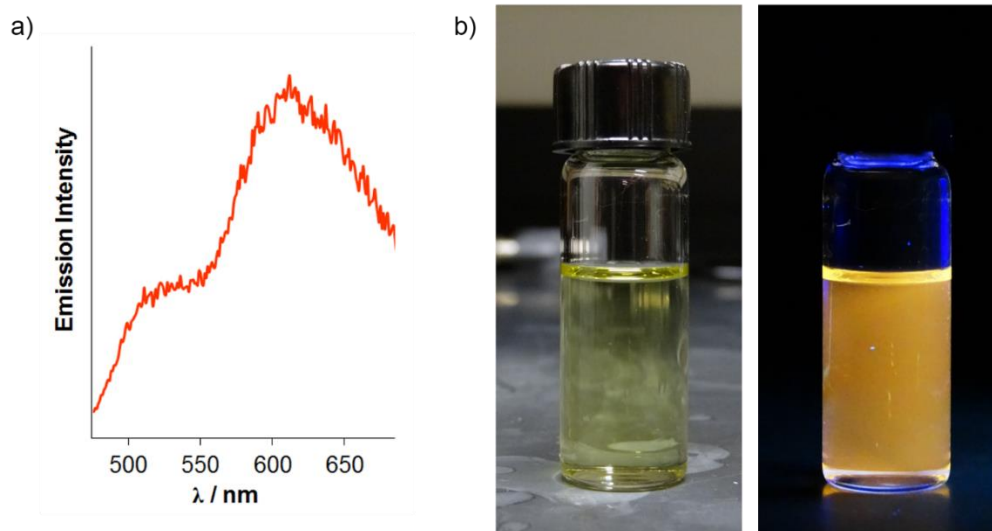
The transitions in the 300–400 nm range arise from  $^1\pi\pi^*$  ligand-centered (LC) transitions of the  $N^{\wedge}O^-$  ligands, since the free ligands dpholH (374 and 393 nm), hbtzH (332 nm) and quoH (312 nm) display absorption maxima in this region (Figure 2.24). The maxima at higher energies ( $\lambda < 300$  nm) correspond to overlapping  $L(\pi) \rightarrow L(\pi^*)$  and  $bpy(\pi) \rightarrow bpy(\pi^*)$  LC transitions in the case of **1** ( $L = \text{dphol}$ ), **3** ( $L = \text{hbtz}$ ) and **5** ( $L = \text{quo}$ ), and overlapping  $L(\pi) \rightarrow L(\pi^*)$  and  $\text{phen}(\pi) \rightarrow \text{phen}(\pi^*)$  LC transitions for **2** ( $L = \text{dphol}$ ) and **4** ( $L = \text{hbtz}$ ).

The Ir compound **6** exhibits absorption maxima in the 340–500 nm range, which has been assigned on the basis of DFT calculations as overlapping  $^{1,3}\text{MLCT}$  ( $\text{Ir}(4d\pi) \rightarrow \text{phpy}(\pi^*)$ ) and  $^{1,3}\text{LLCT}$  (ligand-to-ligand charge transfer,  $\text{hbtz}(\pi) \rightarrow \text{phpy}(\pi^*)$ ) transitions.<sup>152</sup> The strong spin-orbit coupling induced by 5d transition metal ions mixes singlet and triplet states and allows direct excitation into the spin-forbidden triplet excited states.<sup>154,155</sup> The MLCT transitions of **6** occur at higher energies than those of **1–5** because of the greater stabilization of the Ir-5d $\pi$  orbitals with respect to Ru-4d $\pi$  metal orbitals, as described in the previous section. The greater energy of the MLCT transition of **6** with respect to **1–5** also explains the striking difference in colors for these compounds (**1–5**, dark red-purple; **6**, yellow), as shown in Figure 2.25. The intense peaks observed at  $\lambda < 300$  nm are due to spin-allowed  $^1\pi\pi^*$  LC transitions of phpy ( $\text{phpy}(\pi) \rightarrow \text{phpy}(\pi^*)$ ) and hbtz ( $\text{hbtz}(\pi) \rightarrow \text{hbtz}(\pi^*)$ ) ligands. Compound **6** displays orange phosphorescence at room temperature (Figure 2.26) when excited at 350 nm. Two emission maxima at 515 nm and 607 nm ( $\text{CH}_2\text{Cl}_2$  solution) were observed in aerated solutions, in agreement with previous reports.<sup>152</sup> These two emission peaks have

been previously assigned to arise from  $^3\text{MLCT}$  ( $\text{Ir}(4d\pi)\rightarrow\text{phpy}(\pi^*)$ ) and  $^3\text{LLCT}$  ( $\text{hbtz}(\pi)\rightarrow\text{phpy}(\pi^*)$ ), respectively, on the basis of DFT calculations.<sup>152</sup>



**Figure 2. 25** Photograph showing the solid state colors of compounds **4** and **6**.

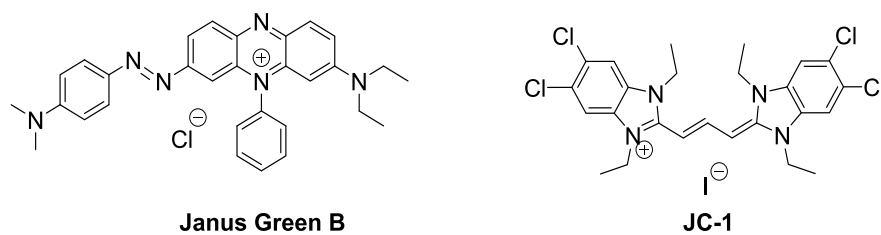


**Figure 2. 26** (a) Emission spectrum of an aerated solution of compound **6** in  $\text{CH}_2\text{Cl}_2$  ( $\lambda_{\text{ex}} = 350 \text{ nm}$ ). (b) Photographs showing phosphorescence from a solution of **6** ( $\sim 10^{-5} \text{ M}$ ) in  $\text{CH}_2\text{Cl}_2$  ( $\lambda_{\text{ex}} = 254 \text{ nm}$  from a hand-held UV lamp).

### *Cytotoxic Properties*

The cellular studies discussed in this part and the following section were performed in collaboration with Professor Rola Barhoumi (Veterinary Integrative Biomedical Sciences, Texas A&M University). To evaluate the cytotoxicity of compounds **1–6** against human lung adenocarcinoma (A549) cells, cell viability was determined using the Janus Green B dye (3-(Diethylamino)-7-((*p*-(dimethylamino)phenyl)azo)-5-phenylphenazinium chloride, Figure 2.27a). In this assay, A549 cells are incubated with increasing concentrations of **1–6** (0–50  $\mu\text{M}$ ) for 48 h. Subsequently, the cells are washed and fixed to the microplate well. Following fixation, living cells are stained with Janus Green B. After removing the excess dye from solution, the amount of dye trapped inside living cells is solubilized with methanol. The absorbance of Janus Green B ( $\lambda_{\text{abs}} = 630 \text{ nm}$ ) is measured using a microplate absorbance reader, whose value is directly proportional to the number of living cells.





**Figure 2. 27** Molecular structures of (a) Janus Green B and (b) JC-1.

**Table 2. 10** Cytotoxicity data for Ru and Ir complexes against A549 cells.

Compound	IC <sub>50</sub> , μM (95% CI <sup>a</sup> )
[Ru(bpy) <sub>2</sub> (dphol)][PF <sub>6</sub> ] ( <b>1</b> )	6.6 (3.2 to 13.9)
[Ru(phen) <sub>2</sub> (dphol)][PF <sub>6</sub> ] ( <b>2</b> )	1.3 (0.8 to 2.1)
[Ru(bpy) <sub>2</sub> (hbtz)][PF <sub>6</sub> ] ( <b>3</b> )	1.1 (0.7 to 1.9)
[Ru(phen) <sub>2</sub> (hbtz)][PF <sub>6</sub> ] ( <b>4</b> )	0.8 (0.5 to 1.2)
[Ru(bpy) <sub>2</sub> (quo)][PF <sub>6</sub> ] ( <b>5</b> )	> 50
Ir(phpy) <sub>2</sub> (hbtz) ( <b>6</b> )	4.7 (2.7 to 8.2)
cisplatin	6.2 (2.9 to 13.5)

<sup>a</sup>Incubation time = 48 h. Values in parenthesis represent the 95% confidence interval.

The IC<sub>50</sub> values (concentration of compound required to inhibit 50% of cell survival) were calculated under reduced light conditions and are listed in Table 2.10. Compounds **1–6** exhibit IC<sub>50</sub> values in the low micromolar range. Cisplatin was used as a positive control (IC<sub>50</sub> = 6.2 μM). Compound **1** exhibits comparable activity than cisplatin, whereas compounds **2–4** are more active than the platinum drug. Compound **4** is the most cytotoxic Ru compound (IC<sub>50</sub> = 0.8 μM) and is 8-fold more cytotoxic than cisplatin. In contrast, compound **5** is not active in the range of concentrations that were tested (0–50 μM). It is likely that the higher cytotoxicity of **1–4** with respect to **5** is due to the increased lipophilicities of **1–4** since they have extended aromatic systems on the ligands dphol (**1** and **2**) and hbtz (**3** and **4**), supporting our initial hypothesis. The higher hydrophobicity of dphol and hbtz with respect to quo may increase the cellular uptake of **1–4**, as also shown in the work of Meggers<sup>135</sup> and in several studies on the anticancer properties of Ru<sup>120,121,124,126,128</sup> complexes. The Ir compound **6** exhibits cytotoxic activity similar to that of cisplatin and will encourage the synthesis and exploration of the anticancer properties of analogs of this Ir compound in the future.

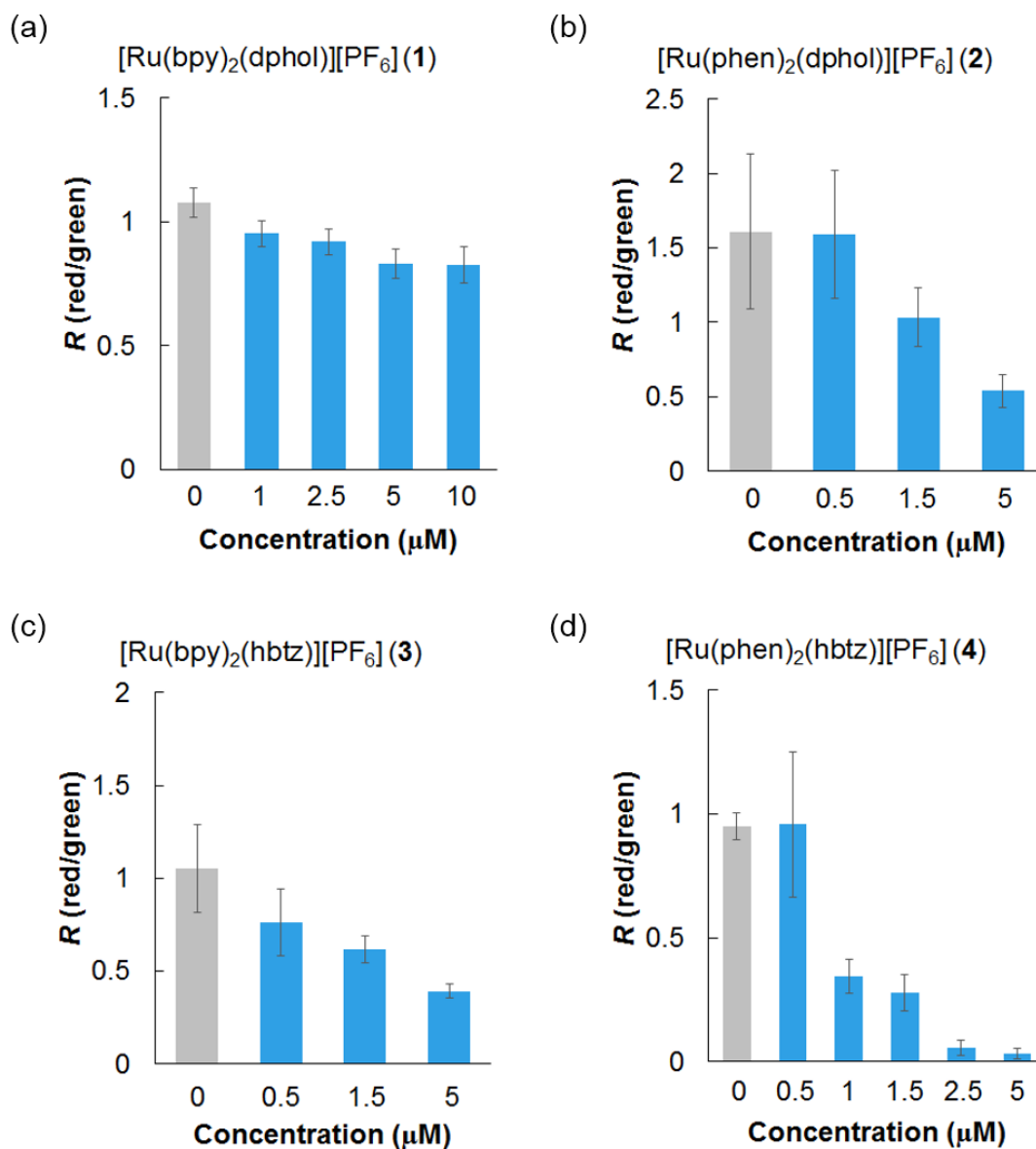
## *Investigation of the Mechanism of Cancer Cell Death*

Disruption and permanent dissipation of the inner mitochondrial transmembrane potential ( $\Delta\Psi_m$ ) is an event that is associated with the intrinsic pathway of apoptosis, as described in Chapter I. To determine the effect of **1–4** on mitochondria, mitochondrial dysfunction was assessed by measuring the changes in  $\Delta\Psi_m$  using JC-1 (5',6,6'-tetrachloro-1,1',3,3'-tetraethylbenzimidazolyl carbocyanine iodide, Figure 2.27b).<sup>127,128</sup> JC-1 is a lipophilic cationic dye that accumulates in mitochondria due to the negative potential of the inner membrane on these organelles ( $-120$  to  $-160$  mV<sup>61,117</sup>), and its fluorescence wavelength is potential-dependent: regions within the cell with high mitochondrial polarization (high  $\Delta\Psi_m$ ) are indicated by red fluorescence (590 nm) due to the formation of dye aggregates (so called J-aggregates). In contrast, green fluorescence (527 nm) of dye monomers is observed when mitochondria is depolarized (low  $\Delta\Psi_m$ ).<sup>61,163</sup> Therefore, mitochondrial depolarization is indicated by a decrease in the red/green emission intensity ratio ( $R$ ) of JC-1.<sup>163</sup>

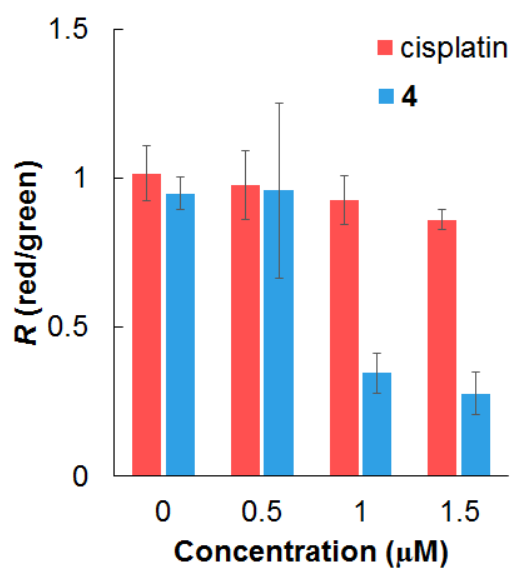
A549 cells were incubated with **1–4** at different concentrations for 48 h. After this period of time the cells were incubated with JC-1 and  $R$  was calculated. The results are shown in Figure 2.28. In general, an increase of the concentration of the compounds is accompanied by a progressive decrease of  $R$ , indicating that **1–4** induce mitochondria depolarization in a dose-dependent fashion and suggesting that cell death occurs via the intrinsic pathway of apoptosis. To compare the changes of  $R$  among **1–4**, the change of  $R$  ( $\Delta R$ ) with respect to a control (no complex added) was calculated at 5  $\mu\text{M}$  concentration

of Ru complex ( $\Delta R = [(R_{5\mu\text{M}} - R_{\text{control}})/R_{\text{control}}] \times 100\%$ ). The observed trend is as follow: **4** ( $-97\%$ ) > **2** ( $-66\%$ )  $\approx$  **3** ( $-63\%$ ) > **1** ( $-23\%$ ), where the values in parenthesis represent  $\Delta R$ . Interestingly,  $\Delta R$  was directly proportional to the cytotoxicity, where the most cytotoxic compound, **4**, decreases  $R$  to the greatest extent. Moreover, **4** induces a greater  $\Delta\Psi_{\text{m}}$  depolarization as compared to cisplatin (Figure 2.29), with  $\Delta R = -70\%$  and  $-15\%$  for **4** and cisplatin at  $1.5 \mu\text{M}$  concentration, respectively.

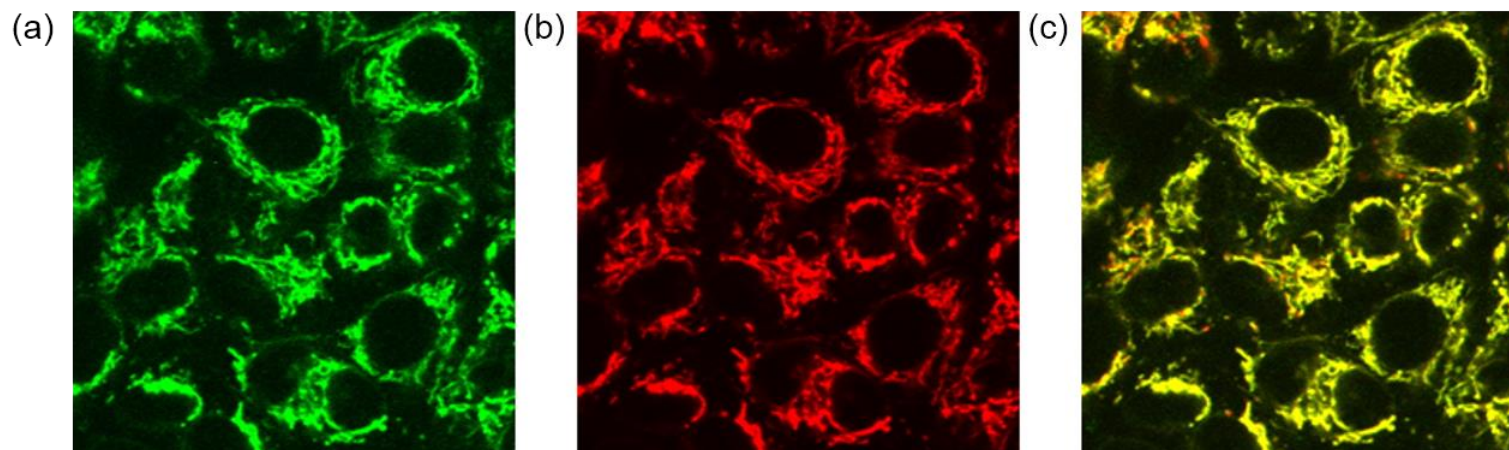
A typical mitochondrion possesses a fibrous structure as can be seen in Figure 2.30, where A549 cells were incubated only with JC-1. Green (Figure 2.30a) and red (Figure 2.30b) fluorescence images are shown to highlight the dual emission of JC-1 in mitochondria. Dramatic morphological changes of mitochondria occur when A549 cells are incubated with **4** for 48 h at concentrations as low as  $500 \text{ nM}$ , as shown in Figure 2.31: complex **4** induces swelling and fragmentation of mitochondria, producing small and rounded organelles.<sup>61,142</sup> Such morphological changes strongly indicate cell death by the intrinsic pathway. A progressive decrease of the red fluorescence intensity from J-aggregates can be also seen when the concentration of **4** increases from 0 to  $1 \mu\text{M}$  (Figure 2.31a-c), indicating loss of  $\Delta\Psi_{\text{m}}$  as described previously.



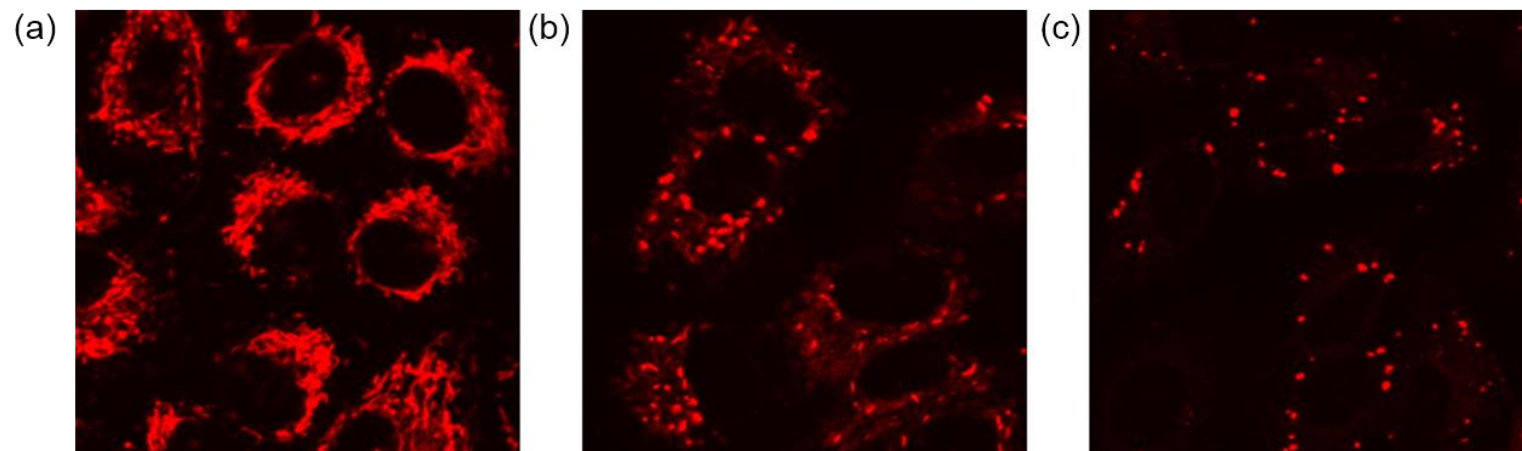
**Figure 2. 28** *R* values from JC-1 when A549 cells are exposed after 48 h of incubation to different concentrations of compounds (a) **1**, (b) **2**, (c) **3** and (d) **4**. The graphs represent means with standard deviation. Control experiments (no metal complex) are depicted in gray color.



**Figure 2. 29** *R* values from JC-1 when A549 cells are exposed after 48 h of incubation to different concentrations of cisplatin and compound **4**. The graphs represent means with standard deviation.



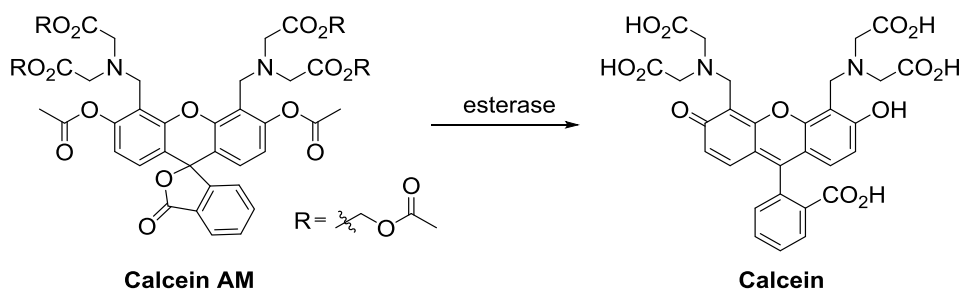
**Figure 2. 30** Confocal fluorescence images of JC-1 in A549 cells in the absence of compound **4**. (a) Green and (b) red fluorescence from JC-1. (c) Overlay of (a,b) images. Field of view =  $75 \times 75 \mu\text{m}$ . Images were collected after 48 h of incubation.



**Figure 2. 31** Confocal red fluorescence images of JC-1 in A549 cells incubated with (a) 0  $\mu\text{M}$  **4**, (b) 500 nM **4** and (c) 1  $\mu\text{M}$  **4**. Field of view =  $75 \times 75 \mu\text{m}$ . Images were collected after 48 h of incubation.



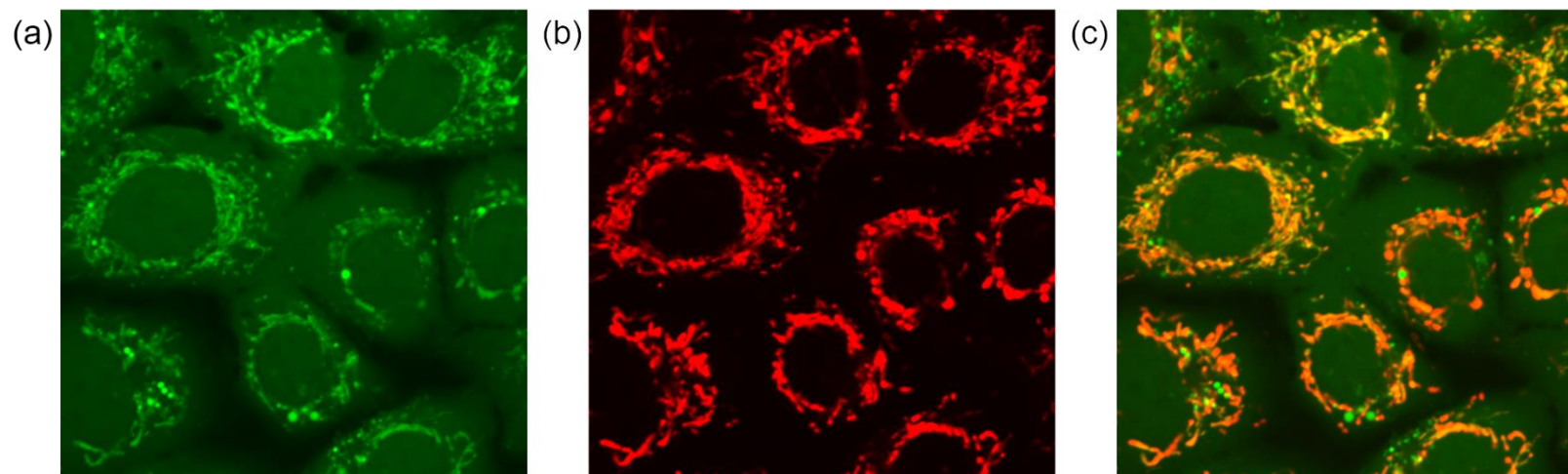
Induction of outer mitochondrial membrane permeabilization (MMP) is a crucial event during cell death via the intrinsic pathway of apoptosis and is often considered as the “point of no return”.<sup>61</sup> Such an event is accompanied by a dissipation of  $\Delta\Psi_m$  and permeabilization of the inner mitochondrial membrane (IMM). To support that the intrinsic pathway of apoptosis is triggered by these series of compounds, a biological assay that uses the calcein AM dye (Figure 2.32) was carried out for compound 4.



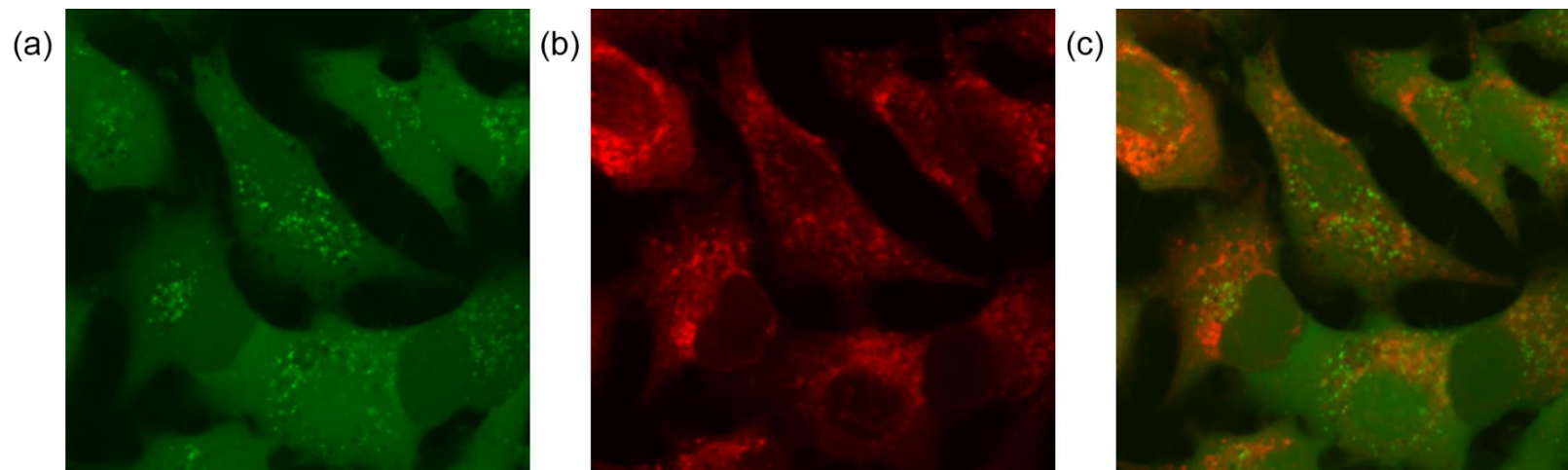
**Figure 2. 32** Molecular structure of calcein AM.

In this experiment A549 cells are loaded with calcein AM and  $\text{CoCl}_2$ . Calcein AM undergoes removal of the ester groups by intracellular esterases and is trapped in cytosolic compartments including mitochondria.<sup>61</sup> The  $\text{Co}^{2+}$  ions quench the fluorescence of calcein in all subcellular compartments except in mitochondria since the

IMM is impermeable to  $\text{Co}^{2+}$  ions and water. When the IMM barriers are functional, a distinct bright green fluorescence signal from calcein identifies mitochondria,<sup>61</sup> as can be observed in Figure 2.33a. Dim green fluorescence from calcein is observed elsewhere because  $\text{Co}^{2+}$  quenches calcein fluorescence. The signal from calcein overlays very well with the red fluorescence from Mitotracker, a mitochondria-specific fluorescent dye, confirming the localization of calcein in mitochondria (Figure 2.33a-c). In contrast, incubation of A549 cells with 1  $\mu\text{M}$  **4** for 48 h leads to calcein fluorescence quenching inside mitochondria and dim green fluorescence is observed throughout the cells (Figure 2.34). These results indicate long-lasting opening of the mitochondrial permeability transition pore (MPTP) complex, which allows  $\text{Co}^{2+}$  ions to enter the mitochondrial matrix and quench calcein fluorescence, supporting the intrinsic pathway of apoptosis as the mechanism of cancer cell death.

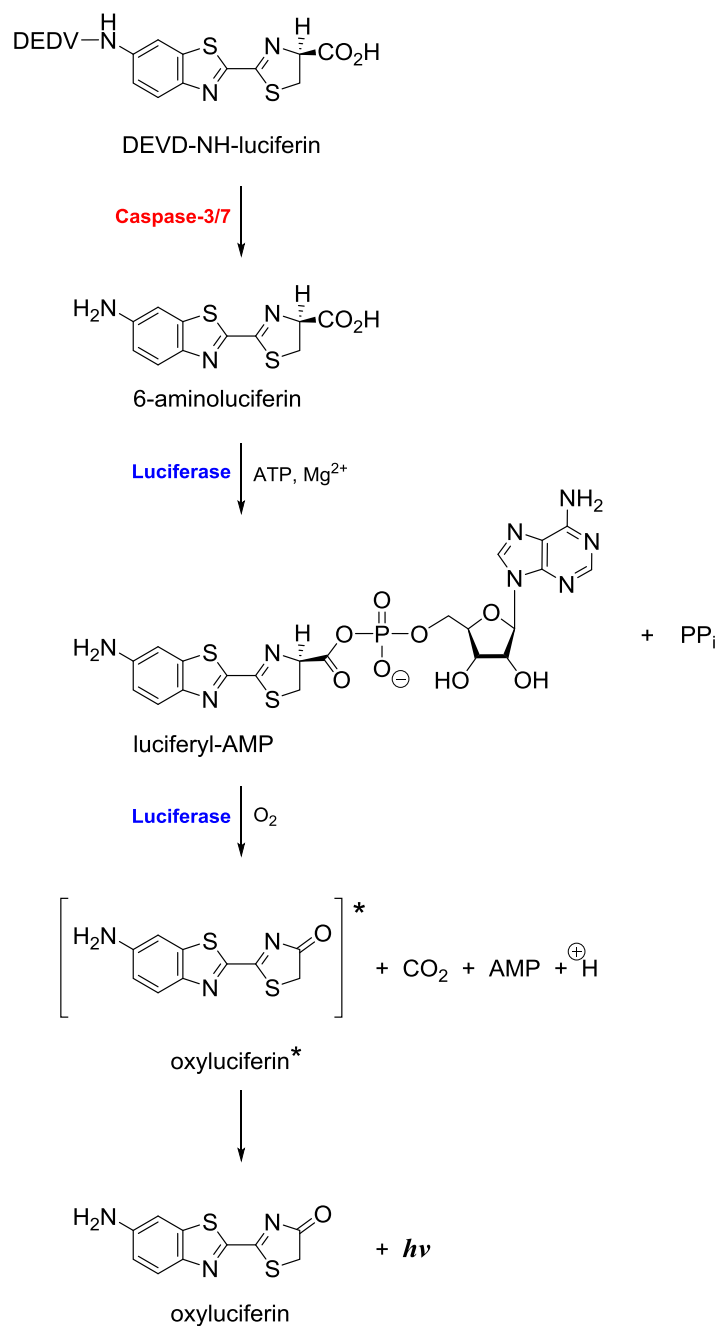


**Figure 2. 33** Confocal fluorescence images of A549 cells coincubated with Calcein AM and Mitotracker. in the absence of compound **4**. (a) Green fluorescence from Calcein (+CoCl<sub>2</sub>), (b) red fluorescence from Mitotracker and (c) overlay of (a,b) images. Field of view = 75 × 75 μm. Images were collected after 48 h of incubation.



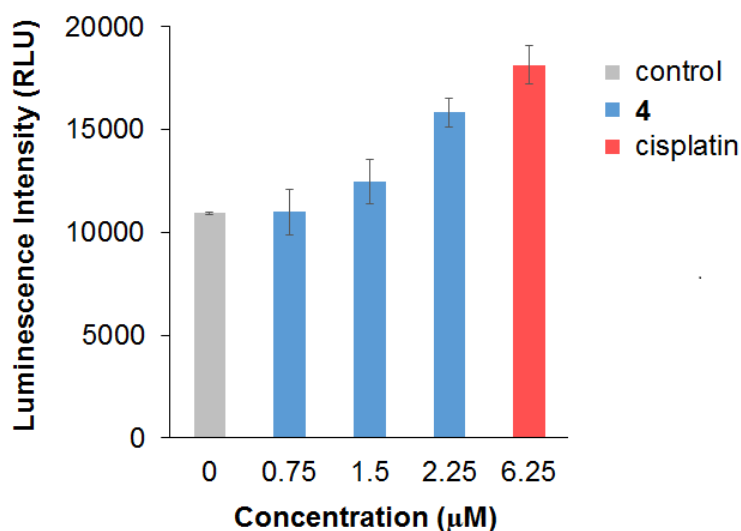
**Figure 2. 34** Confocal fluorescence images of A549 cells coincubated with compound **4** (1  $\mu$ M), Calcein AM and Mitotracker. (a) Green fluorescence from Calcein AM (+CoCl<sub>2</sub>), (b) red fluorescence from Mitotracker and (c) overlay of (a,b) images. Field of view = 75  $\times$  75  $\mu$ m. Images were collected after 48 h of incubation.

Caspases are cysteine proteases which are involved in both the initiation and execution phases of apoptosis and, indeed, the activation of these proteolytic enzymes is often used as a hallmark of apoptosis.<sup>68,126</sup> In particular, caspase-3/7, known as the executioner caspases, are activated after cytochrome c leaks out of mitochondria when a cell dies via the intrinsic pathway of apoptosis.<sup>61</sup> The effect of a chemotherapy drug on the activity of caspase-3/7 can be examined using the Caspase-Glo assay kit, which includes (i) the caspase-3/7 substrate DEVD-NH-luciferin and (ii) the Luciferase enzyme. Cancer cells are incubated with the Caspase-Glo reagents after treatment with the drug. Caspase-3/7 that are activated during apoptosis cleave the amino acid sequence DEVD (Asp-Glu-Val-Asp) releasing 6-amino-luciferin (Figure 2.35). The latter undergoes oxidative decarboxylation catalyzed by the Luciferase enzyme producing oxyluciferin in an electronically excited state (oxyluciferin\*), which emits light ( $h\nu$ ) when it is deactivated and returns to the ground state (oxyluciferin\*  $\rightarrow$  oxyluciferin +  $h\nu$ ). The luminescence intensity is proportional to the amount of caspase-3/7 activity.



**Figure 2. 35** Reaction pathway that leads to oxyluciferin fluorescence during the measurement of caspase-3/7 activity. ATP = adenosine triphosphate. AMP = Adenosine monophosphate. PP<sub>i</sub> = pyrophosphate.

A549 cells were treated with compound **4** at three different concentration (0.75, 1.5 and 2.25  $\mu\text{M}$ ) for 48 h and caspase -3/7 activity was determined after this period of time. Compound **4** induced caspase-3/7 activity in a concentration-dependent fashion as depicted in Figure 2.36, in which an increase in the oxyluciferin luminescence intensity is observed upon increasing the concentration of **4**, confirming that this Ru compound induces cell suicide via the intrinsic pathway. Figure 2.36 also shows that a lower concentration of **4** is needed to induce caspase-3/7 activity with respect to cisplatin, in which 2.25  $\mu\text{M}$  **4** reaches comparable activity to 6.25  $\mu\text{M}$  cisplatin, showing the higher apoptosis inducing ability of **4**.



**Figure 2. 36** Caspase-3/7 activity measurements when A549 cells are exposed to compound **4** and cisplatin (48 h of incubation). The graphs represent means with standard deviation.

## Conclusions

The lack of studies in the literature of the cytotoxic properties of Ru(II) polypyridyl complexes in a  $[\text{Ru}^{\text{II}}\text{N}_5\text{O}]^+$  coordination environment prompted us to explore the biological activities of a new series of Ru polypyridyl compounds with the  $\text{N}^+\text{O}^-$  bidentate ligands dphol and hbtz. Four new Ru complexes (**1–4**) were successfully synthesized and characterized by  $^1\text{H}$  NMR spectroscopy, mass spectrometry, elemental analysis and X-ray crystallography. The  $^1\text{MLCT}$  transitions for these complexes are bathochromically shifted with respect to that of  $[\text{Ru}(\text{bpy})_3]^{2+}$  due to the  $\pi$ -donating ability of the  $\text{O}^-$ -donor of  $\text{N}^+\text{O}^-$ , which destabilizes the  $\text{Ru}(4d\pi)$  HOMOs and decreases the energy of the  $\text{Ru}(4d\pi) \rightarrow \text{L}(\pi^*)$  transition. This effect is also reflected in the less positive oxidation potential for this series of compounds with respect to the prototype complex  $[\text{Ru}(\text{bpy})_3]^{2+}$ .

The four compounds are cytotoxic against human lung adenocarcinoma (A549) cells with  $\text{IC}_{50}$  values in the low micromolar range. Compound **4**, the most active of the series, is  $\sim 8$  times more cytotoxic than cisplatin. The dissipation of  $\Delta\Psi_{\text{m}}$  was evaluated using the JC-1 probe and it was found that the four Ru complexes induce loss of  $\Delta\Psi_{\text{m}}$  in a concentration-dependent fashion. In addition, the cytotoxicity of **1–4** is directly proportional to the loss of  $\Delta\Psi_{\text{m}}$ . The dissipation of  $\Delta\Psi_{\text{m}}$  suggests that **1–4** are inducing apoptosis via the intrinsic pathway in A549 cells. Moreover, compound **4** promotes the long-lasting opening of the MPTP complex and induces the activity of caspase-3/7, confirming that A549 cells die by the intrinsic pathway when incubated with this type of



Ru complex. Therefore, increasing the lipophilicity of the  $\text{N}^{\text{O}^-}$  ligand is a successful strategy to access a new family of pro-apoptotic Ru complexes with a  $[\text{Ru}^{\text{II}}\text{N}_5\text{O}]^+$  coordination environment. This work complements the strategy followed by Meggers<sup>135</sup> to increase cellular uptake and anticancer activity and we believe these results will encourage the exploration of the anticancer activities of octahedral Ru polypyridyl complexes in coordination environments different than  $[\text{Ru}^{\text{II}}\text{N}_6]^{2+}$ .

Finally, although the cellular targets and the mechanism by which the Ir(III) compound **6** promotes cancer cell death have not been studied, the fact that its cytotoxicity is comparable to that of cisplatin makes this class of Ir compounds interesting candidates for further development.

CHAPTER III  
RUTHENIUM CYCLOMETALLATED DYES AS A NEW CLASS OF  
ORGANOMETALLIC ANTICANCER DRUGS\*

**Introduction**

*Bioorganometallic chemistry* is an emerging and vibrant research field that focuses on the study of naturally occurring or synthetic organometallic compounds (those possessing metal-carbon bonds) with biological or medicinal applications.<sup>84,164</sup> The name of this research area was first coined by Gérard Jaouen in 1985 when he described the use of chromium, cobalt and manganese carbonyl compounds to label hormonal steroids.<sup>165</sup>

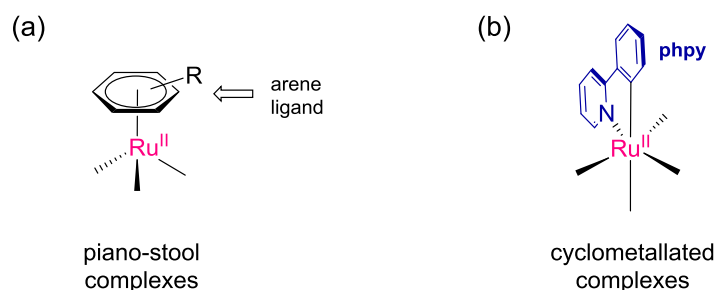
---

\*Reprinted with permission from Peña, B.; David, A.; Pavani, C.; Baptista, M. S.; Pellois, J.-P.; Turro, C.; Dunbar, K. R. "Cytotoxicity Studies of Cyclometallated Ruthenium(II) Compounds: New Applications for Ruthenium Dyes". *Organometallics* **2014**, 33 (5), 1100-1103. Copyright 2014 American Chemical Society.

Reprinted with permission from Peña, B.; Leed, N. A.; Dunbar, K. R.; Turro, C. "Excited State Dynamics of Two New Ru(II) Cyclometallated Dyes: Relation to Cells for Solar Energy Conversion and Comparison to Conventional Systems". *J. Phys. Chem. C* **2012**, 116 (42), 22186-22195. Copyright 2012 American Chemical Society.

Reproduced from Albani, B. A.; Peña, B.; Dunbar, K. R.; Turro, C. "New cyclometallated Ru(II) complex for potential application in photochemotherapy?". *Photochem. Photobiol. Sci.* **2014**, 13 (2), 272-280, with permission from the European Society for Photobiology, the European Photochemistry Association, and The Royal Society of Chemistry.

The first synthetic organometallic compound with demonstrated therapeutic effects that was marketed can be traced back to 1909, when the systematic studies by Paul Ehrlich in Europe on organoarsenic compounds led to the discovery of Salvarsan (3-amino-4-hydroxyphenylarsenic(I), Arsphenamine or Ehrlich 606)<sup>166</sup> which was used to treat syphilis. Ehrlich was awarded the Nobel Prize in Physiology or Medicine in 1908 for his contribution to this area.<sup>164</sup> The subsequent establishment of a theoretical framework for understanding the structure and bonding of organometallic compounds in the second part of the twentieth century, the ability to control the behavior of organometallic complexes in water, and the seminal discovery of the antitumor properties of cisplatin by Barnett Rosenberg in the 1960's,<sup>17,18</sup> led to the emergence and success of this field in our century.<sup>83,84,86,164,167</sup>



**Figure 3. 1** Schematic representations of the molecular structures of (a) ( $\eta^6$ -arene)Ru and (b) Ru(phpy) scaffolds.

Over the past 10 years, the growth of bioorganometallic chemistry has led to the discovery of new families of ruthenium (Ru) compounds with carcinostatic activities, with complexes with the ( $\eta^6$ -arene)Ru(II) scaffold (also known as piano-stool or half-sandwich compounds, Figure 3.1a) being some of the most well studied as described in Chapter I.<sup>82,83,84,86,90,164</sup> In 2005, the anticancer properties of structurally different organometallic Ru(II) compounds were reported by the group of Pfeffer and coworkers, in which the metal center is six-coordinate and contains the orthometallated 2-phenylpyridine ligand (phpy, Figure 3.1b). From a synthetic point of view, this class of Ru organometallic compounds is more appealing than piano-stool complexes since greater structural complexity (and the possibility to modulate the cytotoxic properties) can be introduced by installation of mono-, bi- tri- and tetradentate ligands. In addition, the phpy ligand can be modified more easily than the  $\eta^6$ -arene ring in the piano-stool complexes which allows for the introduction of a variety of functional groups.

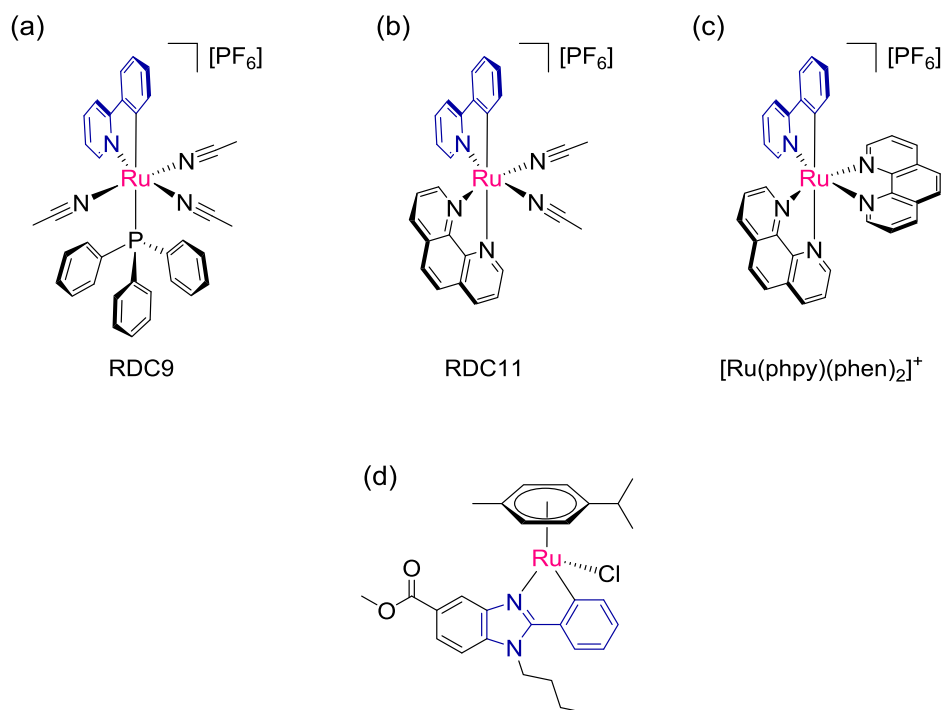
The Pfeffer group evaluated the antiproliferative activities of seven Ru cyclometallated compounds (also called cycloruthenated or ruthenium-derived compounds (RDC) in the literature) and found that [Ru(phpy)(NCCH<sub>3</sub>)<sub>3</sub>(PMe<sub>2</sub>Ph)][PF<sub>6</sub>] (RDC9; Figure 3.2a) and [Ru(phpy)(phen)(NCCH<sub>3</sub>)<sub>2</sub>][PF<sub>6</sub>] (RDC11; phen = 1,10-phenanthroline, Figure 3.2b) exhibit comparable or slightly greater activity than that of cisplatin against a variety of cancer cell lines derived from glioblastoma (A172 and HS683), neuroblastoma (N2A and SH5Y) and adenocarcinoma (HCT116), among others.<sup>168,169</sup> RDC9 and RDC11 induce G<sub>1</sub> cell cycle arrest, DNA condensation and fragmentation, externalization of phosphatidylserine and promote the activity of caspase

3 which are proteolytic enzymes associated with programmed cell death. In addition, the two compounds promote the activity of the tumor suppressor proteins p53 and p73 (that induce cell growth arrest), indicating that apoptosis is the mechanism of cancer cell death.<sup>168</sup> Moreover, RDC9 induces apoptosis in a cell line (TK6) for which the p53 gene has been deleted and maintained its cytotoxicity in a cell line (2008 ATP7B) that overexpressed ATP7B (a membrane transporter that is able to expel cisplatin out of the cell which is associated with cisplatin resistance<sup>170,171</sup>), highlighting the promising anticancer properties of this class of organometallic compounds.

In 2009, the same group reported that RDC11 was more efficient than cisplatin at inhibiting the growth of various tumors implanted in mice and did not cause side effects such as liver or kidney toxicity<sup>172</sup> (commonly associated with cisplatin treatment), results that motivated the study of its mechanism of action. It was determined that RDC11 stimulates the expression of the p53 protein and genes of the endoplasmic reticulum (ER) stress pathway, along with CHOP (CCAAT-enhancer-binding protein homologous protein, a transcription factor that is a critical mediator of ER stress apoptosis), suggesting that its anticancer activity involves the p53 and the ER stress pathways.<sup>172</sup> Two years later, the cytotoxic activity of nearly 15 derivatives of RDC11 of the type  $[\text{Ru}(\text{phpyX})(\text{phen})_2]^+$  were studied, where X represents different electron-withdrawing and electron-donating groups (-NR<sub>2</sub>, -Br, -NO<sub>2</sub>, -CONR). From this series of compounds,  $[\text{Ru}(\text{phpy})(\text{phen})_2][\text{X}]$  (phen = 1,10-phenanthroline, X = PF<sub>6</sub><sup>-</sup> or CF<sub>3</sub>CO<sub>2</sub><sup>-</sup>, Figure 3.2c) was found to be one of the most active, displaying a 5-fold higher cytotoxicity than RDC11 against human colon HCT-116 cancer cells.<sup>173</sup> More

recently, organometallic Ru(II) compounds incorporating both  $\eta^6$ -arene and orthometallated ligands (Figure 3.2d) have been reported to have cytotoxicities higher than those of cisplatin against epithelial ovarian carcinoma (A2780 and A2780cisR (acquired resistance to cisplatin)), breast (T47D) and colon (HT29) cancer cells and to induce apoptosis.<sup>174</sup>

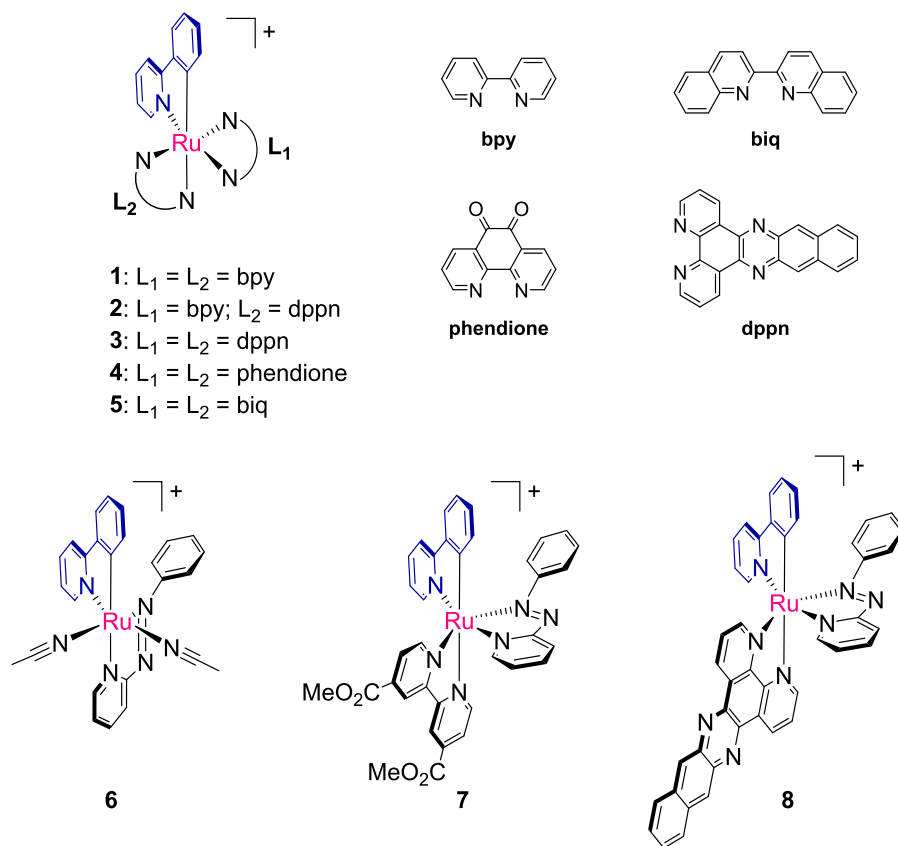
RDC11 and  $[\text{Ru}(\text{phpy})(\text{phen})_2]^+$  have been shown to be more active than their dicationic counterparts,  $[\text{Ru}(\text{phen})_2(\text{NCCH}_3)_2]^{2+}$  and  $[\text{Ru}(\text{phen})_3]^{2+}$ , respectively. It is interesting to note that change of the ligand donor atoms (from N to C<sup>-</sup>) increases the anticancer activity of these metal compounds. The higher cytotoxicity of the cyclometallated complexes has been attributed to their lower positive charge, which increases their lipophilicity and uptake by cancer cells with respect to those of the 2+ charged Ru(II) complexes,<sup>173</sup> as also observed in anticancer active Ir(III) complexes (see Chapter II). In addition, it has been shown that cyclometallation of Ru compounds tunes the  $\text{Ru}^{3+/2+}$  redox potential and allows them to efficiently interfere with oxido-reductase enzymes, which is said to be associated with their biological activities. For example, the cytotoxic compound  $[\text{Ru}(\text{phpy})(\text{phen})_2]^+$  oxidizes efficiently the reduced form of glucose oxidase in the absence of oxygen.<sup>175</sup>



**Figure 3. 2** Molecular structures of (a) RDC9, (b) RDC11, (c) [Ru(phpy)(phen)<sub>2</sub>][PF<sub>6</sub>], and (d) an example of a Ru(II) anticancer compound incorporating both arene and phpy-type ligands.

In light of the very promising biological activities of Ru cyclometallated compounds in cancer drug research, we decided to expand this family of compounds by coordinating a variety of bidentate ligands to the “Ru(phpy)” fragment. The known compound [Ru(phpy)(bpy)<sub>2</sub>][PF<sub>6</sub>] (**1**; bpy = 2,2'-bipyridine) and the four new complexes (Figure 3.3) [Ru(phpy)(bpy)(dppn)][PF<sub>6</sub>] (**2**; bpy = 2,2'-bipyridine, dppn = benzo[i]dipyrido[3,2-*a*:2',3'-*c*]phenazine), [Ru(phpy)(dppn)<sub>2</sub>][PF<sub>6</sub>] (**3**), [Ru(phpy)(phendione)<sub>2</sub>][PF<sub>6</sub>] (**4**; phendione = 1,10-phenanthroline-5,6-dione) and [Ru(phpy)(biq)<sub>2</sub>][PF<sub>6</sub>] (**5**; biq = 2,2'-biquinoline) were synthesized and fully characterized. In addition, the synthesis and acetonitrile ligand substitution studies of the new compound [Ru(phpy)(pap)(NCCH<sub>3</sub>)<sub>2</sub>][PF<sub>6</sub>] (**6**; pap = 2-(phenylazo)pyridine) were undertaken to evaluate its suitability as a new precursor for Ru cyclometallated compounds. Two new tris-heteroleptic compounds [Ru(phpy)(pap)(dcmb)][PF<sub>6</sub>] (**7**; dcmb = 4,4'-dicarboxymethyl-2,2'-bipyridine) and [Ru(phpy)(pap)(dppn)][PF<sub>6</sub>] (**8**) were prepared from **6**. Compounds **2–8** resemble the Ru cyclometallated dyes used in dye-sensitized solar cells in structure, optical and electrochemical properties. We expect that our findings of the cytotoxicity against cancer cells of some of these molecules will encourage the study of the cytotoxic properties of reported Ru dyes since many of them could display antitumor properties of similar or better magnitude than those discovered in this work, making Ru cyclometallated dyes a new and promising class of metal-based anticancer drugs.





**Figure 3. 3** Molecular structures of Ru(II) cyclometallated complexes in this study.

## Experimental Section

### *General Methods*

Standard Schlenk-line techniques (under a N<sub>2</sub> atmosphere) were used to maintain anaerobic conditions during the preparation of the compounds. The solvents were of reagent grade quality. Ethanol (KORTEP, 200 proof) was dried over Mg/I<sub>2</sub>, acetonitrile was dried over 3Å molecular sieves; both were distilled under nitrogen prior to use. All solvents used for chromatography (EMD Chemicals, ACS grade) were used as received without further purification. Analytical thin layer chromatography was performed on aluminum-backed sheets coated with silica gel (SiO<sub>2</sub>) 60 F254 adsorbent (0.20 mm thickness, EMD Chemicals) or coated with aluminum oxide (Al<sub>2</sub>O<sub>3</sub>) neutral 60 F254 adsorbent (0.20 mm thickness, EMD Chemicals). Flash chromatography (FC) was carried out with with SiO<sub>2</sub> 60 (40-63 μm, BDH Chemicals) or Al<sub>2</sub>O<sub>3</sub> (activated, basic, Brockmann I, Sigma Aldrich). RuCl<sub>3</sub>•xH<sub>2</sub>O (Pressure Chemicals Co.), 1,3-cyclohexadiene (Sigma Aldrich), 2,2'-bipyridine (Alfa Aesar), 2,2'-biquinoline (TCI) were purchased and used without further purification. The compounds 1,10-phenanthroline-5,6-dione (phendione),<sup>176</sup> 2-(phenylazo)pyridine (pap),<sup>177</sup> dcmb (4,4'-dicarboxymethyl-2,2'-bipyridine),<sup>178</sup> benzo[*i*]dipyrido[3,2-*a*:2',3'-*c*]phenazine) (dppn)<sup>176</sup> and [Ru(phpy)(bpy)<sub>2</sub>][PF<sub>6</sub>] (**1**)<sup>179</sup> were prepared following reported procedures.

## *Instrumentation*

NMR spectra were recorded on Mercury 300 MHz or an Inova 500 MHz spectrometers. Chemical shifts are reported in  $\delta$  (ppm) and coupling constants ( $J$ ) in hertz (Hz). For  $^1\text{H}$  NMR spectra, the residual solvent peak was used as an internal reference ( $\delta$  1.94 for  $\text{CD}_3\text{CN}$ , 2.05 for  $(\text{CD}_3)_2\text{CO}_2$ ). Spectra were referenced externally to 85%  $\text{H}_3\text{PO}_4$  ( $\delta$  0.00) and  $\text{CF}_3\text{COOH}$  ( $\delta$   $-78.5$ ) for  $^{31}\text{P}$  and  $^{19}\text{F}$  NMR, respectively.  $^1\text{H}$ - $^1\text{H}$  COSY experiments were performed to do the assignment of proton resonances. Electrospray mass spectra were acquired on an Applied Biosystems PE SCIEX QSTAR mass spectrometer (MDS Sciex). Elemental analyses were performed by Atlantic Microlab, Inc. (Norcross, GA). Absorption spectra were recorded on a Shimadzu UVPC-3001 spectrophotometer. Electrochemical measurements were performed under  $\text{N}_2$  atmosphere with a HCH Electrochemical Analyzer model CH 1620A using a BAS Pt disk working electrode, Pt wire auxiliary electrode, Ag/AgCl (3M  $\text{KCl}_{(\text{aq})}$ ) reference electrode and 0.1 M tetra-*n*-butylammonium hexafluorophosphate ( $[\text{nBu}_4\text{N}][\text{PF}_6]$ ) in dry acetonitrile as supporting electrolyte and 0.1 V/s scan rate. The concentration of the Ru complexes was 0.3–0.5 mM for the electrochemical experiments. Ferrocene was used as an internal standard and exhibited a  $E_{1/2} = 0.44$  V vs Ag/AgCl for the  $\text{Fc}^+/\text{Fc}$  couple under the same experimental conditions. The  $E_{1/2}$  of the Ru complexes were referenced vs NHE using the following expression:  $E_{1/2}$  vs NHE =  $[(E_{1/2}$  vs Ag/AgCl of Ru complex) + (0.64 – 0.44)] V, where 0.64 V =  $E_{1/2}$  [ $\text{Fc}^+/\text{Fc}$ ] vs NHE and 0.44 V =  $E_{1/2}$  [ $\text{Fc}^+/\text{Fc}$ ] vs Ag/AgCl.

### *Synthetic Details*

**$[(\eta^6\text{-benzene})\text{RuCl}_2]_2$** . The Ru complex was prepared following reported procedures.<sup>180</sup> The reagent 1,3-cyclohexadiene (5 mL) was added to a dark brown-orange solution of  $\text{RuCl}_3 \cdot x\text{H}_2\text{O}$  (1.21 g, 4.63 mmol) in EtOH (50 mL) and the resulting solution was refluxed for 4 h. The resulting brown precipitate was collected by filtration, washed with EtOH (25 mL) and diethyl ether (25 mL). Yield: 1.00 g (87%).  $^1\text{H}$  NMR (300 MHz,  $\text{CD}_3\text{CN}$ ):  $\delta$  5.70 (s, 6H,  $\eta^6\text{-benzene}$ ).

**$[\text{Ru}(\text{phpy})(\text{NCCH}_3)_4][\text{PF}_6]$** . The Ru complex was prepared following reported procedures.<sup>181,182,183</sup> The compounds  $[(\eta^6\text{-benzene})\text{RuCl}_2]_2$  (760 mg, 1.52 mmol), NaOH (143 mg, 3.58 mmol) and  $\text{KPF}_6$  (1.123 g, 3.2 mmol) were suspended in  $\text{CH}_3\text{CN}$  (25 mL) and 2-phenyl pyridine (0.44 mL, 3.10 mmol) was added. The light brown mixture was heated at  $55^\circ\text{C}$  for 22 hours and the resulting dark lime yellow suspension was reduced to dryness; the residue was dissolved in the minimal amount of  $\text{CH}_2\text{Cl}_2/\text{CH}_3\text{CN}$  and was purified by FC (basic  $\text{Al}_2\text{O}_3$ ,  $\text{CH}_3\text{CN}/\text{CH}_2\text{Cl}_2$ , gradient from 5% to 35%  $\text{CH}_3\text{CN}$ ). The first yellow band was collected and reduced to *ca.* 5 mL. The lime yellow product was precipitated upon addition of diethyl ether/hexanes (1:1, 100 mL) and it was collected by filtration and washed with diethyl ether/hexanes (1:1, 100 mL). Yield: 1.06 g (62%).  $^1\text{H}$  NMR (500 MHz,  $\text{CD}_3\text{CN}$ ):  $\delta$  8.91 (d, 1H,  $^3J = 5.5$ ,  $^4J = 1.0$ , H-8), 7.97 (dd, 1H,  $^3J = 7.5$ ,  $^4J = 1.0$ , H-1), 7.87 (d, 1H, 1H,  $^3J = 8.5$ , H-5), 7.74 (ddd, 1H,  $^3J = 8.0$ ,  $^3J = 8.0$ ,  $^4J = 1.5$ , H-6), 7.71 (dd, 1H,  $^3J = 8.0$ ,  $^4J = 1.0$ , H-4), 7.15 (ddd, 1H,  $^3J = 7.5$ ,  $^3J = 5.5$ ,  $^4J = 1.5$ , H-

7), 7.08 (ddd, 1H,  $^3J = 8.5$ ,  $^3J = 8.5$ ,  $^4J = 1.5$ , H-2), 6.94 (ddd, 1H,  $^3J = 8.5$ ,  $^3J = 8.5$ ,  $^4J = 1.0$ , H-3), 2.51 (s, 3H, NCCH<sub>3</sub>), 2.14 (s, 3H, NCCH<sub>3</sub>), 2.00 (s, 6H, 2NCCH<sub>3</sub>).

**[Ru(phpy)(bpy)(dppn)] (2).** A brown suspension of **9** (155 mg, 0.24 mmol) and dppn (81 mg, 0.24 mmol) in ethanol (20 mL) was heated to reflux. The solution became dark red in color within 5 min. After 8 h the dark red solution was reduced to dryness and the solid residue was purified by FC (SiO<sub>2</sub>, CH<sub>3</sub>CN/toluene, gradient from 10% to 30% CH<sub>3</sub>CN). The second red band was collected and the volume was reduced to *ca.* 15 mL. The dark red solid that precipitated was collected by filtration and washed with diethyl ether (25 mL). Yield: 97 mg (45%). <sup>1</sup>H NMR (500 MHz, (CD<sub>3</sub>)<sub>2</sub>CO):  $\delta$  9.50 (dd, 1H,  $^3J = 8.0$ ,  $^4J = 1.5$ , H-c or H-c'), 9.31 (dd, 1H,  $^3J = 8.0$ ,  $^4J = 1.5$ , H-c' or H-c), 8.97 (s, 1H, H-d or H-d'), 8.96 (s, 1H, H-d' or H-d), 8.64 (d, 2H,  $^3J = 8.0$ , H-4', H-5'), 8.52 (dd, 1H,  $^3J = 5.5$ ,  $^4J = 1.5$ , H-a or H-a'), 8.50 (dd, 1H,  $^3J = 5.5$ ,  $^4J = 1.5$ , H-a' or H-a), 8.31 (m, 2H, H-f, H-f'), 8.21 (d, 1H,  $^3J = 8.0$ , H-5), 8.08 (d, 1H,  $^3J = 5.5$ , H-1'), 8.03-7.97 (m, 5H, H-b or H-b', H-4, H-3', H-6', H-8'), 7.90 (d, 1H,  $^3J = 5.5$ , H-8), 7.77 (m, 2H, H-b' or H-b, H-6), 7.71 (m, 2H, H-e, H-e'), 7.45 (ddd, 1H,  $^3J = 7.5$ ,  $^3J = 5.5$ ,  $^4J = 1.5$ , H-2'), 7.29 (ddd, 1H,  $^3J = 7.5$ ,  $^3J = 5.5$ ,  $^4J = 1.5$ , H-7'), 7.00 (m, 2H, H-3, H-7), 6.91 (ddd, 1H,  $^3J = 7.5$ ,  $^3J = 7.5$ ,  $^4J = 1.5$ , H-2), 6.61 (dd, 1H,  $^3J = 7.5$ ,  $^4J = 1.0$ , H-1). HRMS (ESI+): Calcd. for [C<sub>43</sub>H<sub>28</sub>N<sub>7</sub>Ru]<sup>+</sup> ([M - PF<sub>6</sub>]<sup>+</sup>), 744.1450. Found: 744.1457. Anal. Calcd. for C<sub>43</sub>H<sub>28</sub>F<sub>6</sub>N<sub>7</sub>PRu·0.25H<sub>2</sub>O: C, 57.82; H, 3.22; N, 10.98. Found: C, 57.88; H, 3.21; N, 10.89.

**[Ru(phpy)(dppn)<sub>2</sub>] (3).** A light brown suspension of [Ru(phpy)(NCCH<sub>3</sub>)<sub>4</sub>][PF<sub>6</sub>] (101 mg, 0.18 mmol) and dppn (119 mg, 0.36 mmol) in ethanol (20 mL) was heated to reflux. The mixture turned to a dark brown-red solution within 5 minutes and after 8 h the resulting dark red solution was reduced to dryness. The solid residue was purified by FC (SiO<sub>2</sub>, CH<sub>3</sub>CN/toluene, gradient from 10% to 25% CH<sub>3</sub>CN). The first red band was collected and the volume was reduced to *ca.* 20 mL. The dark red solid precipitate was collected by filtration and washed with diethyl ether (25 mL). Yield: 113 mg (60%). <sup>1</sup>H NMR (500 MHz, (CD<sub>3</sub>)<sub>2</sub>CO): δ 9.53 (dd, 1H, <sup>3</sup>J = 8.0, <sup>4</sup>J = 1.0, H-C), 9.45 (dd, 1H, <sup>3</sup>J = 8.0, <sup>4</sup>J = 1.0, H-C), 9.27 (dd, 1H, <sup>3</sup>J = 8.0, <sup>4</sup>J = 1.0, H-C), 9.17 (dd, 1H, <sup>3</sup>J = 8.0, <sup>4</sup>J = 1.0, H-C), 9.07 (s, 1H, H-D), 9.01 (s, 1H, H-D), 8.98 (s, 1H, H-D), 8.83 (s, 1H, H-D), 8.68 (dd, 1H, <sup>3</sup>J = 5.5, <sup>4</sup>J = 1.5, H-A), 8.62 (dd, 1H, <sup>3</sup>J = 5.5, <sup>4</sup>J = 1.5, H-A), 8.46 (dd, 1H, <sup>3</sup>J = 5.5, <sup>4</sup>J = 1.0, H-A), 8.41 (dd, 1H, <sup>3</sup>J = 5.5, <sup>4</sup>J = 1.0, H-A), 8.39-8.28 (m, 4H, H-F), 8.22 (d, 1H, <sup>3</sup>J = 8.5, H-5), 8.08 (d, 1H, <sup>3</sup>J = 8.0, H-4), 8.06 (d, 1H, <sup>3</sup>J = 5.0, H-8), 7.93-7.83 (m, 3H, 2 H-B, H-6), 7.76-7.66 (m, 6H, 2 H-B, 4 H-E), 7.05 (ddd, 1H, <sup>3</sup>J = 7.0, <sup>3</sup>J = 5.5, <sup>4</sup>J = 1.5, H-7), 7.00 (ddd, 1H, <sup>3</sup>J = 7.5, <sup>3</sup>J = 7.5, <sup>4</sup>J = 1.0, H-3), 6.92 (ddd, 1H, <sup>3</sup>J = 7.5, <sup>3</sup>J = 7.5, <sup>4</sup>J = 1.0, H-2), 6.83 (d, 1H, <sup>3</sup>J = 7.5, H-1). HRMS (ESI<sup>+</sup>): Calcd. for [C<sub>55</sub>H<sub>32</sub>N<sub>9</sub>Ru]<sup>+</sup> ([M - PF<sub>6</sub>]<sup>+</sup>), 920.1824. Found: 920.1820. Anal. Calcd. for C<sub>55</sub>H<sub>32</sub>F<sub>6</sub>N<sub>9</sub>PRu·H<sub>2</sub>O: C, 61.00; H, 3.16; N, 11.64. Found: C, 60.98; H, 2.79; N, 11.59.

**[Ru(phpy)(phendione)<sub>2</sub>][PF<sub>6</sub>] (4).** The ligand 1,10-phenanthroline-5,6-dione (112 mg, 0.53 mmol) was added to a yellow suspension of [Ru(phpy)(NCCH<sub>3</sub>)<sub>4</sub>][PF<sub>6</sub>] (150 mg, 0.26 mmol) in ethanol (15 mL) and the mixture was heated to reflux for 5 h. The

resulting dark red solution was reduced to dryness and the residue was purified by FC (SiO<sub>2</sub>, CH<sub>3</sub>CN/CH<sub>2</sub>Cl<sub>2</sub>, gradient from 10% to 35% CH<sub>3</sub>CN). The main red band was collected and reduced to *ca.* 10 mL. Diethyl ether (15 mL) was added slowly and the flask was left in the refrigerator overnight. The dark red (almost black) microcrystalline solid was collected by filtration and washed with diethyl ether (3 x 15 mL). Yield: 115 mg (53%). <sup>1</sup>H NMR (500 MHz, CD<sub>3</sub>CN): δ 8.50 (dd, 1H, <sup>3</sup>J = 8.0, <sup>4</sup>J = 1.0), 8.33 (m, 2H), 8.30 (dd, 1H, <sup>3</sup>J = 8.0, <sup>4</sup>J = 1.0), 8.26 (dd, 1H, <sup>3</sup>J = 5.5, <sup>4</sup>J = 1.0), 8.23 (dd, 1H, <sup>3</sup>J = 5.5, <sup>4</sup>J = 1.0), 8.09 (d, 1H, <sup>3</sup>J = 8.0), 8.07 (dd, 1H, <sup>3</sup>J = 5.5, <sup>4</sup>J = 1.5), 8.04 (dd, 1H, <sup>3</sup>J = 5.5, <sup>4</sup>J = 1.0), 7.91 (dd, 1H, <sup>3</sup>J = 8.0, <sup>4</sup>J = 1.0), 7.78 (ddd, 1H, <sup>3</sup>J = 8.0, <sup>3</sup>J = 7.5, <sup>4</sup>J = 1.5), 7.70 (d, 1H, <sup>3</sup>J = 5.5), 7.66 (dd, 1H, <sup>3</sup>J = 8.0, <sup>3</sup>J = 5.5), 7.49-7.42 (m, 3H), 7.03-6.95 (m, 2H), 6.91 (ddd, 1H, <sup>3</sup>J = 7.5, <sup>3</sup>J = 7.5, <sup>4</sup>J = 1.5), 6.60 (dd, 1H, <sup>3</sup>J = 7.5, <sup>4</sup>J = 1.0). <sup>19</sup>F NMR (282 MHz, CD<sub>3</sub>CN): δ -97.1 (d, <sup>1</sup>J<sub>F-P</sub> = 704, PF<sub>6</sub><sup>-</sup>). <sup>31</sup>P[<sup>1</sup>H] NMR (121 MHz, CD<sub>3</sub>CN): δ -143.2 (septet, <sup>1</sup>J<sub>P-F</sub> = 704, PF<sub>6</sub><sup>-</sup>). HRMS (ESI<sup>+</sup>): Calcd. for [C<sub>35</sub>H<sub>20</sub>N<sub>5</sub>O<sub>4</sub>Ru]<sup>+</sup> ([M - PF<sub>6</sub>]<sup>+</sup>), 676.0559. Found: 676.0590. Anal. Calcd. for C<sub>35</sub>H<sub>20</sub>N<sub>5</sub>O<sub>4</sub>F<sub>6</sub>PRu·4H<sub>2</sub>O: C, 47.09; H, 3.16; N, 7.85;. Found: C, 47.18; H, 3.06; N, 7.94.

**[Ru(phpy)(biq)<sub>2</sub>][PF<sub>6</sub>] (5).** The ligand 2,2'-biquinoline (100 mg, 0.39 mmol) was added to a yellow suspension of [Ru(phpy)(NCCH<sub>3</sub>)<sub>4</sub>][PF<sub>6</sub>] (103 mg, 0.18 mmol) in ethanol (15 mL) and the mixture was heated to reflux for 5 h. The resulting dark green solution was reduced to dryness and the residue was purified by FC (SiO<sub>2</sub>, CH<sub>3</sub>CN/CH<sub>2</sub>Cl<sub>2</sub>, gradient from 1% to 12% CH<sub>3</sub>CN). The first green band was collected and reduced to dryness. The residue was dissolved with CH<sub>2</sub>Cl<sub>2</sub> (10 mL), hexanes (8 mL) was added

slowly and the green precipitate was collected by filtration and washed with CH<sub>2</sub>Cl<sub>2</sub>/hexanes 1:1 (3 x 20 mL). Yield: 130 mg (78%). <sup>1</sup>H NMR (500 MHz, CD<sub>3</sub>CN): δ 8.93 (d, 1H, <sup>3</sup>J = 8.5), 8.84 (d, 1H, <sup>3</sup>J = 8.5), 8.78 (d, 1H, <sup>3</sup>J = 9.0), 8.70 (d, 1H, <sup>3</sup>J = 8.5), 8.64 (d, 1H, <sup>3</sup>J = 9.0), 8.60 (d, 1H, <sup>3</sup>J = 9.0), 8.28 (d, 1H, <sup>3</sup>J = 8.5), 8.24 (d, 1H, <sup>3</sup>J = 9.0), 8.04 (dd, 1H, <sup>3</sup>J = 8.0, <sup>4</sup>J = 1.5), 7.96 (dd, 1H, <sup>3</sup>J = 8.0, <sup>4</sup>J = 1.5), 7.73 (dd, 1H, <sup>3</sup>J = 8.0, <sup>4</sup>J = 1.5), 7.62 (d, 2H, <sup>3</sup>J = 8.5), 7.43-7.33 (m, 4H), 7.31 (ddd, 1H, <sup>3</sup>J = 8.0, <sup>3</sup>J = 6.5, <sup>4</sup>J = 1.0), 7.27 (m, 2H), 7.22 (ddd, 1H, <sup>3</sup>J = 8.0, <sup>3</sup>J = 6.5, <sup>4</sup>J = 1.0), 7.13 (d, 1H, <sup>3</sup>J = 8.0), 7.08 (d, 1H, <sup>3</sup>J = 9.0), 6.94 (m, 2H), 6.88 (ddd, 1H, <sup>3</sup>J = 8.5, <sup>3</sup>J = 7.0, <sup>4</sup>J = 1.5), 6.85-6.79 (m, 3 H), 6.66 (ddd, 1H, <sup>3</sup>J = 8.5, <sup>3</sup>J = 7.0, <sup>4</sup>J = 1.5), 6.31 (ddd, 1H, <sup>3</sup>J = 7.5, <sup>3</sup>J = 7.5, <sup>4</sup>J = 1.5), 6.25 (dd, 1H, <sup>3</sup>J = 8.0, <sup>4</sup>J = 1.0). <sup>19</sup>F NMR (282 MHz, CD<sub>3</sub>CN): δ -72.8 (d, <sup>1</sup>J<sub>F-P</sub> = 704, PF<sub>6</sub><sup>-</sup>). <sup>31</sup>P[<sup>1</sup>H] NMR (121 MHz, CD<sub>3</sub>CN): δ -143.2 (septet, <sup>1</sup>J<sub>P-F</sub> = 704, PF<sub>6</sub><sup>-</sup>). HRMS (ESI<sup>+</sup>): Calcd. for [C<sub>47</sub>H<sub>32</sub>N<sub>5</sub>Ru]<sup>+</sup> ([M - PF<sub>6</sub>]<sup>+</sup>), 768.1701. Found: 768.1691. Anal. Calcd. for C<sub>47</sub>H<sub>32</sub>N<sub>5</sub>F<sub>6</sub>PRu·0.5H<sub>2</sub>O: C, 61.24; H, 3.61; N, 7.60;. Found: C, 61.40; H, 3.66; N, 7.61.

**[Ru(phpy)(pap)(NCCH<sub>3</sub>)<sub>2</sub>][PF<sub>6</sub>] (6).** [Ru(phpy)(NCCH<sub>3</sub>)<sub>4</sub>][PF<sub>6</sub>] (240 mg, 0.43 mmol) was added to an orange solution of 2-phenylazopyridine (78 mg, 0.42 mmol) in CH<sub>2</sub>Cl<sub>2</sub> (20 mL). The resulting solution acquired a dark red color within 10 minutes. After 18 h of stirring at room temperature, the dark magenta solution was reduced to dryness under reduced pressure and the residue was purified by FC (basic Al<sub>2</sub>O<sub>3</sub>, CH<sub>3</sub>CN/CH<sub>2</sub>Cl<sub>2</sub>, gradient from 2% to 20% CH<sub>3</sub>CN). The second bright magenta band was collected and was reduced to *ca.* 20 mL. A mixture of diethyl ether/hexanes (1:1, 80 mL) was added



and the magenta precipitate was collected by filtration and washed with hexanes (3 x 30 mL). Yield: 214 mg (76%).  $^1\text{H}$  NMR (500 MHz,  $\text{CD}_3\text{CN}$ ):  $\delta$  9.18 (d, 1H,  $^3J = 5.5$ , H-1'), 8.57 (d, 1H,  $^3J = 8.0$ , H-4'), 8.30 (ddd, 1H,  $^3J = 8.0$ ,  $^3J = 8.0$ ,  $^4J = 1.5$ , H-3'), 8.06 (ddd, 1H,  $^3J = 7.0$ ,  $^3J = 5.5$ ,  $^4J = 1.5$ , H-2'), 7.76 (m, 2H, H-1, H-5), 7.67 (ddd, 1H,  $^3J = 7.5$ ,  $^3J = 7.5$ ,  $^4J = 1.5$ , H-6), 7.56 (dd, 1H,  $^3J = 8.0$ ,  $^4J = 1.0$ , H-4), 7.14 (m, 1H, H-p), 7.05 (ddd, 1H,  $^3J = 7.5$ ,  $^3J = 7.5$ ,  $^4J = 1.0$ , H-2), 7.00 (m, 2H, H-m), 6.92 (d, 1H,  $^3J = 5.5$ , H-8), 6.87 (ddd, 1H,  $^3J = 7.5$ ,  $^3J = 7.5$ ,  $^4J = 1.0$ , H-3), 6.83-6.77 (m, 3H, H-7, H-o), 2.40 (s, 3H,  $\text{NCCH}_3$ ), 2.29 (s, 3H,  $\text{NCCH}_3$ ).  $^{19}\text{F}$  NMR (282 MHz,  $\text{CD}_3\text{CN}$ ):  $\delta$  -71.1 (d,  $^1J_{\text{F-P}} = 704$ ,  $\text{PF}_6^-$ ).  $^{31}\text{P}[^1\text{H}]$  NMR (121 MHz,  $\text{CD}_3\text{CN}$ ):  $\delta$  -147.7 (septet,  $^1J_{\text{P-F}} = 704$ ,  $\text{PF}_6^-$ ). MS (ESI+): 439.04 ( $[\text{M} - 2\text{CH}_3\text{CN} - \text{PF}_6]^+$ ), 480.07 ( $[\text{M} - \text{CH}_3\text{CN} - \text{PF}_6]^+$ ). Anal. Calcd. for  $\text{C}_{26}\text{H}_{23}\text{F}_6\text{N}_6\text{PRu}$ : C, 46.92; H, 3.48; N, 12.63. Found: C, 46.90; H, 3.54; N, 12.64.

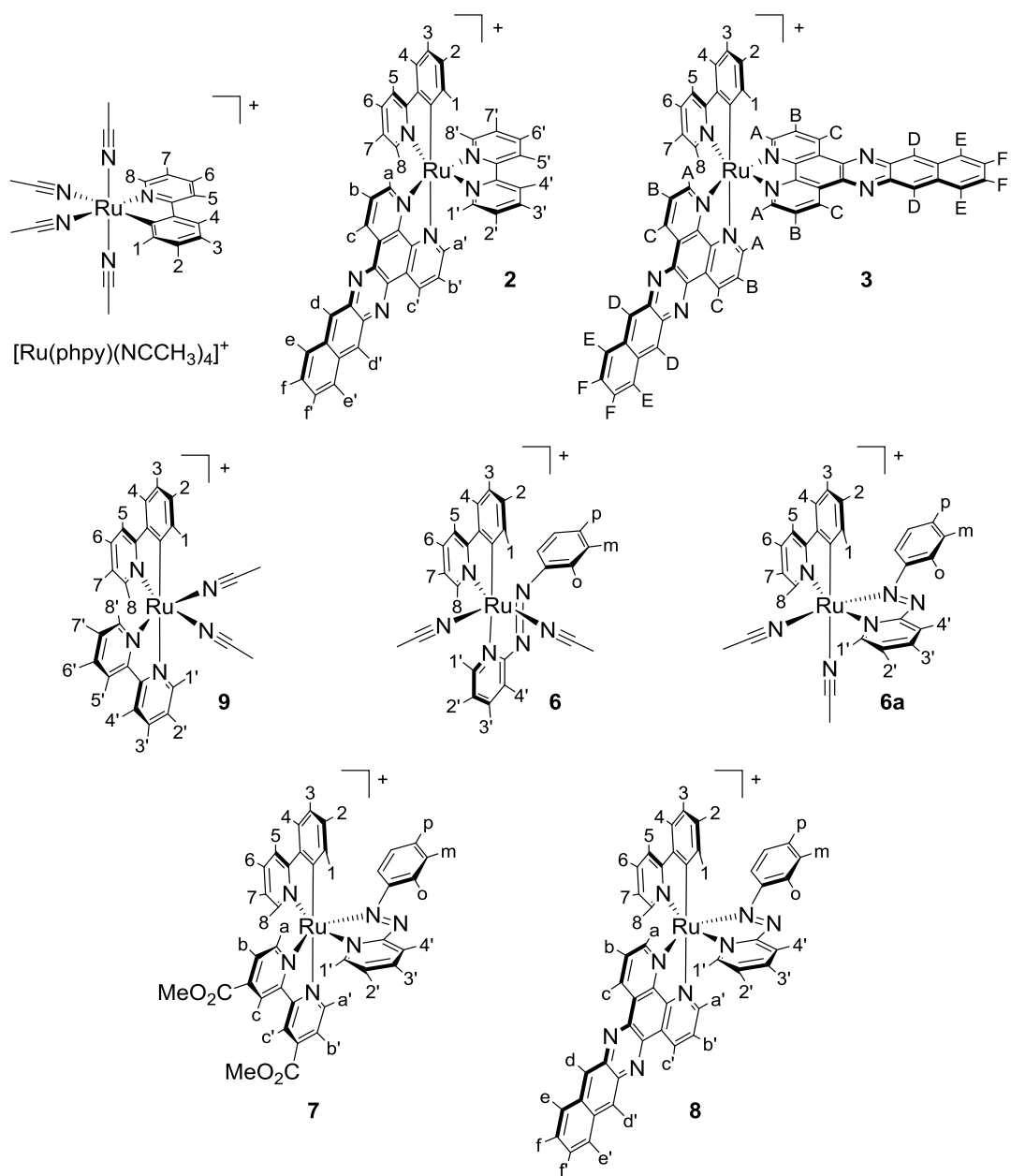
**[Ru(phpy)(pap)(dcmb)][PF<sub>6</sub>] (7).** A mixture of **6** (650 mg, 0.98 mmol) and 4,4'-dicarboxymethyl-2,2'-bipyridine (315 mg, 1.16 mmol) in methanol (25 mL) was heated to reflux for 24 h. The dark red solution was reduced to dryness and the residue was purified by FC ( $\text{SiO}_2$ ,  $\text{CH}_3\text{CN}/\text{CH}_2\text{Cl}_2$ , gradient from 0% to 20%  $\text{CH}_3\text{CN}$ ). The second dark red band was collected and the solvent was removed under reduced pressure. The solid residue was triturated with diethyl ether, collected by filtration and washed with  $\text{CH}_2\text{Cl}_2$ /diethyl ether (1:2.5; 3 x 30 mL). Yield: 400 mg (50%).  $^1\text{H}$  NMR (500 MHz,  $\text{CD}_3\text{CN}$ ):  $\delta$  9.01 (d, 1H,  $^4J = 1.0$ , H-c or H-c'), 8.98 (d, 1H,  $^4J = 1.0$ , H-c' or H-c), 8.53 (d, 1H,  $^3J = 8.0$ , H-4'), 8.30 (dd, 1H,  $^3J = 5.5$ , H-a), 8.03 (dd, 1H,  $^3J = 5.5$ , H-a'), 7.98 (m, 2H, H-3 and H-b or H-b'), 7.85-7.78 (m, 4H, H-4, H-5, H-1' and H-b' or H-b), 7.57

(ddd, 1H,  $^3J = 8.5$ ,  $^3J = 7.5$ ,  $^4J = 1.5$ , H-6), 7.43 (ddd, 1H,  $^3J = 7.5$ ,  $^3J = 5.5$ ,  $^4J = 1.5$ , H-2'), 7.25 (m, 1H, H-p), 7.17 (d, 1H,  $^3J = 5.5$  Hz, H-8), 7.11 (m, 3H, H-m and H-3), 7.05 (m, 3H, H-o and H-2), 6.72 (ddd, 1H,  $^3J = 7.5$ ,  $^3J = 5.5$ ,  $^4J = 1.5$ , H-7), 5.95 (dd, 1H,  $^3J = 7.5$ ,  $^4J = 1.0$ , H-1), 4.00 (s, 3H, -CO<sub>2</sub>CH<sub>3</sub>), 3.96 (s, 3H, -CO<sub>2</sub>CH<sub>3</sub>). <sup>19</sup>F NMR (282 MHz, CD<sub>3</sub>CN):  $\delta$  -73.7 (d,  $^1J_{F-P} = 704$ , PF<sub>6</sub><sup>-</sup>). <sup>31</sup>P[<sup>1</sup>H] NMR (121 MHz, CD<sub>3</sub>CN):  $\delta$  -144.6 (septet,  $^1J_{P-F} = 704$ , PF<sub>6</sub><sup>-</sup>). MS (ESI+): 711.14 ([M - PF<sub>6</sub> + H]<sup>+</sup>). Anal. Calcd. for C<sub>36</sub>H<sub>29</sub>N<sub>6</sub>O<sub>4</sub>F<sub>6</sub>PRu·0.5(C<sub>2</sub>H<sub>5</sub>)<sub>2</sub>O: C, 51.12; H, 3.84; N, 9.41. Found: C, 51.21; H, 3.93; N, 9.48.

**[Ru(phpy)(pap)(dppn)][PF<sub>6</sub>] (8).** A suspension of **6** (82 mg, 1.12 mmol) and dppn (44 mg, 0.13 mmol) in methanol (20 mL) was heated to reflux for 24 h. The dark red-magenta solution was reduced to dryness and the residue was purified by FC (SiO<sub>2</sub>, CH<sub>3</sub>CN/CH<sub>2</sub>Cl<sub>2</sub>, gradient from 5% to 10% CH<sub>3</sub>CN). The first red band was collected and the solvent was removed under reduced pressure. The solid residue was triturated with hexanes, collected by filtration and washed with hexanes (50 mL). Yield: 97 mg (86%). <sup>1</sup>H NMR (500 MHz, CD<sub>3</sub>CN):  $\delta$  9.27 (dd, 1H,  $^3J = 8.0$ ,  $^4J = 1.5$ , H-c or H-c'), 9.15 (dd, 1H,  $^3J = 8.0$ ,  $^4J = 1.5$ , H-c' or H-c), 8.63 (s, 1H, H-d or H-d'), 8.57 (m, 2H, H-a or H-a', H-4), 8.52 (s, 1H, H-d' or H-d), 8.10 (dd, 1H,  $^3J = 5.5$ ,  $^4J = 1.5$ , H-a' or H-a), 8.08 (m, 1H, H-e or H-e'), 8.02-7.93 (m, 4H, H-e' or H-e, H-4, H-5, H-3'), 7.92 (d, 1H,  $^3J = 5.5$ , H-1'), 7.86 (dd, 1H,  $^3J = 8.0$ ,  $^3J = 5.0$ , H-b or H-b'), 7.64-7.59 (m, 2H, H-b' or H-b, H-6), 7.56-7.50 (m, 2H, H-f and H-f'), 7.43-7.39 (m, 2H, H-8, H-2'), 7.33 (m, 1H, H-p), 7.26-7.17 (m, 5H, H-3, H-o, H-m), 7.14 (ddd, 1H,  $^3J = 8.0$ ,  $^3J = 8.0$ ,  $^4J = 1.0$ , H-2),

6.72 (ddd, 1H,  $^3J = 8.0$ ,  $^3J = 5.5$ ,  $^4J = 1.5$ , H-7), 6.12 (dd, 1H,  $^3J = 5.5$ ,  $^4J = 1.0$ , H-1). HRMS (ESI+): Calcd. for  $[C_{44}H_{29}N_8Ru]^+$  ( $[M - PF_6]^+$ ), 771.1559. Found: 771.1535. Anal. Calcd. for  $C_{44}H_{29}N_8F_6PRu \cdot 0.5H_2O$ : C, 57.15; H, 3.27; N, 12.12. Found: C, 57.26; H, 3.48; N, 12.11.

**[Ru(phpy)(bpy)(NCCH<sub>3</sub>)<sub>2</sub>] (9).** The Ru complex was prepared following reported procedures.<sup>182,183</sup> A solution of  $[Ru(phpy)(NCCH_3)_4][PF_6]$  (200 mg, 0.35 mmol) and bpy (51 mg, 0.33 mmol) in  $CH_2Cl_2$  (15 mL) was stirred at room temperature under reduced light conditions. After 20 h, the dark orange solution was reduced to dryness and purified by FC (basic  $Al_2O_3$ ,  $CH_3CN/CH_2Cl_2$ , gradient from 0% to 30%  $CH_3CN$ ). The orange band was collected, reduced *ca.* 2 mL and diluted with  $CH_2Cl_2/CH_3CN$  (1:1, 10 mL). Diethyl ether was added slowly until a small amount of solid precipitated and the flask was stored at 0°C overnight. The dark orange crystals that had formed were collected by filtration and washed with diethyl ether (30 mL). Yield: 150 mg (77%). <sup>1</sup>H NMR (500 MHz,  $CD_3CN$ ):  $\delta$  9.37 (d, 1H,  $^3J = 5.0$ , H-1'), 8.45 (d, 1H,  $^3J = 8.0$ , H-4'), 8.22 (m, 2H, H-1 and H-5'), 8.17 (ddd, 1H,  $^3J = 8.0$ ,  $^3J = 8.0$ ,  $^4J = 1.5$ , H-3'), 7.90 (d, 1H,  $^3J = 6.0$ , H-8'), 7.87-7.82 (m, 3H, H-4, H-5 and H-2'), 7.67 (ddd, 1H,  $^3J = 8.0$ ,  $^3J = 8.0$ ,  $^4J = 1.5$ , H-6'), 7.54 (ddd, 1H,  $^3J = 8.0$ ,  $^3J = 8.0$ ,  $^4J = 1.5$ , H-6), 7.45 (d, 1H,  $^3J = 6.0$ , H-8), 7.25 (ddd, 1H,  $^3J = 7.5$ ,  $^3J = 7.5$ ,  $^4J = 1.5$ , H-2), 7.07 (ddd, 1H,  $^3J = 8.0$ ,  $^3J = 8.0$ ,  $^4J = 1.5$ , H-3), 7.01 (ddd, 1H,  $^3J = 7.5$ ,  $^3J = 6.0$ ,  $^4J = 1.5$ , H-7'), 6.74 (ddd, 1H,  $^3J = 7.5$ ,  $^3J = 6.0$ ,  $^4J = 1.5$ , H-7), 2.23 (s, NCCH<sub>3</sub>), 2.18 (s, NCCH<sub>3</sub>).



**Figure 3.** 4 Numbering scheme used to assign the  $^1\text{H}$  NMR spectra of selected Ru complexes.

## *X-Ray Crystallography*

Single crystals of **5** were obtained by slow diffusion of hexanes into a CH<sub>2</sub>Cl<sub>2</sub> solution of the compound in a thin diameter tube at room temperature. Single crystals of **6** were obtained by slow diffusion of hexanes into a CH<sub>2</sub>Cl<sub>2</sub>/CH<sub>3</sub>CN solution of the compound in a thin tube at room temperature. Single crystals of **7** were obtained by slow evaporation of a CH<sub>2</sub>Cl<sub>2</sub>/ethyl acetate solution of the compound at room temperature. Single crystals of **9** were obtained by keeping a CH<sub>2</sub>Cl<sub>2</sub>/CH<sub>3</sub>CN/diethyl ether solution of the compound at 0°C. X-ray data was collected on a Bruker APEX II CCD X-ray diffractometer equipped with a graphite monochromated MoK<sub>α</sub> radiation source ( $\lambda = 0.71073 \text{ \AA}$ ). The data sets were integrated with the Bruker SAINT software package.<sup>148</sup> The absorption correction (SADABS)<sup>149</sup> was based on fitting a function to the empirical transmission surface as sampled by multiple equivalent measurements. Solution and refinement of the crystal structures was carried out using the SHELX<sup>150</sup> (2013) suite of programs and the graphical interface *ShelXle*<sup>151</sup> was used for the refinement. The structures were solved by direct (**5**, **6**, **7**) or Patterson methods (**9**) and all non-hydrogen atoms were refined with anisotropic displacement parameters using a full-matrix least-squares technique on  $F^2$ . Hydrogen atoms were fixed to parent atoms and refined using the riding model. PLATON/SQUEEZE was employed in the case of **6** after attempts to model disordered ethyl acetate solvent molecules failed. The SAME, SIMU AND DELU restraints were applied during the refinement of the structure of **9** to model the disorder of the [PF<sub>6</sub>]<sup>-</sup> anion.

### *Cell Culture Details*

Cell culture reagents and 3-(4,5-dimethylthiazol-2-yl)-2,5-diphenyltetrazolium bromide (MTT) were purchased from Invitrogen. The HeLa cell line was obtained from the American Type Culture Collection, cell line CCL-2. HeLa cells were cultured in Dulbecco's modified Eagle medium, supplemented with 10% fetal bovine serum (Life Technologies), 50  $\mu\text{g}/\text{mL}$  gentamicin, 4.5  $\text{mg}/\text{mL}$  glucose, and 4  $\text{mM}$  L-glutamine (Invitrogen Life Technology). Cell cultures were incubated in a humidified atmosphere containing 5%  $\text{CO}_2$  at 37°C.

### *In Vitro Cytotoxicity, SYTOX® Green and MitoProbe® JC-1 Assay*

Cytotoxicity and live cell imaging studies of compounds **1**, **2**, **4**, **5** and **8** were performed by Amanda David (Dunbar Group, Chemistry Department, Texas A&M University) in collaboration with Professor Jean-Philippe Pellois (Department of Biochemistry and Biophysics, Texas A&M University). The experimental procedures for these assays have been excluded from this dissertation because they will be included in Amanda David's dissertation. Details of the procedure can be found in the literature since this work has been recently published (Peña, B; David, A.; Pavani, C.; Baptista, M. S.; Pellois, J. P.; Turro, C.; Dunbar, K. R. *Organometallics* **2014**, *33*, 1100-1103).

### *Phototoxicity of Complex 5*

These experiments were performed in collaboration with Professor Mauricio S. Baptista (Department of Biochemistry, University of São Paulo, São Paulo, Brazil). Cell viability for phototoxicity studies was undertaken using two 48-well plates with density of  $1.5 \times 10^4$  HeLa cells per well. The plates were maintained in DMEM (Dulbecco's Minimum Eagle Medium) supplemented with 10% FCS (fetal calf serum) and 1% penicillin/streptomycin, in an incubator at 37°C in a humid atmosphere with 5% CO<sub>2</sub> for 18 to 24 h. The plates were washed with PBS and DMEM 1% FCS solutions containing the desired concentration of complex were added to the plates. After 24 h incubation, each well was washed with PBS and fresh PBS was added to the wells. One plate was then irradiated for 20 min (LED system  $633 \pm 20\text{nm}$ ;  $6.50 \text{ mW/cm}^2$ ) while the other was kept in the dark during that time. After irradiation, PBS was replaced with DMEM 1% FCS, and the plates were kept in the in the incubator at 37°C in 5% CO<sub>2</sub> for an additional 48 h, at which time the MTT assay was conducted using typical methods.

### *Theoretical Calculations*

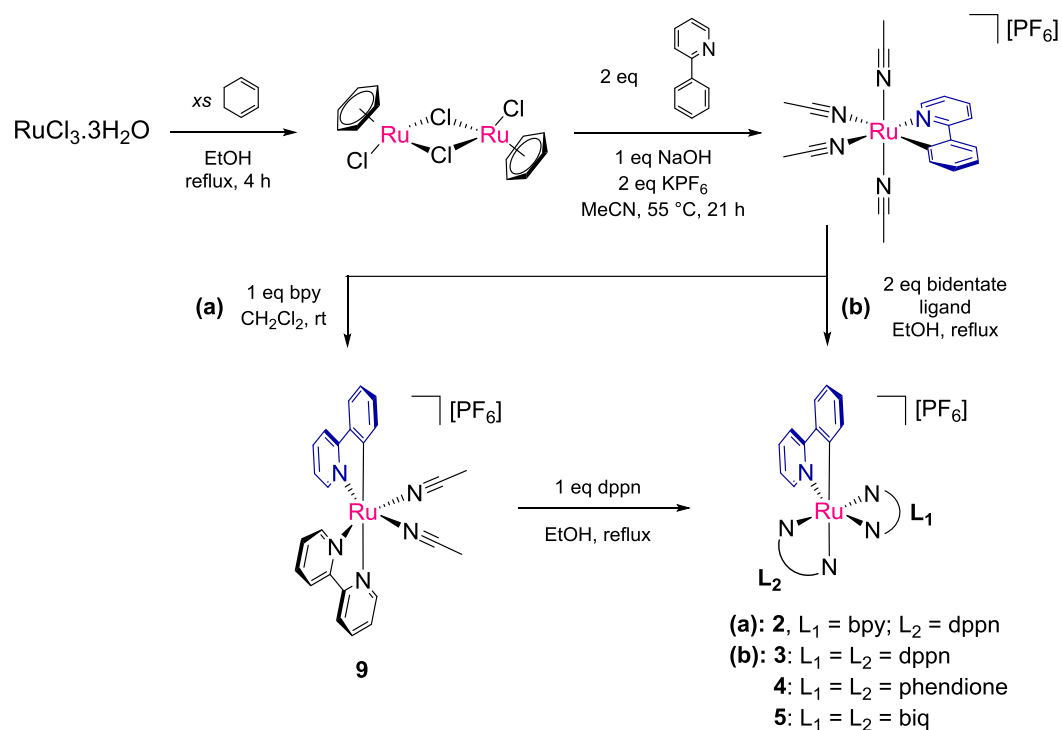
Density functional theory (DFT) calculations were performed with the Gaussian09 package<sup>184</sup> using the Becke's three-parameter hybrid functional and the Lee-Yang-Parr's gradient-corrected correlation functional (B3LYP).<sup>185,186</sup> The Stuttgart RSC 1997 Electron Core Potential<sup>187</sup> (ECP) basis set and effective core potential were used for the Ru atom and the split-valence 6-311G\* basis set was used for C, H, N and O. The geometry optimizations were performed using the polarized continuum medium model (PCM, acetonitrile) to include solvent polarization effects and without symmetry restraints, with subsequent frequency analysis. The molecular orbitals (MOs) were plotted with Ampac GUI 9 (Semichem, Inc; [www.semichem.com](http://www.semichem.com)) with the isovalue = 0.04. Fragment contributions to the MOs were calculated using the Chemissian v2.2 software ([www.chemissian.com](http://www.chemissian.com)). Time-dependent density functional theory (TD-DFT) calculations were performed to arrive at the vertical singlet excited states for each complex from the corresponding optimized singlet ground state geometry using the PCM model with acetonitrile as the solvent.



## Results and Discussion

### *Synthesis and Characterization of Compounds 1–5*

Compounds **1**,<sup>179</sup>  $[\text{Ru}(\text{phpy})(\text{bpy})(\text{NCCH}_3)_2][\text{PF}_6]$  (**9**)<sup>182</sup> and the starting material to prepare complexes **2–5**,  $[\text{Ru}(\text{phpy})(\text{NCCH}_3)_4][\text{PF}_6]$ <sup>181,182,183</sup> (Figure 3.5), were synthesized according to reported procedures.



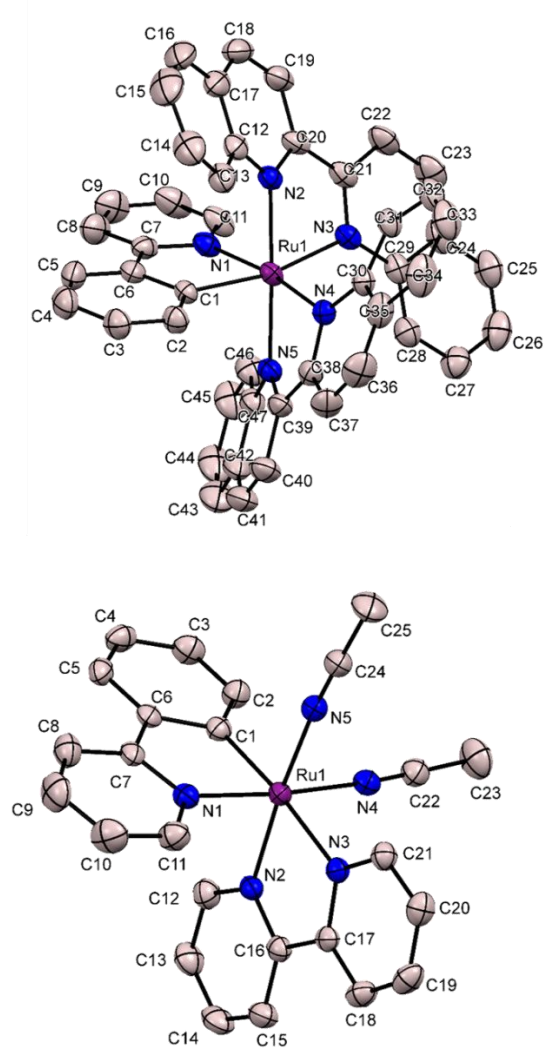
**Figure 3. 5** Reaction scheme for the synthesis of **2–5**.

Compounds **3–5** were prepared in 60%, 78% and 53% yields, respectively, by heating a suspension of  $[\text{Ru}(\text{phpy})(\text{NCCH}_3)_4][\text{PF}_6]$  and 2 eq of bidentate ligand (dppn, phendione and biq, respectively) to reflux in ethanol (Figure 3.5). The synthesis of the tris-heteroleptic compound **2** required an additional step. First,  $[\text{Ru}(\text{phpy})(\text{bpy})(\text{NCCH}_3)_2][\text{PF}_6]$  (**9**) was prepared by reacting  $[\text{Ru}(\text{phpy})(\text{NCCH}_3)_4][\text{PF}_6]$  with 1 eq of bpy in  $\text{CH}_2\text{Cl}_2$  at room temperature and under reduce light conditions. The two remaining acetonitrile ligands in **9** were substituted by dppn in refluxing ethanol to afford **2** in a 45% yield (Figure 3.5). Compounds **2–4** were obtained as dark red solids, whereas **5** has a dark green color. In all cases, the compounds were purified by flash column chromatography with silicagel using  $\text{CH}_3\text{CN}/\text{CH}_2\text{Cl}_2$  or  $\text{CH}_3\text{CN}/\text{toluene}$  mixtures as eluent.

The new complexes were characterized by electrospray ionization mass spectrometry (ESI+), elemental analyses and NMR spectroscopies ( $^1\text{H}$ ,  $^1\text{HH}$  COSY,  $^{19}\text{F}$  and  $^{31}\text{P}$ ). Their ESI(+) mass spectra contain only one peak corresponding to the  $[\text{M} - \text{PF}_6]^+$  cation and their  $C_1$  symmetric structures were confirmed by  $^1\text{H}$  NMR spectroscopy. There is an upfield doublet resonance in the  $^1\text{H}$  NMR spectra of **2–5** in the 6.83–6.25 ppm range that is characteristic of the proton *ortho* to the organometallic Ru–C bond in Ru(II) cyclometallated complexes.<sup>179</sup>

The X-ray structures of the compounds **5** and **9** are depicted in Figure 3.6 and the crystallographic data is compiled in Tables 3.1–3.3. Single crystals of **5** were grown by slow diffusion of hexanes into a dichloromethane solution of the compound at room temperature. The compound crystallizes in the monoclinic space group  $P2_1/n$  and there are two interstitial dichloromethane molecules in the asymmetric unit. The coordination sphere of the metal center consists of five N atoms and one C<sup>-</sup> atom in a distorted octahedral environment. The Ru1–C1 bond length of 2.095(4) Å is longer than the corresponding bond distances in [Ru(phpy)(bpy)<sub>2</sub>]<sup>+</sup> (2.044(1) Å<sup>188</sup>) and [Ru(phpy)(phen)<sub>2</sub>]<sup>+</sup> (2.036(7) Å<sup>175</sup>) which is attributed to the steric repulsion between the biq ligands. Three of the Ru–N bond lengths with the biq ligands, Ru1–N2, Ru1–N4 and Ru1–N5, are similar (~2.09 Å) and within the range of those found in the closely related compounds [Ru(bpy)(biq)<sub>2</sub>]<sup>2+</sup> and [Ru(bpy)<sub>2</sub>(biq)]<sup>2+</sup> (2.079(2) to 2.112(3) Å).<sup>189</sup> In contrast, the Ru1–N3 bond located *trans* to C1 is the longest, 2.148(3) Å, reflecting the strong *trans* influence of the phenyl ring of phpy. The angle between adjacent biq ligands (N3–Ru1–N4) is 98.3(1)° and is larger than the angles formed between each biq and phpy ligands, *viz.*, N1–Ru1–N3 and C1–Ru1–N4, which are 90.8(1) and 92.4(2)°, respectively. The more obtuse N3–Ru1–N4 angle is likely a consequence of steric repulsion between the two bulky biq ligands. The biq ligand *trans* to the C1 atom of phpy is twisted about the C–C bond (N2–C20–C21–N3, –9.9(6)°) whereas such a distortion is not observed in the other biq ligand (N4–C38–C39–N5, 0.9(6)°). In addition, the quinoline moieties of both biq ligands are bent by ~15° out of the plane

formed with the metal center, a distortion that was also observed in  $[\text{Ru}(\text{biq})_2(\text{bpy})][\text{PF}_6]_2$ .<sup>189</sup>



**Figure 3. 6** Thermal ellipsoid plots at the 50% probability level of the X-ray structures of  $[\text{Ru}(\text{phpy})(\text{biq})_2][\text{PF}_6]$  (**5**, top) and  $[\text{Ru}(\text{phpy})(\text{bpy})(\text{NCCH}_3)_2][\text{PF}_6]$  (**9**, bottom). The  $[\text{PF}_6]^-$  anions and H atoms have been omitted for the sake of clarity.

**Table 3. 1** Crystal Structural Data and Refinement Parameters for the compounds [Ru(phpy)(biq)<sub>2</sub>][PF<sub>6</sub>]<sub>2</sub>·2CH<sub>2</sub>Cl<sub>2</sub> (**5**) and [Ru(phpy)(bpy)(NCCH<sub>3</sub>)<sub>2</sub>][PF<sub>6</sub>]<sub>2</sub>·NCCH<sub>3</sub> (**9**).

Compound	<b>5</b>	<b>9</b>
CCDC number	961134	980890
Empirical Formula	C <sub>49</sub> H <sub>36</sub> N <sub>5</sub> F <sub>6</sub> Cl <sub>4</sub> PRu	C <sub>27</sub> H <sub>25</sub> F <sub>6</sub> N <sub>6</sub> P Ru
Formula weight	1082.67	679.57
Temperature, K	291(2)	110(2)
Crystal system	Monoclinic	Triclinic
Space group	<i>P</i> 2 <sub>1</sub> / <i>n</i>	<i>P</i> -1
Unit cell dimensions	<i>a</i> = 13.314(3), $\alpha$ = 90 <i>b</i> = 22.497(5), $\beta$ = 100.67(3) <i>c</i> = 15.709(3), $\gamma$ = 90	<i>a</i> = 9.5728(19), $\alpha$ = 102.34(3) <i>b</i> = 12.372(3), $\beta$ = 106.91(3) <i>c</i> = 12.792(3), $\gamma$ = 94.04(3)
Volume, Å <sup>3</sup>	4623.8(16)	1401.7(6)
Z	4	2
Density, g/cm <sup>3</sup>	1.555	1.610
Absorption coefficient, mm <sup>-1</sup>	0.671	0.685
<i>F</i> (000)	2184	684
Crystal color, morphology	green, needle	orange, needle
Crystal size, mm <sup>3</sup>	0.37 × 0.14 × 0.10	0.17 × 0.07 × 0.06
Reflections collected	49647	15519
Independent reflections	10375 [R <sub>int</sub> = 0.0609]	5921 [R <sub>int</sub> = 0.0311]
Data/restraints/parameters	10375/595/0	5921/ 0 / 373
Goodness-of-fit on F <sup>2</sup>	1.075	1.046
R indices [I > 2σ(I)]	R1 = 0.0637 wR2 = 0.1918	R1 = 0.0367 wR2 = 0.0886
R indices (all data)	R1 = 0.0828, wR2 = 0.2107	R1 = 0.0444 wR2 = 0.0936
Largest diff. peak, hole, e/Å <sup>3</sup>	1.82 / -1.23	1.33 / -0.78

**Table 3. 2** Selected bond distances and angles for [Ru(phpy)(biq)<sub>2</sub>][PF<sub>6</sub>]·2CH<sub>2</sub>Cl<sub>2</sub> (**5**).

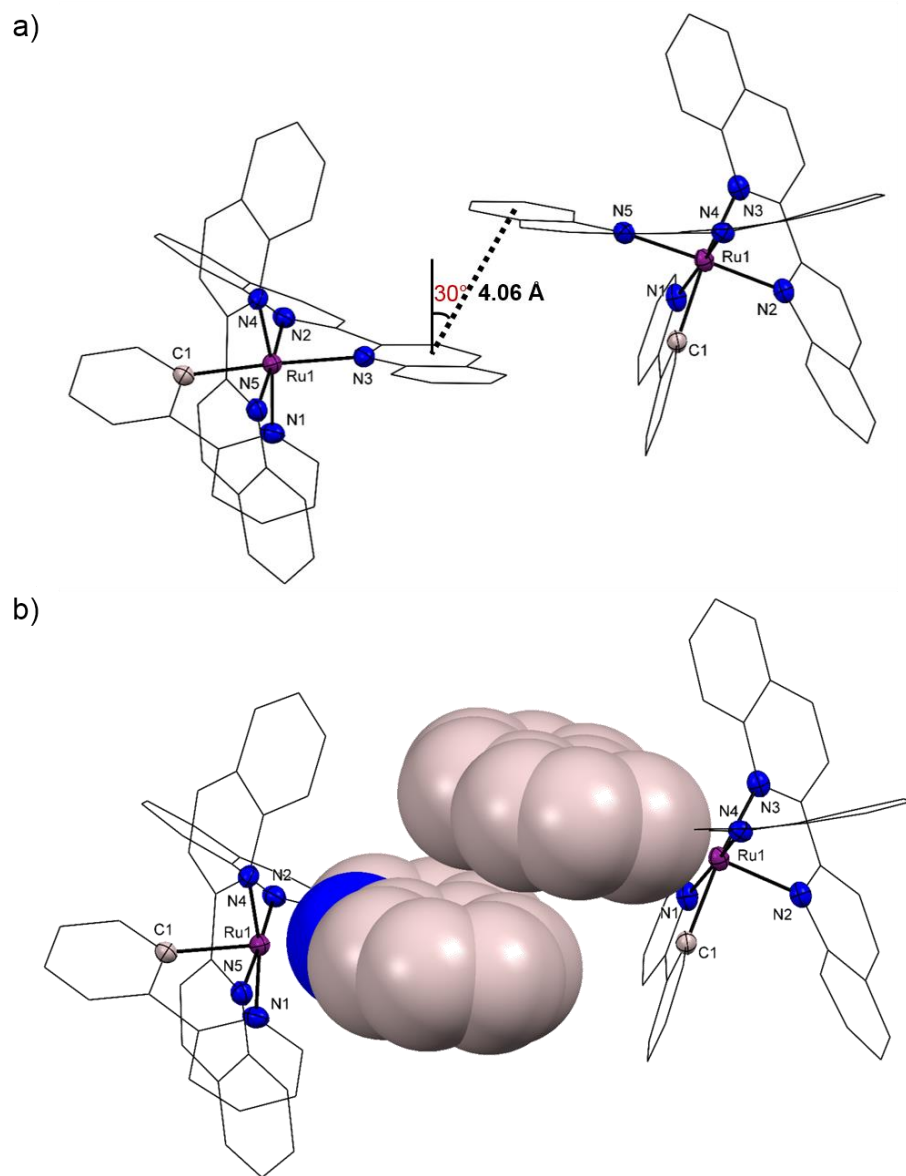
Bond lengths (Å)		Bond angles (°)	
Ru1–C1	2.095(4)	C1–Ru1–N1	78.8(2)
Ru1–N1	2.087(4)	N2–Ru1–N3	76.8(1)
Ru1–N2	2.092(3)	N4–Ru1–N5	76.7(1)
Ru1–N3	2.148(3)	N1–Ru1–N3	90.8(1)
Ru1–N4	2.091(4)	N3–Ru1–N4	98.3(1)
Ru1–N5	2.096(3)	C1–Ru1–N4	92.4(2)
Dihedral angles (°)			
N2–C20–C21–N3		–9.9(6)	
C19–C20–C21–C22		–11.9(8)	
N4–C38–C39–N5		–0.9(6)	
C37–C38–C39–C40		0.9(8)	
N2–Ru1–N3–C29		–165.1(4)	
N4–Ru1–N5–C47		166.2(4)	

**Table 3. 3** Selected bond distances and angles for Ru((phpy)(bpy)(NCCH<sub>3</sub>)<sub>2</sub>)[PF<sub>6</sub>]·NCCH<sub>3</sub> (**9**).

Bond lengths (Å)		Bond and dihedral angles (°)	
Ru1–C1	2.026(3)	C1–Ru1–N1	79.8(1)
Ru1–N1	2.055(3)	N2–Ru1–N3	77.94(9)
Ru1–N2	2.042(2)	N4–Ru1–N5	88.3(1)
Ru1–N3	2.145(3)	C1–Ru1–N3	174.7(1)
Ru1–N4	2.028(3)	N1–Ru1–N4	173.7(1)
Ru1–N5	2.022(3)	N2–Ru1–N5	172.6(1)
		N1–C7–C6–C1	–0.6(3)
		N2–C16–C17–N3	0.3(3)

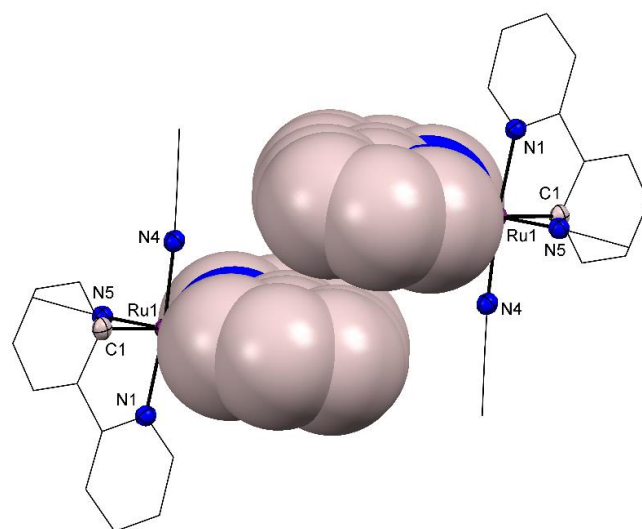
The crystal packing of compound **5** displays  $\pi$ - $\pi$  stacking interaction between the biquinoline moieties of different  $[\text{Ru}(\text{phpy})(\text{biq})_2]^+$  cations (Figure 3.7), with an interplanar distance of 3.52 Å and shortest centroid-centroid distance of 4.06 Å. The parallel displacement was measured by the angle formed between the ring centroid vector and the distance normal to one of the planes<sup>157,158</sup> and was calculated as 30°.

Single crystals of **9** were grown by keeping a solution of acetonitrile/diethyl ether of the compound at 0°C. The compound crystallizes in the triclinic space group  $P\bar{1}$  with one acetonitrile solvent molecule in the asymmetric unit. The distorted octahedral coordination sphere around the Ru ion contains by five N and one C<sup>-</sup> atom donors; the Ru–C bond distance (2.026(3) Å) is similar to the value observed in  $[\text{Ru}(\text{phpy})(\text{phen})(\text{NCCH}_3)_2]^+$  (2.029(3) Å).<sup>190</sup> The longest Ru–N bond (Ru–N3, 2.145(3) Å) is the one *trans* to the Ru–C bond and the rest of the Ru–N bond distances are similar to the distances reported for  $[\text{Ru}(\text{phpy})(\text{phen})(\text{NCCH}_3)_2]^+$ .<sup>190</sup> Intermolecular  $\pi$ - $\pi$  stacking interactions are also observed between the cations of this complex (Figure 3.8), where the bpy ligands are parallel displaced with an interplanar distance, shortest centroid-centroid distance and displacement angle of 3.31 Å, 3.76 Å and 28°, respectively.



**Figure 3. 7** Intermolecular  $\pi$ - $\pi$  stacking interactions in the crystal packing of compound **5**. (a) Shortest centroid-centroid distance and slippage angle and (b) space filling model highlighting the stacking of  $\pi$ -systems of biquinoline moieties.





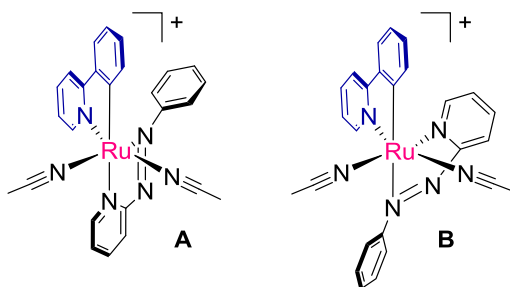
**Figure 3. 8** Space filling model highlighting intermolecular  $\pi$ - $\pi$  interactions in the crystal packing of compound **9**.

### *Synthesis and Characterization of Compounds 6–8*

Compound **6** was prepared by reacting  $[\text{Ru}(\text{phpy})(\text{NCCH}_3)_4][\text{PF}_6]$  with 1 eq of pap in  $\text{CH}_2\text{Cl}_2$  at room temperature under reduced light conditions and was obtained as a magenta solid in 76% yield after flash chromatography in basic  $\text{Al}_2\text{O}_3$ . This compound may exist as different geometric isomers due to the asymmetry of both phpy and pap ligands, but only one isomer is produced under this experimental conditions. Since the longest Ru–N bond in  $[\text{Ru}(\text{phpy})(\text{NCCH}_3)_4][\text{PF}_6]$  corresponds to the acetonitrile ligand *trans* to the Ru–C bond,<sup>182</sup> this coordination position will be occupied by one of the two N atom donors of pap in **6**, and if it is assumed that there is a *cis* configuration of the two acetonitrile ligands, two geometric isomers are possible for **6**, as shown in Figure 3.9.

There are two singlet proton resonances at 2.29 and 2.40 ppm in the  $^1\text{H}$  NMR spectrum of **6** which corresponds to the methyl groups of the two acetonitrile ligands, as expected for a *cis* configuration. The proton resonances of the pyridyl moiety of pap (H-1' to H-4', Figure 3.10) appear downfield with respect to the phpy protons. The proton *ortho* to the N atom in the pyridyl ring of pap, H-1', appears at 9.18 ppm and it is the most deshielded; therefore, it must be directed toward one acetonitrile ligand. This characteristic has also been observed for the same pyridyl proton of bpy in *cis*- $[\text{Ru}(\text{phpy})(\text{bpy})(\text{NCCH}_3)_2]^+$  (9.35 ppm)<sup>182</sup> and *cis*- $[\text{Ru}(\text{phpy4thio})(\text{bpy})(\text{NCCH}_3)_2]^+$  (9.44 ppm, where phpy4thio = orthometallated 5-[3-(pyridin-2-yl)phenyl]thiophene-2-carbaldehyde).<sup>183</sup> Geometric isomer B is ruled out because H-1' is pointing toward the

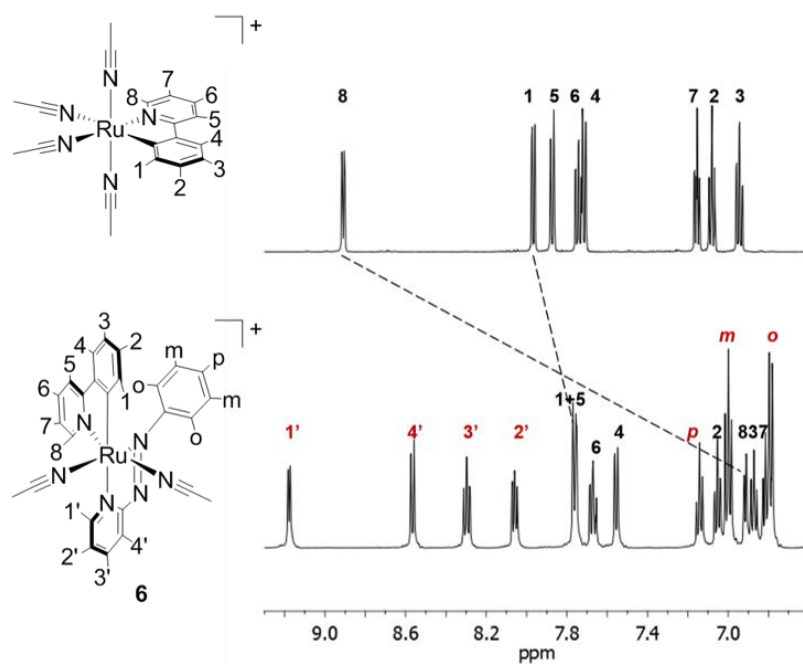
phenyl ring in this geometric isomer and it would appear upfield, at *ca.* 7–8 ppm, due to ring current effects.



**Figure 3. 9** Possible geometric isomers of compound **6** with *cis* arrangement of acetonitrile ligands

The proton *ortho* to the N atom in phpy (H-8) appears at 6.92 ppm, which is ~2 pm upfield with respect to its chemical shift in  $[\text{Ru}(\text{phpy})(\text{NCCH}_3)_4]^+$  (8.91 ppm, Figure 3.10) as a consequence of being shielded by the adjacent pyridyl ring of the pap ligand. The proton that is *ortho* to the Ru–C bond (H-1) has a similar chemical shift in **6** and  $[\text{Ru}(\text{phpy})(\text{NCCH}_3)_4]^+$  (~0.2 ppm difference) confirming that is directed at an acetonitrile ligand as in the tetrakis(acetonitrile) compound. It can also be observed that protons H-1 to H-7 in both  $[\text{Ru}(\text{phpy})(\text{NCCH}_3)_4]^+$  and **6** appear at approximately the same chemical shift (within 0.03–0.33 ppm), whereas the chemical shift for H-8 is

drastically changed as described above. The proposed structure of **6** was confirmed by X-ray crystallography (see below).

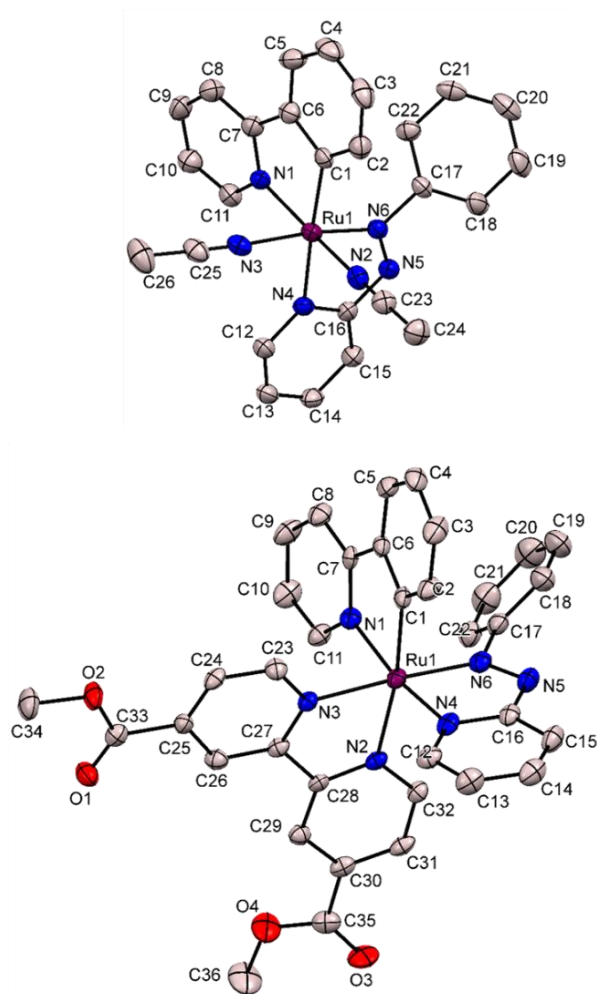


**Figure 3. 10** Comparison of the proton resonances in the aromatic region of  $[\text{Ru}(\text{phpy})(\text{NCCH}_3)_4]^+$  and  $[\text{Ru}(\text{phpy})(\text{pap})(\text{NCCH}_3)_2]$  (**6**).

Substitution of the acetonitrile ligands in **6** was explored to demonstrate its suitability as precursor for expanding the structural diversity of Ru cyclometallated compounds. Reaction of **6** with 1 eq of dcmb (4,4'-dicarboxymethyl-2,2'-bipyridine) or 1 eq of dpbn in refluxing MeOH afforded the tris-heteroleptic compounds **7** and **8**, respectively. Both compounds were also obtained as single geometric isomers. The X-ray structures of compounds **6** and **7** are shown in Figure 3.11 and the crystallographic data are compiled in Tables 3.4–3.6. Compounds **6** and **7** crystallize in the monoclinic space groups  $P2_1/c$  and  $C2/c$ , respectively. The metal center is located in a distorted octahedral environment in both compounds. The geometric isomer proposed for **6** is in agreement with its X-ray structure.

The Ru1–C1 bond lengths of **6** and **7** (2.039(4) and 2.047(4) Å, respectively) are similar to those observed for related cyclometallated compounds.<sup>169,182</sup> The Ru–N bond in the *trans* position to the Ru1–C1 bond is the longest in both complexes (Ru1–N4, 2.125(4), and Ru1–N2, 2.127(3) Å, respectively) due to the strong *trans* influence of phpy. The Ru–N bond with the azo moiety is the shortest in both compounds (Ru1–N6 1.960(3) and 1.944(3) Å, respectively) because of increased  $\pi$ -backbonding into the azo moiety to stabilize the additional electron density on the metal center donated by phpy, which is also accompanied by an elongation of the N–N bond of the azo group (1.304(5) and 1.306(5) Å, respectively) with respect to uncoordinated pap (1.25 Å).<sup>191</sup> There is a small deviation from planarity between the pyridyl and phenyl rings (torsion angle  $\sim 5^\circ$ ) of phpy in **6** and **7**. The pyridyl ring and the N–N azo bond of pap are essentially

coplanar in both compounds, but this moiety is not coplanar with the phenyl ring within the same ligand and they exhibit a torsion angle of  $125^\circ$  and  $136^\circ$ , respectively.



**Figure 3. 11** Thermal ellipsoid plots at the 50% probability level of the X-ray structures of compounds [Ru(phpy)(pap)(NCCH<sub>3</sub>)<sub>2</sub>][PF<sub>6</sub>] (**6**, top) and [Ru(phpy)(pap)(dcmb)][PF<sub>6</sub>] (**7**, bottom). The [PF<sub>6</sub>]<sup>-</sup> anions and H atoms have been omitted for the sake of clarity.

**Table 3. 4** Crystal Structural Data and Refinement Parameters for the compounds [Ru(phpy)(pap)(NCCH<sub>3</sub>)<sub>2</sub>][PF<sub>6</sub>] (**6**) and [Ru(phpy)(pap)(dcmb)][PF<sub>6</sub>] (**7**).

Compound	<b>6</b>	<b>7</b>
CCDC number	978317	978318
Empirical Formula	C <sub>26</sub> H <sub>23</sub> F <sub>6</sub> N <sub>6</sub> PRu	C <sub>36</sub> H <sub>29</sub> F <sub>6</sub> N <sub>6</sub> O <sub>4</sub> PRu
Formula weight	665.54	855.69
Temperature, K	110(2)	110(2)
Crystal system	Monoclinic	Monoclinic
Space group	<i>P2<sub>1</sub>/c</i>	<i>C2/c</i>
Unit cell dimensions	<i>a</i> = 8.3581(17), $\alpha$ = 90 <i>b</i> = 13.855(3), $\beta$ = 92.49(3) <i>c</i> = 23.624(5), $\gamma$ = 90	<i>a</i> = 47.073(9), $\alpha$ = 90 <i>b</i> = 7.9141(16), $\beta$ = 104.83(3) <i>c</i> = 22.064(4), $\gamma$ = 90
Volume, Å <sup>3</sup>	2733.1(10)	7946(3)
Z	4	8
Density, g/cm <sup>3</sup>	1.617	1.431
Absorption coefficient, mm <sup>-1</sup>	0.701	0.507
<i>F</i> (000)	1336	3456
Crystal color, morphology	red, block	purple, plate
Crystal size, mm <sup>3</sup>	0.34 × 0.13 × 0.10	0.23 × 0.10 × 0.03
Reflections collected	18651	40551
Independent reflections	4952 [R <sub>int</sub> = 0.0309]	8091 [R <sub>int</sub> = 0.0810]
Data/restraints/parameters	4952 / 0 / 363	8091 / 0 / 489
Goodness-of-fit on F <sup>2</sup>	1.112	1.045
R indices [I > 2σ(I)]	R <sub>1</sub> = 0.044 wR <sub>2</sub> = 0.1054	R <sub>1</sub> = 0.0471 wR <sub>2</sub> = 0.1062
R indices (all data)	R <sub>1</sub> = 0.0526 wR <sub>2</sub> = 0.1167	R <sub>1</sub> = 0.0757 wR <sub>2</sub> = 0.1171
Largest diff. peak/hole, e/Å <sup>3</sup>	1.40 / -0.77	1.01 / -1.08

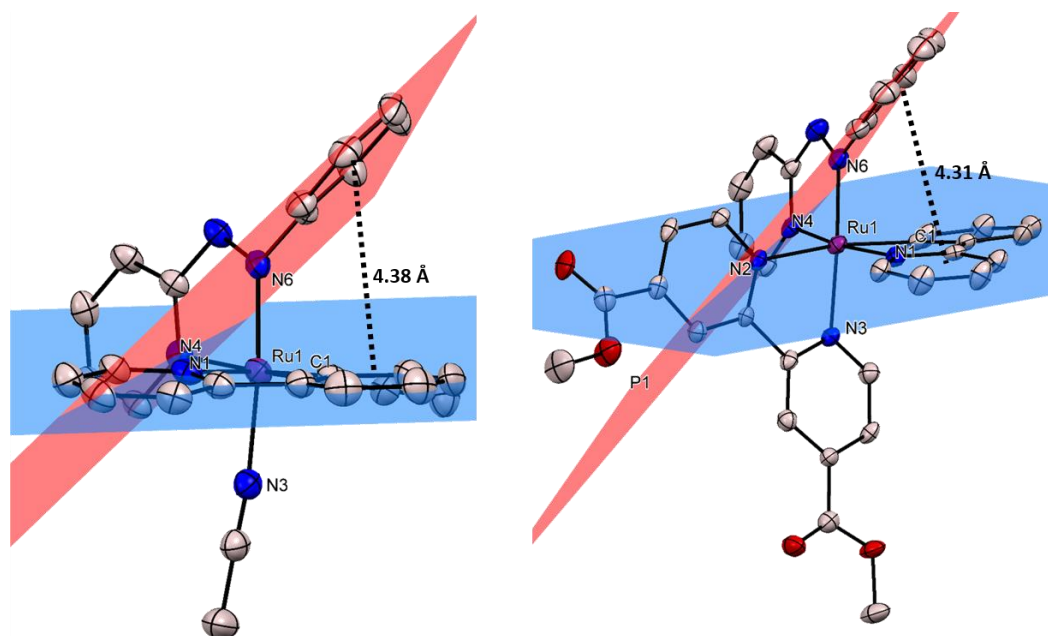
**Table 3. 5** Selected bond distances and angles for [Ru(phpy)(pap)(NCCH<sub>3</sub>)<sub>2</sub>][PF<sub>6</sub>] (**6**).

Bond lengths (Å)		Bond and dihedral angles (°)	
Ru1–C1	2.039(4)	C1–Ru1–N1	80.0(2)
Ru1–N1	2.049(4)	N2–Ru1–N3	89.9(1)
Ru1–N2	2.047(4)	N4–Ru1–N6	75.9(1)
Ru1–N3	2.056(4)	C1–Ru1–N4	174.3(2)
Ru1–N4	2.125(4)	N1–Ru1–N2	170.6(1)
Ru1–N6	1.960(3)	N3–Ru1–N6	172.3(1)
N5–N6	1.304(5)	N1– C7–C6–C1	–5.8(5)
		N4– C16–N5–N6	–1.2(5)
		N5– N6–C17–C22	125.1(4)

**Table 3. 6** Selected bond distances and angles for [Ru((phpy)(pap)(dcmb))][PF<sub>6</sub>] (**7**).

Bond lengths (Å)		Bond and dihedral angles (°)	
Ru1–C1	2.047(4)	C1–Ru1–N1	78.9(1)
Ru1–N1	2.088(3)	N2–Ru1–N3	76.1(1)
Ru1–N2	2.127(3)	N4–Ru1–N6	76.6(1)
Ru1–N3	2.094(3)	C1–Ru1–N2	171.7(1)
Ru1–N4	2.016(3)	N1–Ru1–N4	170.6(1)
Ru1–N6	1.944(3)	N3–Ru1–N6	176.6(1)
N5–N6	1.306(5)	N1– C7–C6–C1	–4.6(5)
		N4– C16–N5–N6	0.6(5)
		N5– N6–C17–C22	136.3(4)
		N2– C28–C27–N3	–5.8(4)

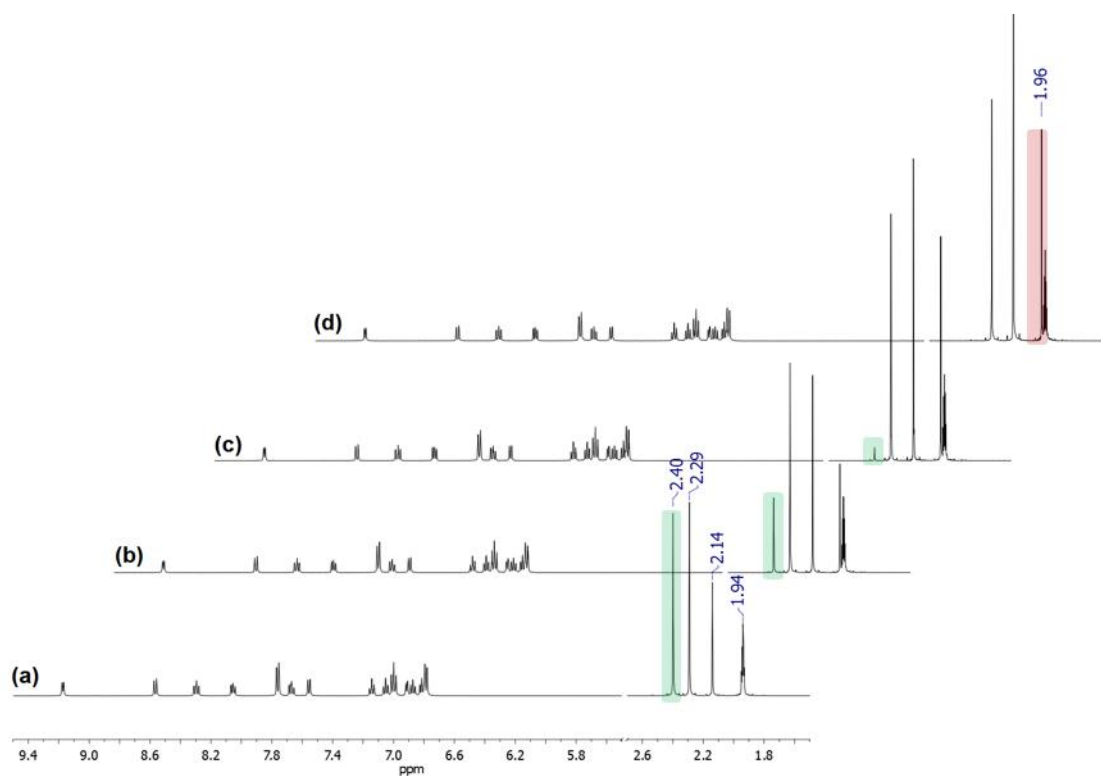




**Figure 3.12** Centroid-to-centroid distances in compounds **6** (left) and **7** (right).

In compound **6**, the plane of the phenyl ring of pap forms an angle of  $48^\circ$  with the plane that contains phpy and the centroid-centroid distance between the phenyl ring of pap and the phenyl ring of phpy is 4.38 Å (Figure 3.12). Similarly, the plane of the phenyl ring of pap and the plane of phpy form an angle of  $49^\circ$  in **7** and the centroid-centroid distance between the phenyl ring of pap and the pyridyl ring of phpy is 4.31 Å. Usual  $\pi$ - $\pi$  stacking interactions in metal complexes incorporating polypyridyl ligands display a parallel displaced stacking of  $\pi$ -systems with centroid-to-centroid distances of  $\sim 3.8$ – $4.0$  Å and slipped angles of  $\sim 20$ – $30^\circ$ ;<sup>157,158</sup> such interactions are not evident in either **6** or **7**.

It is interesting to note that the coordinating moiety that is *trans* to the pyridyl group of the pap ligand in **6** is the orthometallated phenyl ring of phpy, but changes to the pyridyl ring of the phpy ligand in **7**. Such a difference in the arrangement of the ligands suggests that **6** isomerizes prior to coordination of dcmb. Thermal isomerization has been recently reported during the formation of tris-heteroleptic compounds of the type  $[\text{Ru}(\text{phpy})(\text{phen})(\text{L})]^+$  (L = bpy and phen derivatives) using  $[\text{Ru}(\text{phpy})(\text{phen})(\text{NCCH}_3)_2]^+$  as the starting material.<sup>192</sup> Therefore, the thermal stability of **7** was investigated by <sup>1</sup>H NMR spectroscopy in CD<sub>3</sub>CN (the sample was kept in the dark during the experiments). One acetonitrile ligand exchanges with CD<sub>3</sub>CN at 21°C and complete mono-substitution occurs within a period of a week, as can be observed from the spectra in Figure 3.13. The resonances at 2.40 and 2.29 ppm correspond to the two coordinated CH<sub>3</sub>CN ligands; residual H<sub>2</sub>O from the solvent appears at 2.14 ppm and the quintet at 1.94 ppm corresponds to the residual solvent peak from CD<sub>3</sub>CN. The disappearance of the peak at 2.40 ppm and the increase of a new peak for free CH<sub>3</sub>CN at 1.96 pm indicates CH<sub>3</sub>CN ligand dissociation.

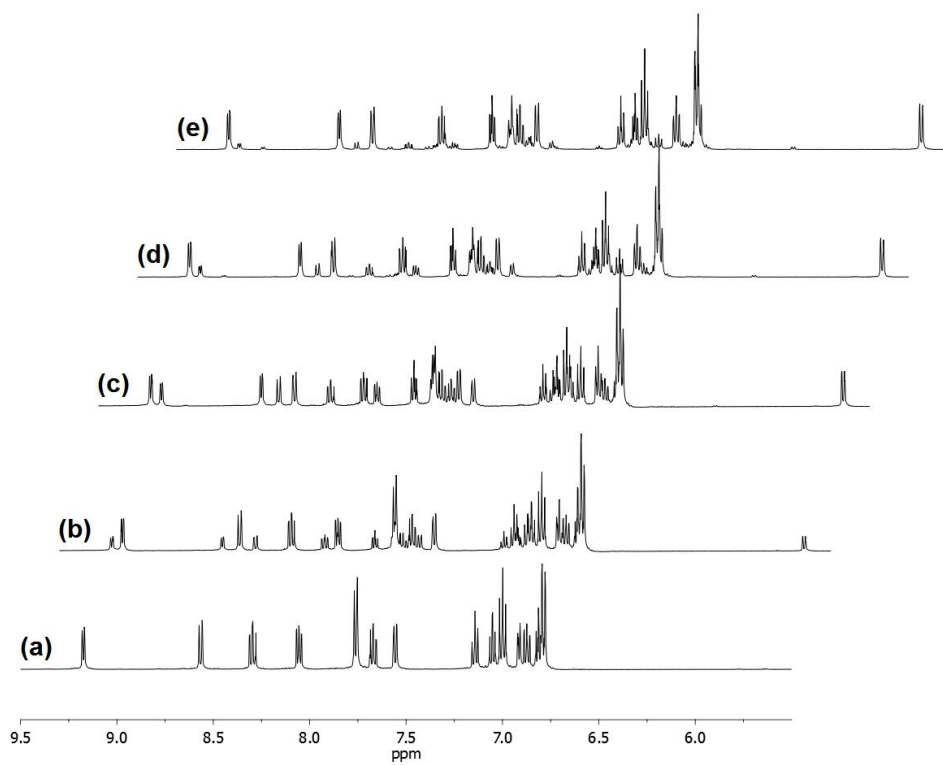


**Figure 3.13**  $^1\text{H}$  NMR (500 MHz) spectra of **6** in  $\text{CD}_3\text{CN}$  at  $21^\circ\text{C}$ : (a) 0 d, (b) 1 d, (c) 3 d, (d) 7 d.

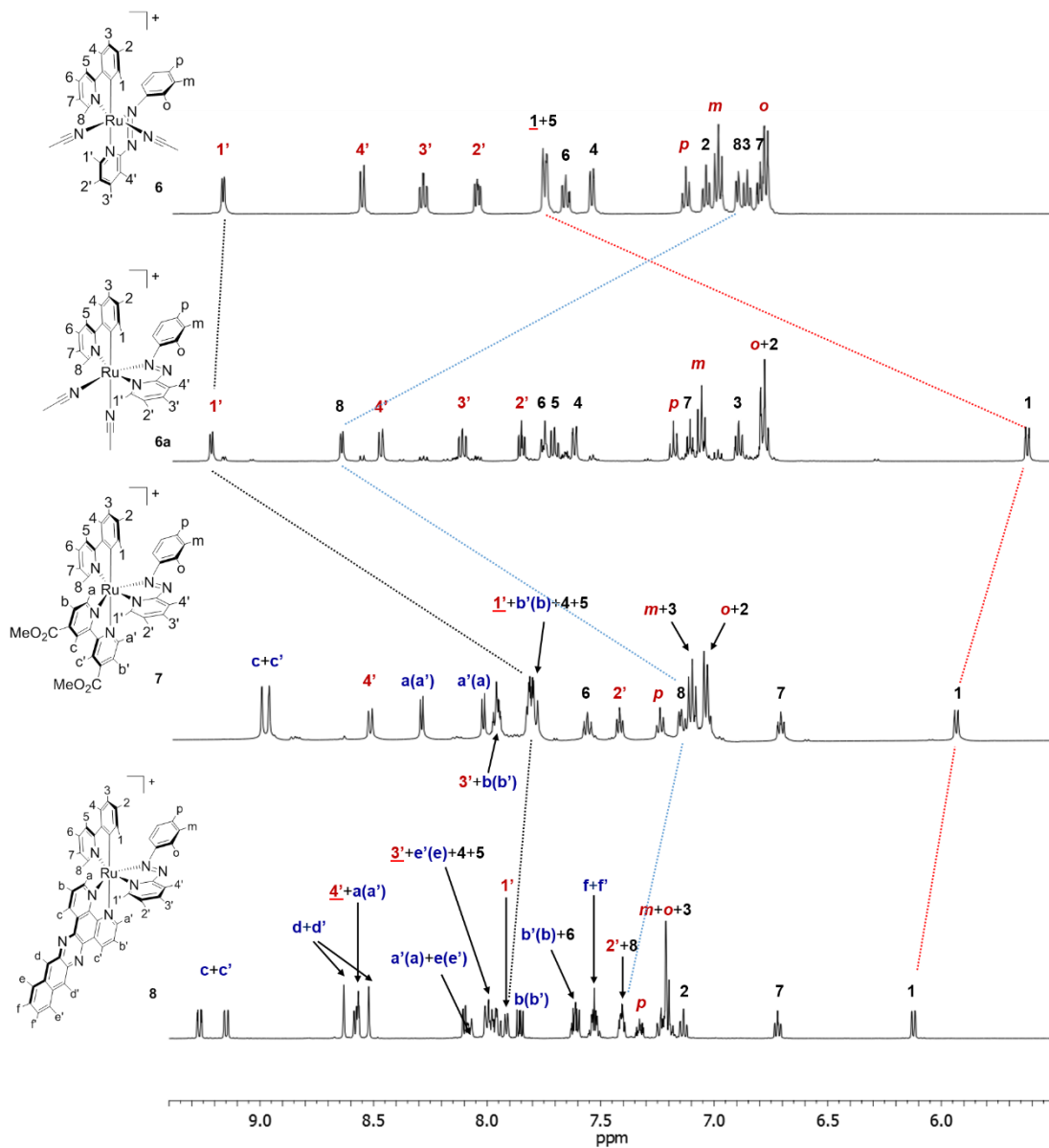
The second acetonitrile ligand does not exchange even after one month at  $21^\circ\text{C}$ . Isomerization is not observed judged by the fact that the aromatic signals remain unchanged. The labile acetonitrile ligand is likely to be *trans* to the azo group since the  $\text{Ru1-N3}$  bond ( $2.056(4)$  Å) is longer than the  $\text{Ru1-N2}$  bond ( $2.047(4)$  Å). Dissociation of the second acetonitrile ligand is observed upon heating at  $70^\circ\text{C}$  (Figure 3.14) and it is accompanied by isomerization to a new species, **6a**; nearly complete formation to this

new compound is observed after 6 h (Figure 3.14). This isomer exhibits a doublet resonance at 5.64 ppm that corresponds to the proton *ortho* to the Ru–C bond (H1, Figure 3.15). The higher field chemical shift of H1 in **6a** with respect to **6** (7.76 ppm) indicates that H1 is directed toward the pyridyl ring of pap and it appears at a higher field because of ring current effects. In addition, the proton *ortho* to the N atom (H8) in phpy is deshielded (8.65 ppm) in **6a** with respect to **6** (6.92 ppm), indicating that it must be directed toward an acetonitrile ligand. The proton *ortho* to the N atom of the pyridyl ring of pap (H1') has a similar chemical shift in both geometric isomers (**6**: 9.18 ppm; **6a**: 9.22 ppm, Figure 3.15), indicating that this proton is directed toward an acetonitrile ligand in **6a** too.

Therefore, it is proposed that **6a** is formed by dissociation of the pyridyl donor moiety of pap in **6** (facilitated by the strong donating properties of the orthometallated phenyl ring),<sup>192</sup> followed by re-coordination to the metal center in a *trans* position to the pyridyl group of phpy. The orthometallated phenyl ring in **6a** labilizes the acetonitrile ligand in *trans* position and facilitates the coordination of the dcmb (or dppn in case of **8**) ligand to afford **7**, explaining the relative position of the three bidentate ligands in this tris-heteroleptic compound. Coordination of dcmb (or dppn) shields protons H1' and H8 and they appear at higher field in **7** (H1', ~7.8 ppm; H8, 7.17 ppm) and **8** (H1', ~7.8 ppm; H8, 7.17 ppm) with respect to **6a** (H1', 9.22; H8, 8.65 ppm, respectively) due to ring current effects.



**Figure 3. 14** Aromatic region of the <sup>1</sup>H NMR (500 MHz) spectra of **6** in CD<sub>3</sub>CN at 70°C: (a) 0 h, (b) 1 h, (c) 2 h, (d) 4 h, (e) 6 h.



**Figure 3. 15** Comparison of the aromatic region of the  $^1\text{H}$  NMR spectra (500 MHz,  $\text{CD}_3\text{CN}$ ) of compounds **6**, **6a**, **7** and **8**.

## Electrochemistry

The electrochemical properties of complexes **1–8** were assessed by cyclic voltammetry in acetonitrile. The half-wave potential values ( $E_{1/2}$ ) vs Ag/AgCl were obtained from the cyclic voltammograms of **1–8**; representative voltammograms are provided in Figures 3.16–3.18. The  $E_{1/2}$  values have been referenced vs NHE for the discussion of the results (NHE = normal hydrogen electrode) as described in the Experimental Section and the values are compiled in table 3.7.

The oxidation events ( $E_{1/2} > 0$  V) are associated with the metal, whereas the reduction events ( $E_{1/2} < 0$  V) are associated with the ligands in this type of Ru(II) complexes.<sup>193,194</sup> Compounds **1–5** exhibit quasi-reversible ( $i_{pa}/i_{pc} \approx 1$ ) redox events in the +1 to –2 V interval (Figures 3.16 and 3.17). Their  $E_{1/2}$  values for the Ru<sup>3+/2+</sup> couple ( $E_{1/2}$  [Ru]<sup>3+/2+</sup>) is observed in the 0.72–0.93 V range of potential and are less positive with respect to their non-cyclometallated counterparts such as [Ru(bpy)<sub>3</sub>]<sup>2+</sup>, which has a  $E_{1/2}$  [Ru]<sup>3+/2+</sup> = 1.54 V.<sup>159</sup> Such a shift to lower potentials is ascribed to the strong donating ability and anionic character of phpy; this metal-ligand interaction destabilizes the metal-based HOMOs and facilitates the oxidation of the metal.

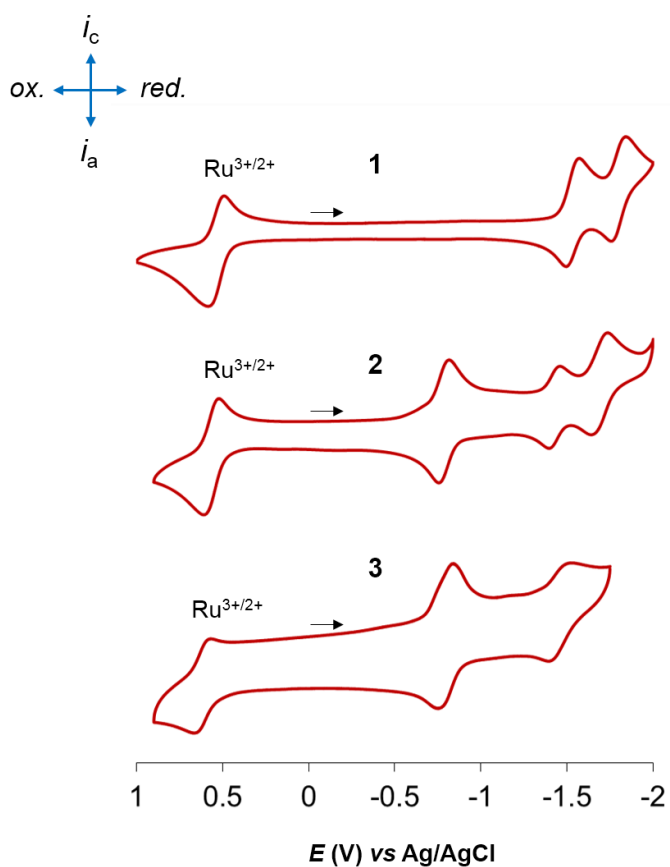
In the case of compounds **2** and **3**, the first ligand-based reduction wave ( $E_{1/2,red1}$  = –0.61 V) is assigned to the dppn ligand, whereas the first reduction event in **1** corresponds to bpy ( $E_{1/2,red1}$  = –1.35 V). The dppn ligand is easier to reduce than bpy because of the more delocalized  $\pi$ -system of the former. Similar redox behavior has been observed in [Ru(bpy)<sub>2</sub>(dppn)]<sup>2+</sup> ( $E_{1/2,red1}$  = –0.46 V; dppn-based reduction) and

[Ru(bpy)<sub>3</sub>]<sup>2+</sup> ( $E_{1/2,red1} = -1.07$  V; bpy-based reduction).<sup>159</sup> Due to the strong donating ability and negative charge of phpy, there is greater  $\pi$ -backbonding into the pyridyl rings of the dppn/bpy ligands in the cyclometallated compounds **1–3** with respect to their non-cyclometallated counterparts of formula [Ru(bpy)<sub>2</sub>(L)]<sup>2+</sup> (L = bpy, dppn). As a consequence, the bpy/dppn ligands are more difficult to reduce and  $E_{1/2,red1}$  are more negative in **1–3** with respect to [Ru(bpy)<sub>2</sub>(L)]<sup>2+</sup> (L = bpy, dppn). The  $E_{1/2}$  [Ru]<sup>3+/2+</sup> becomes more positive in the order **1** < **2** < **3**, indicating the increasing stabilization of the metal based HOMOs by  $\pi$ -backbonding with the number of dppn ligands.

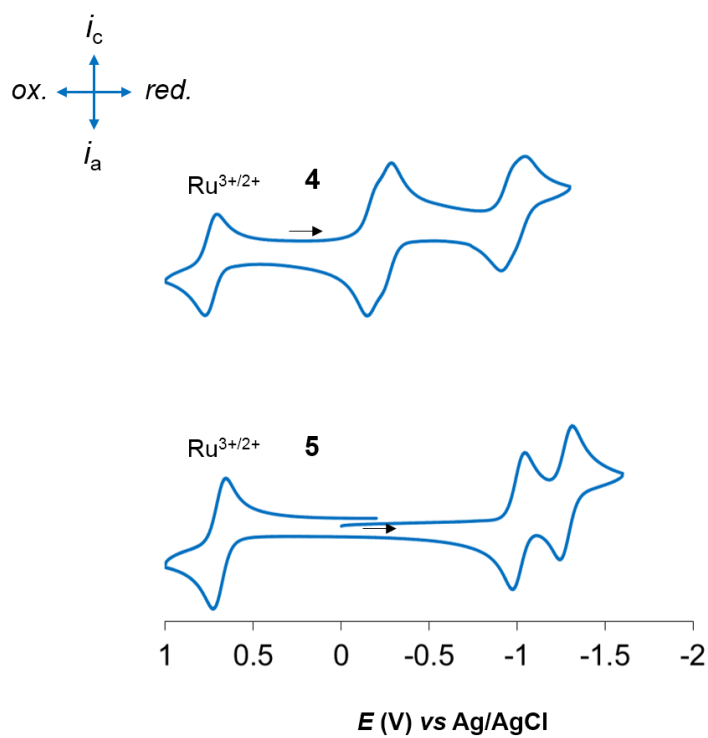
**Table 3. 7** Half wave redox potentials ( $E_{1/2}$ ) of **1–8** recorded in acetonitrile.

Compound	$E_{1/2}$ (V) vs NHE ( $\Delta E = E_{pa} - E_{pc}$ in mV)			
	$E_{1/2}$ [Ru <sup>3+/2+</sup> ]	$E_{1/2,red1}$	$E_{1/2,red2}$	$E_{1/2,red3}$
[Ru(phpy)(bpy) <sub>2</sub> ][PF <sub>6</sub> ] ( <b>1</b> )	0.72 (94)	-1.35 (77)	-1.62 (83)	-
[Ru(phpy)(bpy)(dppn)][PF <sub>6</sub> ] ( <b>2</b> )	0.76 (85)	-0.61 (84)	-1.23 (63)	-1.52 (69)
[Ru(phpy)(dppn) <sub>2</sub> ][PF <sub>6</sub> ] ( <b>3</b> )	0.80 (90)	-0.61 (95)	-1.27 (133)	-
[Ru(phpy)(phendione) <sub>2</sub> ][PF <sub>6</sub> ] ( <b>4</b> )	0.93 (60)	-0.02 (135)	-0.78 (134)	-
[Ru(phpy)(biq) <sub>2</sub> ][PF <sub>6</sub> ] ( <b>5</b> )	0.89 (75)	-0.82 (65)	-1.09 (80)	-
[Ru(phpy)(pap)(NCCH <sub>3</sub> ) <sub>2</sub> ][PF <sub>6</sub> ] ( <b>6</b> )	1.14 (80)	-0.61 (70)	-1.33 (65)	-
[Ru(phpy)(pap)(dcmb)][PF <sub>6</sub> ] ( <b>7</b> )	1.31 (86)	-0.59 (60)	-1.01 (70)	-1.51 (85)
[Ru(phpy)(pap)(dppn)][PF <sub>6</sub> ] ( <b>8</b> )	1.24 (70)	-0.55 (65)	-0.76 (60)	-1.28 (65)





**Figure 3. 16** Cyclic voltammograms (vs Ag/AgCl) of compounds **1–3** in acetonitrile (0.1 M  $[\text{nBu}_4\text{N}][\text{PF}_6]$ , 100 mV/s scan rate).  $i_c$  = cathodic current,  $i_a$  = anodic current, ox. = oxidation, red. = reduction. The black arrows indicate the direction of the scan.



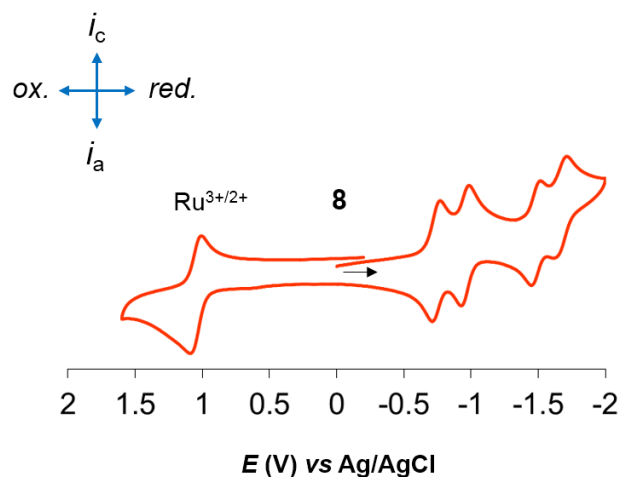
**Figure 3. 17** Cyclic voltammograms (vs Ag/AgCl) of compounds **4–5** in acetonitrile (0.1 M [<sup>n</sup>Bu<sub>4</sub>N][PF<sub>6</sub>], 100 mV/s scan rate).  $i_c$  = cathodic current,  $i_a$  = anodic current, ox. = oxidation, red. = reduction. The black arrows indicate the direction of the scan.

The  $E_{1/2}$  [ $\text{Ru}^{3+/2+}$ ] of **4** occurs at 0.93 V and it is shifted to more positive potentials with respect to those of **1–3**. The strong electron-withdrawing properties of the phendione ligands stabilize the Ru-based HOMOs of **4**, explaining its more positive  $E_{1/2}$  [ $\text{Ru}^{3+/2+}$ ] than **1–3**. This complex also exhibits two phendione ligand-based reduction events at  $E_{1/2} = -0.02$  and  $-0.78$  V, where  $2e^-$  ( $\Delta E = E_{\text{pa}} - E_{\text{pc}} \sim 135$  mV) are transferred on each redox event, as also reported for  $[\text{Ru}(\text{bpy})(\text{phendione})_2]^{2+}$  ( $E_{1/2} = +0.08$  and  $-0.65$  V).<sup>195</sup>

In the case of **5**, the  $E_{1/2}$  [ $\text{Ru}^{3+/2+}$ ] is 0.89 V and is also shifted to more positive potentials with respect to those of **1–3**. The longer Ru–C bond in **5** with respect to those reported for related compounds, such as **1**, decreases the destabilization of Ru-based HOMOs and explains its more positive  $E_{1/2}$  [ $\text{Ru}^{3+/2+}$ ]. Additionally, compound **5** shows two biq ligand-based reduction waves at  $E_{1/2} = -0.82$  and  $-1.09$  V.

Compound **6** displays a  $E_{1/2}$  [ $\text{Ru}^{3+/2+}$ ] = 1.14 V; this value is shifted to more positive potentials with respect to the related compounds of formula  $[\text{Ru}(\text{phpy})(\text{L})(\text{NCCH}_3)_2]^+$ , where L = bpy (**9**) or phen,  $E_{1/2}$  [ $\text{Ru}^{3+/2+}$ ]  $\sim 0.80$  V,<sup>182</sup> due to the stabilization of the metal-based orbitals of **6** by  $\pi$ -backbonding into the low-lying  $\pi^*$  MOs of pap. The greater  $\pi$ -acceptor ability of pap with respect to bpy is shown in the  $E_{1/2, \text{red1}}$  values of **6**, which are less negative for pap ( $E_{1/2} = -0.61$  and  $-1.33$  V).<sup>196</sup> The  $E_{1/2}$  [ $\text{Ru}^{3+/2+}$ ] of **7** (1.31 V) and **8** (1.24 V) are anodically shifted with respect to that of **6** since dcmb in **7** and dppn in **8** are better  $\pi$ -acceptors than acetonitrile and stabilize the Ru-based HOMOs to a greater extent. The tris-heteroleptic compound **7** possesses three reversible ligand reductions tentatively assigned to pap ( $E_{1/2} = -0.59$  and  $-1.01$  V)<sup>196</sup> and

dcmb ( $E_{1/2} = -1.51$  V). The  $E_{1/2, \text{red1}}$  ( $\text{pap}^{0/1-}$ ) of **6** and **7** ( $\sim -0.60$  V) is similar to the  $E_{1/2, \text{red1}}$  ( $\text{dppn}^{0/1-}$ ) of **2** and **3** ( $-0.61$  V), suggesting that the lowest-lying  $\pi^*$  MOs of pap and dppn have similar energy (also reproduced by DFT calculations, see below). Interestingly, compound **8** exhibits two ligand-based reduction events at  $E_{1/2} = -0.55$  and  $-0.75$  V attributed to the reduction of dppn and pap ligands (Figure 3.18), respectively (see DFT studies for an explanation of the assignment of these reduction events).



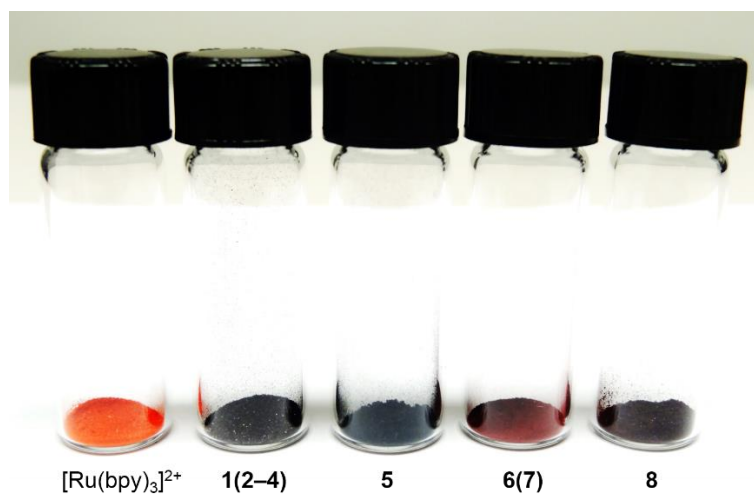
**Figure 3. 18** Cyclic voltammogram (vs Ag/AgCl) of compound **8** in acetonitrile (0.1 M [ $^n\text{Bu}_4\text{N}$ ][PF<sub>6</sub>], 100 mV/s scan rate).  $i_c$  = cathodic current,  $i_a$  = anodic current, ox. = oxidation, red. = reduction. The black arrows indicate the direction of the scan.

## Electronic Absorption Spectroscopy Studies

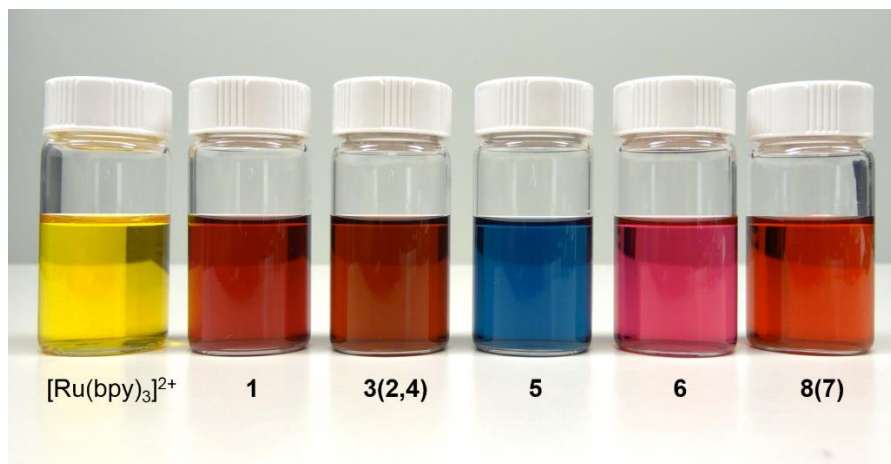
The absorption maxima ( $\lambda_{\text{abs}}$ ) and molar extinction coefficients ( $\epsilon$ ) of **1–8** in acetonitrile are listed in Table 3.8. Pictures of selected compounds in the solid state (Figure 3.19) and acetonitrile solution (Figure 3.20) are shown below and clearly demonstrates that the electronic structure of Ru(II) complexes can be modulated by the choice of ligands. The eight compounds exhibit strong singlet metal-to-ligand charge transfer ( $^1\text{MLCT}$ ) transitions in the visible region explaining why cyclometallated compounds have emerged as great candidates for light harvesting units in dye-sensitized solar cells.<sup>194,193</sup>

**Table 3. 8** Absorption maxima of **1–8** recorded in acetonitrile.

Compound	$\lambda_{\text{max}}$ , nm ( $\epsilon \times 10^4 \text{ M}^{-1} \text{ cm}^{-1}$ )
<b>1</b>	546 (0.74), 492 (0.65), 404 (0.82), 369 (0.89), 293 (4.64), 249 (2.88)
<b>2</b>	546 (1.10), 485 (1.20), 411 (1.87), 391 (1.60), 320 (7.44), 298 (6.91), 248 (5.54)
<b>3</b>	525 (1.63), 460 (1.79), 412 (2.70), 391 (2.09), 323 (14.3), 247 (7.48)
<b>4</b>	530 (1.03), 470 (0.90), 428 (0.99), 372 (0.59), 292 (2.68), 251 (5.73)
<b>5</b>	640 (1.05), 544 (0.44), 406 (0.93), 351 (4.47), 266 (7.80)
<b>6</b>	523 (0.78), 335 (1.13), 281 (1.89), 247 (2.22)
<b>7</b>	527 (0.97), 470 (0.66), 315 (2.95), 282 (2.41)
<b>8</b>	517 (1.08), 410 (1.71), 388 (1.67), 322 (9.00), 284 (4.45), 243 (5.66)

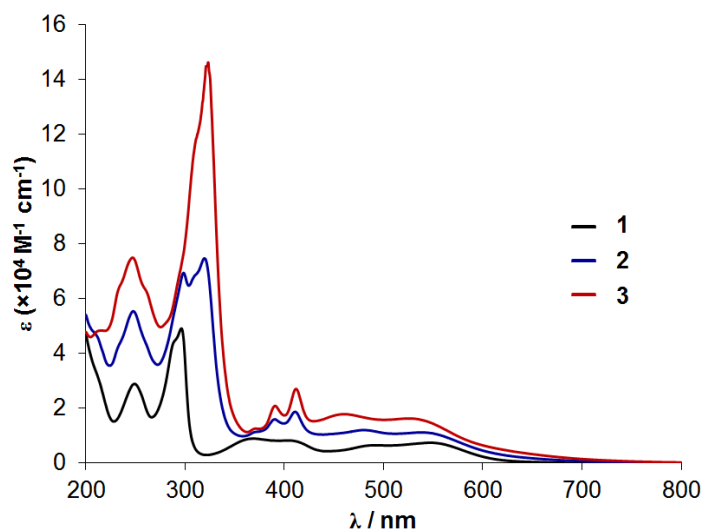


**Figure 3.19** Solid state colors of selected Ru cyclometallated compounds. Compounds 2–4 display the same color of 1 in the solid state; compound 7 displays the same color of 6 in the solid state.



**Figure 3.20** Solution colors of selected Ru cyclometallated compounds in acetonitrile (100  $\mu\text{M}$ ). Compounds 2 and 4 display the same color of 3 in solution; compound 7 displays the same color of 8 in solution.

The electronic absorption spectra of **1–3** are displayed in Figure 3.21 and differ significantly from that of related non-cyclometallated Ru polypyridyl compounds (*e.g.*  $[\text{Ru}(\text{bpy})_2(\text{L})]^{2+}$ , L = bpy, dppn). In particular, **1–3** exhibit substantial bathochromic shifts of the  $^1\text{MLCT}$  transitions: the  $^1\text{MLCT}$  maxima of **1–3** (546, 546 and 525 nm, respectively) are bathochromically shifted by 75–102 nm with respect to  $[\text{Ru}(\text{bpy})_2(\text{L})]^{2+}$  (L = bpy,  $^1\text{MLCT}$  = 450 nm; L = dppn,  $^1\text{MLCT}$  = 444 nm).<sup>159,197</sup> The  $^1\text{MLCT}$  transitions of **1** at 492 and 546 nm have been previously assigned as  $\text{Ru}(4d\pi) \rightarrow \text{bpy}(\pi^*)$ , while those at higher energies in the 350–430 nm range arise from  $\text{Ru}(4d\pi) \rightarrow \text{phpy}(\pi^*)$  transitions.<sup>179</sup> Thus, the lower energy  $^1\text{MLCT}$  bands observed for **2** and **3** between 450 and 600 nm can be assigned to  $\text{Ru}(4d\pi) \rightarrow \text{bpy/dppn}(\pi^*)$  transitions whereas the transitions corresponding to  $\text{Ru}(4d\pi) \rightarrow \text{phpy}(\pi^*)$  are likely obscured by the  $^1\pi\pi^*$  dppn ligand-centered (LC) transitions in the 320–420 nm range in both compounds. It can be also noticed that the  $^1\text{MLCT}$  peaks of **1–3** possess absorption tails that extend beyond 750 nm, a feature that is not observed in  $[\text{Ru}(\text{bpy})_2(\text{L})]^{2+}$  (L = bpy, dppn).<sup>159,197</sup>

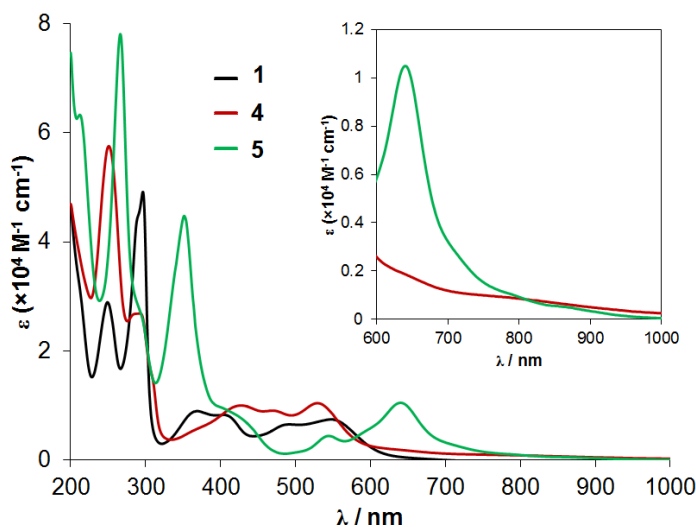


**Figure 3.21** Electronic absorption spectra of **1–3** in acetonitrile.

The  $^1\pi\pi^*$  dppn ligand-centered (LC) transitions of **2** (411, 391 and 320 nm) and **3** (412, 391 and 323 nm) do not shift with respect to  $[\text{Ru}(\text{bpy})_2(\text{dppn})]^{2+}$  (414, 390 and 320 nm) or the free dppn ligand (412, 390 and 313 nm), consistent with the effect of Ru-ppy bonding destabilizing “ $t_{2g}$ -type” occupied metal orbitals without significant perturbations to the energies of the  $\pi$  and  $\pi^*$  orbitals of the other ligands in the complex. The intensity of the dppn-centered transition at  $\sim 410$  nm is generally commensurate with the number of dppn ligands present in the complex. For example, the intensity of this transition is increased in **3** ( $2.70 \times 10^3 \text{ M}^{-1} \text{ cm}^{-1}$ ) as compared to **2** ( $1.87 \times 10^3 \text{ M}^{-1} \text{ cm}^{-1}$ ). Similarly, the molar extinction coefficients for **3** are higher than those of **2** in the ultraviolet (UV) regions.



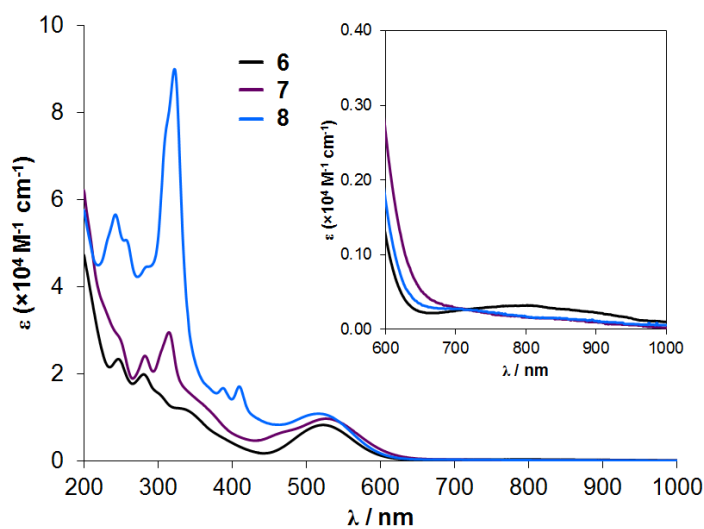
The electronic absorption spectra of **4** and **5** are shown in Figure 3.22. Compound **4** displays two absorption maxima at 530 and 470 nm that are assigned as  $^1\text{MLCT}$  transitions from the Ru center to the pyridyl moiety of phendione ( $\text{Ru}(4d\pi)\rightarrow\text{py}_{\text{phendione}}(\pi^*)$ ) and are bathochromically shifted with respect to the non-cyclometallated analog  $[\text{Ru}(\text{bpy})(\text{phendione})_2]^{2+}$  ( $^1\text{MLCT}$  at 432 and 352 nm).<sup>195</sup> Compound **4** also possesses a higher energy maxima at 428 that may correspond to a  $\text{Ru}(4d\pi)\rightarrow\text{phpy}(\pi^*)$   $^1\text{MLCT}$  transition, as also observed in **1**. Interestingly, it exhibits broad absorption (albeit weak) in the red and near-IR region ascribed to  $^1\text{MLCT}$  transitions to the dione moiety of phendione. In the UV region, **4** exhibits a maximum at 292 nm corresponding to a phendione-based  $^1\pi\pi^*$  LC transition, as also reported for  $[\text{Ru}(\text{bpy})(\text{phendione})_2]^{2+}$  (288 nm).<sup>195</sup> Compound **5** has two  $\text{Ru}(4d\pi)\rightarrow\text{biq}(\pi^*)$   $^1\text{MLCT}$  transitions at 640 and 544 nm that are bathochromically shifted with respect to  $[\text{Ru}(\text{phen})(\text{biq})_2]^{2+}$ .<sup>189</sup> An additional  $^1\text{MLCT}$  band is observed at 406 nm that is likely to correspond to  $\text{Ru}(4d\pi)\rightarrow\text{phpy}(\pi^*)$  transitions. An intense  $^1\pi\pi^*$  biq LC transition at 351 nm is present in the UV region.



**Figure 3. 22** Electronic absorption spectra of **1**, **4** and **5**. Inset: red and near-IR absorption of **4** and **5**.

Compound **6** exhibits a  $^1\text{MLCT}$  transition at 523 nm (Figure 3.23) assigned as  $\text{Ru}(4d\pi) \rightarrow \text{azo}(\pi^*)$  and it is bathochromically shifted by  $\sim 30$  nm with respect to  $[\text{Ru}(\text{phpy})(\text{L})(\text{NCCH}_3)_2]^+$  ( $\text{L} = \text{bpy}$  (**9**), phen), reflecting the lower energy of the  $\text{azo}(\pi^*)$  MOs with respect to bpy or phen.<sup>196</sup> The  $\text{Ru}(4d\pi) \rightarrow \text{azo}(\pi^*)$   $^1\text{MLCT}$  transition in **7** occurs at 527 and an additional  $\text{Ru}(4d\pi) \rightarrow \text{dcmb}(\pi^*)$   $^1\text{MLCT}$  band is observed at 470 nm (Figure 3.23). In the case of **8**, the  $^1\text{MLCT}$  band at 517 nm is likely to correspond to a combination of  $\text{Ru}(4d\pi) \rightarrow \text{pap}(\pi^*)$  and  $\text{Ru}(4d\pi) \rightarrow \text{dppn}(\pi^*)$  transition, whereas its  $\text{Ru}(4d\pi) \rightarrow \text{bpy}(\pi^*)$   $^1\text{MLCT}$  transition may be obscured by the  $^1\pi\pi^*$  dppn LC transitions at 410 and 388 nm (Figure 3.23). Absorption in the near-IR region at  $\sim 810$  nm is also

observed for **6–8** and it is tentatively assigned as  $\text{Ru}(4d\pi) \rightarrow \text{azo}(\pi^*)$   $^1\text{MLCT}$  transitions. The bpy, dppn and pap  $^1\pi\pi^*$  LC transitions are observed in the UV region.

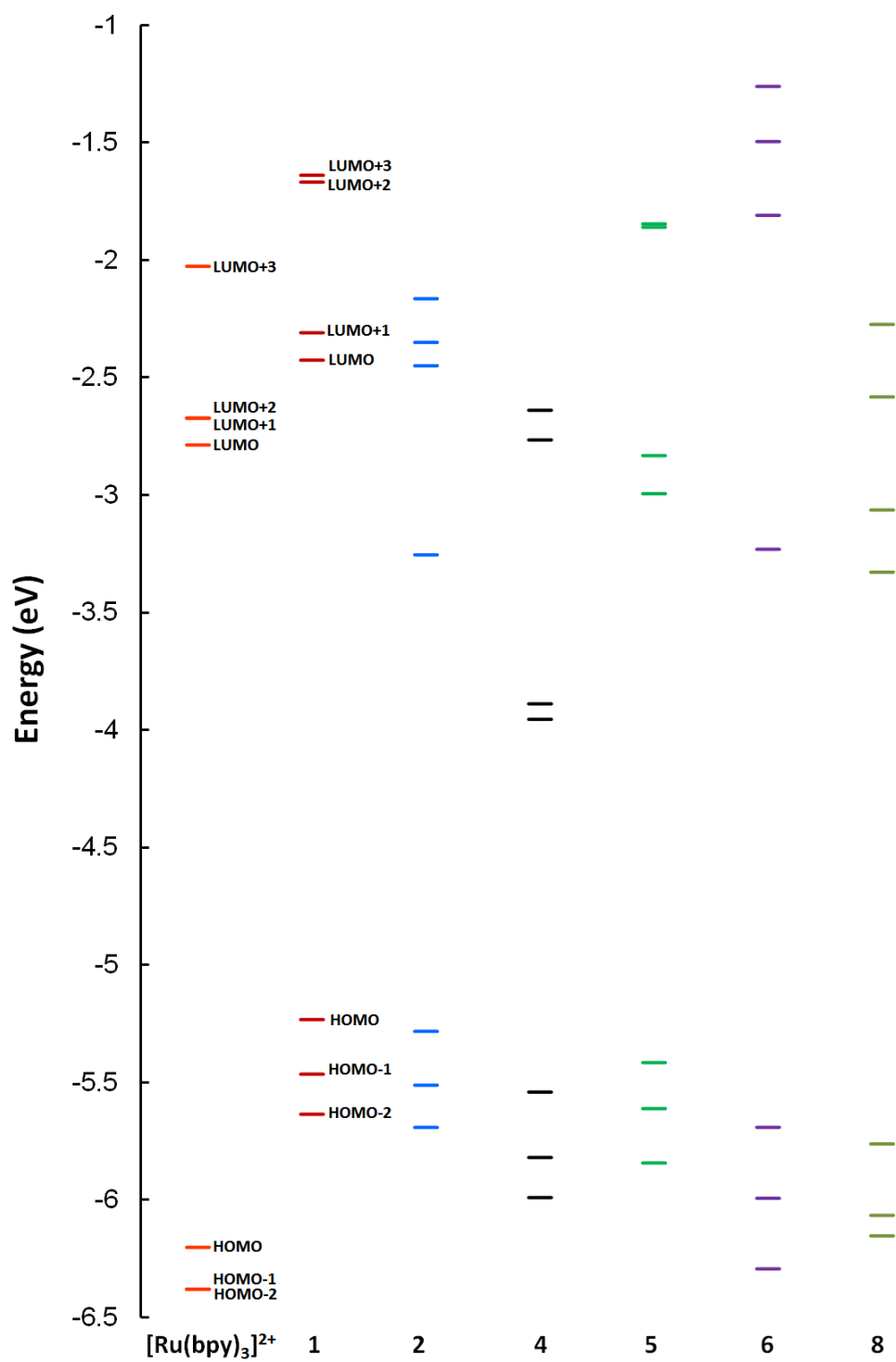


**Figure 3.23** Electronic absorption spectra of **6–8**. Inset: red and near-IR absorption of the three complexes.

### *Electronic Structure Calculations*

Density Functional Theory (DFT) calculations were undertaken on **1**, **2**, **4–6** and **8** and the results were compared to those for  $[\text{Ru}(\text{bpy})_3]^{2+}$  to gain further insight into the electrochemical and optical properties of the cyclometallated complexes. The MO diagrams (Figure 3.24), energies of the frontier molecular orbitals (MOs) and the contributions from the Ru and the ligands (Tables 3.9 and 3.10), and the electron densities of selected MOs (Tables 3.11–3.14) are shown below.

The HOMO, HOMO-1, and HOMO-2 of **1**, **2**, **4–6** and **8** are primarily localized on the metal center (Tables 3.11 and 3.13) and represent the occupied  $\text{Ru}(d\pi)$  “ $t_{2g}$ -type” orbitals in a pseudo-octahedral environment. However, there is significant contribution of the orthometallated phpy ligand (24 to 48%) to the HOMO. The energies of these three HOMOs are greater than in  $[\text{Ru}(\text{bpy})_3]^{2+}$  (Figure 3.24), in agreement with the less positive oxidation potentials ( $E_{1/2} [\text{Ru}^{3+/2+}]$ ) and bathochromically shifted  $^1\text{MLCT}$  transitions of the cyclometallated compounds with respect to  $[\text{Ru}(\text{bpy})_3]^{2+}$ .<sup>179,198</sup> The  $\text{Ru}(d\pi)$  HOMOs in the cyclometallated compounds are destabilized with respect to  $[\text{Ru}(\text{bpy})_3]^{2+}$  as a consequence of the electronic repulsion between the anionic phpy ligand and these filled d orbitals. In addition, the strong Ru-phpy interaction increases the energy of the  $\text{Ru}(d\sigma)$  “ $e_g^*$ -type” orbitals with respect to  $[\text{Ru}(\text{bpy})_3]^{2+}$  (see Figure 3.25 for a representative example).



**Figure 3. 24** Molecular orbital diagrams (HOMO-2 to LUMO+3) of **1**, **2**, **4–6** and **8**.

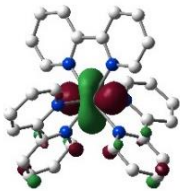
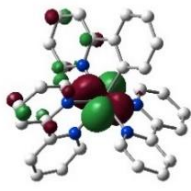
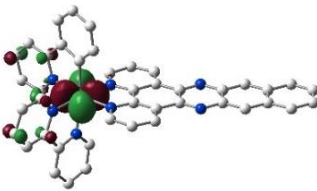
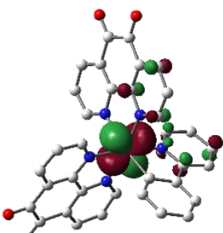
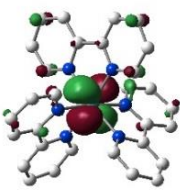
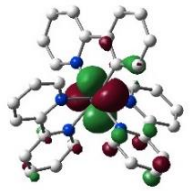
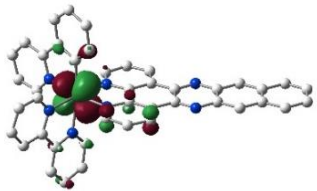
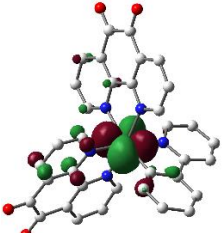

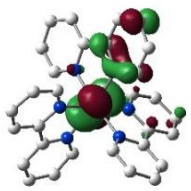
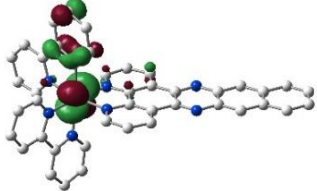
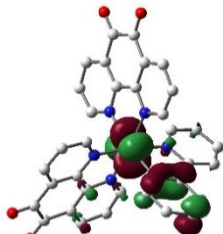
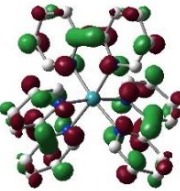
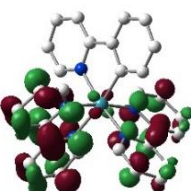
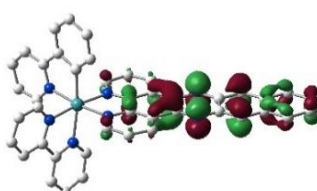
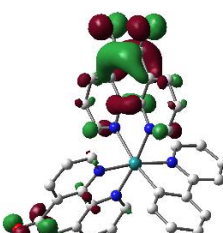
**Table 3. 9** Energies ( $E_{MO}$ ) and percent contributions of selected MOs of  $[Ru(bpy)_3]^{2+}$ , **1** and **2** and **4**.

MO	$[Ru(bpy)_3]^{2+}$			$[Ru(phpy)(bpy)_2]^+$ ( <b>1</b> )				$[Ru(phpy)(bpy)(dppn)]^+$ ( <b>2</b> )					$[Ru(phpy)(phendione)_2]^+$ ( <b>4</b> )			
	% Contribution		$E_{MO}$ (eV)	% Contribution			$E_{MO}$ (eV)	% Contribution`				$E_{MO}$ (eV)	% Contribution			$E_{MO}$ (eV)
	Ru	bpy		Ru	phpy	bpy		Ru	phpy	bpy	dppn		Ru	phpy	phendione	
LUMO+5	3	97	-1.7024	7	8	85	-1.2896	3	76	18	3	-1.5932	1	0	99	-2.1908
LUMO+4	3	97	-1.7032	2	21	77	-1.3927	2	24	69	5	-1.6705	3	0	97	-2.2221
LUMO+3	2	98	-2.0264	7	67	26	-1.6392	11	4	26	59	-2.1641	11	0	89	-2.6390
LUMO+2	7	93	-2.6719	4	33	63	-1.6683	4	3	5	89	-2.3503	4	1	95	-2.7655
LUMO+1	6	94	-2.6730	6	14	80	-2.3089	3	3	63	31	-2.4496	0	0	100	-3.8885
<b>LUMO</b>	<b>2</b>	<b>98</b>	<b>-2.7872</b>	<b>2</b>	<b>3</b>	<b>95</b>	<b>-2.4259</b>	<b>0</b>	<b>0</b>	<b>1</b>	<b>99</b>	<b>-3.2542</b>	<b>0</b>	<b>0</b>	<b>100</b>	<b>-3.9544</b>
<b>HOMO</b>	<b>72</b>	<b>28</b>	<b>-6.2018</b>	<b>56</b>	<b>26</b>	<b>18</b>	<b>-5.2325</b>	<b>43</b>	<b>24</b>	<b>9</b>	<b>24</b>	<b>-5.2896</b>	<b>62</b>	<b>30</b>	<b>8</b>	<b>-5.5408</b>
HOMO-1	69	31	-6.3792	60	11	29	-5.4649	70	10	11	9	-5.5114	75	7	18	-5.8192
HOMO-2	69	31	-6.3806	74	9	17	-5.6350	65	15	13	7	-5.6913	77	10	13	-5.9898

**Table 3. 10** Energies ( $E_{MO}$ ) and percent contributions of selected MOs of **4–6** and **8**.

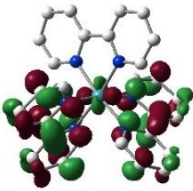
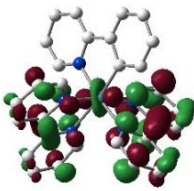
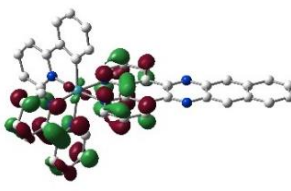
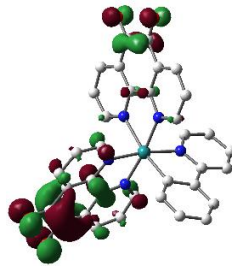
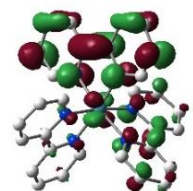
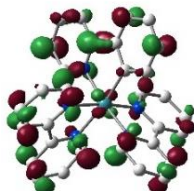
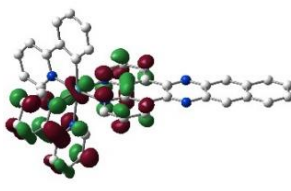
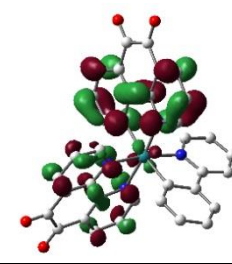
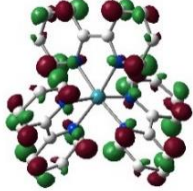
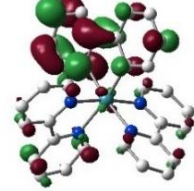
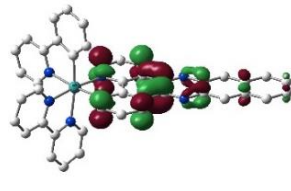
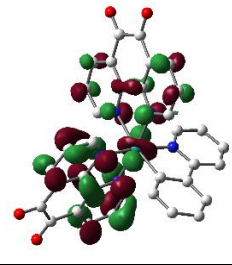
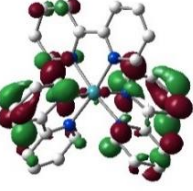
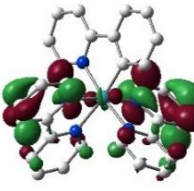
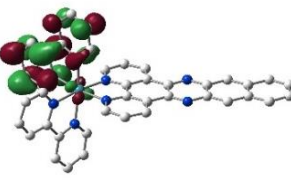
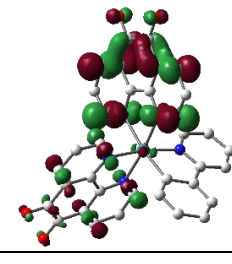
MO	[Ru(phpy)(biq) <sub>2</sub> ] <sup>+</sup> ( <b>5</b> )				[Ru(phpy)(pap)(NCCH <sub>3</sub> ) <sub>2</sub> ] <sup>+</sup> ( <b>6</b> )					[Ru(phpy)(pap)(dppn)] <sup>+</sup> ( <b>8</b> )				
	% Contribution			$E_{MO}$ (eV)	% Contribution				$E_{MO}$ (eV)	% Contribution				$E_{MO}$ (eV)
	Ru	phpy	biq		Ru	phpy	pap	NCCH <sub>3</sub>		Ru	phpy	pap	dppn	
LUMO+5	2	15	83	-1.5756	5	12	83	0	-0.6743	3	9	46	43	-1.5153
LUMO+4	5	68	27	-1.7241	6	0	94	0	-0.7099	5	95	0	0	-1.8034
LUMO+3	2	9	89	-1.8458	3	75	22	0	-1.2610	5	0	0	95	-2.2741
LUMO+2	3	1	96	-1.8599	4	32	64	0	-1.4956	6	0	7	87	-2.5825
LUMO+1	9	5	86	-2.8319	6	79	15	0	-1.8094	12	0	77	11	-3.0637
<b>LUMO</b>	<b>8</b>	<b>1</b>	<b>91</b>	<b>-2.9941</b>	<b>11</b>	<b>5</b>	<b>82</b>	<b>0</b>	<b>-3.2308</b>	<b>0</b>	<b>0</b>	<b>0</b>	<b>100</b>	<b>-3.3281</b>
<b>HOMO</b>	<b>63</b>	<b>26</b>	<b>11</b>	<b>-5.4154</b>	<b>42</b>	<b>48</b>	<b>6</b>	<b>4</b>	<b>-5.6910</b>	<b>56</b>	<b>28</b>	<b>7</b>	<b>9</b>	<b>-5.7614</b>
HOMO-1	58	16	26	-5.6110	66	10	15	9	-5.9931	62	18	11	9	-6.0655
HOMO-2	67	6	27	-5.8429	56	22	18	5	-6.2930	47	23	19	11	-6.1527

**Table 3. 11** Frontier orbitals (HOMO-2 to LUMO) for  $[\text{Ru}(\text{bpy})_3]^{2+}$ , **1**, **2** and **4** (isovalue = 0.04).

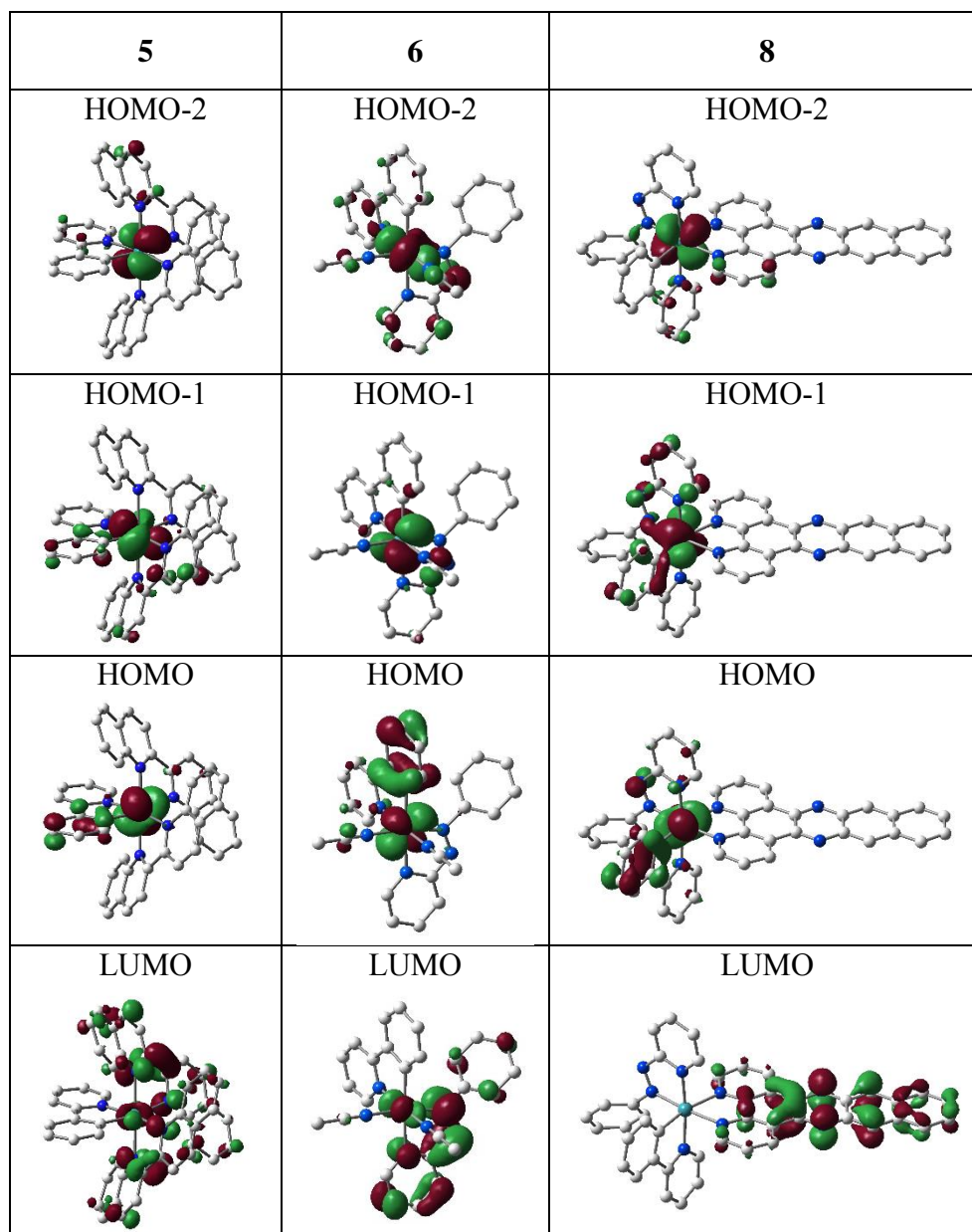
$[\text{Ru}(\text{bpy})_3]^{2+}$	<b>1</b>	<b>2</b>	<b>4</b>
HOMO-2	HOMO-2	HOMO-2	HOMO-2
			
HOMO-1	HOMO-1	HOMO-1	HOMO-1
			
HOMO	HOMO	HOMO	HOMO
			
LUMO	LUMO	LUMO	LUMO
			



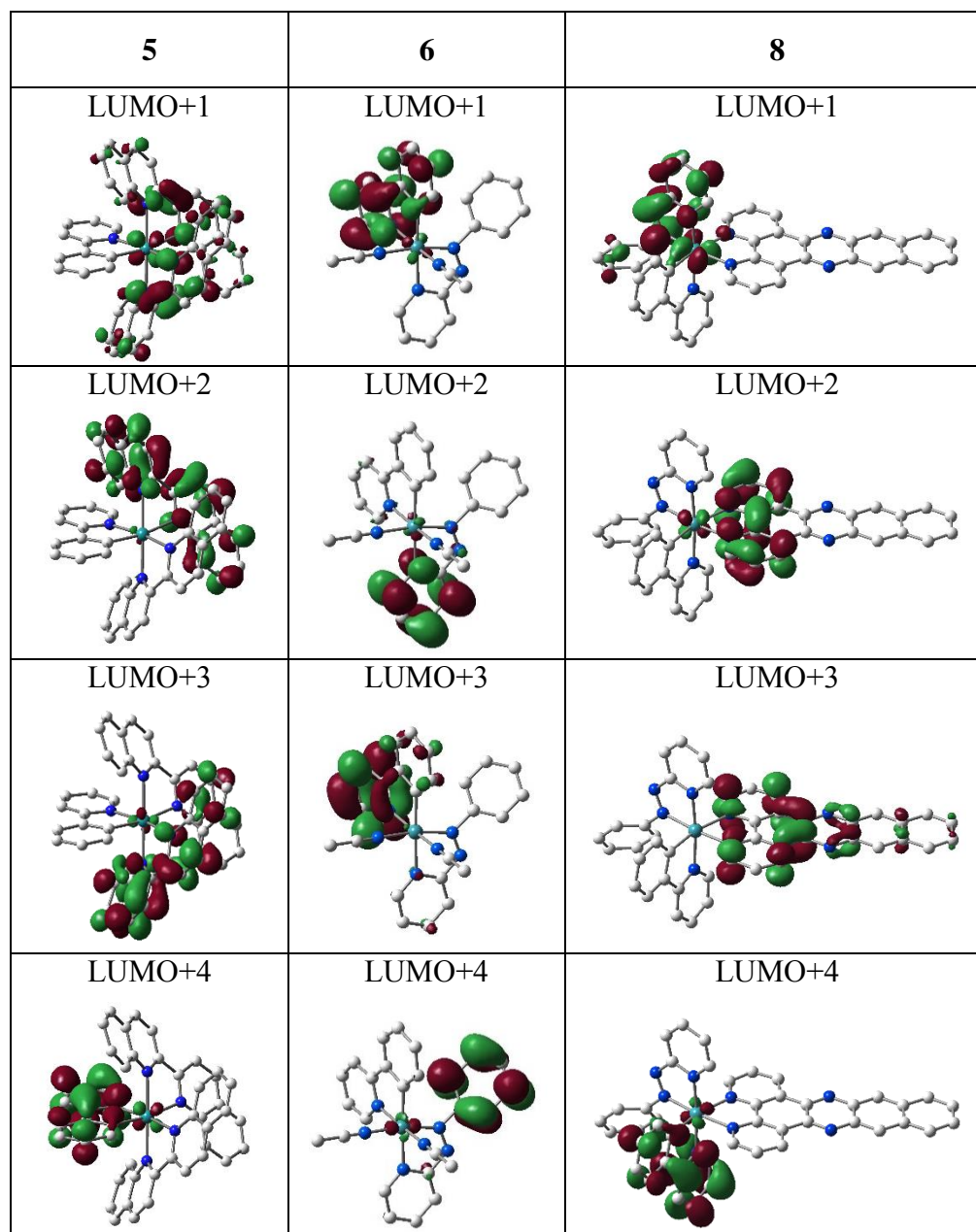
**Table 3. 12** Frontier orbitals (LUMO+1 to LUMO+4) for  $[\text{Ru}(\text{bpy})_3]^{2+}$ , **1**, **2** and **4** (isovalue = 0.04).

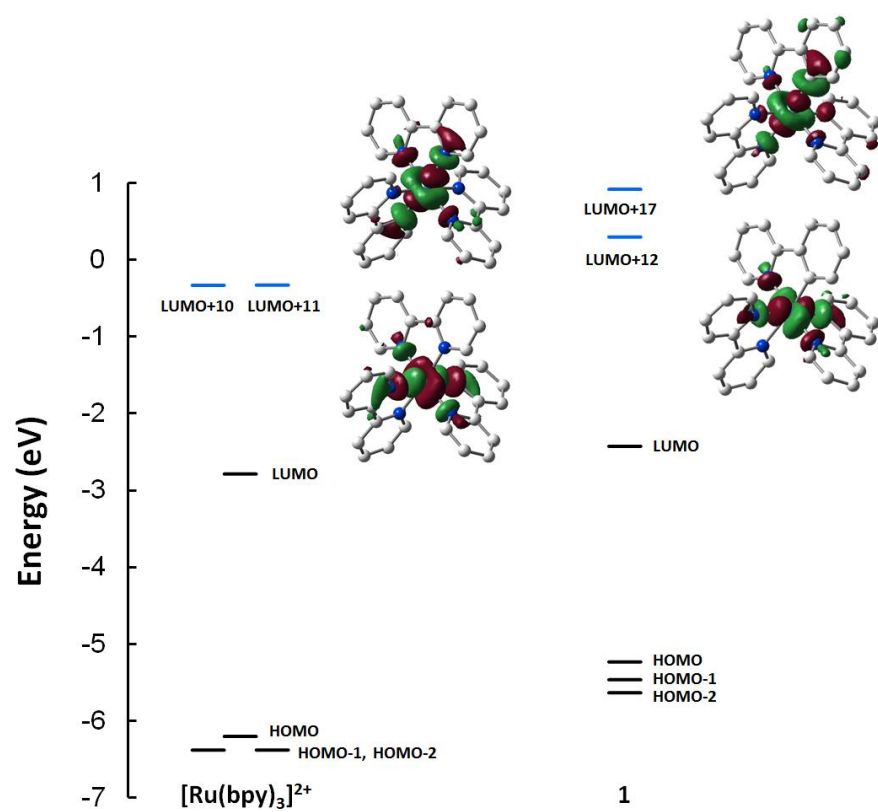
$[\text{Ru}(\text{bpy})_3]^{2+}$	<b>1</b>	<b>2</b>	<b>4</b>
LUMO+1 	LUMO+1 	LUMO+1 	LUMO+1 
LUMO+2 	LUMO+2 	LUMO+2 	LUMO+2 
LUMO+3 	LUMO+3 	LUMO+3 	LUMO+3 
LUMO+4 	LUMO+4 	LUMO+4 	LUMO+4 

**Table 3. 13** Frontier orbitals (HOMO-2 to LUMO) for **5**, **6** and **8** (isovalue = 0.04).



**Table 3. 14** Frontier orbitals (LUMO+1 to LUMO+4) for **5**, **6** and **8** (isovalue = 0.04).





**Figure 3. 25** Ru( $d\sigma$ ) “ $e_g^*$ -type” MOs of  $[\text{Ru}(\text{bpy})_3]^{2+}$  and **1** (isovalue = 0.04)

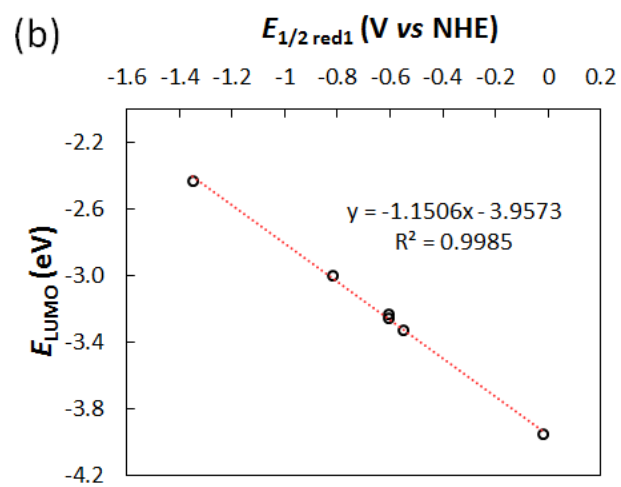
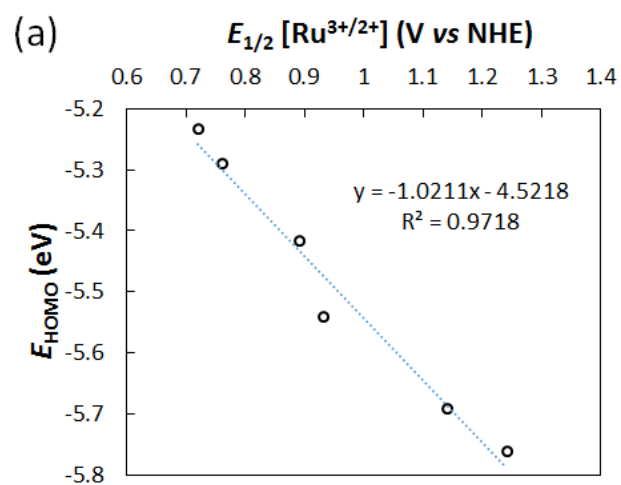
The LUMO is delocalized on the neutral polypyridyl ligands (Tables 3.11–3.14). For **1** and **5**, the LUMO is delocalized over both bpy (95% contribution) and biq (91% contribution) ligands, respectively. The  $\pi$ -system of the dppn ligand that is distal to the metal center (dppn<sup>dis</sup>) is the main contributor to the LUMO of **2** (99% contribution). The LUMO of **4** is centered in the dione moiety of one of the phendione ligands (100% contribution) and the LUMO+1, which lies close in energy to the LUMO (0.07 eV of difference), is centered in the same moiety of the second phendione ligand (100% contribution). The LUMO of **6** is delocalized over the pyridyl and azo moieties of pap (86% contribution). As also observed for **2**, the LUMO of **8** is delocalized over dppn<sup>dis</sup> (100% contribution) and the LUMO+1 is delocalized over the pyridyl and azo moieties of pap (77% contribution). The  $E_{\text{LUMO}}-E_{\text{LUMO}+1}$  energy difference (0.26 eV) in compound **8** is also in agreement with the difference between the first and second reduction potentials ( $E_{\text{red1}} - E_{\text{red2}} = 0.21$  V), so it is proposed that dppn is easier to reduce than pap when both ligands are present in the same Ru complex. The phpy-based  $\pi^*$  MOs appear at higher energies in all the complexes, explaining the higher energy of the Ru(4d $\pi$ ) $\rightarrow$ phpy( $\pi^*$ ) transitions with respect to Ru(4d $\pi$ ) $\rightarrow$ L( $\pi^*$ ), where L is any of the neutral polypyridyl ligands used in this work.

The relative ordering of the calculated HOMO energies of these compounds,  $E_{\text{HOMO}}$ : **1** (less stabilized) < **2** < **5** < **4** < **6** < **8** (more stabilized), is in very good agreement with their experimental metal-based oxidation potentials,  $E_{1/2}$  [Ru<sup>3+/2+</sup>]: **1** < **2** < **5** < **4** < **6** < **8**. In fact, there is a linear correlation between the  $E_{\text{HOMO}}$  and  $E_{1/2}$  [Ru<sup>3+/2+</sup>]

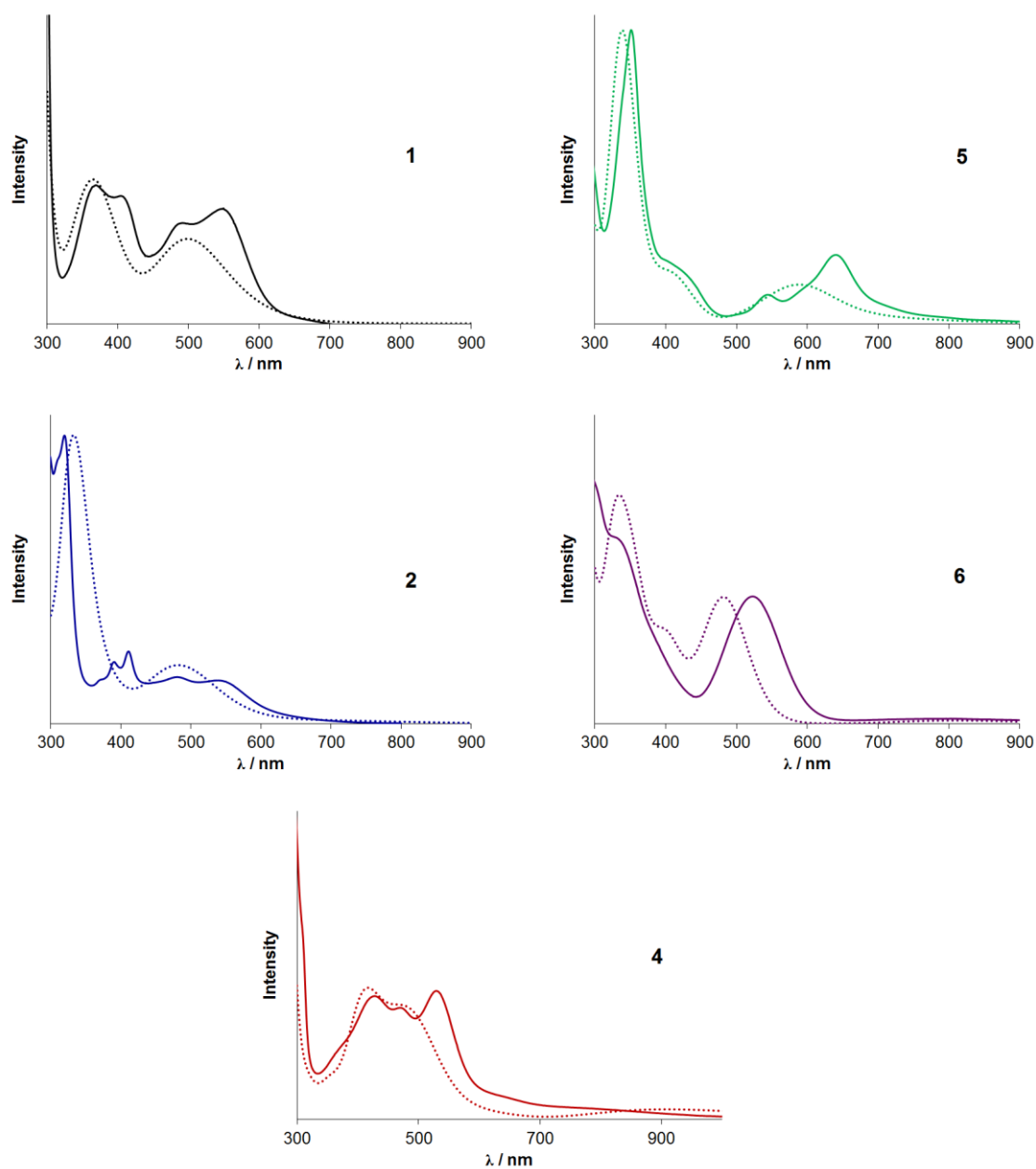
(Figure 3.26a), indicating that a more stabilized HOMO is associated with a more positive  $E_{1/2}$  [Ru<sup>3+/2+</sup>].

Similarly, the calculated LUMO energies,  $E_{\text{LUMO}}$ : **4** (lower energy) < **8** < **6**  $\approx$  **2** < **5** < **1** (higher energy) correlate linearly (Figure 3.26b) with the first ligand-based reduction events,  $E_{1/2,\text{red1}}$ : **4** (easier to reduce) < **8** < **6**  $\approx$  **2** < **5** < **1**, indicating that a more stabilized LUMO is associated with a less negative  $E_{1/2,\text{red1}}$ . Thus, a series of “ease of reduction” of bidentate ligands bound in Ru(II) cyclometallated compounds is proposed based on the experimental  $E_{1/2,\text{red1}}$  and calculated  $E_{\text{LUMO}}$  values: bpy < biq < dppn  $\approx$  pap << phendione.

Time-dependent DFT (TDDFT) calculations were also performed (using the optimized geometries of the ground state of **1**, **2**, **4–6** in acetonitrile) to aid in the interpretation of the experimental electronic absorption spectra. The most relevant vertical transitions ( $\lambda_{\text{calc}}$ ) of the singlet excited states ( $^1\text{ES}_\text{N}$ ) calculated in acetonitrile (PCM model), along with extinction coefficients ( $f$ ), percent transition contributions, assignments and experimental absorption maxima ( $\lambda_{\text{exp}}$ ) values are summarized in Tables 3.15–3.20. The calculated singlet electronic transitions predict qualitatively the experimental absorption spectra of the complexes in the near UV/Visible region (Figure 3.27), although they are hypsochromically shifted with respect to the experimental absorption spectra. Overestimation of the energy of the absorption maxima of Ru(II) polypyridyl complexes using TDDFT calculations has also been reported by others.<sup>198</sup> The calculated singlet excited states of [Ru(bpy)<sub>3</sub>]<sup>2+</sup> and **1**, **2**, **4–6** in the visible region are mainly  $^1\text{MLCT}$  in nature, whereas those at  $\lambda < 350$  nm are predominantly LC ( $^1\pi\pi^*$ ).



**Figure 3. 26** Correlation between (a)  $E_{1/2} [\text{Ru}^{3+/2+}]$  vs  $E_{\text{HOMO}}$  and (b)  $E_{1/2 \text{red1}}$  vs  $E_{\text{LUMO}}$ .



**Figure 3. 27** Experimental (solid lines) and calculated (dotted lines) electronic absorption spectra of **1**, **2**, **4–6** in acetonitrile.



The calculated  $^1\text{MLCT}$  bands for **1** (Table 3.16) in the 450–600 nm region are dominated by  $\text{Ru}(4d\pi)\rightarrow\text{bpy}(\pi^*)$  transitions, whereas those calculated in the 360–400 nm interval are originated from  $\text{Ru}(4d\pi)\rightarrow\text{phpy}(\pi^*)$  transitions and reflect the experimental spectrum. These results are also in good agreement with calculations reported by others for the same complex.<sup>179</sup> In the case of **2**, the experimental broad  $^1\text{MLCT}$  bands at 546 and 485 nm are calculated as charge transfer transitions from the metal to  $\text{bpy}(\pi^*)$  and  $\text{dppn}^{\text{prox}}(\pi^*)$ , where  $\text{dppn}^{\text{prox}}$  is the moiety of this ligand that is in proximity to the metal center. The fact that there are several calculated transitions for each experimental  $\lambda_{\text{max}}$  value in the visible region reproduces the broadness of the observed  $^1\text{MLCT}$  bands of **2** (Table 3.17). Additionally, there are two calculated (703 and 798 nm) weak transitions ( $f < 0.015$ ) in the near-IR region that correspond to transitions from Ru-based orbitals to the LUMO, which is delocalized over  $\text{dppn}^{\text{prox}}(\pi^*)$ , where  $\text{dppn}^{\text{dis}}$  is the moiety of this ligand that is further from the metal center. This calculated low-energy absorption is in agreement with the absorption tail (plateau-like) observed for **2** in the 600–750 nm interval. The poor overlap between the filled  $\text{Ru}(d\pi)$  and empty  $\text{dppn}^{\text{dis}}(\pi^*)$  orbital explains why an intense  $^1\text{MLCT}$  transition of  $\lambda > 550$  nm is not observed for **2** in spite of having a lower energy LUMO with respect to **1**.

**Table 3. 15** TDDFT data of [Ru(bpy)<sub>3</sub>]<sup>2+</sup>.

N	$\lambda_{\text{calc}}$ (nm)	$f$	Major contributions <sup>a</sup>	Assignment	$\lambda_{\text{exp}}$ (nm)
1	480.9	0.0017	H → L (96%)	MLCT	450
5	443.4	0.0158	H-1 → L (83%)	MLCT	
6	442.9	0.0167	H-2 → L (81%)	MLCT	
7	424.6	0.1257	H-2 → L (17%), H-2 → L+2 (40%), H-1 → L+1 (40%)	MLCT	
8	424.4	0.1266	H-2 → L+1 (40%), H-1 → L (16%), H-1 → L+2 (41%)	MLCT	

<sup>a</sup>Percent contribution = (configuration coefficient)<sup>2</sup> × 2 × 100%.

**Table 3. 16** TDDFT data of **1**.

N	$\lambda_{\text{calc}}$ (nm)	$f$	Major contributions <sup>a</sup>	Assignment	$\lambda_{\text{exp}}$ (nm)
1	617.6	0.0036	H → L (45%), H → L+1 (45%)	MLCT	546
3	551.6	0.0185	H-1 → L (77%), H-1 → L+1 (12%)	MLCT	
5	509.6	0.1183	H-2 → L (16%), H-1 → L (15%), H-1 → L+1 (51%)	MLCT	
6	474.5	0.0732	H-2 → L (35%), H-2 → L+1 (30%), H-1 → L+1 (23%)	MLCT	492
11	399.5	0.0125	H-1 → L+3 (20%), H → L+4 (62%)	MLCT	404
12	389.4	0.0500	H-2 → L+2 (39%), H → L+6 (54%)	MLCT	
13	385.0	0.0353	H → L+5 (82%)	MLCT	
15	377.9	0.0406	H-2 → L+2 (16%), H-2 → L+3 (31%), H-1 → L+4 (27%), H → L+6 (13%)	MLCT	369
16	370.2	0.0332	H-1 → L+4 (50%), H-1 → L+6 (25%), H → L+4 (4%), H → L+5 (4%), H → L+6 (4%)	MLCT	
17	364.5	0.0252	H → L+7 (88%)	MLCT	

<sup>a</sup>Percent contribution = (configuration coefficient)<sup>2</sup> × 2 × 100%.

**Table 3. 17** TDDFT data of **2**.

N	$\lambda_{\text{calc}}$ (nm)	$f$	Major contributions <sup>a</sup>	Assignment	$\lambda_{\text{exp}}$ (nm)
1	797.3	0.0037	H → L (98%)	MLCT	tail
2	703.7	0.0149	H-1 → L (98%)	MLCT	
6	544.8	0.0302	H-1 → L+1 (67%), H-1 → L+2 (22%)	MLCT	546
8	513.9	0.0298	H-3 → L (61%), H-1 → L+2 (14%), H → L+3 (13%)	MLCT/LC	
9	513.5	0.0389	H-3 → L (37%), H-1 → L+2 (22%), H → L+3 (22%)	MLCT/LC	
10	489.6	0.2088	H-2 → L+1 (20%), H-2 → L+2 (24%), H → L+3 (42%)	MLCT	485
11	464.1	0.0349	H-2 → L+1 (10%), H-2 → L+2 (17%), H-1 → L+2 (16%), H-1 → L+3 (30%), H → L+3 (16%)	MLCT	
12	450.7	0.0873	H-1 → L+2 (6%), H-1 → L+3 (52%), H → L+4 (28%)	MLCT	
14	433.6	0.0176	H-2 → L+3 (91%)	MLCT	411
15	433.0	0.0131	H-4 → L (97%)	LC	
20	385.1	0.0957	H-6 → L (15%), H-5 → L (55%), H-3 → L+3 (23%)	LC	391

<sup>a</sup>Percent contribution = (configuration coefficient)<sup>2</sup> × 2 × 100%

The experimental <sup>1</sup>MLCT bands of **4** at 530 and 470 nm were calculated to originate from Ru(4dπ)→py<sub>phendione</sub>(π\*) transitions (py<sub>phendione</sub> = pyridyl moieties of phendione), the band at 428 nm has contributions from Ru(4dπ)→py<sub>phendione</sub>(π\*), Ru(4dπ)→phpy(π\*) and <sup>1</sup>LLCT (ligand-to-ligand charge transfer) transitions from phpy to the diketo moiety phendione (dione<sub>phendione</sub>), whereas the band at 372 corresponds mainly to Ru(4dπ)→phpy(π\*) transitions (Table 3.18). The extended absorption tail in the near-IR region of **4** is also reproduced by the calculations and corresponds to

Ru(4d $\pi$ ) $\rightarrow$ dione<sub>phendione</sub>( $\pi^*$ ) transitions, supporting the assignment made for this plateau-like absorption in the previous section. Since the LUMO and LUMO +1 of **4** is centered on dione<sub>phendione</sub>, the poor HOMO-to-LUMO (and HOMO-to-LUMO+1) overlap explains the weak absorption of **4** at  $\lambda > 550$  nm.

**Table 3. 18** TDDFT data of **4**.

N	$\lambda_{\text{calc}}$ (nm)	$f$	Major contributions <sup>a</sup>	Assignment	$\lambda_{\text{exp}}$ (nm)
1	1209.09	0.0016	H $\rightarrow$ L (96%)	MLCT	tail
2	1142.78	0.0021	H $\rightarrow$ L+1 (96%)	MLCT	
3	970.84	0.0076	H-2 $\rightarrow$ L (97%)	MLCT	
5	855.46	0.0075	H-3 $\rightarrow$ L (98%)	MLCT	
10	548.94	0.0204	H-1 $\rightarrow$ L+2 (77%), H-1 $\rightarrow$ L+3 (12%)	MLCT	
15	504.19	0.1023	H-2 $\rightarrow$ L+2 (18%), H-1 $\rightarrow$ L+2 (12%), H-1 $\rightarrow$ L+3 (47%), H $\rightarrow$ L+5 (7%)	MLCT	530
16	478.54	0.0433	H-2 $\rightarrow$ L+2 (18%), H-2 $\rightarrow$ L+3 (17%), H $\rightarrow$ L+4 (55%)	MLCT	470
17	463.52	0.0551	H-2 $\rightarrow$ L+2 (7%), H $\rightarrow$ L+4 (19%), H $\rightarrow$ L+5 (60%)	MLCT	
19	448.74	0.0451	H-1 $\rightarrow$ L+3 (14%), H-1 $\rightarrow$ L+4 (20%), H $\rightarrow$ L+4 (17%), H $\rightarrow$ L+5 (28%)	MLCT	
21	424.41	0.0326	H-1 $\rightarrow$ L+4 (18%), H $\rightarrow$ L+6 (75%)	MLCT	428
22	422.15	0.0363	H-1 $\rightarrow$ L+5 (93%)	MLCT	
23	416.46	0.0163	H-5 $\rightarrow$ LUMO (62%), H-1 $\rightarrow$ L+4 (15%)	MLCT/LC	
24	415.57	0.0478	H-5 $\rightarrow$ L (23%), H-2 $\rightarrow$ L+5 (9%), H-1 $\rightarrow$ L+4 (34%), H $\rightarrow$ L+6 (11%)	MLCT/LC	
26	408.00	0.0100	H-5 $\rightarrow$ L+1 (79%), H-2 $\rightarrow$ L+4 (10%)	LC	
38	350.97	0.0472	H-2 $\rightarrow$ L+6 (42%), H $\rightarrow$ L+7 (42%)	MLCT	372

<sup>a</sup>Percent contribution = (configuration coefficient)<sup>2</sup>  $\times$  2  $\times$  100%.

The experimental electronic absorption spectrum of **5** shows an intense  $^1\text{MLCT}$  band at a lower energy (640 nm) than those of **2** (546 nm) and **4** (530 nm) despite of possessing a higher energy LUMO. The corresponding intense calculated transition (592 nm,  $f \sim 0.12$ ) is blue-shifted with respect to the experimental  $^1\text{MLCT}$  band and it originates from  $\text{Ru}(\text{d}\pi) \rightarrow \text{biq}(\pi^*)$  transitions (Table 3.19). This low energy  $^1\text{MLCT}$  band in the 600–650 nm region for **5** can be explained by increased overlap between the Ru-based HOMOs with the LUMO and LUMO+1, which are delocalized over the entire  $\pi$  system of the biq ligands (with a higher contribution on the central pyridyl rings proximal to the metal center). The experimental  $^1\text{MLCT}$  band at 544 nm is also calculated as  $\text{Ru}(\text{d}\pi) \rightarrow \text{biq}(\pi^*)$  transitions and the band at 406 nm has contributions from  $\text{Ru}(\text{d}\pi) \rightarrow \text{biq}(\pi^*)$ ,  $\text{Ru}(\text{d}\pi) \rightarrow \text{phpy}(\pi^*)$  and  $^1\pi\pi^*$  biq LC transitions. In contrast, the higher energy band at 351 nm is calculated to be mainly of biq character ( $\text{biq}(\pi^*) \rightarrow \text{biq}(\pi^*)$ ).

Finally, the calculated  $^1\text{MLCT}$  transition at 484 nm for **6** (Table 3.20) is blue shifted with respect to the experimental value (523 nm) and corresponds to  $\text{Ru}(\text{d}\pi) \rightarrow \text{pap}(\pi^*)$  transitions, whereas the experimental band at 335 nm is calculated to originate from a combination of  $\text{Ru}(\text{d}\pi) \rightarrow \text{phpy}(\pi^*)$ ,  $\text{pap}(\pi) \rightarrow \text{pap}(\pi^*)$ ,  $\text{phpy}(\pi^*) \rightarrow \text{pap}(\pi)$  transitions.

**Table 3. 19** TDDFT data of **5**.

N	$\lambda_{\text{calc}}$ (nm)	$f$	Major contributions <sup>a</sup>	Assignment	$\lambda_{\text{exp}}$ (nm)
1	792.94	0.0054	H → L (87%)	MLCT	tail
2	712.97	0.0106	H → L+1 (84%)	MCLT	
3	665.97	0.0056	H-1 → L (73%), H-1 → L+1 (22%)	MLCT	640
4	622.39	0.0031	H-2 → L (49%), H-2 → L+1 (35%)	MLCT	
5	592.54	0.1227	H-2 → L (27%), H-1 → L (13%), H-1 → L+1 (50%)	MLCT	
6	528.05	0.0378	H-2 → L (12%), H-2 → L+1 (52%), H-1 → L+1 (16%)	MLCT	
9	424.91	0.0270	H → L+2 (73%), H → L+4 (15%)	MLCT	
10	423.07	0.0521	H-3 → L (39%), H-1 → L+4 (4%), H → L+3 (41%)	MLCT/LC	406
11	404.95	0.0250	H-3 → L+1 (49%), H-1 → L+3 (36%)	MLCT/LC	
12	402.59	0.0409	H-3 → L+1 (35%), H-1 → L+3 (36%), H-1 → L+4 (18%)	MLCT/LC	
30	347.82	0.1573	H-9 → L (29%), H-2 → L+5 (44%)	MLCT/LC	351
31	344.98	0.2349	H-10 → L (5%), H-8 → L (48%), H-7 → L (15%), H-6 → L (5%)	LC	
41	329.21	0.2739	H-11 → L (16%), H-9 → L+1 (7%), H-8 → L+1 (41%), H-7 → L+1 (6%)	LC	
42	328.06	0.1254	H-9 → L+1 (72%)	LC	

<sup>a</sup>Percent contribution = (configuration coefficient)<sup>2</sup> × 2 × 100%.

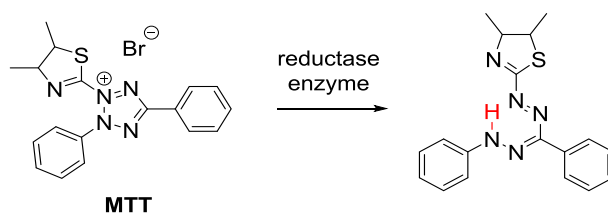
**Table 3. 20** TDDFT data of **6**.

N	$\lambda_{\text{calc}}$ (nm)	$f$	Major contributions <sup>a</sup>	Assignment	$\lambda_{\text{exp}}$ (nm)
1	817.31	0.0038	H → L (92%)	MLCT	tail
2	737.31	0.0005	H-1 → L (97%)	MLCT	
3	484.58	0.1559	H-2 → L (90%)	MLCT	523
9	358.95	0.0680	H-5 → L (76%), H-4 → L (8%)	LC	335
11	349.43	0.1035	H-7 → L (10%), h-6 → L (62%)	LC	
13	332.11	0.0893	H-2 → L+1 (47%), H-1 → L+2 (22%), H → L+3 (14%)	MLCT	

<sup>a</sup>Percent contribution = (configuration coefficient)<sup>2</sup> × 2 × 100%.

### *Cytotoxicity Studies*

The chloride salts of **1**, **2**, **3** and **5** were prepared by anion metathesis with  $[\text{Bu}_4\text{N}][\text{Cl}]$  in acetone to improve the water solubility of these complexes. The reduction of viability of HeLa cervical cancer cells by compounds **1**, **2**, **3** and **5** was tested using the colorimetric MTT assay as a preliminary study to determine the suitability of using this type of cyclometallated compounds as cytotoxic agents against cancer cells and the results were compared to cisplatin.



**Figure 3. 28** Reduction of MTT.

The MTT reagent ((3-(4,5-dimethylthiazol-2-yl)-2,5-diphenyltetrazolium bromide, Figure 3.28) is a permeable water soluble dye (pale yellow color) that is reduced by the NADH cofactor (reduced nicotinamide adenine dinucleotide) in the

cytosol or by NAD(P)H-dependent oxido-reductases and succinate dehydrogenase in mitochondria of living cells,<sup>199</sup> and forms insoluble dark blue-purple formazan crystals that are impermeable to cell membranes and accumulates inside the cells.<sup>200</sup> The amount of formazan that is produced is determined by absorption spectroscopy after solubilization with dimethylsulfoxide using a microplate absorbance reader, where the formazan absorbance is directly proportional to the number of living, metabolically active cells.

**Table 3. 21** Cytotoxicity data of Ru complexes against HeLa cells.

Compound	IC <sub>50</sub> (μM) <sup>a</sup>
[Ru(phpy)(bpy) <sub>2</sub> ][Cl] ( <b>1</b> )	34 ± 3
[Ru(phpy)(bpy)(dppn)][Cl] ( <b>2</b> )	7 ± 1
[Ru(phpy)(phendione) <sub>2</sub> ][Cl] ( <b>4</b> )	57 ± 7
[Ru(phpy)(biq) <sub>2</sub> ][Cl] ( <b>5</b> )	51 ± 8
cisplatin	40 ± 9

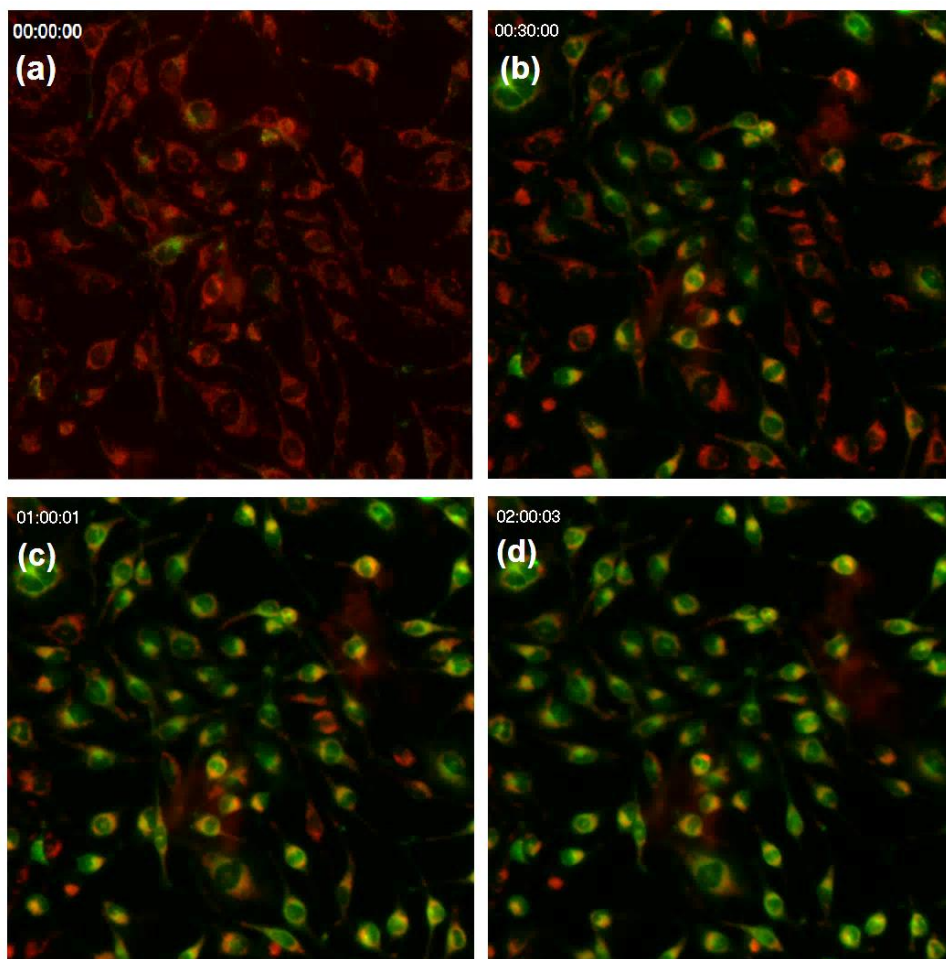
<sup>a</sup>Incubation time = 2 h. Results are the means of three independent experiments and are expressed as mean ± SD.

The IC<sub>50</sub> values (concentration of compound required to inhibit 50% of cell survival) were calculated after 2 h of incubation under reduced light conditions and are listed in Table 3.21. In general, **1**, **4** and **5** exhibit toxicity toward HeLa cells similar to cisplatin, but **2** is ~6 times more active than cisplatin under similar experimental



conditions. The higher cytotoxicity of the tris-heteroleptic compound can be attributed to its greater lipophilicity and cellular uptake due to the presence of the dppn ligand and monocationic charge, as described in Chapter 1.

The ability of compound **2**, the most cytotoxic of this series, to induce the loss of inner mitochondrial membrane potential ( $\Delta\Psi_m$ ) was studied using the JC-1 probe. As described in Chapter 2, this lipophilic cationic dye accumulates selectively in mitochondria and exhibits dual fluorescence: red fluorescence ( $\lambda_{em} = 590$  nm) from dye aggregate and green fluorescence ( $\lambda_{em} = 527$  nm) from dye monomers. Since JC-1 aggregates are formed due to the negative  $\Delta\Psi_m$ , mitochondrial depolarization and permanent depletion of  $\Delta\Psi_m$  is indicated by a reduction of red fluorescence and simultaneous increase in green fluorescence. Incubation of HeLa cells with **2** showed a time-dependent mitochondrial depolarization as can be observed in Figure 3.29, where a shift in the fluorescence emission wavelength from red to green occurs in a 2 h period. These findings suggest that mitochondria are possible cellular targets of compound **2** in HeLa cells and that it could induce apoptosis via the mitochondrial pathway.<sup>122,123</sup>



**Figure 3. 29** JC-1 fluorescence (overlay of green and red channels) images of HeLa cells treated with **2** ( $7 \mu\text{M}$ ) at (a) 0 h, (b) 30 min, (c) 1 h and (d) 2 h.

**Table 3. 22** Cytotoxicity data of compounds **2** and **8** against ovarian cancer cells.

Compound	IC <sub>50</sub> (μM) <sup>a</sup>	
	OVCAR-8	NCI/ADR-RES
[Ru(phpy)(bpy)(dppn)][Cl] ( <b>2</b> )	10 ± 4	16 ± 1
[Ru(phpy)(pap)(dppn)][PF <sub>6</sub> ] ( <b>8</b> )	15 ± 7	12 ± 4

<sup>a</sup>Incubation time = 2 h. Results are the means of three independent experiments and are expressed as mean ± SD.

The cytotoxicity of compounds **2** and **8**, both possessing the dppn ligand, was evaluated in the human ovarian adenocarcinoma cell lines OVCAR-8 and NCI/ADR-RES using the MTT assay. NCI/ADR-RES is a cell line derived from OVCAR-8 that is resistant to doxorubicin (also known as adriamycin, a broad-spectrum chemotherapeutic agent), cisplatin and paclitaxel. The resistance of this cell line towards chemotherapeutic agents is owing to its high expression level of P-glycoprotein (multidrug resistance protein 1, MDR1), which is an ATP-dependent efflux pump of the cell membrane that has a broad substrate specificity and is able to pump the above mentioned drugs out of the cells.<sup>201,202,203,204</sup> In addition, OVCAR-8 and NCI/ADR-RES are included in The U.S. National Cancer Institute 60 human tumor cell line panel (NCI60), which is a platform high throughput screening of the cytotoxicity of potential anticancer drugs.<sup>205,206</sup> Both compounds exhibit IC<sub>50</sub> values in the low micromolar range (10–15 μM, Table 3.22) against OVCAR-8 cells. Moreover, its cytotoxic properties did not decrease when incubated with the resistant NCI/ADR-RES cell line. For comparison, the reported IC<sub>50</sub> values (74 h of incubation) of doxorubicin in OVCAR-8 and NCI/ADR-

RES cells are 0.6  $\mu\text{M}$  and  $>20 \mu\text{M}$ , respectively.<sup>204</sup> Therefore, compounds **2** and **8** are more active than doxorubicin against NCI/ADR-RES and require only 2 h to display cytotoxic effects.

Because of the intense absorption of **5** with a maximum at 640 nm ( $\epsilon = 1.05 \times 10^4 \text{ M}^{-1} \text{ cm}^{-1}$ ), the complex was investigated as a potential agent for photochemotherapy (PCT) in collaboration with Prof. Claudia Turro (The Ohio State University) and Prof. Mauricio S. Baptista (University of São Paulo, Brazil). PCT has emerged as a non-invasive treatment with low systemic toxicity for the treatment and cure of early stage lesions of endoscopically accessible tumors<sup>207</sup> and excitation in the 600–850 nm range is desirable for deeper tissue penetration of light.<sup>208</sup> Thus, HeLa cells were incubated with **5** for a longer period of time (48 h) than the previous experiment, under reduced light conditions, and the calculated  $\text{IC}_{50}$  using the MTT assay was 7  $\mu\text{M}$ . In a different experiment, when the cells treated with **5** were irradiated for 20 min with light of 633 nm (red light) followed by 48 h incubation in the dark, the  $\text{IC}_{50}$  decreased to 1  $\mu\text{M}$ . Therefore, the cytotoxicity of compound **5** increased 7-fold upon red light irradiation, showing the potential of Ru cyclometallated compounds as PCT agents.

## Conclusions

Seven new Ru(II) cyclometallated compounds (**2–8**) displaying rich electrochemical and optical properties have been synthesized and thoroughly characterized. These molecules exhibit lower energy <sup>1</sup>MLCT transitions (Ru(4dπ)→L(π\*), L = neutral polypyridyl ligand) than their non-cyclometallated counterparts (*e.g.* [Ru(bpy)<sub>3</sub>]<sup>2+</sup>) due the destabilization of the Ru(4dπ) HOMOs, which in turn explains their strong absorption in the visible region ( $\epsilon \sim 1\text{--}2 \times 10^4 \text{ M}^{-1} \text{ cm}^{-1}$ ), as well as plateau-like absorptions in the near-IR region. The metal-based oxidation potentials ( $E_{1/2} [\text{Ru}^{3+/2+}]$ ) of these complexes occur in the 1.5–0.70 V (*vs* NHE) range, whereas the ligand-based reduction events occur at negative potentials ( $< -0.5 \text{ V vs NHE}$ ). Interestingly,  $E_{1/2} [\text{Ru}^{3+/2+}]$  and the first ligand-based reduction potential ( $E_{1/2,\text{red1}}$ ) are linearly correlated with the calculated (DFT) HOMO and LUMO energies and such correlation could be used in the future to predict experimental half-wave potentials using results from theoretical calculations (at the same theoretical level) of related compounds.

It has been also shown that compounds **1**, **4** and **5** display cytotoxicity comparable to cisplatin against HeLa cancer cells, whereas compound **2** is 6-fold more active than cisplatin at very short incubation times (2 h). The latter compound caused loss of the mitochondrial membrane potential indicating that apoptosis via the mitochondrial pathway may be the mechanism of cancer cell death. Compounds **2** and **8** were also found to be cytotoxic against the sensitive OVCAR-8 and multidrug resistant NIC/ADR-RES cancer cell lines, revealing the high potential of Ru cyclometallated

compounds incorporating the lipophilic dppn ligand as chemotherapy agents. In addition, a 7-fold increase in the cytotoxicity of **5** was observed when irradiated with low energy red light, making it potentially useful as a photochemotherapy agent.

These findings show that coordinately saturated Ru(II) cyclometallated dyes typically used in solar energy applications could emerge as a new family of antitumor drugs since the compounds shown here resemble them in structure, optical and electrochemical properties. The cytotoxicity and thorough investigation of potential mechanism(s) of cell death for a more extensive series of compounds including derivatives of the newly synthesized precursor **6** are currently under investigation in the laboratories of Prof. Kim R. Dunbar.

## CHAPTER IV

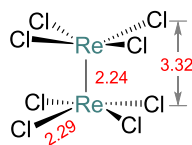
### LIVE CELL IMAGING STUDIES OF A FLUOROPHORE-LABELED METAL-METAL BONDED DIRHODIUM COMPOUND\*

#### Multiple Bonds Between Metal Atoms

Compounds with direct metal-metal (M–M) bonds are a fascinating class of inorganic molecules that are considered to be part of a second kind of transition metal chemistry or *non-Wernerian transition metal chemistry*, as described by F. A. Cotton, C. A. Murillo and R. A. Walton,<sup>209</sup> in the sense that they do not fit into the conceptual framework of a single metal atom surrounded by a set of ligands (*one-center coordination chemistry*) established by Alfred Werner in the early 1900's. A milestone of this multicenter transition chemistry was established in 1963–1965 when the structure of the octachlorodirrenate(III,III) anion,  $[\text{Re}_2\text{Cl}_8]^{2-}$  (Figure 4.1) was correctly elucidated and the first quadruple bond was recognized by F. A. Cotton and coworkers.<sup>210,211</sup> Such a discovery stimulated the exploration of M–M bonding across the transition metal series with a rapid expansion of the field ensuing. Since then, these type of molecules have found many applications in catalysis,<sup>212,213,214,215,216,217</sup> medicinal chemistry,<sup>218,219</sup> magnetism<sup>220,221</sup> and spectroscopy.<sup>222</sup>

---

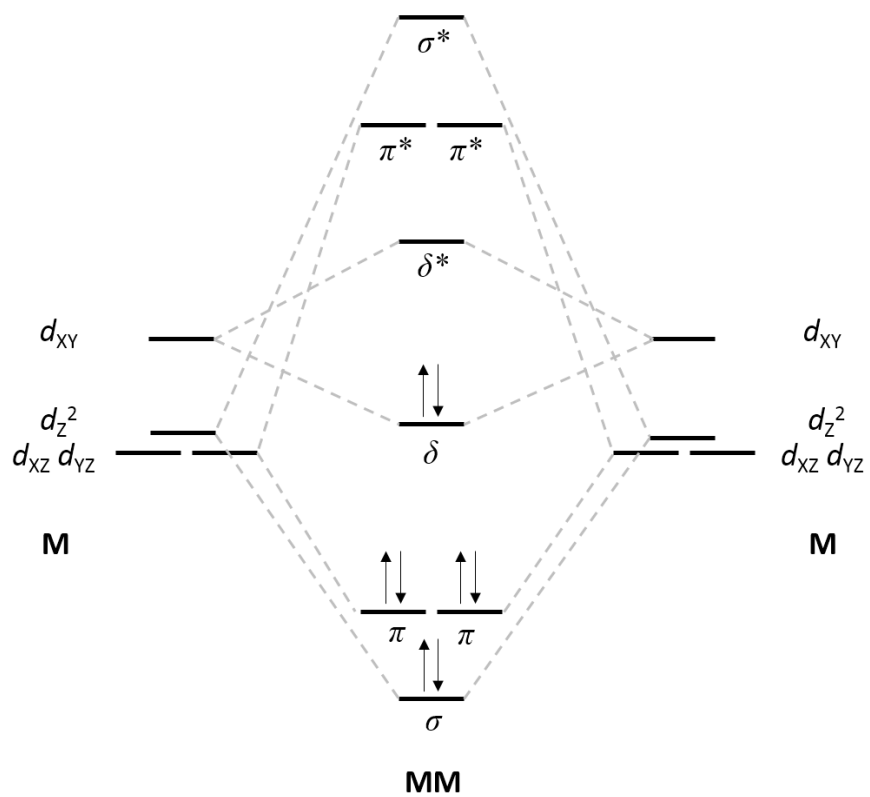
\*Reprinted with permission from Peña, B.; Barhoumi, R.; Burghardt, R. C.; Turro, C.; Dunbar, K. R. “Confocal Fluorescence Microscopy Studies of a Fluorophore-labeled Dirhodium Compound: Visualizing Metal-Metal Bonded Molecules in Lung Cancer (A549) Cells”. *J. Am. Chem. Soc.* **2014**, *136* (22), 7861-7864. Copyright 2014 American Chemical Society.



**Figure 4. 1** Schematic representation of the molecular structure of the  $[\text{Re}_2\text{Cl}_8]^{2-}$  anion. Distances are indicated in Å.

A qualitative picture of the M–M quadruple bond in  $[\text{Re}_2\text{Cl}_8]^{2-}$  is shown in Figure 4.2 and can also be used to explain the bonding in the general class of face-to-face M–M bonded compounds.<sup>209,223</sup> Multiple bonds between two metal atoms are formed by the positive overlap of their *d* orbitals: one  $\sigma$  molecular orbital (MO) is formed by overlap of two  $dz^2$  orbitals, two equivalent and orthogonal  $\pi$  MOs are formed by overlap of two  $dxz$  and two  $dyz$  orbitals, and one  $\delta$  MO is produced by the face-to-face overlap of two  $dxy$  orbitals. There are also four antibonding MOs (one  $\sigma^*$ , two  $\pi^*$  and one  $\delta^*$ ) formed by the negative overlap of the above mentioned *d* orbitals. The  $dx^2-y^2$  orbitals on each metal atom are not involved in the M–M bonding because they are primarily involved in the bonding with the ligands ( $\text{Cl}^-$  ligands in the case of  $[\text{Re}_2\text{Cl}_8]^{2-}$ ). The eight electrons of the  $\text{Re}_2^{6+}$  core ( $\text{Re}_2(\text{III},\text{III})$ ) fill the bonding MOs giving a  $(\sigma)^2(\pi)^4(\delta)^2$  configuration and a bond order of 4, a quadruple bond.<sup>209</sup>



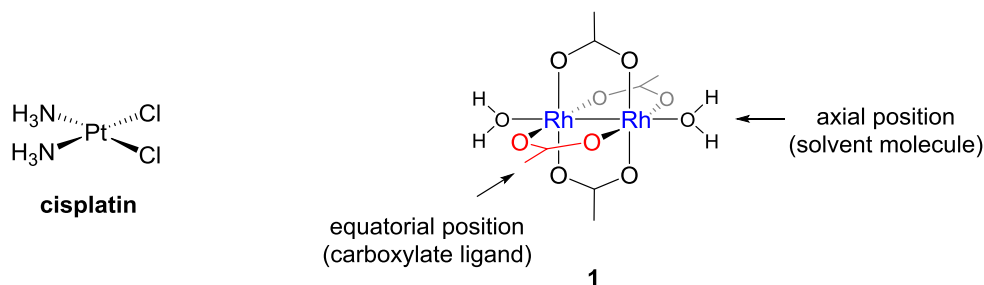


**Figure 4. 2** Qualitative molecular orbital diagram in M–M bonded compounds.

## Anticancer Active Dirhodium Compounds

### *Dirhodium Tetraacetate and its Derivatives*

Within the field of cancer drug research, dirhodium complexes based in  $\text{Rh}_2^{4+}$  core ( $\text{Rh}_2(\text{II},\text{II})$ , 14 electrons) are the most studied M–M bonded compounds. Such molecules exhibit the  $(\sigma)^2(\pi)^4(\delta)^2(\delta^*)^2(\pi^*)^4$  electronic configuration corresponding to a bond order of 1 (a single bond). The first compound to be tested as an antineoplastic agent is dirhodium tetraacetate (**1**;  $\text{Rh}_2(\mu\text{-O}_2\text{CCH}_3)_4$ , Figure 4.3). The report appeared in 1972, three years after the discovery of the antitumor properties of cisplatin (*cis*- $\text{Pt}(\text{NH}_3)_2\text{Cl}_2$ , Figure 4.3),<sup>18</sup> in which John Bear and coworkers (University of Houston, Texas) reported that **1**, in combination with arabinosylcitosine (Cytarabine, Cytosar-U®, an anticancer drug used to treat different forms of leukemia), increased the survival time of mice bearing lymphocytic leukemia (L1210) tumors.<sup>224</sup>

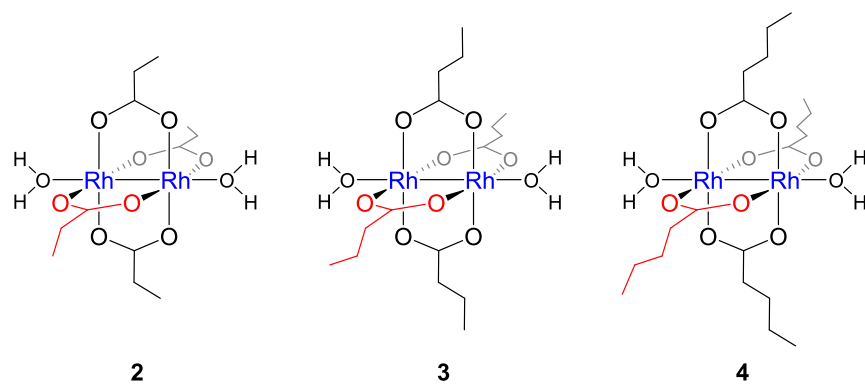


**Figure 4. 3** Molecular structures of cisplatin and compound **1**. One of the equatorial carboxylate ligands in **1** is highlighted in red.

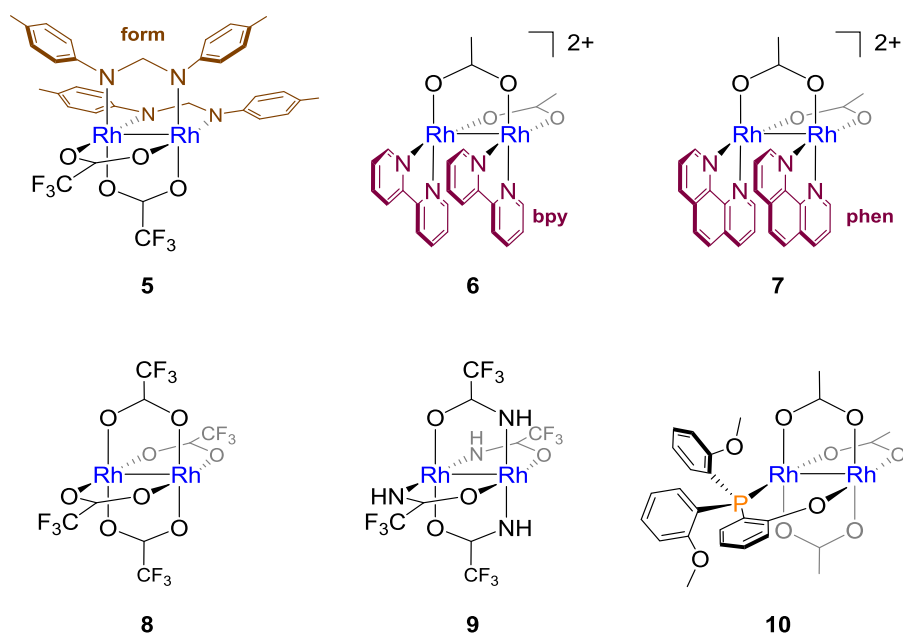
Compound **1** adopts the “so-called” paddlewheel structure; it possesses four bridging acetate ( $\text{CH}_3\text{CO}_2^-$ ) ligands occupying equatorial positions and two weakly bound axial ligands, typically solvent molecules such as water (Figure 4.3). After their initial report of the anticancer properties of the acetate derivative, Bear and coworkers later reported that other dirhodium tetracarboxylate compounds such as dirhodium tetrapropionate (**2**;  $\text{Rh}_2(\mu\text{-O}_2\text{CCH}_2\text{CH}_3)_4$ , Figure 4.4), dirhodium tetrabutyrate (**3**;  $\text{Rh}_2(\mu\text{-O}_2\text{CCH}_2\text{CH}_2\text{CH}_3)_4$ , Figure 4.4) and dirhodium tetrapentanoate (**4**;  $\text{Rh}_2(\mu\text{-O}_2\text{CCH}_2\text{CH}_2\text{CH}_2\text{CH}_3)_4$ , Figure 4.4), were more effective than **1** at increasing the survival time of mice bearing the Ehrlich ascites tumors. In addition, compounds **1–4** were able to inhibit DNA and RNA synthesis *in vitro*.<sup>225,226,227</sup> Structure–activity relationship studies showed that the antitumor activity and cellular uptake of dirhodium tetracarboxylate compounds increases with the length (and lipophilicity) of the bridging carboxylate ligand, **1** < **2** < **3** < **4**, but a further lengthening of the alkyl chain beyond the

pentanoate group decreases their activity,<sup>228,229</sup> underscoring the dependence of the cytotoxicity on the ability of the compounds to traverse the plasma membrane.

Following these series of reports, the structural diversity of cytotoxic dirhodium compounds was expanded when four new studies appeared during the 1990's (Figure 4.5). The formamidinate compound *cis*-Rh<sub>2</sub>(μ-O<sub>2</sub>CCF<sub>3</sub>)<sub>2</sub>(form)<sub>2</sub> (**5**; form = *N,N'*-di-*p*-tolylformamidinate) was shown to have similar antineoplastic activity to cisplatin in mice bearing tumors (Guerink T8 and Yoshida ascites sarcoma), with the advantage of exhibiting considerably lower side effects.<sup>230</sup> The dicationic compounds [Rh<sub>2</sub>(μ-O<sub>2</sub>CCH<sub>3</sub>)<sub>2</sub>(bpy)<sub>2</sub>]<sup>2+</sup> (**6**; 2,2'-bipyridine (bpy)) and [Rh<sub>2</sub>(μ-O<sub>2</sub>CCH<sub>3</sub>)<sub>2</sub>(phen)<sub>2</sub>]<sup>2+</sup> (**7**; 1,10-phenanthroline (phen)) were shown to display cytotoxic properties against a human oral carcinoma (KB) cancer cell line.<sup>231</sup> Dirhodium tetrakis(trifluoroacetate), Rh<sub>2</sub>(μ-O<sub>2</sub>CCF<sub>3</sub>)<sub>4</sub> (**8**), was found to increase the survival rate of mice bearing Ehrlich ascites cells,<sup>232</sup> and the dirhodium tetrakisacetamidate compound Rh<sub>2</sub>(μ-NHCOCF<sub>3</sub>)<sub>4</sub> (**9**) was reported to be more active than cisplatin both *in vitro* (human leukemia cells (U937 and K562) and Ehrlich ascite cancer cells) and *in vivo* (Ehrlich ascite tumors implanted in mice).<sup>233</sup> In 2001, a dirhodium compound incorporating a *O*-methallated methoxyphenylphosphine ligand, [Rh<sub>2</sub>(μ-O<sub>2</sub>CCH<sub>3</sub>)<sub>3</sub>(μ-(*o*-OC<sub>6</sub>H<sub>4</sub>)P(*o*-OCH<sub>3</sub>C<sub>6</sub>H<sub>4</sub>)<sub>2</sub>)] (**10**), was also shown to be more active than cisplatin against several tumor cell lines (oral carcinoma (KB), bladder cancer (Hu1703), colon adenocarcinoma (SW707) and breast cancer (T47D)).<sup>234</sup>



**Figure 4. 4** Molecular structures of compounds **2–4**. One of the equatorial carboxylate ligands is highlighted in red.



**Figure 4. 5** Molecular structures of cytotoxic dirhodium compounds developed during the 1990–2001 period. The axial ligands have been omitted for the sake of clarity.

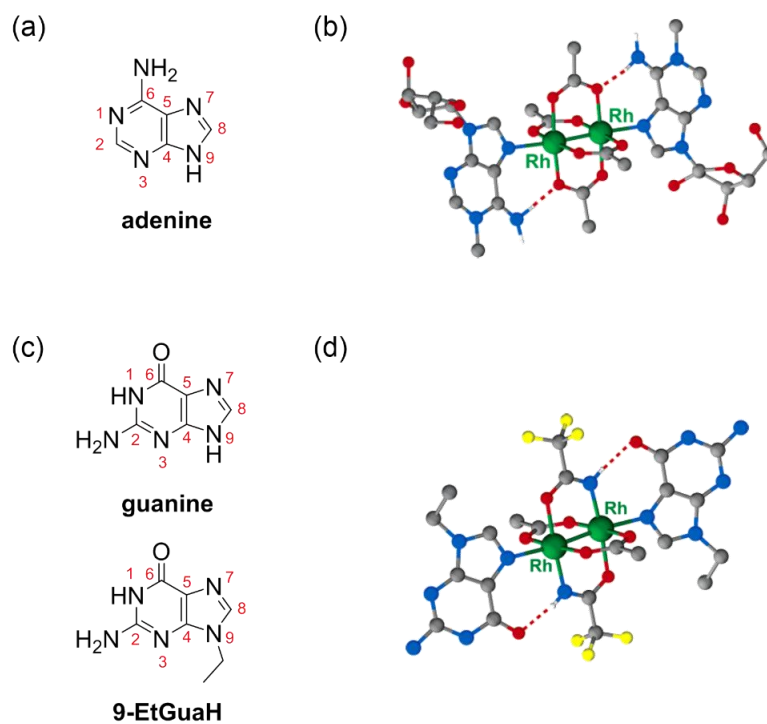
## *Interactions of Dirhodium Compounds with DNA*

Over the past 20 years, considerable efforts mainly from the Dunbar group but also from other research groups have been devoted to elucidate the interactions of Rh–Rh bonded compounds with DNA models. The results from these studies have been thoroughly reviewed<sup>218</sup> and have led to the main conclusion that dirhodium compounds are able to bind covalently to DNA purines, nucleotides, dinucleotides, single-stranded and double-stranded DNA, suggesting that nuclear DNA is a potential target of dirhodium compounds *in vivo*. A summary of the most relevant results is provided below.

### **Interactions with DNA Base Models and Dinucleotides**

The nucleobase adenine binds axially to the Rh<sub>2</sub><sup>4+</sup> core and forms adducts that are stabilized by the formation of hydrogen bonds between the N6 amino group of adenine (Figure 4.6a) and the O atom of the carboxylate ligand bound to the dimetal unit. Two crystal structures showing this type of interaction have been reported: Rh<sub>2</sub>(μ-O<sub>2</sub>CCH<sub>3</sub>)<sub>4</sub>(1-MeAdo)<sub>2</sub><sup>235</sup> (1-MeAdo = 1-methyladenosine, Figure 4.6b) and [Rh<sub>2</sub>(μ-O<sub>2</sub>CCH<sub>3</sub>)<sub>2</sub>(μ-HNCOCF<sub>3</sub>)<sub>2</sub>(9-MeAdeH<sub>2</sub>)<sub>2</sub>](NO<sub>3</sub>)<sub>2</sub>. (9-MeAdeH<sub>2</sub> = 9-methyladenine protonated at the N1 position).<sup>236</sup> In contrast, guanine do not form axial adducts with dirhodium tetracarboxylate compounds (Rh<sub>2</sub>(μ-O<sub>2</sub>CR)<sub>4</sub>, R = alkyl, aryl) due to electrostatic repulsions between the O6 atom of guanine (Figure 4.6c) and the O atom of

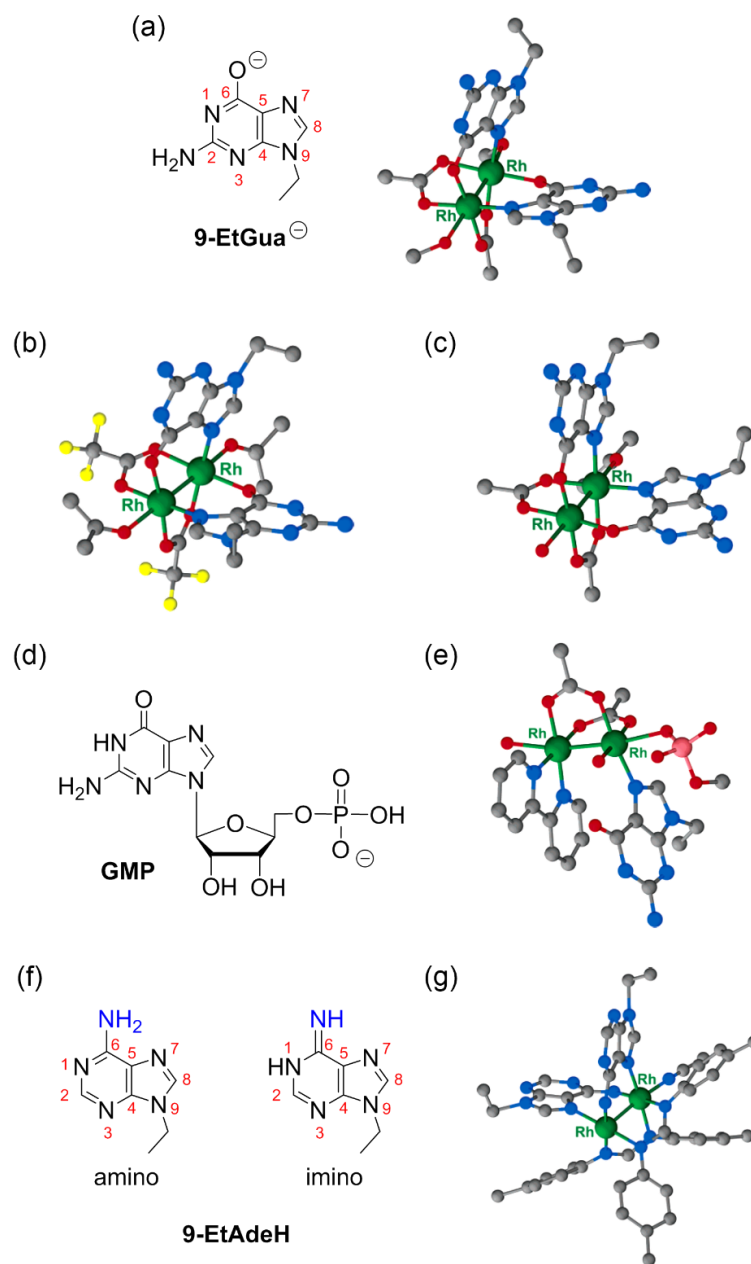
the carboxylate ligands bound to the  $\text{Rh}_2^{4+}$  core. Guanine, however, binds axially via the N7 atom to the dimetal unit when at least two of the carboxylate ligands are replaced by equatorial bridging ligands possessing hydrogen-bonding donor moieties (such as acetamidate). The X-ray structures of *trans*- $\text{Rh}_2(\mu\text{-O}_2\text{CCH}_3)_2(\mu\text{-HNCOCF}_3)_2(9\text{-EtGuaH})_2$  (9-EtGuaH = 9-ethylguanine, Figure 4.6d)<sup>236</sup> and  $\text{Rh}_2(\mu\text{-HNCOCF}_3)_4(\text{dGuo})_2$  (dGuo = deoxyguanosine)<sup>236</sup> reveal this type of interaction.



**Figure 4. 6** Axial interactions of the  $\text{Rh}_2^{4+}$  core with purines. Adapted with permission from reference 218. Copyright 2005 American Chemical Society.

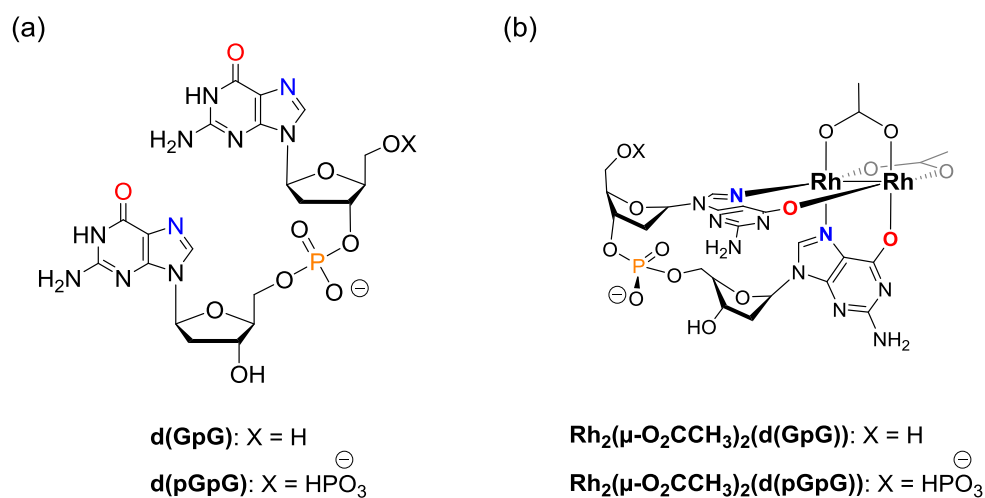


Guanine displays a second binding mode that involves the displacement of equatorial bridging ligands. Such an unprecedented binding mode involving the N7 and O6 atoms (Figure 4.7a) occurs in the crystal structures of H–T *cis*-Rh<sub>2</sub>(μ-O<sub>2</sub>CCH<sub>3</sub>)<sub>2</sub>(μ-9-EtGua)<sub>2</sub>(CH<sub>3</sub>OH)<sub>2</sub> (9-EtGua = deprotonated 9-ethylguanine, Figure 4.7a),<sup>237</sup> H–T *cis*-Rh<sub>2</sub>(μ-O<sub>2</sub>CCF<sub>3</sub>)<sub>2</sub>(μ-9-EtGuaH)<sub>2</sub>((CH<sub>3</sub>)<sub>2</sub>CO)<sub>2</sub>[(CF<sub>3</sub>CO<sub>2</sub>)<sub>2</sub>] (Figure 4.7b),<sup>237</sup> and H–H *cis*-[Rh<sub>2</sub>(μ-O<sub>2</sub>CCH<sub>3</sub>)<sub>2</sub>(μ-9-EtGuaH)<sub>2</sub>(H<sub>2</sub>O)((CH<sub>3</sub>)<sub>2</sub>CO)](BF<sub>4</sub>)<sub>2</sub> (Figure 4.7c).<sup>238</sup> A similar bridging mode for guanine have been reported for the formamidinate compound H–H *cis*-[Rh<sub>2</sub>(μ-form)<sub>2</sub>(μ-9-EtGuaH)<sub>2</sub>(NCCH<sub>3</sub>)](BF<sub>4</sub>)<sub>2</sub><sup>239</sup> and when **1** is reacted with guanosine-5'-monophosphate (GMP, Figure 4.7d).<sup>240</sup> The H–T geometry (head-to-tail) indicates that each Rh atom is bound to a O6 and a N7 atom; the H–H geometry (head-to-head) indicates that one Rh atom is bound to two N7 atoms and the other Rh atom is bound to two O6 atoms. A third binding mode has been observed for guanine, where it binds to the Rh<sub>2</sub><sup>4+</sup> core at an equatorial position as a monodentate ligand, as shown in the X-ray crystal structure of Rh<sub>2</sub>(μ-O<sub>2</sub>CCH<sub>3</sub>)<sub>2</sub>(bpy)(9-EtGuaH)(H<sub>2</sub>O)<sub>2</sub>(CH<sub>3</sub>SO<sub>4</sub>)](CH<sub>3</sub>SO<sub>4</sub>) (Figure 4.7e).<sup>241</sup> In the case of adenine, it is also able to bind the dimetal unit in an equatorial bridging mode, as shown in the X-ray structure of [Rh<sub>2</sub>(μ-form)<sub>2</sub>(μ-9-EtAdeH)<sub>2</sub>(NCCH<sub>3</sub>)](BF<sub>4</sub>)<sub>2</sub> (9-EtAdeH = 9-ethyl adenine, Figure 4.7g), where 9-EtAdeH binds in its unusual imino form (Figure 4.7f).<sup>239,242</sup>



**Figure 4. 7** Equatorial binding of guanine and adenine base models to the Rh<sub>2</sub><sup>4+</sup> core. Adapted with permission from reference 218. Copyright 2005 American Chemical Society.

The reaction of dirhodium tetraacetate (**1**) with deoxydinucleotides (d(GpG) or d(pGpG), Figure 4.8a) affords  $\text{Rh}_2(\mu\text{-O}_2\text{CCH}_3)_2(\text{deoxydinucleotide})$ , where the two guanine (G) bases of the dinucleotide are bound to the dimetal core in a bridging equatorial mode (via N7/O6 donor atoms) and adopt a H–H arrangement, as determined by 1D and 2D NMR experiments.<sup>240,243</sup> The structural conformations of  $\text{Rh}_2(\mu\text{-O}_2\text{CCH}_3)_2(\text{d(GpG)})$  and  $\text{Rh}_2(\mu\text{-O}_2\text{CCH}_3)_2(\text{d(pGpG)})$  (Figure 4.8b) resemble the X-ray structure of cisplatin bound to d(pGpG) reported by Stephen Lippard and coworkers,<sup>41,244</sup> establishing that dirhodium tetraacetate could bind to nuclear DNA *in vivo* in a similar fashion as cisplatin.



**Figure 4. 8** Molecular structures of (a) d(GpG) and d(pGpG) and (b) H–H conformation of  $\text{Rh}_2(\mu\text{-O}_2\text{CCH}_3)_2(\text{deoxydinucleotide})$ .

## Interactions with Single-stranded and Double-stranded DNA

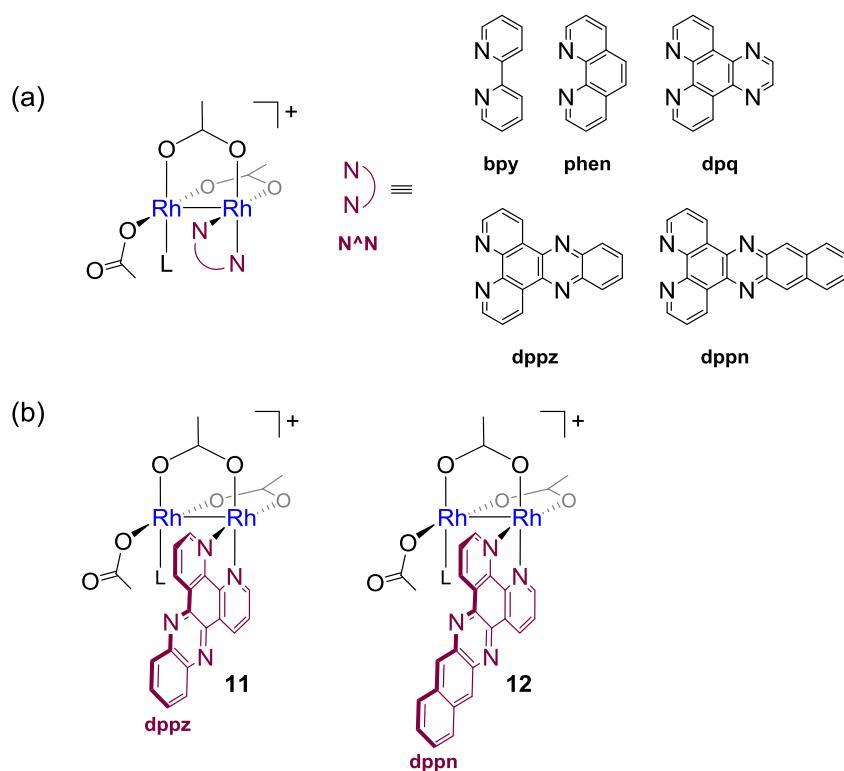
The interactions between **1**, **8** and  $[\text{Rh}_2(\mu\text{-O}_2\text{CCH}_3)_2(\text{NCCH}_3)_6](\text{BF}_4)_2$  with single-stranded oligonucleotides of different lengths (tetra- to dodecamers) containing dipurine sites (AA, AG, GA and GG) were studied by matrix-assisted laser desorption ionization (MALDI) mass spectrometry and nanoelectrospray ionization (nanoESI) coupled to time-of-flight (TOF) mass spectrometry to determine the binding site of these metal compounds.<sup>245,246</sup> Cisplatin ( $\text{cis-Pt}(\text{NH}_3)_2\text{Cl}_2$ ), its activated form ( $\text{cis-Pt}(\text{NH}_3)_2(\text{H}_2\text{O})_2^{2+}$ ) and carboplatin ( $\text{cis-Pt}(\text{C}_6\text{H}_6\text{O}_4)(\text{NH}_3)_2$ ) were included for comparison. It was found that GG and AA sites are the preferred binding sites for the three dirhodium complexes and that the main products of the reactions are dirhodium bis-acetate oligonucleotides. In addition, their reactivity towards single-stranded DNA decreased in the following order:  $\text{cis-Pt}(\text{NH}_3)_2(\text{H}_2\text{O})_2^{2+} \approx \text{Rh}_2(\mu\text{-O}_2\text{CCF}_3)_4$  (**8**) >  $\text{cis-Pt}(\text{NH}_3)_2\text{Cl}_2 \gg [\text{Rh}_2(\mu\text{-O}_2\text{CCH}_3)_2(\text{NCCH}_3)_6](\text{BF}_4)_2 > \text{Rh}_2(\mu\text{-O}_2\text{CCH}_3)_4$  (**1**)  $\approx \text{Pt}(\text{C}_6\text{H}_6\text{O}_4)(\text{NH}_3)_2$ , which is associated with the relative lability of the leaving groups. Compounds **1**, **8** and  $[\text{Rh}_2(\mu\text{-O}_2\text{CCH}_3)_2(\text{NCCH}_3)_6](\text{BF}_4)_2$  were also capable of binding covalently to double-stranded DNA forming stable intrastrand and interstrand crosslinks,<sup>247</sup> refuting early claims that  $\text{Rh}_2(\mu\text{-O}_2\text{CCH}_3)_4$  does not bind to double-stranded DNA.<sup>225,226</sup>

### *Dirhodium Anticancer Drugs Containing Polypyridyl Ligands*

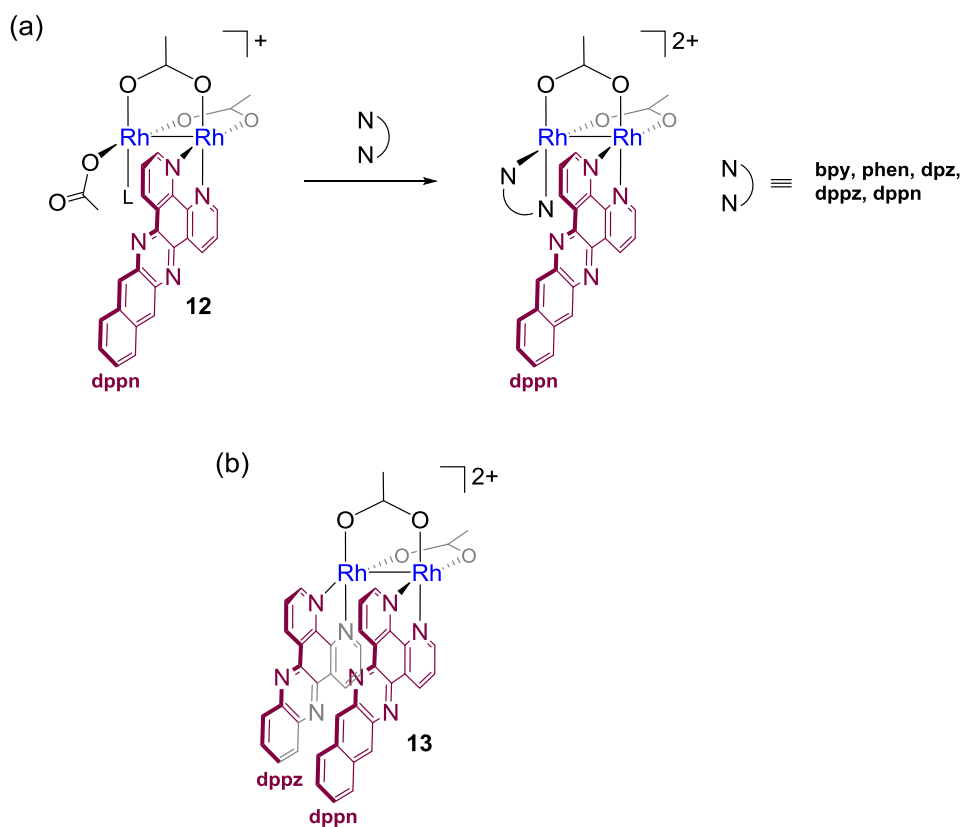
In 2009, the cytotoxic properties against cancer cells of the monocationic compounds of general formula  $[\text{Rh}_2(\mu\text{-O}_2\text{CCH}_3)_2(\eta^1\text{-O}_2\text{CCH}_3)(\text{N}^{\wedge}\text{N})(\text{CH}_3\text{OH})_3][\text{O}_2\text{CCH}_3]$ , where  $\text{N}^{\wedge}\text{N}$  are polypyridyl ligands (bpy, phen, dpq, dppz, dppn), were reported (Figure 4.9a).<sup>248</sup> The five compounds showed  $\text{IC}_{50}$  values ( $\text{IC}_{50}$  is the concentration of compound required to inhibit 50% of cell survival) in the 80–130  $\mu\text{M}$  and 50–70  $\mu\text{M}$  range against HeLa and COLO-316 tumor cells, respectively. Those incorporating the dppz and dppn ligands (**11** and **12**, respectively, Figure 4.9b) were the most active. These two compounds interact strongly with DNA through intercalation *in vitro* and induce DNA strand breaks *in cellulo*, as assessed by the comet assay (a cell-based assay that detects single- and double-strand breaks, as well as DNA crosslinking after treatment of cells with a cytotoxic compound<sup>249</sup>). It was also proven that the generation of reactive oxygen species is not responsible for the observed DNA damage. Therefore, it was concluded that nuclear DNA is a potential cellular target for these type of compounds and that the DNA strand breaks that were observed are a consequence of a direct interaction of nuclear DNA with the dirhodium compounds.<sup>248</sup>

Substitution of the  $\eta^1\text{-O}_2\text{CCH}_3$  ligand in **12** by  $\text{N}^{\wedge}\text{N}$  (bpy, phen, dpq, dppz, dppn) afforded the dicationic compounds of general formula  $[\text{Rh}_2(\mu\text{-O}_2\text{CCH}_3)_2(\text{dppn})(\text{N}^{\wedge}\text{N})(\text{CH}_3\text{OH})_2][\text{O}_2\text{CCH}_3]_2$  (Figure 4.10a).<sup>250</sup> Among this series, compound **13** ( $\text{N}^{\wedge}\text{N} = \text{dppz}$ , Figure 4.10b) neither intercalates into DNA nor produces significant DNA strand breaks. Nevertheless, it is the most cytotoxic among these five

compounds with IC<sub>50</sub> values of 82 and 68 μM against HeLa and COLO-316 cells, respectively, supporting the contention that other cellular targets/mechanism of action are possible by changing the ligand environment around the dimetal unit, a finding that opens up new opportunities for dirhodium compounds in cancer drug research.<sup>250</sup>



**Figure 4. 9** Dirhodium compounds with one polypyridyl bidentate ligand (N<sup>N</sup>) in the equatorial position. L denotes an equatorially bound methanol ligand; the axial methanol ligands have been omitted for the sake of clarity.

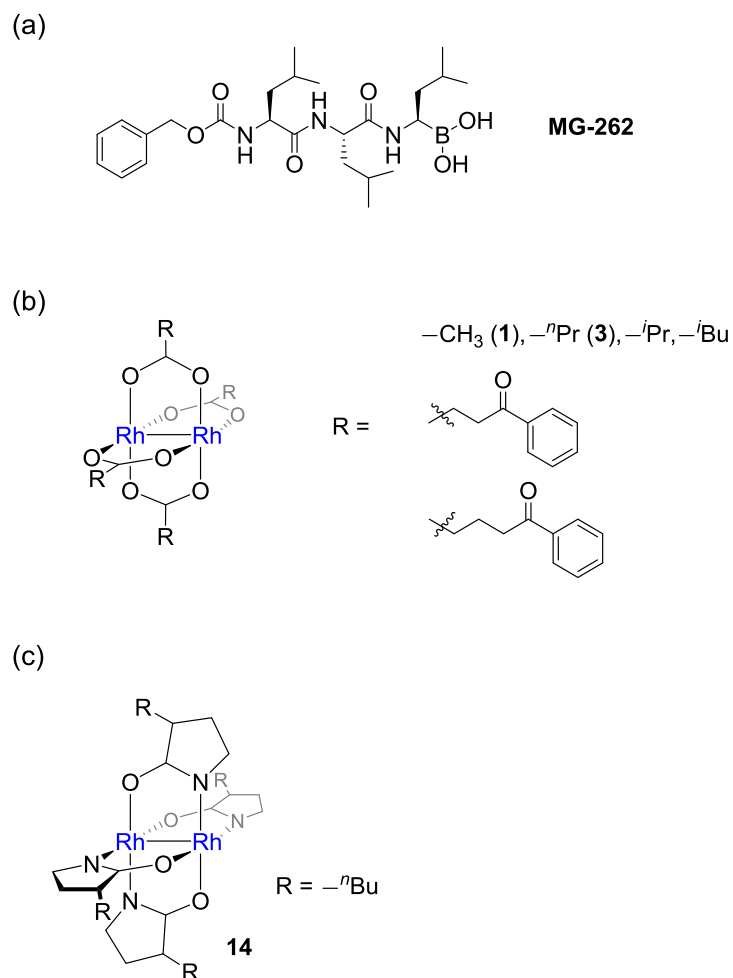


**Figure 4. 10**  $\text{Rh}_2^{4+}$  compounds with two polypyridyl bidentate ligand ( $\text{N}^{\text{N}}$ ) in the equatorial position. L denotes an equatorially bound methanol ligand; the axial methanol ligands have been omitted for the sake of clarity.

### *Ubiquitin-Proteasome System as a Potential Target*

Che and coworkers very recently reported (2012) a new target for compounds **1** and **3**.<sup>251</sup> They first determined the global transcriptional changes and the cytotoxicity profiles of these dirhodium compounds against the NCI-60 cancer cell line panel (National Cancer Institute, USA; it represents 60 cell lines from nine tumor types). The gene expression patterns altered by **1** and **3**, and their cytotoxicity profiles, were compared with those of known drugs using a bioinformatics approach to find similar patterns of activity. It was found that the signatures of **1** and **3** are similar to that of the cell permeable proteasome inhibitor MG-262 (*Z*-Leu-Leu-Leu-B(OH)<sub>2</sub>, Figure 4.11a), indicating that the ubiquitin-proteasome system (UPS; a system that consists of the degradation of ubiquitinated proteins by proteasome) may be a target of these dirhodium compounds. They also found that the cytotoxicity profile of **3** against the NCI-60 panel is very different than that of cisplatin, suggesting a different mechanism of action between **3** and the platinum (Pt) drug.





**Figure 4. 11** Molecular structures of (a) MG-262, (b) dirhodium tetracarboxylate compounds that behave as UPS inhibitors, and (c) dirhodium tetrapyrrolidinonato (**14**). The axial ligands have been omitted for the sake of clarity.

Subsequently, the authors determined that the highly cytotoxic compound **3** induces the accumulation of polyubiquitinated proteins in HeLa cells in a similar fashion as MG-262, whereas cisplatin is not able to produce the same effect, which further supports the different mechanism of action of **3** and cisplatin.<sup>251</sup> Additional *in vitro* experiments revealed that **3** inhibits both the proteolytic activity of proteasome (purified 20S proteasome) and the deubiquitinating activity of proteasomal deubiquitinating enzymes (UCH-L5), indicating that **3** may interact directly with UPS. They extended the study to other dirhodium tetracarboxylates (Figure 4.11b) and found a significant correlation between the cytotoxicity of all the tested compounds and their proteasome inhibitory activities, as well as their ability to induce the accumulation of ubiquitinated proteins, concluding that the inhibition of UPS is an important mechanism of action of the dirhodium tetracarboxylate compounds evaluated in that study.<sup>251</sup>

The authors also assessed the ability of **3** to damage DNA *in cellulo* by using the comet assay. In contrast to doxorubicin or cisplatin (which rapidly produced DNA damage), compound **3** did not affect the DNA of HeLa cells at its cytotoxic IC<sub>50</sub> concentration (0.5 μM). Significant DNA damage was observed only at concentrations higher (~10-fold) than that required to inhibit UPS activity or to induce cell death. Additionally, HeLa cells were incubated with the six dirhodium tetracarboxylate compounds (Figure 4.11b); the nuclear and cytoplasmic fractions were isolated and the metal content was analyzed by inductively coupled plasma mass spectrometry (ICP-MS). Only 10–25% rhodium content was found in the nuclear fraction, whereas the remaining ~80% was found in cytoplasmic fractions,<sup>251</sup> supporting that contention that

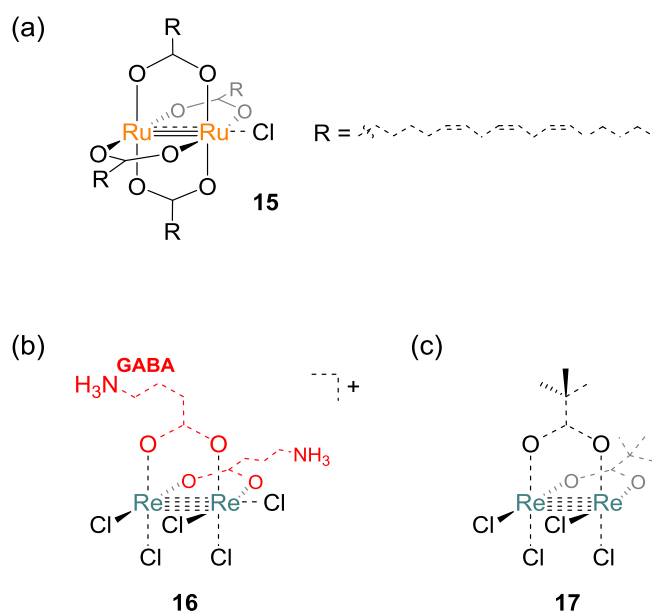
UPS inhibition plays an important role in the cytotoxic effect of dirhodium tetracarboxylates and complementing the DNA binding studies reported before.

The UPS inhibitory activity of the highly cytotoxic tetrapyrrolidinonato compound  $\text{Rh}_2(\mu\text{-NObutyl})_4$  (**14**; Figure 4.11c,  $\text{IC}_{50} \sim 1 \mu\text{M}$  against several cancer cell lines) was also evaluated. It was found that incubation of cancer cells with **14** neither induced the accumulation of polyubiquitinated proteins nor affected the proteolytic activity of proteasome. Compound **14** does not induce DNA damage (as determined by the comet assay) at its  $\text{IC}_{50}$  concentration, but it does it at higher concentrations ( $\sim 10$ -fold) as in the case of **3**, and it shows low accumulation in the nucleus ( $< 20\%$ ) of HeLa cells. Therefore, these studies also reveal that other cellular targets may be reached by fine-tuning the nature of the equatorial ligands,<sup>251</sup> as was demonstrated by the studies from the Dunbar group in previous cases.<sup>250</sup>

#### *Other M–M Bonded Anticancer Compounds*

Diruthenium and dirhenium compounds have been less studied than their dirhodium counterparts, but there are remarkable examples of potential antitumor compounds. For instance, the tetracarboxylate  $\text{Ru}_2^{5+}$  compound  $\text{Ru}_2(\text{aGLA})\text{Cl}$  (**15**; aGLA = deprotonated  $\gamma$ -linolenic acid, Figure 4.12a) inhibits C6 rat glioma cell proliferation and induces apoptosis *in vitro*.<sup>219,252</sup> The  $\text{Re}_2^{6+}$  compound *cis*- $[\text{Re}_2(\text{GABA})_2\text{Cl}_5]^+$  (**16**, Figure 4.12b) was shown to be effective at inhibiting tumor growth (Guerink T8) in mice<sup>253</sup> and the combination of *cis*- $\text{Re}_2(\mu\text{-O}_2\text{CC}(\text{CH}_3)_3)_2\text{Cl}_4$  (**17**;

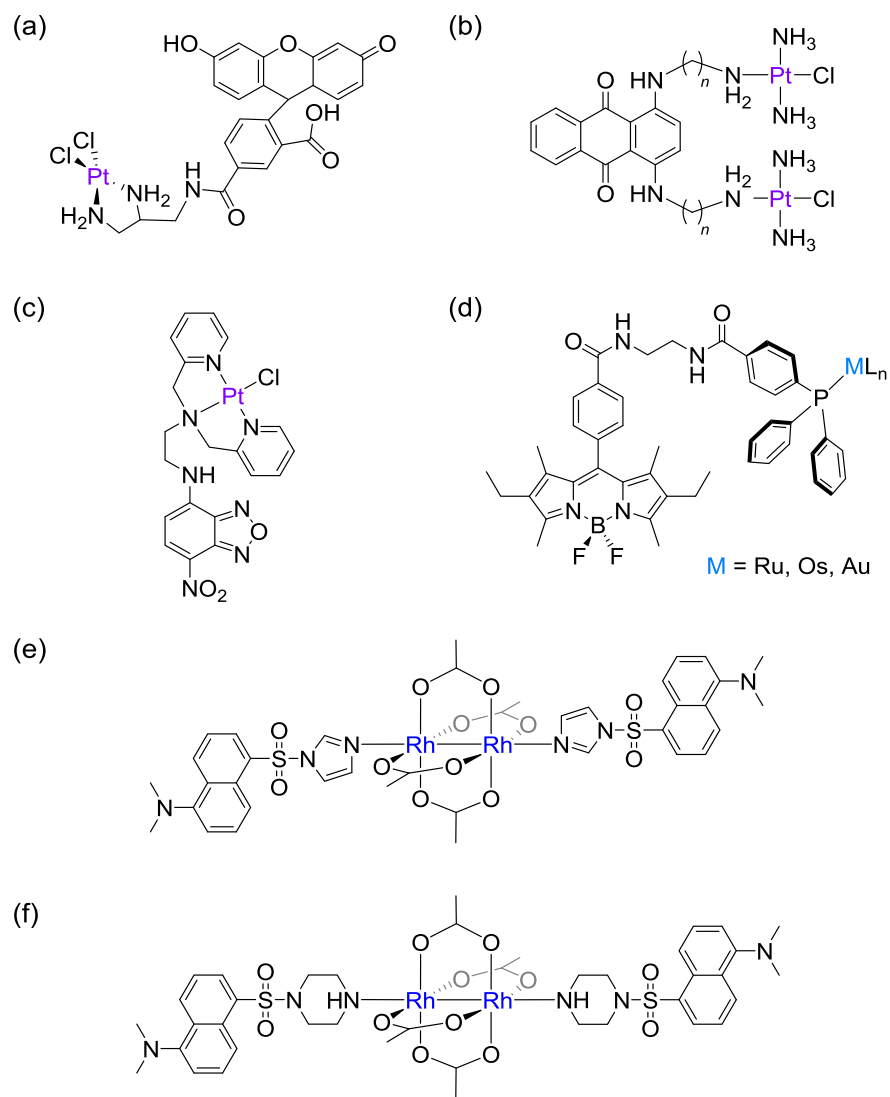
Figure 4.12c) and cisplatin lead to suppression of tumor growth or complete tumor elimination in mice.<sup>254</sup>



**Figure 4. 12** Molecular structures of antitumor diruthenium and dirhenium compounds. The axial solvent molecules have been omitted for the sake of clarity.

## Intracellular Distribution of Metal-Based Drugs

Although the interactions of dirhodium compounds with DNA have been studied extensively,<sup>218</sup> less is known about the cellular distribution of this class of inorganic molecules in living cancer cells. Tethering an organic fluorophore to non-photoluminescent metal anticancer drugs is a successful strategy to map their intracellular distribution using fluorescence microscopy.<sup>255</sup> In fact, this approach has been vital for understanding the intracellular behavior of Pt drugs. For example, live cell imaging studies of fluorescein-labeled cisplatin analogs (Figure 4.13a) in human osteosarcoma and ovarian carcinoma cells showed that these Pt drugs were sequestered into lysosomes, accumulated in the nucleus and Golgi-derived vesicles, and colocalized with the copper efflux transporters ATP7A and ATP7B.<sup>256,257,258</sup> Also Pt drugs formed by linking cisplatin units with the fluorescent intercalator anthraquinone<sup>259</sup> (Figure 4.13b) or with fluorescein-labeled diamine linkers<sup>260</sup> have also been shown to accumulate in the nucleus of human osteosarcoma cells.

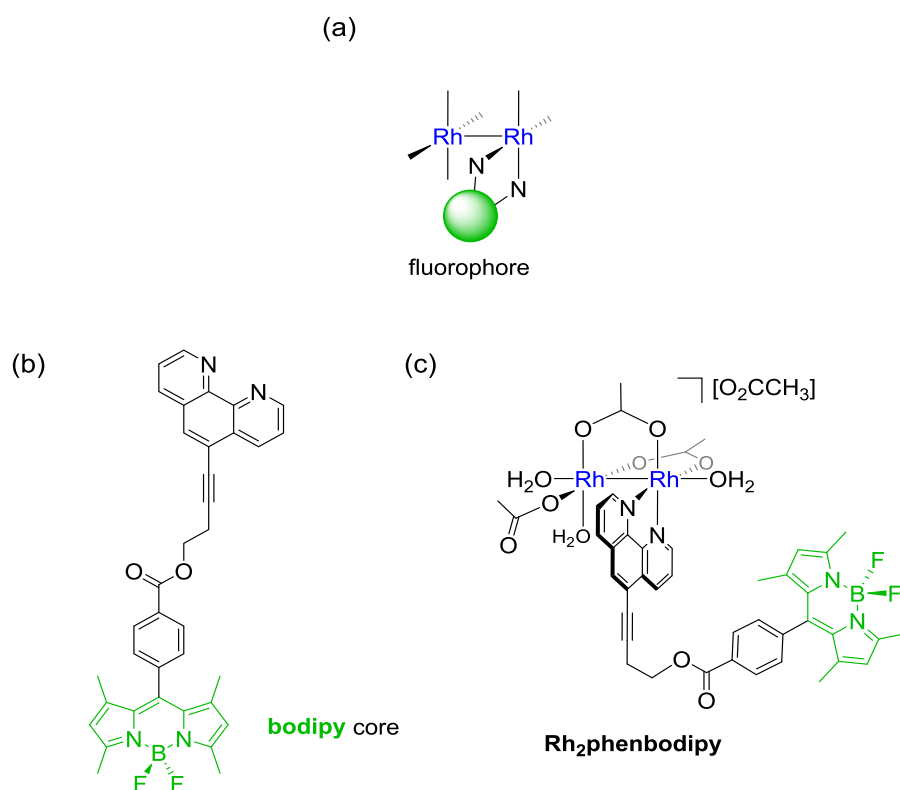


**Figure 4. 13** Molecular structures of fluorophore-labeled metal complexes.

*In vivo* fluorescence imaging studies of a NBD-tethered Pt drug (NBD = nitrobenzoxadiazole, Figure 4.13c) in zebrafish larve (a transparent small animal model) has also been reported.<sup>261</sup> More recently, mononuclear ruthenium(II), osmium(II) and gold(I) anticancer complexes were tagged with a bodipy-phosphine (bodipy = 4,4-difluoro-4-bora-3a,4a-diaza-s-indacene) fluorescent monodentate ligand (Figure 4.13d).<sup>262</sup> Lippard and coworkers reported in 2004 that dirhodium acetate can be labeled with dansyl-imidazole (Figure 4.13e) or dansyl-piperazine (Figure 4.13f) via coordination to the axial position.<sup>263</sup> Such compounds were not photoluminescent due to fluorescence quenching by the dimetal core. However, reaction with nitric oxide (NO) in CH<sub>2</sub>Cl<sub>2</sub> releases the axial ligands and “turns-on” the fluorescence of either free dansyl-imidazole or dansyl-piperazine, making these compounds useful NO sensors. If dissolved in water, these Rh<sub>2</sub>-fluorophore adducts are not stable since water, as well as N-donor ligands such as pyridine, can easily displace the fluorophore from the labile axial positions.<sup>263</sup>

In an effort to obtain further insight into the intracellular fate of dirhodium compounds and identify other key targets, and taking into consideration the fact that close attachment of a fluorophore to the Rh<sub>2</sub><sup>4+</sup> core leads to fluorescence quenching, we sought to attach a bidentate ligand tagged with a fluorophore to the equatorial position Rh<sub>2</sub><sup>4+</sup> core (Figure 4.14a). Therefore, a 1,10-phenanthroline derivative tethered to a bodipy fluorescent tag, phenbodipy (Figure 4.14b), was synthesized and coordinated to the dirhodium unit to afford the fluorophore-labeled compound [Rh<sub>2</sub>(μ-O<sub>2</sub>CCH<sub>3</sub>)<sub>2</sub>(η<sup>1</sup>-O<sub>2</sub>CCH<sub>3</sub>)(phenbodipy)(H<sub>2</sub>O)<sub>3</sub>][O<sub>2</sub>CCH<sub>3</sub>] (**Rh<sub>2</sub>phenbodipy**, Figure 4.14c). The

subcellular localization of this novel fluorescent dirhodium compound has been studied in human lung adenocarcinoma (A549) cells using laser scanning confocal fluorescence microscopy. To our knowledge, **Rh<sub>2</sub>phenbodipy** constitutes the first fluorescent M–M bonded compound.



**Figure 4. 14** (a) Schematic representation of a dirhodium compound tagged with a fluorophore in the equatorial position. Molecular structures of (b) phenbodipy and (c) **Rh<sub>2</sub>phenbodipy**.



## Experimental Section

### *General Methods*

The solvents used were of reagent grade quality. Dichloromethane ( $\text{CH}_2\text{Cl}_2$ , EMD Chemicals) was dried over  $4\text{\AA}$  and diisopropylamine (Alfa Aesar) was dried with  $\text{CaH}_2$ , which were distilled prior to use. The solvents methanol (MeOH, EMD Chemicals) and acetone (EMD Chemicals) were used as received without further purification. Standard Schlenk-line techniques ( $\text{N}_2$  atmosphere) were used to maintain anaerobic conditions during preparation of the compounds. Analytical thin layer chromatography (TLC) was performed on aluminum-backed sheets coated with silica 60 F254 adsorbent (0.20 mm thickness, EMD Chemicals). Flash chromatography (FC) was carried out with silica gel 60 (40-63  $\mu\text{m}$ , Fluka).  $\text{RhCl}_3 \cdot n\text{H}_2\text{O}$  (Pressure Chemical Co.), anhydrous DMF (Sigma Aldrich), 1,10-phenanthroline (Alfa Aesar), 3-butyn-1-ol (Sigma Aldrich),  $\text{Pd}(\text{PPh}_3)_2\text{Cl}_2$  (Sigma Aldrich), CuI (Spectrum Chemicals), KCN (Alfa Aesar), DMAP (Acros Organics) and EDAC $\cdot\text{HCl}$  (AKScientific) were purchased and used without further characterization. The compounds 5-bromo-1,10-phenanthroline (**18**),<sup>264</sup>  $\text{Rh}_2(\mu\text{-O}_2\text{CCH}_3)_4 \cdot 2\text{MeOH}$ ,<sup>265</sup>  $[\text{Rh}_2(\mu\text{-O}_2\text{CCH}_3)_2(\eta^1\text{-O}_2\text{CCH}_3)(\text{L})(\text{CH}_3\text{OH})_3][\text{O}_2\text{CCH}_3]$  (L= bpy, phen)<sup>266</sup> and bodipy-COOH<sup>267</sup> were prepared according to published procedures.

## *Instrumentation*

<sup>1</sup>H NMR spectra were recorded on Mercury 300 MHz or Inova 500 MHz spectrometers. Chemical shifts are reported in  $\delta$  (ppm) and coupling constants ( $J$ ) in hertz (Hz). The residual solvent peak was used as an internal reference ( $\delta$  3.31 for CD<sub>3</sub>OD,  $\delta$  7.26 for CDCl<sub>3</sub>). Electrospray mass spectra were acquired on an Applied Biosystems PE SCIEX QSTAR mass spectrometer (MDS Sciex). Elemental analyses were performed by Atlantic Microlab, Inc. (Norcross, GA). Absorption spectra were recorded on a Shimadzu UVPC-3001 spectrophotometer.

A PTI QuantaMaster series spectrophotometer was used to perform the steady-state fluorescence spectroscopic studies at room temperature. Measurements were taken in aerated solutions. The slit width was set to 1 nm for both excitation and emission, the step size was set to 1 nm and the integration time to 0.1 s. All the spectra were corrected (real time correction) to account for variances in the arc lamp intensity and PMT voltage across the range of wavelengths. A long pass filter (455 nm) was placed between the sample and detector before the acquisition of the spectra. The relative fluorescence quantum yields ( $\Phi$ ) were calculated using fluorescein (Sigma Aldrich) as reference ( $\Phi_F = 0.95$  in 0.1M NaOH) and the following equation:

$$\Phi_x = \Phi_r \left[ \left( \frac{I_x}{A_x} \right) / \left( \frac{I_r}{A_r} \right) \right] \left( \frac{\eta_x}{\eta_r} \right)^2$$

where the subscripts “r” and “x” are used to denote the reference and the sample, respectively,  $I$  is the integrated sum of the emission intensity,  $A$  is the absorbance at the excitation wavelength ( $\lambda_{\text{ex}} = 496 \text{ nm}$ ) and  $\eta$  is the refractive index of the solvents used.

### *Synthetic Procedures*

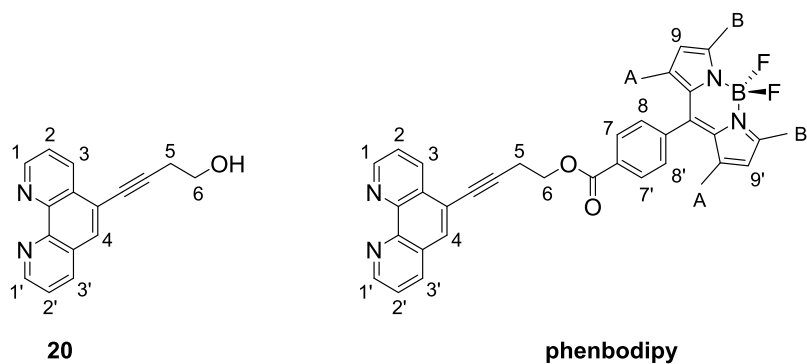
**4-(1,10-phenanthrolin-5-yl)but-3-yn-1-ol (20).** A Schlenk flask was charged with  $\text{Pd}(\text{PPh}_3)_2\text{Cl}_2$  (109 mg, 0.15 mmol), CuI (30 mg, 0.16 mmol) and DMF (3 mL). Then, 5-bromo-1,10-phenanthroline (400 mg, 1.54 mmol), diisopropyl amine (2 mL) and 3-butyn-1-ol (235  $\mu\text{L}$ , 3.08 mmol) were added. The resulting dark brown solution was heated at  $80^\circ\text{C}$  for 2 h and the solvent was removed under reduced pressure to give a dark brown oily residue, which was dissolved in MeOH (10 mL). A solution of KCN (100 mg, 1.54 mmol) in  $\text{H}_2\text{O}$  (5 mL) was added and the color of the solution changed instantaneously from dark brown to light yellow. The resulting solution was stirred for 1 h and then was diluted with  $\text{H}_2\text{O}$  (30 mL) and extracted with  $\text{CH}_2\text{Cl}_2$  (5 x 40 mL). The combined organic layers were dried with  $\text{MgSO}_4$ , and reduced to dryness. The residue was purified by FC ( $\text{SiO}_2$ ,  $\text{CH}_2\text{Cl}_2/\text{MeOH}/\text{Et}_3\text{N}$  91:8:1) to afford **3** as a light beige solid. Yield: 307 mg (80%).  $^1\text{H}$  NMR (300 MHz,  $\text{CDCl}_3$ ):  $\delta$  9.20 (dd, 1H,  $^3J = 4.2$ ,  $^4J = 1.8$ , H-1 or H-1'), 9.17 (dd, 1H,  $^3J = 4.2$ ,  $^4J = 1.8$ , H-1' or H-1), 8.70 (dd, 1H,  $^3J = 8.1$ ,  $^4J = 1.5$ , H-3), 8.17 (dd, 1H,  $^3J = 8.1$ ,  $^4J = 1.5$ , H-3'), 7.92 (s, 1H, H-4), 7.68 (dd, 1H,  $^3J = 8.1$ ,  $^3J = 4.2$ , H-2 or H-2'), 7.63 (dd, 1H,  $^3J = 8.1$ ,  $^3J = 4.2$ , H-2' or H-2), 3.99 (t, 2H,  $^3J = 6.3$ ,

H-6), 2.89 (t, 2H,  $^3J = 6.3$ , H-5), 2.27 (s, 1H, -OH). HRMS (ESI<sup>+</sup>): Calcd for C<sub>16</sub>H<sub>13</sub>N<sub>2</sub>O ([M + H]<sup>+</sup>), 249.1028. Found 249.1035.

**Phenbodipy.** A solution of bodipy-COOH (67 mg, 0.18 mmol) and **20** (55 mg, 0.22 mmol) in CH<sub>2</sub>Cl<sub>2</sub> (25 mL) was cooled to 0°C, and EDAC•HCl (62 mg, 0.32 mmol) and DMAP (23 mg, 0.19 mmol) were added. The resulting green-orange solution was stirred at 0°C for 6 h and then warmed up to ambient temperature slowly before being stirred for a further 48 h. The solution was washed with 0.1 M HCl (20 mL) and a saturated solution of NaHCO<sub>3</sub> (20 mL). The organic phase was dried with anhydrous MgSO<sub>4</sub> and purified by FC (SiO<sub>2</sub>, CH<sub>2</sub>Cl<sub>2</sub>/EtOAc/MeOH/Et<sub>3</sub>N 50:46:2:2) to afford phenbodipy as a bright orange solid. Yield: 93 mg (85%). <sup>1</sup>H NMR (300 MHz, CDCl<sub>3</sub>): δ 9.19 (m, 2H, H-1 and H-1'), 8.74 (d, 1H,  $^3J = 8.4$ , H-3), 8.26 (d, 2H,  $^3J = 7.8$ , H-7, H-7'), 8.19 (d, 1H,  $^3J = 8.1$ , H-3'), 7.99 (s, 1H, H-4), 7.65 (m, 2H, H-2, H-2'), 7.43 (d, 2H,  $^3J = 7.8$ , H-8, H-8'), 5.98 (s, 2H, H-9, H-9'), 4.70 (t, 2H,  $^3J = 6.6$ , H-6), 3.15 (t, 2H,  $^3J = 6.6$ , H-5), 2.56 (s, 6H, CH<sub>3</sub><sup>B</sup>), 1.33 (s, 6H, CH<sub>3</sub><sup>A</sup>). HRMS (ESI<sup>+</sup>): Calcd for C<sub>36</sub>H<sub>30</sub>BF<sub>2</sub>N<sub>4</sub>O<sub>2</sub> ([M + H]<sup>+</sup>), 599.2430. Found 599.2457.

**Rh<sub>2</sub>phenbodipy.** Rh<sub>2</sub>(μ-O<sub>2</sub>CCH<sub>3</sub>)<sub>4</sub>•2MeOH (60 mg, 0.12 mmol) and phenbodipy (71 mg, 0.12 mmol) were dissolved in acetone (20 mL). The resulting dark green-orange solution was stirred at ambient temperature. An orange solid precipitated within 30 minutes and the mixture was left stirring for 24 h. The bright orange-red solid was collected by filtration and washed with acetone (3 x 10 mL) and then suspended in

MeOH (40 mL) and stirred for 24 h at ambient temperature. The resulting dark green-orange solution was concentrated to *ca.* 2 mL and diethyl ether (20 mL) was added slowly while stirring. The hygroscopic brown-orange precipitate was collected by filtration and washed with copious amounts of diethyl ether. Yield: 32 mg (25%). This compound was obtained as a 1:1 mixture of two geometric isomers.  $^1\text{H}$  NMR (500 MHz,  $\text{CD}_3\text{OD}$ ):  $\delta$  8.98 (m, 2H, H-1 or H-1'), 8.83-8.68 (m, 4H, H-1' or H-1, H-3 or H-3'), 8.65 (d, 2H,  $^3J = 8.5$ , H-3' or H-3), 8.29 (m, 6H, H-7, H-7', H-4), 8.00 (m, 2H, H-2 or H-2'), 7.95 (m, 2H, H-2' or H-2), 7.51 (d, 2H,  $^3J = 8.5$ , H-8, H-8'), 6.06 (s, 4H, H-9, H-9'), 4.72 (t, 4H,  $^3J = 6.0$ , H-6), 3.21 (m, 4H, H-5), 2.49 (s, 12H,  $\text{CH}_3^{\text{B}}$ ), 2.37 (s, 3H,  $\mu\text{-O}_2\text{CCH}_3^-$ ), 2.36 (s, 3H,  $\mu\text{-O}_2\text{CCH}_3^-$ ), 2.32 (s, 3H,  $\mu\text{-O}_2\text{CCH}_3^-$ ), 2.31 (s, 3H,  $\mu\text{-O}_2\text{CCH}_3^-$ ), 1.88 (s, 6H,  $\text{O}_2\text{CCH}_3^-$ ), 1.35 (s, 12H,  $\text{CH}_3^{\text{A}}$ ), 1.06 (s, 3H,  $\eta^1\text{-O}_2\text{CCH}_3^-$ ), 1.02 (s, 3H,  $\eta^1\text{-O}_2\text{CCH}_3$ ). MS (ESI+): 921.06 ( $[\text{M} - \text{O}_2\text{CCH}_3 - \text{H}]^+$ ), 981.01 ( $[\text{M}]^+$ ), 1013.12 ( $[\text{M} + \text{CH}_3\text{OH}]^+$ ), where M is  $[\text{Rh}_2(\mu\text{-O}_2\text{CCH}_3)_2(\eta^1\text{-O}_2\text{CCH}_3)(\text{phenbodipy})]^+$ . Anal. Calcd. for  $\text{C}_{44}\text{H}_{47}\text{BF}_2\text{N}_4\text{O}_{13}\text{Rh}_2 \cdot 2\text{H}_2\text{O}$ : C, 46.75; H, 4.55; N, 4.96. Found: C, 46.45; H, 4.47; N, 5.19.



**Figure 4. 15** Numbering scheme used to describe the  $^1\text{H}$  NMR spectra of **20** and phenbodipy.

### *Cell Culture*

The A549 cell line, derived from type II pneumocytes (CCL 185), was obtained from American Type Culture Collection (Manassas, VA). The cells were cultured in DMEM-F12 medium (Dulbecco's Modified Eagle Medium: Nutrient Mixture F-12) with 10% FBS. Cultures were approximately 80% confluent at the time of analysis. Cell cultures were incubated in a humidified atmosphere containing 5%  $\text{CO}_2$  at 37°C.

### *In vitro Cytotoxicity*

Cells were plated in 96 well plate and were pre-incubated at 37°C for 24 h. Solutions of **Rh<sub>2</sub>phenbodipy** complex in DMEM/F12 medium were added at different concentrations (final concentrations: 0–100  $\mu\text{M}$  range) and the cells were incubated for

another 48 h. Cells were then washed twice with PBS and fixed with methanol for 30 min. Following fixation, Janus green B (1 mg/mL, Alfa Aesar) was added to each well and incubated at room temperature for 5 min. Cells were again washed twice with PBS and 100  $\mu$ L of methanol was added to each well to extract the dye. Janus green B signal was then measured using a BioTek Synergy 4 plate reader set to an absorbance of 630 nm. The experiment was performed in triplicate.

### *Confocal Fluorescence Microscopy Studies*

Live cell imaging studies were performed using a Zeiss 510 META NLO multiphoton system consisting of an Axiovert 200 MOT inverted laser scanning confocal microscope (Carl Zeiss Microimaging, Thornwood, NY). A Zeiss Plan-Apochromat 63x/NA=1.4 oil immersion objective was used to acquire the images.

The compounds phenbodipy and **Rh<sub>2</sub>phenbodipy** were excited with an Ar-ion laser at 488 nm and emission was monitored using a band pass 500–550 filter. To collect Hoechst 33258 (Invitrogen) fluorescence, cells were irradiated with the Chameleon tunable Ti:Sapphire laser (Coherent Inc., Santa Clara, CA) at an excitation wavelength of 740 nm (which is roughly equivalent to 370 nm in single photon excitation with a continuous wavelength laser system) and emission was collected at 430–480 nm. Lysotracker Red DND-99 (Invitrogen) was excited with a He-Ne laser at 543 nm and emission was monitored using a BP 565–615 filter. Mitotracker Deep Red FM (Invitrogen) was excited with a He-Ne laser at 633 nm and emission was collected using

a BP 650–710 filter. Image acquisition was performed sequentially to reduce the possibility of bleedthrough between channels.

The cellular distribution of phenbodipy and **Rh<sub>2</sub>phenbodipy** was studied in A549 lung cancer cells. Cells were incubated (37°C) with either phenbodipy or **Rh<sub>2</sub>phenbodipy** at 1 μM concentration for 2 and 24 h and the cells were washed before collecting the images. In the case of the localization experiments with lysosomes, cells were incubated with **Rh<sub>2</sub>phenbodipy** (10 and 100 μM) for 5 and 24 h. Cells were then washed with PBS and loaded with 1 μg/mL Hoechst 33258 and 50 nM LysoTracker Red DND-99 for 30 min. Cells were then washed and imaged. At least 10 images were collected per time point per treatment. For analyzing the localization with mitochondria, cells were incubated with **Rh<sub>2</sub>phenbodipy** (10 and 100 μM) for 5 and 24 h. Cells were then washed with PBS and loaded with 1 μg/mL Hoechst 33258 and 100 nM Mitotracker Deep Red FM for 30 min. Cells were then washed and imaged. At least 10 images were collected per time point per treatment. Mander's colocalization coefficients of **Rh<sub>2</sub>phenbodipy** with either LysoTracker or Mitotracker were determined using the Image J software (National Institutes of Health, USA).

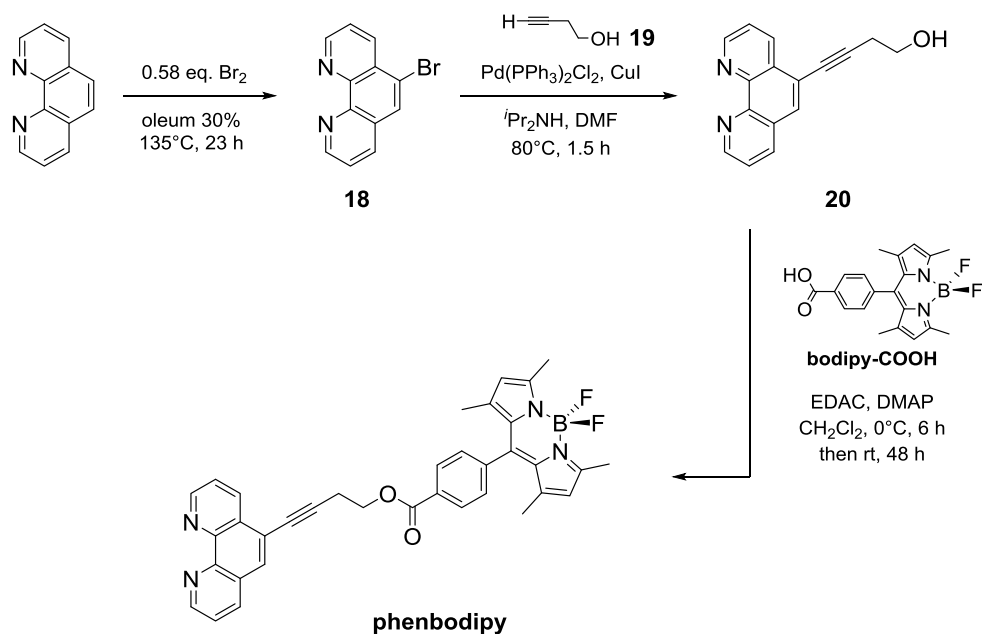
To monitor the cellular uptake of **Rh<sub>2</sub>phenbodipy**, cells were incubated with the metal complex at 10, 50 and 100 μM for 24 h. Cells were then washed and at least 8 images per concentration were collected and fluorescence intensities were recorded.



## Results and Discussion

### *Synthesis and Characterization*

The synthetic route to prepare phenbodipy is shown in Figure 4.16. First, 1,10-phenanthroline was brominated in the 5-position using Br<sub>2</sub> in 30% oleum (30% SO<sub>3</sub> in concentrated H<sub>2</sub>SO<sub>4</sub>) as previously described,<sup>264</sup> affording **9** in > 90% yield. The alcohol intermediate **20** was obtained in 80% yield by coupling **18** and the alkyne **19** by means of a Pd-catalyzed Sonogashira cross-coupling reaction using Pd(PPh<sub>3</sub>)<sub>2</sub>Cl<sub>2</sub>/CuI as catalyst system.<sup>268</sup> The synthesis of **20** has been reported using Pd(PPh<sub>3</sub>)<sub>4</sub> as catalyst, albeit in lower yield (58%).<sup>269</sup> The fluorescent compound bodipy-COOH was prepared following reported procedures<sup>267</sup> and was coupled to **20** via ester bond formation using 1-ethyl-3-(3-dimethylaminopropyl) carbodiimide (EDAC). The desired ligand phenbodipy was obtained in 85% yield as a bright orange solid after column chromatography and was characterized by mass spectrometry (HR-MS-ESI,  $m/z = 599.2457$  for [phenbodipy + H]<sup>+</sup>) and NMR.

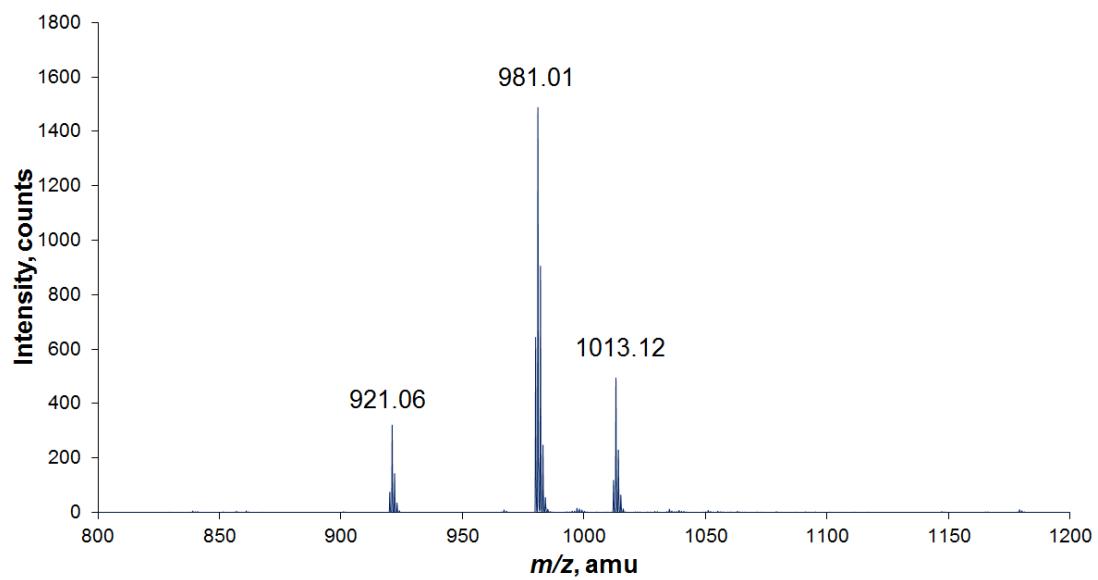


**Figure 4. 16** Synthesis of phenbodipy.

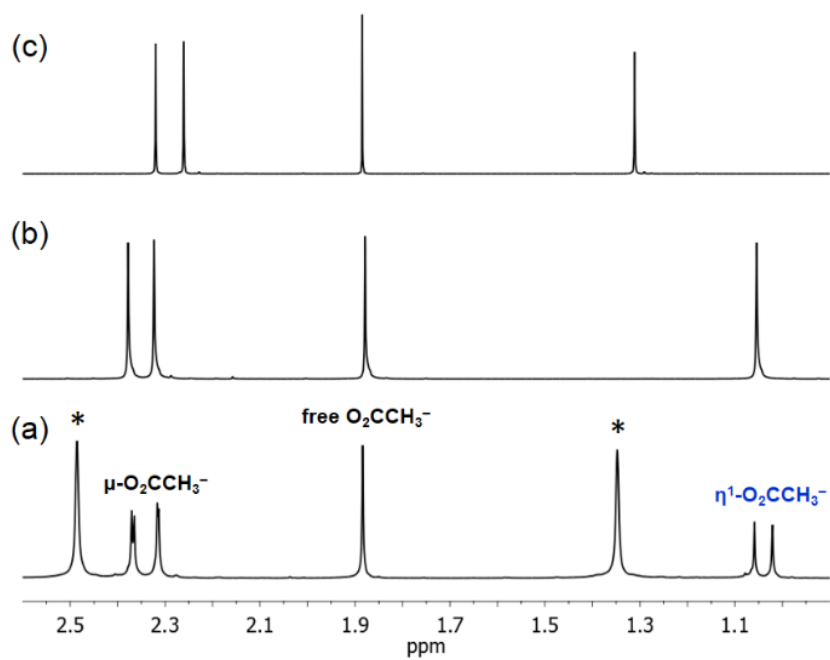
The fluorophore-labeled dirhodium compound was synthesized following the same synthetic methodology developed for the preparation of [Rh<sub>2</sub>(μ-O<sub>2</sub>CCH<sub>3</sub>)<sub>2</sub>(η<sup>1</sup>-O<sub>2</sub>CCH<sub>3</sub>)(N<sup>^</sup>N)(CH<sub>3</sub>OH)<sub>3</sub>][O<sub>2</sub>CCH<sub>3</sub>].<sup>248,266</sup> The Rh<sub>2</sub>(μ-O<sub>2</sub>CCH<sub>3</sub>)<sub>4</sub> compound was first reacted with 1 eq of phenbodipy in acetone for 24 h. The resulting orange precipitate was isolated, suspended in methanol and stirred for further 24 h. **Rh<sub>2</sub>phenbodipy** was obtained as a orange-brown solid upon precipitation with diethyl ether and it was characterized by elemental analysis, mass spectrometry (ESI+) and <sup>1</sup>H NMR. The mass spectrum of **Rh<sub>2</sub>phenbodipy** (Figure 4.17) showed three main peaks corresponding to

$[M - O_2CCH_3 - H]^+$  ( $m/z = 921.06$ ),  $[M]^+$  ( $m/z = 981.01$ ), and  $[M + CH_3OH]^+$  ( $m/z = 1013.12$ ), where M is  $[Rh_2(\mu-O_2CCH_3)_2(\eta^1-O_2CCH_3)(phenbodipy)]^+$ .

A section of the  $^1H$  NMR spectrum of **Rh<sub>2</sub>phenbodipy** is shown in Figure 4.18, including the spectra of the related compounds  $[Rh_2(\mu-O_2CCH_3)_2(\eta^1-O_2CCH_3)(phen)(CH_3OH)_3][O_2CCH_3]$  (**Rh<sub>2</sub>phen**) and  $[Rh_2(\mu-O_2CCH_3)_2(\eta^1-O_2CCH_3)(bpy)(CH_3OH)_3][O_2CCH_3]$  (**Rh<sub>2</sub>bpy**)<sup>248</sup> and the full spectrum of **Rh<sub>2</sub>phenbodipy** is shown in Figure 4.20. **Rh<sub>2</sub>phenbodipy** exhibits two singlet resonances at 1.02 and 1.06 ppm for the methyl group of the  $\eta^1-O_2CCH_3$  ligand, in contrast to the single singlet resonance observed in **Rh<sub>2</sub>phen** (1.05 ppm), **Rh<sub>2</sub>bpy** (1.31 ppm), **12** (1.11 ppm)<sup>270</sup> and **13** (1.23 ppm)<sup>271</sup> for the same ligand. Since phenbodipy does not possess the  $C_{2v}$  symmetry of phen or bpy, **Rh<sub>2</sub>phenbodipy** exists as a 1:1 mixture of two geometric isomers that differ just by the relative position of the  $\eta^1-O_2CCH_3^-$  ligand with respect to the triple bond of phenbodipy (Figure 4.19). The presence of four singlet resonances for the bridging ligands ( $\mu-O_2CCH_3^-$ , Figure 4.18) at 2.31, 2.32, 2.36 and 2.37 ppm supports the formation of two isomers.

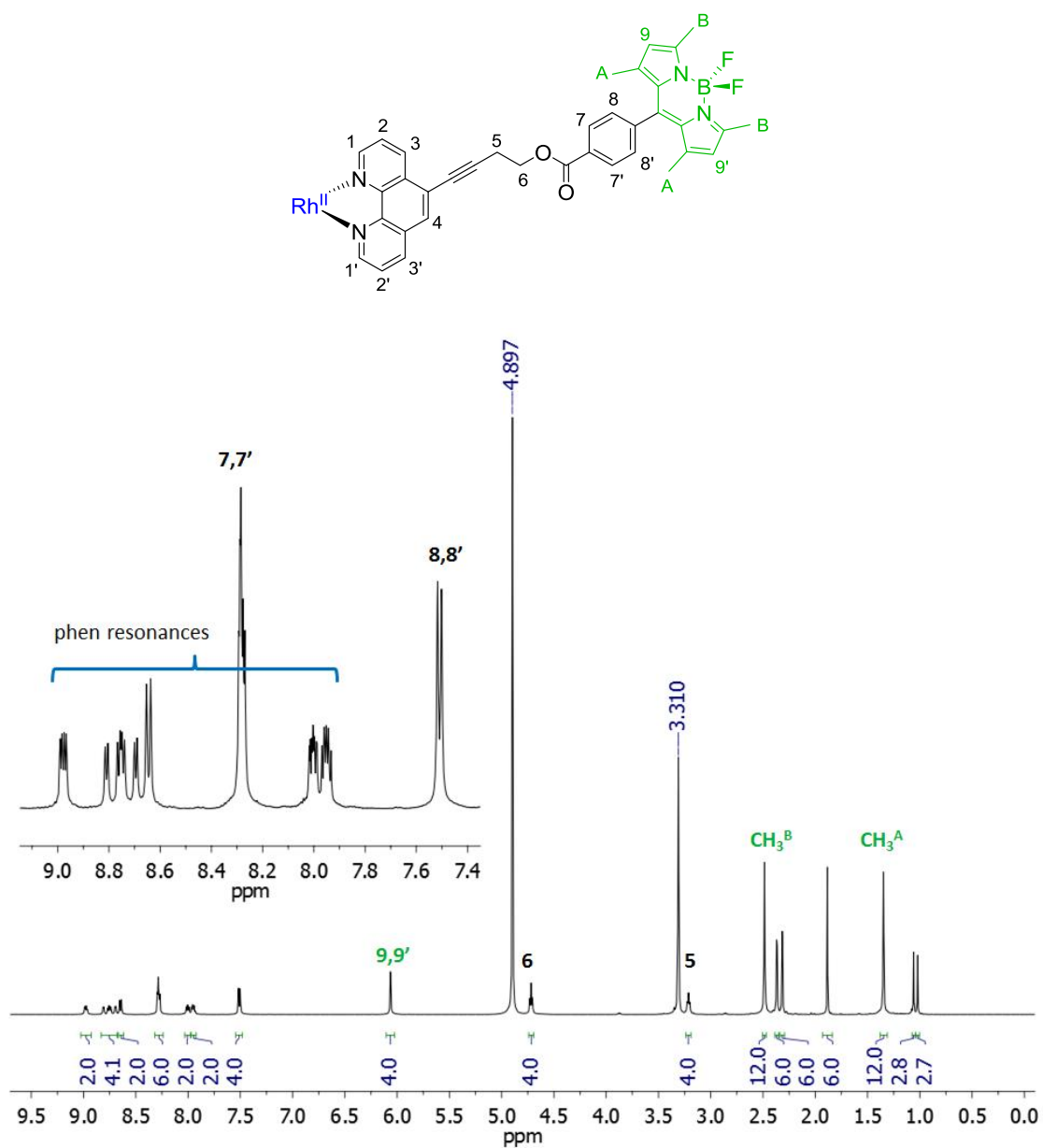


**Figure 4. 17** ESI(+) mass spectrum of **Rh<sub>2</sub>phenbodipy** in methanol.



**Figure 4. 18** Portion of the spectra of (a) **Rh<sub>2</sub>phenbodipy**, (b) Rh<sub>2</sub>phen and (c) Rh<sub>2</sub>bpy (500 MHz, CD<sub>3</sub>OD). The proton resonances marked with (\*) correspond to the methyl groups of bound phenbodipy.





**Figure 4. 20**  $^1\text{H}$  NMR spectrum of  $\text{Rh}_2\text{phenbodipy}$  (500 MHz,  $\text{CD}_3\text{OD}$ ). See experimental section for complete proton assignments.

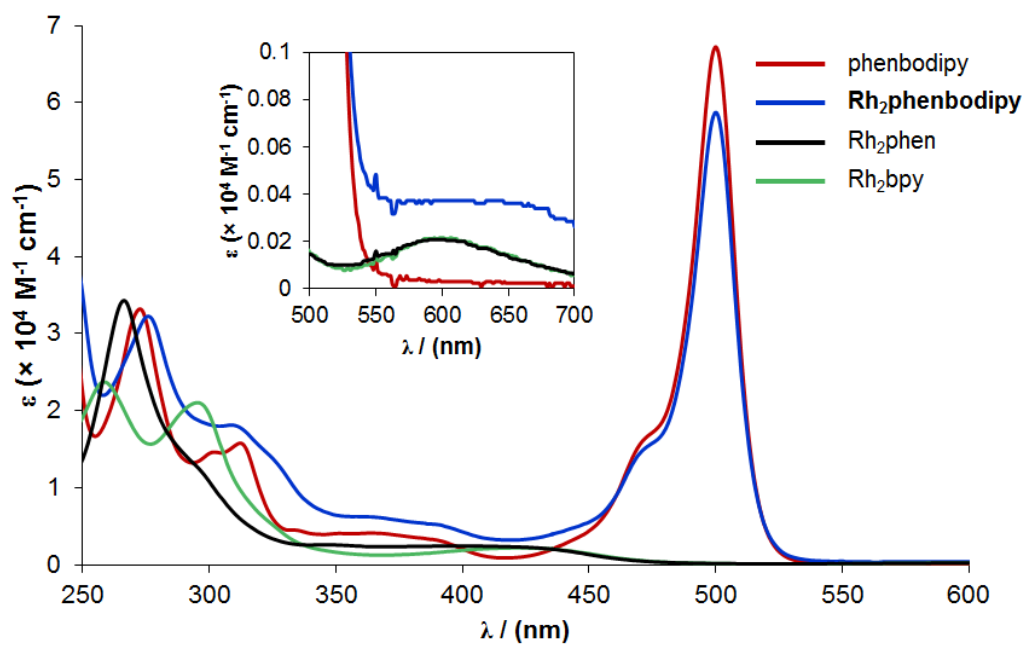
The electronic absorption spectra of phenbodipy and **Rh<sub>2</sub>phenbodipy** are shown in Figure 4.21. Both compounds exhibit an absorption maximum at 500 nm with similar intensities ( $\epsilon = 6.7 \times 10^4$  and  $5.9 \times 10^4 \text{ M}^{-1} \text{ cm}^{-1}$ , respectively) that corresponds to  $^1\pi\pi^*$  ligand-centered (LC) transitions from the bodipy moiety. The absorption maxima of both compounds in the UV region arise from superposed  $^1\pi\pi^*$  LC transitions of both bodipy and phenanthroline moieties.

**Rh<sub>2</sub>phenbodipy** exhibits a metal-to-ligand charge transfer ( $^1\text{MLCT}$ ) transition in the 400–450 nm region ( $\epsilon \sim 4 \times 10^3 \text{ M}^{-1} \text{ cm}^{-1}$ ) involving the  $\text{Rh}_2^{4+}$  core and the phenanthroline moiety of phenbodipy ( $\text{Rh}_2(\pi^*) \rightarrow \text{phen}(\pi^*)$ ), as also reported for  $\text{Rh}_2\text{phen}$  (415 nm,  $\epsilon = 2.4 \times 10^3 \text{ M}^{-1} \text{ cm}^{-1}$ ) and  $\text{Rh}_2\text{bpy}$  (424 nm,  $\epsilon = 2.1 \times 10^3 \text{ M}^{-1} \text{ cm}^{-1}$ ).<sup>266</sup> Additionally, **Rh<sub>2</sub>phenbodipy** exhibits a weak metal-centered (MC)  $\text{Rh}_2(\pi^*) \rightarrow \text{Rh}_2(\sigma^*)$  transition at 625 nm ( $360 \text{ M}^{-1} \text{ cm}^{-1}$ ) which is also observed in  $\text{Rh}_2\text{phen}$  (600 nm,  $220 \text{ M}^{-1} \text{ cm}^{-1}$ ),  $\text{Rh}_2\text{bpy}$  (598 nm,  $215 \text{ M}^{-1} \text{ cm}^{-1}$ ) and related dirhodium compounds.<sup>266,272,273</sup>

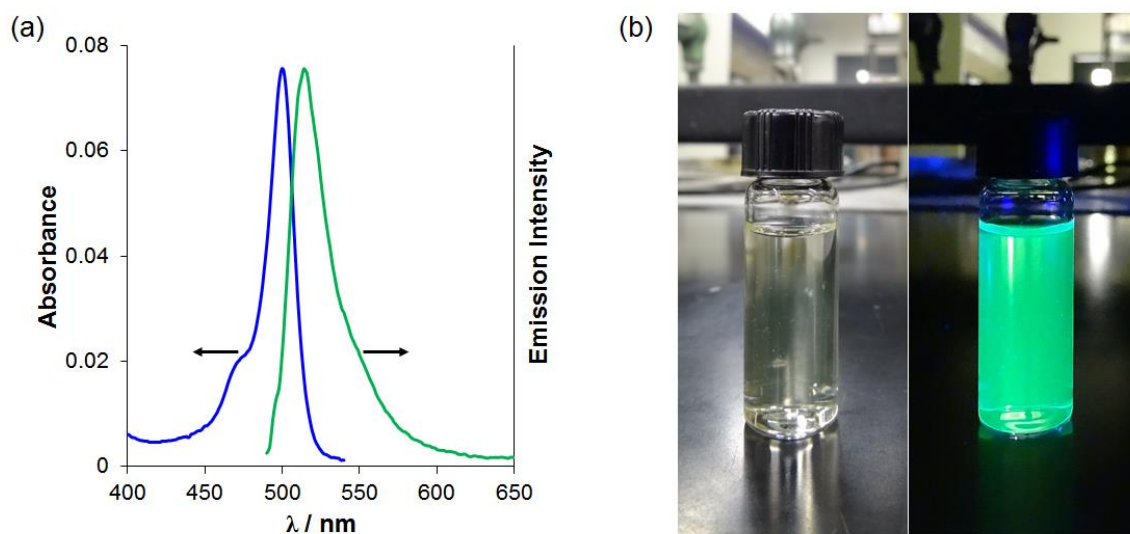
The ligand phenbodipy exhibits green fluorescence emission in methanol solution (Figure 4.22b) with a maximum at 512 nm ( $\lambda_{\text{ex}} = 496 \text{ nm}$ ) and a fluorescence quantum yield ( $\Phi_{\text{F}}$ ) of 20%. **Rh<sub>2</sub>phenbodipy** also exhibits green fluorescence emission with a maximum at 514 nm (Figure 4.22a) and  $\Phi_{\text{F}}$  of 0.05 ( $\lambda_{\text{ex}} = 496 \text{ nm}$ ) in the same solvent. Although the emission from phenbodipy is partially quenched when bound to the dimetal unit, it allows us to perform live cell imaging studies in the 1–100  $\mu\text{M}$  range.



Therefore, increasing the distance between the  $\text{Rh}_2^{4+}$  core and the fluorophore was a successful strategy to afford a fluorescent dirhodium compound.



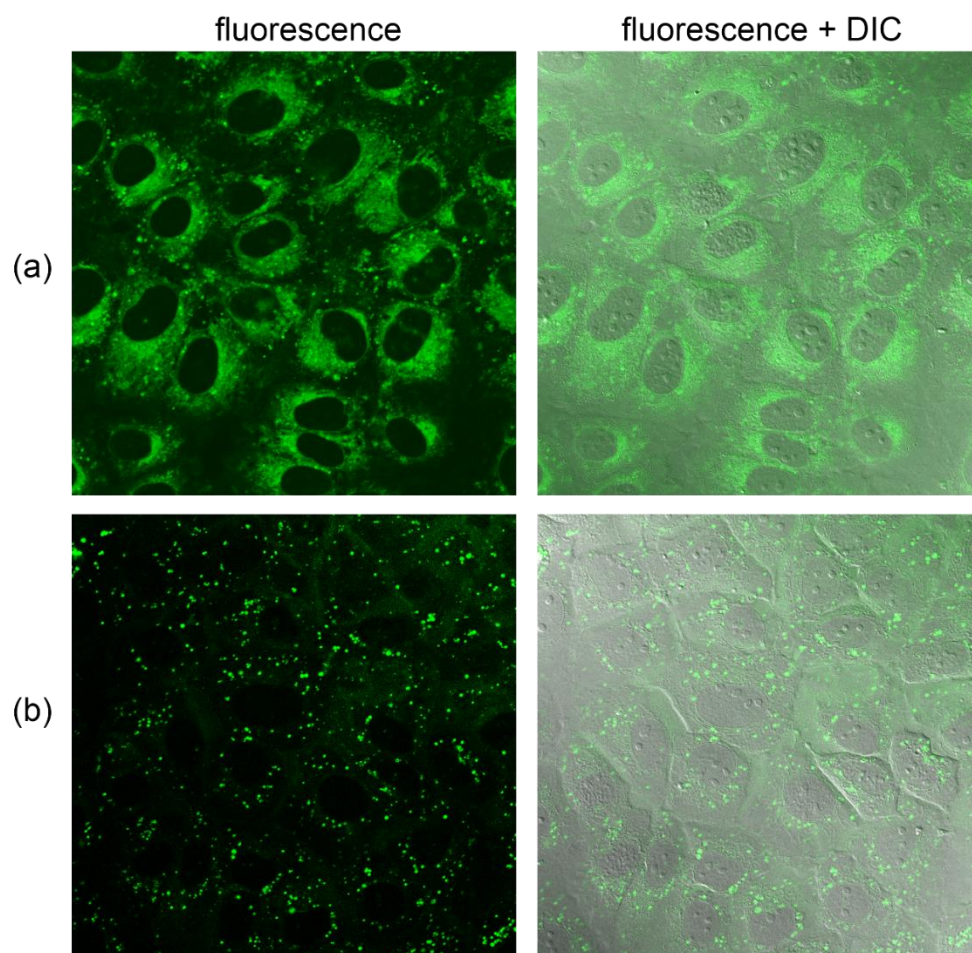
**Figure 4. 21** Electronic absorption spectrum of phenbodipy and dirhodium compounds in methanol. Inset: absorption maxima in the 500–700 nm region corresponding to the MC  $\text{Rh}_2(\pi^*) \rightarrow \text{Rh}_2(\sigma^*)$  transition.



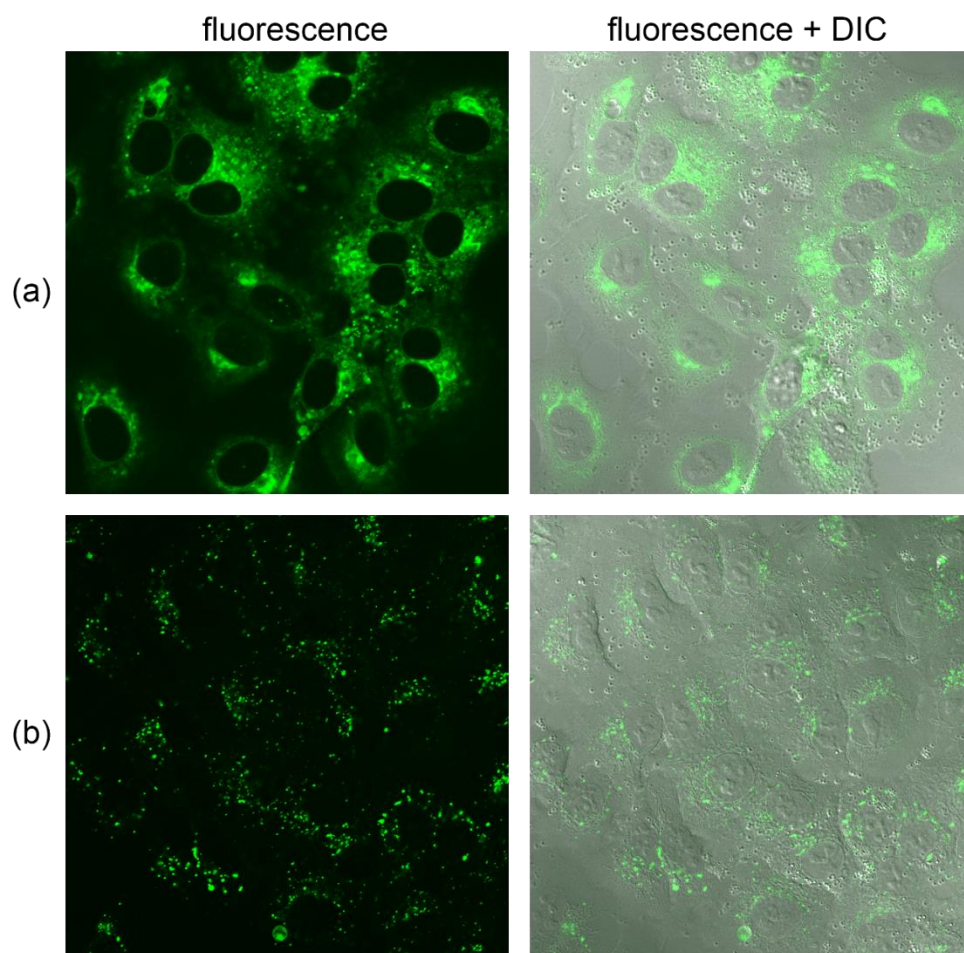
**Figure 4. 22** (a) Absorption (blue) and normalized emission (green,  $\lambda_{\text{ex}} = 496$  nm) spectra of **Rh<sub>2</sub>phenbodipy** in methanol. (b) Photograph depicting green fluorescence ( $\lambda_{\text{ex}} = 254$  nm from a hand-held UV lamp) of a 1  $\mu\text{M}$  solution of phenbodipy in methanol.

### *Laser Scanning Confocal Fluorescence Microscopy Studies*

Human lung adenocarcinoma (A549) cells were incubated with phenbodipy (1  $\mu\text{M}$ ) and **Rh<sub>2</sub>phenbodipy** (1  $\mu\text{M}$ ) at 37°C. As shown in Figure 4.23, the cellular distribution of both compounds were different. The green fluorescence emission from phenbodipy indicates that the organic ligand is diffused throughout the cytoplasm, whereas the dirhodium compound showed a punctuate distribution pattern after 2 h of incubation. The same subcellular distribution of each compound is observed after 24 h of incubation (Figure 4.24). The distribution pattern of **Rh<sub>2</sub>phenbodipy** is similar to that reported for Ru-polyarginine conjugates and could indicate that endocytosis is the mechanism of uptake.<sup>274,275,276</sup> The fact that the fluorescence distribution of phenbodipy and **Rh<sub>2</sub>phenbodipy** are different suggests that the fluorophore is not detached from the dirhodium core during the time frame of the experiments and that the cellular localization of **Rh<sub>2</sub>phenbodipy** is dictated at least in part by the dimetal moiety.<sup>255</sup> If detachment of the fluorophore was occurring, its emission intensity would increase considerably (since the  $\Phi_{\text{F}}$  for phenbodipy is 4-fold greater than when it is bound to the Rh<sub>2</sub><sup>4+</sup> fragment) and the cellular distribution would change, but that was not observed.

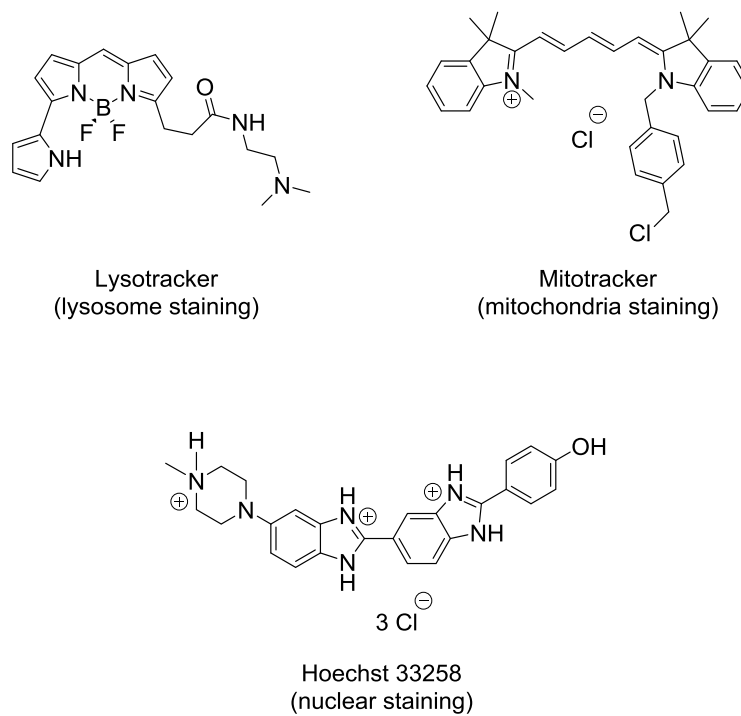


**Figure 4. 23** Microscopy images of (a) phenbodipy (1  $\mu\text{M}$ ) and (b) **Rh<sub>2</sub>phenbodipy** (1  $\mu\text{M}$ ) after 2 h of incubation. DIC = differential interference contrast. Field of view = 143  $\mu\text{m} \times 143 \mu\text{m}$ .

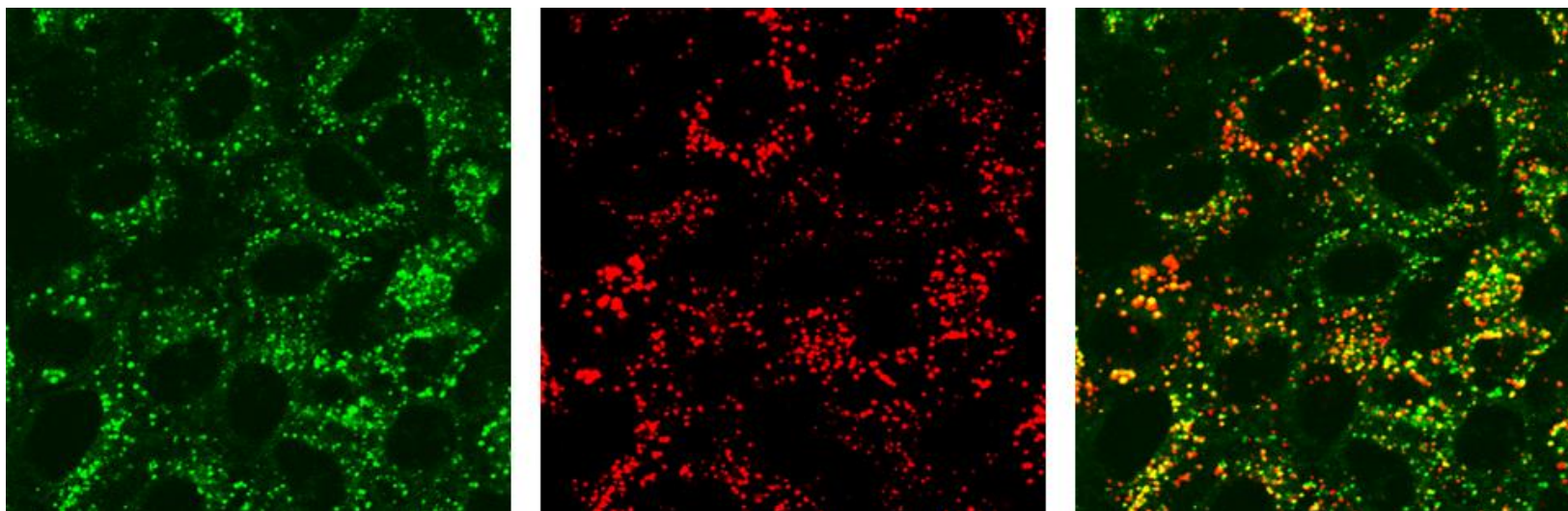


**Figure 4. 24** Microscopy images of (a) phenbodipy (1  $\mu\text{M}$ ) and (b) **Rh<sub>2</sub>phenbodipy** (1  $\mu\text{M}$ ) after 24 h of incubation. DIC = differential interference contrast. Field of view = 143  $\mu\text{m}$   $\times$  143  $\mu\text{m}$ .

In order to obtain further information on the subcellular localization of **Rh<sub>2</sub>phenbodipy**, colocalization experiments with LysoTracker and Mitotracker (lysosome- and mitochondria-specific fluorescent trackers, respectively, Figure 4.25) were performed. These experiments were carried out at 10 and 100  $\mu\text{M}$  concentrations since **Rh<sub>2</sub>phenbodipy** is not cytotoxic in the 1–100  $\mu\text{M}$  range. As shown in Figure 4.26, there is a good superposition pattern between the green fluorescence from **Rh<sub>2</sub>phenbodipy** and the red fluorescence from LysoTracker after 5 h of incubation. The Mander's colocalization coefficient is  $39.9 \pm 4.0\%$  (mean  $\pm$  SD) at 10  $\mu\text{M}$  **Rh<sub>2</sub>phenbodipy**, indicating that there is  $\sim 40\%$  colocalization of the green fluorescence signal of **Rh<sub>2</sub>phenbodipy** with the red fluorescence signal of LysoTracker. The coefficient is slightly greater ( $44.8 \pm 4.4\%$ ) when the cells are incubated with 100  $\mu\text{M}$  **Rh<sub>2</sub>phenbodipy** for 5 h. After 24 h of incubation, the colocalization coefficients with LysoTracker decrease to  $33.5 \pm 6.0\%$  and  $32.3 \pm 3.8\%$  for 10  $\mu\text{M}$  and 100  $\mu\text{M}$  **Rh<sub>2</sub>phenbodipy**, respectively (Figure 4.28a).

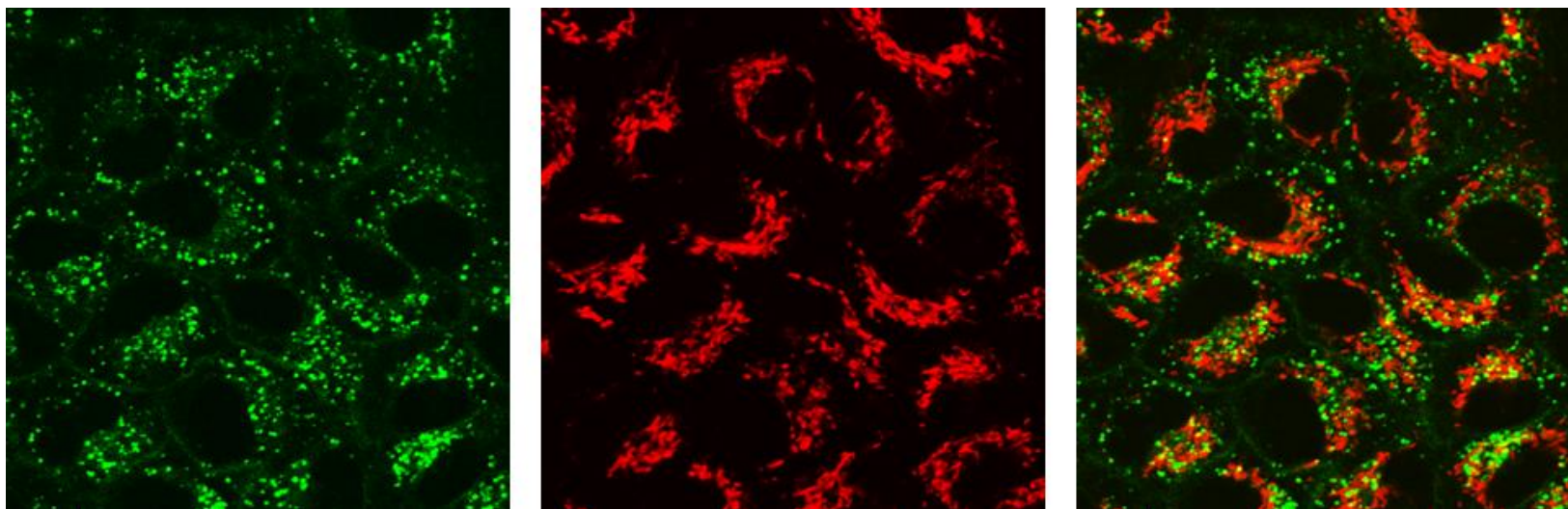


**Figure 4. 25** Molecular structures of organic fluorescent dyes used on the colocalization experiments.

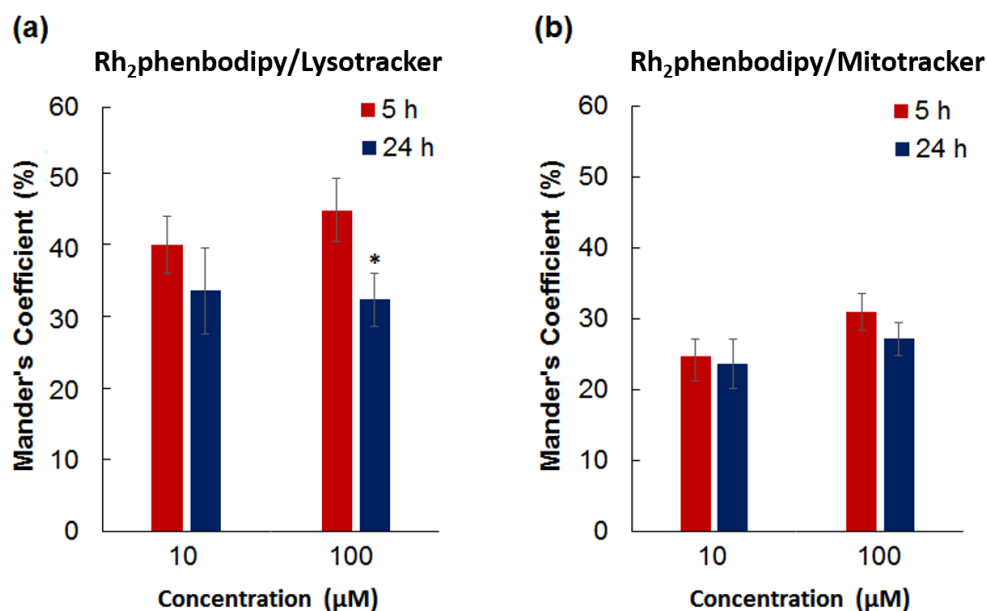


**Figure 4. 26** Confocal fluorescence images of 10  $\mu$ M **Rh<sub>2</sub>phenbodipy** (left), Lysotracker (middle), and overlay (right) after 5 h incubation. Field of view = 105  $\times$  105  $\mu$ m.





**Figure 4. 27** Confocal fluorescence images of 10  $\mu\text{M}$  **Rh<sub>2</sub>phenbodipy** (left) Mitotracker (middle), and overlay (right) after 5 h incubation. Field of view = 105  $\times$  105  $\mu\text{m}$ .

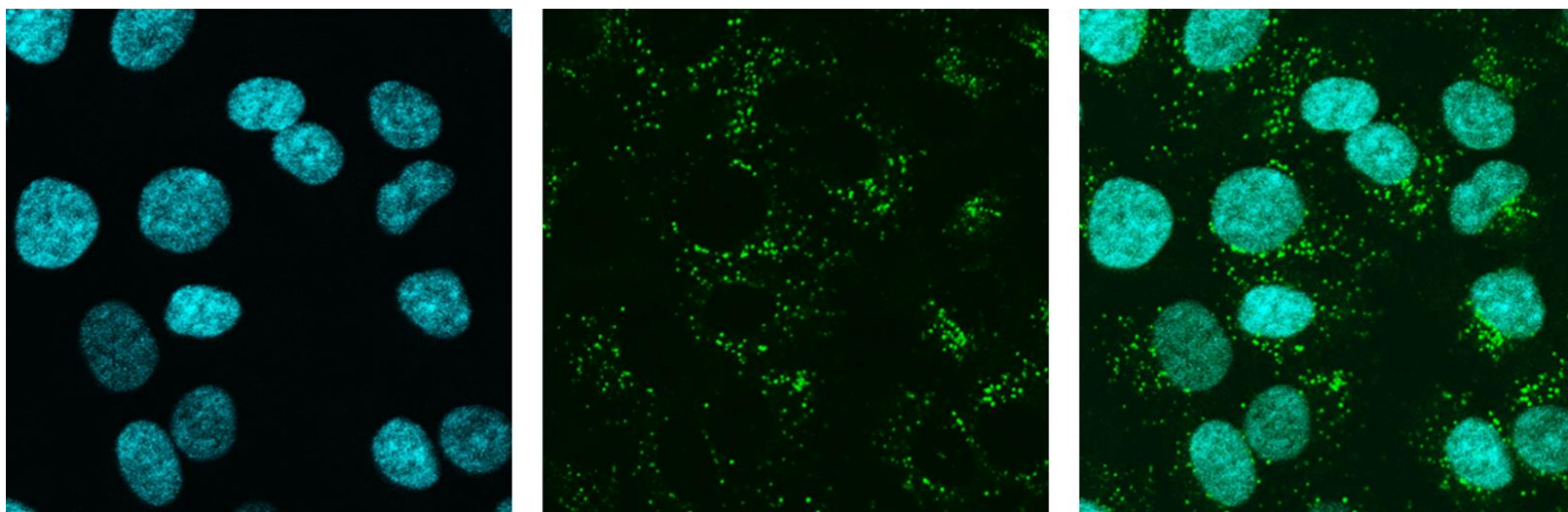


**Figure 4. 28** Mander's colocalization coefficients of (a) **Rh<sub>2</sub>phenbodipy** over Lysotracker signals and (b) **Rh<sub>2</sub>phenbodipy** over Mitotracker signals. The graphs represent means with standard deviation. The asterisk (\*) indicates significant difference (at  $p < 0.05$ ) between the colocalization coefficients at 5 and 24 h for 100 μM **Rh<sub>2</sub>phenbodipy**.

In the case of the localization of **Rh<sub>2</sub>phenbodipy** in mitochondria (Figure 4.27), the colocalization coefficients with Mitotracker were calculated as  $24.8 \pm 2.3\%$  and  $31.0 \pm 2.7\%$  for 10 μM and 100 μM **Rh<sub>2</sub>phenbodipy**, respectively, after 5 h of incubation. They remain essentially the same after 24 h of incubation at both concentrations ( $23.7 \pm 3.5\%$  and  $27.2 \pm 2.3\%$  for 10 μM and 100 μM **Rh<sub>2</sub>phenbodipy**, respectively, Figure 4.28b). These results indicate that **Rh<sub>2</sub>phenbodipy** localizes preferentially in lysosomes

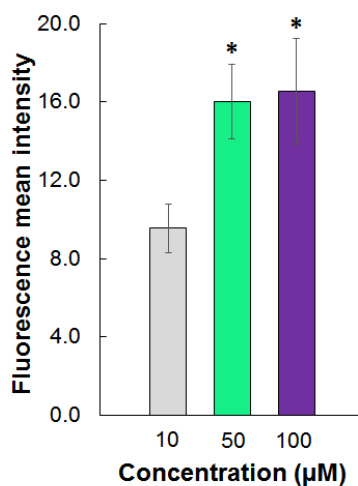
over mitochondria and that increasing the incubation time or concentration of the dimetal compound does change its subcellular localization. Lysosomal or mitochondrial localization has also been reported for Ru compounds incorporating the dppz ligand<sup>127</sup> and free-base porphyrin-Ru conjugates.<sup>277</sup>

Interestingly, green fluorescence emission from **Rh<sub>2</sub>phenbodipy** was not observed in the nucleus of the cells in the 1–100  $\mu\text{M}$  range of concentrations (Figure 4.29). Although the intracellular distribution of **Rh<sub>2</sub>phenbodipy** appears to be affected mainly by the Rh<sub>2</sub><sup>4+</sup> moiety, it is possible that the tethered bodipy fluorophore is influencing its biological properties and subcellular localization, which could explain the exclusion of **Rh<sub>2</sub>phenbodipy** from the nucleus. The influence of a fluorophore on the localization of Ru(II) polypyridyl complexes conjugated to D-octaarginine peptides has been documented by Barton and coworkers,<sup>275</sup> where the intracellular localization of the Ru-peptide conjugate changed when fluorescein was covalently attached to the conjugate.



**Figure 4. 29** Confocal fluorescence images of Hoechst 33258 dye (nuclear stain, left), 10  $\mu\text{M}$  **Rh<sub>2</sub>phenbodipy** (middle), and overlay of images (right) after 24 h of incubation in A549 cells. Field of view = 75  $\mu\text{m}$   $\times$  75  $\mu\text{m}$ .

The uptake of **Rh<sub>2</sub>phenbodipy** was also measured after 24 h of incubation at 10, 50 and 100  $\mu$ M concentrations. The mean fluorescence intensity of **Rh<sub>2</sub>phenbodipy** did not increase at concentrations greater than 50  $\mu$ M (Figure 4.30), which could explain why the colocalization coefficients with Lysotracker (or Mitotracker) did not increase when the concentration was increased ten-fold, as well as the lack of cytotoxicity of **Rh<sub>2</sub>phenbodipy**.



**Figure 4. 30** Fluorescence mean intensity of **Rh<sub>2</sub>phenbodipy** in A549 cancer cells measured after 24 h incubation. The graphs represent means with standard deviation. The asterisk (\*) indicates significant difference compared to the 10  $\mu$ M concentration at  $p < 0.05$ .

## Conclusions

The compound  $[\text{Rh}_2(\mu\text{-O}_2\text{CCH}_3)_2(\eta^1\text{-O}_2\text{CCH}_3)(\text{phenbodipy})(\text{H}_2\text{O})_3][\text{O}_2\text{CCH}_3]$  is the first example of a M–M bonded fluorescent compound. This dirhodium compound actually exists as a 1:1 mixture of two geometric isomers due to the  $C_1$  symmetric structure of the fluorescent phenbodipy ligand. The compound displays an intense  $^1\pi\pi^*$  bodipy LC transition at 500 nm ( $5.9 \times 10^4 \text{ M}^{-1} \text{ cm}^{-1}$ ) and exhibits weak green fluorescence emission ( $\Phi_F = 5\%$ ) with maximum at 514 nm in aerated methanol solution. This molecule provides the first evidence that Rh–Rh bonded compounds can be tagged with fluorescent probes without total quenching of fluorescence and that the intracellular localization is dictated at least in part by the dirhodium core since the cellular distribution pattern of  $[\text{Rh}_2(\mu\text{-O}_2\text{CCH}_3)_2(\eta^1\text{-O}_2\text{CCH}_3)(\text{phenbodipy})(\text{H}_2\text{O})_3][\text{O}_2\text{CCH}_3]$  differs from that of the free phenbodipy ligand.

The compound targets mainly lysosomes and mitochondria in the 1–100  $\mu\text{M}$  range of concentration, with a slight preference for the former organelle ( $\sim 1.4$ -fold). In contrast to the closely related compound **11** (see molecular structure in Figure 4.9), which targets the nucleus and induces DNA damage,  $[\text{Rh}_2(\mu\text{-O}_2\text{CCH}_3)_2(\eta^1\text{-O}_2\text{CCH}_3)(\text{phenbodipy})(\text{H}_2\text{O})_3][\text{O}_2\text{CCH}_3]$  does not show nuclear localization in A549 cells which supports the hypothesis that other cellular organelles can be targeted by ligand design around the dimetal unit.

Further studies are currently underway in the laboratories of Professor Kim R. Dunbar to modify the nature and lipophilicity of the fluorophore, to change its position

relative to the dirhodium core (equatorial binding or covalently attached to bridging carboxylate ligands) and to improve the uptake and cytotoxicity of this new type of fluorescent dirhodium compounds, which we expect will provide a deeper understanding of the anticancer properties of this interesting class of inorganic compounds.

## CHAPTER V

### CONCLUSIONS AND FUTURE OUTLOOK

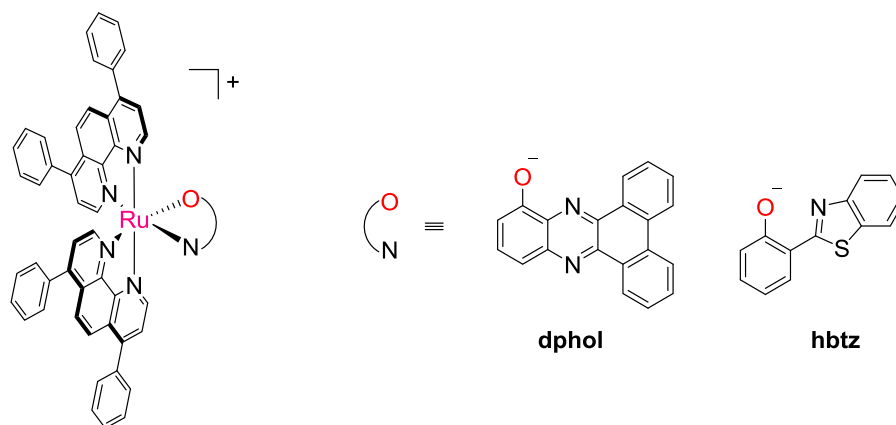
Medicinal inorganic chemistry offers an opportunity to capitalize on the chemical properties of transition metal ions and organic compounds and to simultaneously tailor their biological properties as anticancer drugs. The increasing interest in the development of metallodrugs based on Ru have led to the discovery of compounds with improved anticancer activities, novel mechanisms of action and lower side effects compared to Pt drugs. Moreover their study has shifted the paradigm towards the design of metal drugs with non-classical targets rather than nuclear DNA. In this dissertation, two new families of Ru compounds and a novel fluorescent dirhodium compound are reported. The results described herein help to expand the current state-of-the art in metal-based anticancer drugs.

In Chapter II, four new monocationic Ru(II) complexes of the type  $[\text{Ru}(\text{N}^{\wedge}\text{N})_2(\text{N}^{\wedge}\text{O}^-)]^+$ , with  $\text{N}^{\wedge}\text{N}$  = polypyridyl ligand and  $\text{N}^{\wedge}\text{O}^-$  = anionic bidentate ligand, were successfully synthesized and characterized. Their cytotoxic properties and mitochondrial changes that these compounds induced in human lung adenocarcinoma (A549) cells were also examined. The compounds exhibit  $\text{IC}_{50}$  values in the low micromolar range that are comparable or lower than that of the prototype anticancer drug cisplatin and promote cancer cell death via the mitochondrial pathway of apoptosis. From this study it is evident that the lipophilicity of the  $\text{N}^{\wedge}\text{O}^-$ -donor ligand plays an important role in the cytotoxicity of the Ru complexes and provides a new strategy to



design anticancer active Ru compounds with  $[\text{RuN}_5\text{O}]^+$  pseudo-octahedral coordination environment. This work represents a second report that reveals that the exploration of the anticancer properties of this type of Ru complexes is highly worth investigating.

To better understand the correlation between the lipophilicity of the  $\text{N}^{\text{O}^-}$ -donor ligand, cellular uptake and anticancer activity of the Ru compounds, it will be necessary to determine the Ru content inside A549 cells using ICP-MS. Selective isolation of mitochondria, nuclei and cytosol of cancer cells exposed to these Ru compounds, followed by determination of metal content in each fraction will be fundamental to determine cellular targets and to tailor their anticancer properties. Additionally, the synthesis of two new compounds containing 4,7-diphenyl-1,10-phenanthroline (DIP) as  $\text{N}^{\text{N}}$  ligand is proposed (Figure 5.1) since Ru(II) polypyridyl complexes containing DIP are usually very cytotoxic. Finally, it was shown that the Ir(III) compound  $\text{Ir}(\text{phpy})(\text{hbtz})$  is cytotoxic against A549 cells which clearly hints that the synthesis of Ir(III) analogs incorporating a variety of  $\text{N}^{\text{O}^-}$  ligands is of interest. Importantly, the intrinsic photoluminescent properties of Ir compounds can be exploited to study its mechanism of action by using confocal fluorescence microscopy.



**Figure 5. 1** Molecular structures of monocationic Ru compounds containing the DIP ligand.

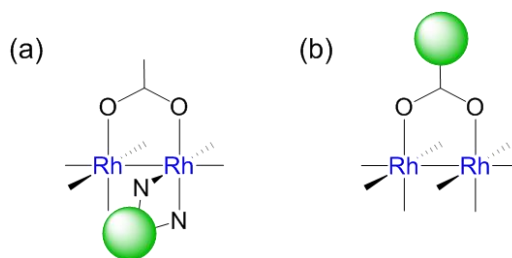
Chapter III describes a study aimed at exploring the cytotoxic properties of Ru(II) cyclometallated compounds equipped with a variety of neutral bidentate ligands. Such organometallic compounds were studied because of the increasing interest in this class of molecules in bioorganometallic chemistry. Moreover, they represent an important class of inorganic dyes for solar energy conversion purposes whose properties in other totally unrelated areas such as cancer drug research have not been extensively studied. Additionally, their light absorption in the visible region render them interesting candidates for photochemotherapy. It was found that two cyclometallated compounds containing the dppn ligand,  $[\text{Ru}(\text{phpy})(\text{bpy})(\text{dppn})]^+$  and  $[\text{Ru}(\text{phpy})(\text{pap})(\text{dppn})]^+$ , are the most cytotoxic from the series of compounds that were synthesized, displaying greater cytotoxic properties than cisplatin in cervical (HeLa) and ovarian (OVCAR-8) cancer

cells. Even more exciting is the fact that they are cytotoxic against the multidrug resistant NCI/ADR-RES ovarian cancer cell, revealing the great potential of Ru cyclometallated dyes for cancer drug research. Additional biological studies to confirm the mechanism of cancer cell death promoted by these compounds are currently underway, as well as the exploration of their photochemical properties in order to find suitable candidates for photochemotherapy applications.

In Chapter IV, the first example of a fluorescent metal-metal bonded compound,  $[\text{Rh}_2(\mu\text{-O}_2\text{CCH}_3)_2(\eta^1\text{-O}_2\text{CCH}_3)(\text{phenbodipy})(\text{H}_2\text{O})_3][\text{O}_2\text{CCH}_3]$ , is reported and its fluorescent properties exploited in order to decipher its cellular distribution, subcellular localization and cellular uptake in A549 cancer cells. This dirhodium compound targets lysosomes and mitochondria, but does not show nuclear localization. These findings demonstrate the versatility of dirhodium compounds in cancer drug research because it suggests that different cellular organelles can be targeted by fine tuning the ligand environment around the dimetal unit. Further studies are currently underway to modify the nature and lipophilicity of the fluorophore, to change its position relative to the dirhodium core (equatorial binding via a chelating ligand or a bridging carboxylate ligand, Figure 5.2) and to improve the uptake and cytotoxicity of this new type of compounds, which is expected will provide a deeper understanding of the anticancer properties of dirhodium drugs.

The strategy of appending a fluorophore to a dimetal core will also expand the toolbox for studying the biological properties of multicenter inorganic complexes since the same approach can be used to label diruthenium and dirhenium anticancer molecules.

It is worth pointing out that our findings that Rh–Rh bonded compounds can be tagged with light harvesting units, such as bodipy, are expected to positively impact other research areas where dirhodium compounds are used in photocatalysis, since attaching a moiety with a high molar absorptivity to the dimetal core could improve the efficiency of such catalytic systems.



**Figure 5. 2** Schematic representation of the (a) equatorial and (b) axial positions from which a fluorophore can be attached to the dirhodium core.

Taken together as a body of work, the research described in this dissertation provides a new platform for studying anticancer active Ru(II) compounds with  $[\text{Ru}^{\text{II}}\text{N}_5\text{O}]^+$  pseudo-octahedral coordination environments and is expected to encourage further explorations of this type of molecule and studies of the biological properties of analogs containing anionic ligands with other heteroatoms. The findings that Ru

cyclometallated dyes display promising cytotoxic properties have diversified the architectures of organometallic anticancer drugs and opens up new avenues for the development of bifunctional compounds that can be structurally modified to act as either anticancer drugs or light harvesting units for solar energy conversion. Finally, the cellular studies of a fluorophore-labeled dirhodium compound have increased our knowledge of the intracellular distribution and cellular targets of Rh–Rh bonded compounds in living cancer cells and will help to guide the design of anticancer dirhodium compounds towards a targeted therapy.

## REFERENCES

1. Ruddon, R. W. *Cancer Biology*. 4th ed.; New York, NY: Oxford University Press, 2007.
2. Clark, W. H. *Br. J. Cancer*. **1991**, *64*, 631-644.
3. *Cancer Facts & Figures 2014*. Atlanta, GA: American Cancer Society, 2014.
4. Hesketh, R. *Introduction to Cancer Biology*. New York, NY: Cambridge University Press, 2013.
5. *Global Cancer, Facts & Figures 2008*. 2nd ed.; Atlanta, GA: American Cancer Society, 2011.
6. *Centers For Disease Control and Prevention: Leading Causes of Death in the United States*. <http://www.cdc.gov/nchs/fastats/lcod.htm>. Web. Accessed 9 May 2014.
7. David, A. R.; Zimmerman, M. R. *Nat. Rev. Cancer* **2010**, *10*, 728-733.
8. *National Cancer Institute: SEER Stat Fact Sheets for Lung and Bronchus Cancer*. <http://seer.cancer.gov/statfacts/>. Web. Accessed 8 May 2014.
9. Kozarich John, W. Medicinal Inorganic Chemistry: Promises and Challenges, In *Medicinal Inorganic Chemistry*. American Chemical Society, 2005. Vol. 903, 4-14.
10. Bertini, I.; Gray, H. B.; Lippard, S. J.; Valentine, J. S.; Eds. *Bioinorganic Chemistry*. Mill Valley, CA: University Science Books, 1994.
11. Orvig, C.; Abrams, M. J. *Chem. Rev.* **1999**, *99*, 2201-2203.

12. Mjos, K. D.; Orvig, C. *Chem. Rev.* **2014**, *114*, 4540-4563.
13. Thompson, K. H.; Orvig, C. *Science* **2003**, *300*, 936-939.
14. Bruijninx, P. C. A.; Sadler, P. J. *Curr. Opin. Chem. Biol.* **2008**, *12*, 197-206.
15. Sadler, P. J. *Dalton Trans.* **2009**, 10647.
16. Rijt, S. H. v.; Sadler, P. J. *Drug Discovery Today* **2009**, *14*, 1089-1097.
17. Rosenberg, B.; VanCamp, L.; Krigas, T. *Nature* **1965**, *205*, 698-699.
18. Rosenberg, B.; VanCamp, L.; Trosko, J. E. *Nature* **1969**, *222*, 385-386.
19. Kelland, L. *Nat. Rev. Cancer* **2007**, *7*, 573-584.
20. Jamieson, E. R.; Lippard, S. J. *Chem. Rev.* **1999**, *99*, 2467-2498.
21. Wheate, N. J.; Walker, S.; Craig, G. E.; Oun, R. *Dalton Trans.* **2010**, *39*, 8113-8127.
22. Reedijk, J. *Proc. Natl. Acad. Sci. U.S.A.* **2003**, *100*, 3611-3616.
23. Feldman, D. R.; Bosl, G. J.; Sheinfeld, J.; Motzer, R. J. *JAMA* **2008**, *299*, 672-684.
24. DeConti, R. C.; Toftness, B. R.; Lange, R. C.; Creasey, W. A. *Cancer Res.* **1973**, *33*, 1310-1315.
25. Alderden, R. A.; Hall, M. D.; Hambley, T. W. *J. Chem. Educ.* **2006**, *83*, 728-734.
26. Siddik, Z. H. *Oncogene* **2003**, *22*, 7265-7279.
27. Rabik, C. A.; Dolan, M. E. *Cancer Treat. Rev.* **2007**, *33*, 9-23.
28. Binks, S. P.; Dobrota, M. *Biochem. Pharmacol.* **1990**, *40*, 1329-1336.
29. Gately, D. P.; Howell, S. B. *Br. J. Cancer.* **1993**, *67*, 1171-1176.
30. Arnesano, F.; Natile, G. *Coord. Chem. Rev.* **2009**, *253*, 2070-2081.

31. Jung, Y.; Lippard, S. J. *Chem. Rev.* **2007**, *107*, 1387-1407.
32. Wang, D.; Lippard, S. J. *Nat. Rev. Drug. Discov.* **2005**, *4*, 1474-1776.
33. Ishida, S.; Lee, J.; Thiele, D. J.; Herskowitz, I. *Proc. Natl. Acad. Sci. U. S. A.* **2002**, *99*, 14298-14302.
34. Katano, K.; Kondo, A.; Safaei, R.; Holzer, A.; Samimi, G.; Mishima, M.; Kuo, Y.-M.; Rochdi, M.; Howell, S. B. *Cancer Res.* **2002**, *62*, 6559-6565.
35. Safaei, R.; Holzer, A. K.; Katano, K.; Samimi, G.; Howell, S. B. *J. Inorg. Biochem.* **2004**, *98*, 1607-1613.
36. Holzer, A. K.; Samimi, G.; Katano, K.; Naerdemann, W.; Lin, X.; Safaei, R.; Howell, S. B. *Mol. Pharmacol.* **2004**, *66*, 817-823.
37. Davies, M. S.; Berners-Price, S. J.; Hambley, T. W. *J. Inorg. Biochem.* **2000**, *79*, 167-172.
38. Davies, M. S.; Berners-Price, S. J.; Hambley, T. W. *Inorg. Chem.* **2000**, *39*, 5603-5613.
39. Segal, E.; Le Pecq, J.-B. *Cancer Res.* **1985**, *45*, 492-498.
40. Bruijninx, P. C. A.; Sadler, P. J. *Adv. Inorg. Chem.* **2009**, *61*, 1-62.
41. Sherman, S.; Gibson, D.; Wang, A.; Lippard, S. *Science* **1985**, *230*, 412-417.
42. Takahara, P. M.; Rosenzweig, A. C.; Frederick, C. A.; Lippard, S. J. *Nature* **1995**, *377*, 649-652.
43. Reedijk, J. *Platinum Metals Rev.* **2008**, *52*, 2-11.
44. Knox, R. J.; Friedlos, F.; Lydall, D. A.; Roberts, J. J. *Cancer Res.* **1986**, *46*, 1972-1979.



45. Giaccone, G. *Drugs* **2000**, *59*, 9-17.
46. Fuertes, M. A.; Alonso, C.; Pérez, J. M. *Chem. Rev.* **2003**, *103*, 645-662.
47. Samimi, G.; Safaei, R.; Katano, K.; Holzer, A. K.; Rochdi, M.; Tomioka, M.; Goodman, M.; Howell, S. B. *Clin. Cancer Res.* **2004**, *10*, 4661-4669.
48. Mistry, P.; Kelland, L. R.; Abel, G.; Sidhar, S.; Harrap, K. R. *Br. J. Cancer* **1991**, *64*, 215-220.
49. Ishikawa, T. *Trends Biochem. Sci.* **1992**, *17*, 463-468.
50. Fink, D.; Nebel, S.; Aebi, S.; Zheng, H.; Cenni, B.; Nehmé, A.; Christen, R. D.; Howell, S. B. *Cancer Res.* **1996**, *56*, 4881-4886.
51. Bassett, E.; Vaisman, A.; Tropea, K. A.; McCall, C. M.; Masutani, C.; Hanaoka, F.; Chaney, S. G. *DNA Repair* **2002**, *1*, 1003-1016.
52. Albertella, M. R.; Green, C. M.; Lehmann, A. R.; O'Connor, M. J. *Cancer Res.* **2005**, *65*, 9799-9806.
53. Raymond, E.; Faivre, S.; Chaney, S.; Woynarowski, J.; Cvitkovic, E. *Mol. Cancer Ther.* **2002**, *1*, 227-235.
54. Zhang, S.; Lovejoy, K. S.; Shima, J. E.; Lagpacan, L. L.; Shu, Y.; Lapuk, A.; Chen, Y.; Komori, T.; Gray, J. W.; Chen, X.; Lippard, S. J.; Giacomini, K. M. *Cancer Res.* **2006**, *66*, 8847-8857.
55. Reedijk, J. *Eur. J. Inorg. Chem.* **2009**, 1303-1312.
56. Wong, E.; Giandomenico, C. M. *Chem. Rev.* **1999**, *99*, 2451-2466.
57. Johnstone, T. C.; Park, G. Y.; Lippard, S. J. *Anticancer Res.* **2014**, *34*, 471-476.
58. Zutphen, S. v.; Reedijk, J. *Coord. Chem. Rev.* **2005**, *249*, 2845-2853.

59. *Evaluate. Platinum Compounds.* <http://www.evaluategroup.com>. Web. Accessed 5 May 2014.
60. *Statista. Top 10 cancer drugs in the U.S. based on revenue in 2011.* <http://www.statista.com>. Web. Accessed 5 May 2014.
61. Kroemer, G.; Galluzzi, L.; Brenner, C. *Physiol. Rev.* **2007**, *87*, 99-163.
62. Alberts, B.; Johnson, A.; Lewis, J.; Raff, M.; Roberts, K.; Walter, P., *Molecular Biology of the Cell*. 2nd ed.; Garland Science: New York, NY, 2002. <http://www.ncbi.nlm.nih.gov/books/NBK21054/>.
63. Kimball, J. W. *Kimball's Biology Pages, An Online Biology Textbook.* <http://users.rcn.com/jkimball.ma.ultranet/BiologyPages/>. Web. Accessed 21 April 2014.
64. Pommier, Y.; Sordet, O.; Antony, S.; Hayward, R. L.; Kohn, K. W. *Oncogene* **2004**, *23*, 2934-2949.
65. Green, D. R. *Cancer Cell* **2006**, *9*, 328-330.
66. Debatin, K.-M. *Toxicol. Lett.* **2000**, *112-113*, 41-48.
67. Boehning, D.; Patterson, R. L.; Sedaghat, L.; Glebova, N. O.; Kurosaki, T.; Snyder, S. H. *Nat. Cell Biol.* **2003**, *5*, 1051-1061.
68. Li, J.; Yuan, J. *Oncogene* **2008**, *27*, 6194-6206.
69. Bergamo, A.; Sava, G. *Dalton Trans.* **2011**, *40*, 7817-7823.
70. Antonarakis, E. S.; Emadi, A. *Cancer Chemother. Pharmacol.* **2010**, *66*, 1-9.
71. Bratsos, I.; Jedner, S.; Gianferrara, T.; Alessio, E. *Chimia* **2007**, *61*, 692-697.

72. Sava, G.; Zorzet, S.; Turrin, C.; Vita, F.; Soranzo, M.; Zabucchi, G.; Cocchietto, M.; Bergamo, A.; DiGiovine, S.; Pezzoni, G.; Sartor, L.; Garbisa, S. *Clin. Cancer. Res.* **2003**, *9*, 1898-1905.
73. Rademaker-Lakhai, J. M.; Bongard, D. v. d.; Pluim, D.; Beijnen, J. H.; Schellens, J. H. M. *Clin. Cancer. Res.* **2004**, *10*, 3717-3727.
74. Clarke, M. J.; Zhu, F.; Frasca, D. R. *Chem. Rev.* **1999**, *99*, 2511-2534.
75. Hartinger, C. G.; Zorbas-Seifried, S.; Jakupec, M. A.; Kynast, B.; Zorbas, H.; Keppler, B. K. *J. Inorg. Biochem.* **2000**, *100*, 891-904.
76. Depenbrock, H.; Schmelcher, S.; Peter, R.; Keppler, B. K.; Weirich, G.; Block, T.; Rastetter, J.; Hanauske, A.-R. *Eur. J. Cancer* **1997**, *33*, 2404-2410.
77. Hartinger, C. G.; Jakupec, M. A.; Zorbas-Seifried, S.; Groessler, M.; Egger, A.; Berger, W.; Zorbas, H.; Dyson, P. J.; Keppler, B. K. *Chem. Biodiversity* **2008**, *5*, 2140-2155.
78. Sun, H.; Li, H.; Sadler, P. J. *Chem. Rev.* **1999**, *99*, 2817-2842.
79. Smith, C. A.; Sutherland-Smith, A. J.; Keppler, B. K.; Kratz, F.; Baker, E. N. *J. Biol. Inorg. Chem.* **1996**, *1*, 424-431.
80. Hann, H.-W. L.; Stahlhut, M. W.; Blumberg, B. S. *Cancer Res.* **1988**, *48*, 4168-4170.
81. Clarke, M. J. *Coordination Chemistry Reviews* **2003**, *236*, 209-233.
82. Suss-Fink, G. *Dalton Trans.* **2010**, *39*, 1673-1688.
83. Hartinger, C. G.; Metzler-Nolte, N.; Dyson, P. J. *Organometallics* **2012**, *31*, 5677-5685.

84. Ang, W. H.; Casini, A.; Sava, G.; Dyson, P. J. *J. Organomet. Chem.* **2011**, *696*, 989-998.
85. Sava, G.; Bergamo, A.; Dyson, P. J. *Dalton Trans.* **2011**, *40*, 9069-9075.
86. Peacock, A. F. A.; Sadler, P. J. *Chem. Asian J.* **2008**, *3*, 1890-1899.
87. Morris, R. E.; Aird, R. E.; del Socorro Murdoch, P.; Chen, H.; Cummings, J.; Hughes, N. D.; Parsons, S.; Parkin, A.; Boyd, G.; Jodrell, D. I.; Sadler, P. J. *J. Med. Chem.* **2001**, *44*, 3616-3621.
88. Aird, R. E.; Cummings, J.; Ritchie, A. A.; Muir, M.; Morris, R. E.; Chen, H.; Sadler, P. J.; Jodrell, D. I. *Br. J. Cancer* **2002**, *86*, 1652-1657.
89. Guichard, S. M.; Else, R.; Reid, E.; Zeitlin, B.; Aird, R.; Muir, M.; Dodds, M.; Fiebig, H.; Sadler, P. J.; Jodrell, D. I. *Biochem. Pharmacol.* **2006**, *71*, 408-415.
90. Pizarro, A. M.; Habtemariam, A.; Sadler, P. J. *Top. Organomet. Chem.* **2010**, *32*, 21-56.
91. Wang, F.; Chen, H.; Parsons, S.; Oswald, I. D. H.; James E. Davidson; Sadler, P. *J. Chem. Eur. J.* **2003**, *9*, 5810-5820.
92. Chen, H.; Parkinson, J. A.; Morris, R. E.; Sadler, P. J. *J. Am. Chem. Soc.* **2002**, *125*, 173-186.
93. Liu, H.-K.; Berners-Price, S. J.; Wang, F.; Parkinson, J. A.; Xu, J.; Bella, J.; Sadler, P. J. *Angew. Chem. Int. Ed.* **2006**, *118*, 8333-8336.
94. Liu, H.-K.; Sadler, P. J. *Acc. Chem. Res.* **2011**, *44*, 349-359.
95. Pizarro, A. M.; Sadler, P. J. *Biochimie* **2009**, *91*, 1198-1211.

96. Scolaro, C.; Bergamo, A.; Brescacin, L.; Delfino, R.; Cocchietto, M.; Laurencyzy, G.; Geldbach, T. J.; Sava, G.; Dyson, P. J. *J. Med. Chem.* **2005**, *48*, 4161-4171.
97. Alberta Bergamo, A. M., Paul J. Dyson, Gianni Sava. *Int. J. Oncol.* **2008**, *33*, 1281-1289.
98. Wu, B.; Ong, M. S.; Groessler, M.; Adhireksan, Z.; Hartinger, C. G.; Dyson, P. J.; Davey, C. A. *Chem. Eur. J.* **2011**, *17*, 3562-3566.
99. Townsend, D. M.; Tew, K. D. *Oncogene* **2003**, *22*, 7369-7375.
100. Ang, W. H.; Parker, L. J.; Luca, A. D.; Juillerat-Jeanneret, L.; Morton, C. J.; Bello, M. L.; Parker, M. W.; Dyson, P. J. *Angew. Chem. Int. Ed.* **2009**, *48*, 3854-3857.
101. Debreczeni, J. É.; Bullock, A. N.; Atilla, G. E.; Williams, D. S.; Bregman, H.; Knapp, S.; Meggers, E. *Angew. Chem. Int. Ed.* **2006**, *45*, 1580-1585.
102. Meggers, E. *Curr. Opin. Chem. Biol.* **2007**, *11*, 287-292.
103. Xie, P.; Streu, C.; Qin, J.; Bregman, H.; Pagano, N.; Meggers, E.; Marmorstein, R. *Biochemistry* **2009**, *48*, 5187-5198.
104. Meggers, E. *Chem. Commun.* **2009**, 1001-1010.
105. Blanck, S.; Maksimoska, J.; Baumeister, J.; Harms, K.; Marmorstein, R.; Meggers, E. *Angew. Chem. Int. Ed.* **2012**, *51*, 5244-5246.
106. Feng, L.; Geisselbrecht, Y.; Blanck, S.; Wilbuer, A.; Atilla-Gokcumen, G. E.; Filippakopoulos, P.; Kräling, K.; Celik, M. A.; Harms, K.; Maksimoska, J.; Marmorstein, R.; Frenking, G.; Knapp, S.; Essen, L.-O.; Meggers, E. *J. Am. Chem. Soc.* **2011**, *133*, 5976-5986.

107. Dwyer, F. P.; Gyarfas, E. C.; Rogers, W. P.; Koch, J. H. *Nature* **1952**, 190-191.
108. *Pfizer-Products. Material Safety Data Sheet for Cisplatin Solution for Injection - 0.5 and 1 mg/mL.* <http://www.pfizer.com>. Web. Accessed 21 Apr 2014.
109. Dwyer, F. P.; Gyarfas, E. C.; Wright, R. D.; Shulman, A. *Nature* **1957**, *179*, 425-426.
110. Koch, J. H.; Rogers, W. P.; Dwyer, F. P.; Gyarfas, E. C. *Aust. J. Biol. Sci.* **1957**, *10*, 342-50.
111. Dwyer, F. P.; Mayhew, E.; Roe, E. M. F.; Shulman, A. *Br. J. Cancer* **1965**, *19*, 195-199.
112. Puckett, C. A.; Barton, J. K. *Biochemistry* **2008**, *47*, 11711-11716.
113. Puckett, C. A.; Barton, J. K. *J. Am. Chem. Soc.* **2007**, *129*, 46-47.
114. Puckett, C. A.; Ernst, R. J.; Barton, J. K. *Dalton Trans.* **2010**, *39*, 1159-1170.
115. Komor, A. C.; Barton, J. K. *Chem. Commun.* **2013**, *49*, 3617-3630.
116. Koepsell, H. *Trends Pharmacol. Sci.* **2004**, *25*, 375-381.
117. Lemasters, J. J.; Ramshesh, V. K. *Methods Cell Biol.* **2007**, *80*, 283-95.
118. Ehrenberg, B.; Montana, V.; Wei, M. D.; Wuskell, J. P.; Loew, L. M. *Biophys. J.* **1988**, *53*, 785-794.
119. Gill, M. R.; Thomas, J. A. *Chem. Soc. Rev.* **2012**, *41*, 3179-3192.
120. Schatzschneider, U.; Niesel, J.; Ott, I.; Gust, R.; Alborzina, H.; Wolf, S. *ChemMedChem* **2008**, *3*, 1104-1109.
121. Schäfer, S.; Ott, I.; Gust, R.; Sheldrick, W. S. *Eur. J. Inorg. Chem.* **2007**, 3034-3046.

122. Chen, T.; Liu, Y.; Zheng, W.-J.; Liu, J.; Wong, Y.-S. *Inorg. Chem.* **2010**, *49*, 6366-6368.
123. Chen, T.; Mei, W.-J.; Wong, Y.-S.; Liu, J.; Liu, Y.; Xieb, H.-S.; Zheng, W.-J. *Med. Chem. Commun.* **2010**, *1*, 73-75.
124. Tan, C.; Lai, S.; Wu, S.; Hu, S.; Zhou, L.; Chen, Y.; Wang, M.; Zhu, Y.; Lian, W.; Peng, W.; Ji, L.; Xu, A. *J. Med. Chem.* **2010**, *53*, 7613-7624.
125. Chen, Y.; McMillan-Ward, E.; Kong, J.; Israels, S. J.; Gibson, S. B. *Cell Death Differ.* **2008**, *15*, 171-182.
126. Tan, C.; Wu, S.; Lai, S.; Wang, M.; Chen, Y.; Zhou, L.; Zhu, Y.; Lian, W.; Peng, W.; Ji, L.; Xu, A. *Dalton Trans.* **2011**, *40*, 8611-8621.
127. Pierroz, V.; Joshi, T.; Leonidova, A.; Mari, C.; Schur, J.; Ott, I.; Spiccia, L.; Ferrari, S.; Gasser, G. *J. Am. Chem. Soc.* **2012**, *134*, 20376-20387.
128. Qian, C.; Wang, J.-Q.; Song, C.-L.; Wang, L.-L.; Ji, L.-N.; Chao, H. *Metallomics* **2013**, *5*, 844-854.
129. Gill, M. R.; Derrat, H.; Smythe, C. G. W.; Battaglia, G.; Thomas, J. A. *ChemBioChem* **2011**, *12*, 877-880.
130. Gill, M. R.; Cecchin, D.; Walker, M. G.; Mulla, R. S.; Battaglia, G.; Smythe, C.; Thomas, J. A. *Chem. Sci.* **2013**, *4*, 4512-4519.
131. Gill, M. R.; Garcia-Lara, J.; Foster, S. J.; Smythe, C.; Battaglia, G.; Thomas, J. A. *Nature Chem.* **2009**, *1*, 662 - 667.
132. Schatzschneider, U. *Eur. J. Inorg. Chem.* **2010**, 1451-1467.
133. Levina, A.; Mitra, A.; Lay, P. A. *Metallomics* **2009**, *1*, 458-570.

134. Ma, D.-L.; He, H.-Z.; Leung, K.-H.; Chan, D. S.-H.; Leung, C.-H. *Angew. Chem. Int. Ed.* **2013**, *52*, 7666-7682.
135. Mulcahy, S. P.; Grundler, K.; Frias, C.; Wagner, L.; Prokop, A.; Meggers, E. *Dalton Trans.* **2010**, *39*, 8177–8182.
136. Sears, R. B.; Joyce, L. E.; Turro, C. *Photochem. Photobiol.* **2010**, *86*, 1230-1236.
137. Warren, J.; Chen, W.; Johnston, D.; Turro, C. *Inorg. Chem.* **1999**, *38*, 6187-6192.
138. Liu, Z.; Sadler, P. J. *Acc. Chem. Res.* **2014**, *54*, 3011-3026.
139. Liu, Z.; Habtemariam, A.; Pizarro, A. M.; Fletcher, S. A.; Kisova, A.; Vrana, O.; Salassa, L.; Bruijninx, P. C. A.; Clarkson, G. J.; Brabec, V.; Sadler, P. J. *J. Med. Chem.* **2011**, *54*, 3011-3026.
140. Liu, Z.; Salassa, L.; Habtemariam, A.; Pizarro, A. M.; Clarkson, G. J.; Sadler, P. *J. Inorg. Chem.* **2011**, *50*, 5777-5783.
141. Liu, Z.; Habtemariam, A.; Pizarro, A. M.; Clarkson, G. J.; Sadler, P. J. *Organometallics* **2011**, *30*, 4702-4710.
142. Cao, R.; Jia, J.; Ma, X.; Zhou, M.; Fei, H. *J. Med. Chem.* **2013**, *56*, 3636-3644.
143. Lee, P.-K.; Law, W. H.-T.; Liu, H.-W.; Lo, K. K.-W. *Inorg. Chem.* **2011**, *50*, 8570-8579.
144. Sullivan, B. P.; Salmon, D. J.; Meyer, T. *Inorg. Chem.* **1978**, *17*, 3334-3341.
145. Sprouse, S.; King, K. A.; Spellane, P. J.; Watts, R. J. *J. Am. Chem. Soc.* **1984**, *106*, 6637-6653.
146. Lowry, M. S.; Hudson, W. R.; Robert A. Pascal, J.; Bernhard, S. *J. Am. Chem. Soc.* **2004**, *126*, 14129-14135.



147. Whang, D. R.; You, Y.; Chae, W.-S.; Heo, J.; Kim, S.; Park, S. Y. *Langmuir* **2012**.
148. *SMART and SAINT*. Madison, WI: Siemens Analytical X-ray Instruments Inc., 1996.
149. Sheldrick, G. M. *SADABS*. Gottingen, Germany: University of Gottingen, 1996.
150. Sheldrick, G. M. *Acta Crystallogr., Sect. A* **2008**, *64*, 112-122.
151. Hübschle, C. B.; Sheldrick, G. M.; Dittrich, B. *J. Appl. Cryst.* **2011**, *44*, 1281-1284.
152. Hao, Y.; Guo, X.; Lei, L.; Yu, J.; Xu, H.; Xu, B. *Synth. Met.* **2010**, *160*, 1210-1215.
153. Brissard, M.; Convert, O.; Gruselle, M.; Guyard-Duhayon, C.; Thouvenot, R. *Inorg. Chem.* **2003**, *42*, 1378-1385.
154. Flamigni, L.; Barbieri, A.; Sabatini, C.; Ventura, B.; Barigelletti, F. *Top. Curr. Chem.* **2007**, *281*, 143-203.
155. Liu, Z.; Bian, Z.; Huang, C. *Top. Organomet. Chem.* **2010**, *28*, 113-142.
156. Kappaun, S.; Eder, S.; Sax, S.; Mereiter, K.; List, E. J. W.; Slugovc, C. *Eur. J. Inorg. Chem.* **2007**, *2007*, 4207-4215.
157. Janiak, C. *J. Chem. Soc., Dalton Trans.* **2000**, 3885-3896.
158. Yang, X.-J.; Drepper, F.; Wu, B.; Sun, W.-H.; Haehnel, W.; Janiak, C. *Dalton Trans.* **2005**, 256-267.
159. Sun, Y.; Joyce, L. E.; Dickson, N. M.; Turro, C. *Chem. Commun.* **2010**, *46*, 2426-2428.

160. Zhao, H. C.; Harney, J. P.; Huang, Y.-T.; Yum, J.-H.; Nazeeruddin, M. K.; Grätzel, M.; Tsai, M.-K.; Rochford, J. *Inorg. Chem.* **2011**, *51*, 1-3.
161. Bhattacharya, S. *Polyhedron* **1993**, *12*, 235-239.
162. Pramanik, N. C.; Bhattacharya, S. *J. Chem. Res. (S)* **1997**, 98-99.
163. Johnson, I.; Spence, M. T. Z. *The Molecular Probes® Handbook: A Guide to Fluorescent Probes and Labeling Technologies*. Life Technologies. <http://www.lifetechnologies.com/ipac/en/home/references/molecular-probes-the-handbook.html>. Web. Accessed 17 Jan 2014.
164. Jaouen, G.; Beck, W.; McGlinchey, M. J. A Novel Field of Research: Bioorganometallic Chemistry, Origins, and Founding Principles, In *Bioorganometallics*. Ed. Jaouen, G. Weinheim: Wiley-VCH, 2006.
165. Jaouen, G.; Vessières, A. *Pure & Appl. Chem.* **1985**, *57*, 865-1874.
166. Lloyd, N. C.; Morgan, H. W.; Nicholson, B. K.; Ronimus, R. S. *Angew. Chem. Int. Ed.* **2005**, *44*, 941-944.
167. Cisnetti, F.; Gautier, A. *Angew. Chem. Int. Ed.* **2013**, *52*, 11976-11978.
168. Gaidon, C.; Jeannequin, P.; Bischoff, P.; Pfeffer, M.; Sirlin, C.; Loeffler, J. P. *J. Pharmacol. Exp. Ther.* **2005**, *315*, 1403-1411.
169. Leyva, L.; Sirlin, C.; Rubio, L.; Franco, C.; Lagadec, R. L.; Spencer, J.; Bischoff, P.; Gaidon, C.; Loeffler, J.-P.; Pfeffer, M. *Eur. J. Inorg. Chem.* **2007**, 3055-3066.

170. Komatsu, M.; Sumizawa, T.; Mutoh, M.; Chen, Z.-S.; Terada, K.; Furukawa, T.; Yang, X.-L.; Gao, H.; Miura, N.; Sugiyama, T.; Akiyama, S.-i. *Cancer Res.* **2000**, *60*, 1312-1316.
171. Howell, S. B.; Safaei, R.; Larson, C. A.; Sailor, M. J. *Mol. Pharmacol.* **2010**, *77*, 887-894.
172. Meng, X.; Leyva, M. L.; Jenny, M.; Gross, I.; Benosman, S.; Fricker, B.; Harlepp, S.; Hebraud, P.; Boos, A.; Wlosik, P.; Bischoff, P.; Sirlin, C.; Pfeffer, M.; Loeffler, J.-P.; Gaiddon, C. *Cancer Res.* **2009**, *69*, 5458-5466.
173. Fetzer, L.; Boff, B.; Ali, M.; Xiangjun, M.; Collin, J.-P.; Sirlin, C.; Gaiddon, C.; Pfeffer, M. *Dalton Trans.* **2011**, *40*, 8869-8878.
174. Yellol, G. S.; Donaire, A.; Yellol, J. G.; Vasylyeva, V.; Janiak, C.; Ruiz, J. *Chem. Commun.* **2013**, *49*, 11533-11535.
175. Ryabov, A. D.; Sukharev, V. S.; Alexandrova, L.; Lagadec, R. L.; Pfeffer, M. *Inorg. Chem.* **2001**, *40*, 6529-6532.
176. Che, G.; Li, W.; Kong, Z.; Zisheng Su; Chu, B.; Li, B.; Zhang, Z.; Hu, Z.; Chi, H. *Synth. Commun.* **2006**, *36*, 2519-2524.
177. Krause, R. A. K. K. *Inorg. Chem.* **1980**, *19*, 2600-2603.
178. Wang, F.; Chen, H.; Parkinson, J. A.; Murdoch, P. d. S.; Sadler, P. J. *Inorg. Chem.* **2002**, *41*, 4509-4523.
179. Bomben, P. G.; Robson, K. C. D.; Sedach, P. A.; Berlinguette, C. P. *Inorg. Chem.* **2009**, *48*, 9631-9643.
180. Zelonka, R. A.; Baird, M. C. *Can. J. Chem.* **1972**, *50*, 3063-3072.

181. Fernandez, S.; Pfeffer, M.; Ritleng, V.; Sirlin, C. *Organometallics* **1999**, *18*, 2390-2394.
182. Ryabov, A. D.; Lagadec, R. L.; Estevez, H.; Toscano, R. A.; Hernandez, S.; Alexandrova, L.; Kurova, V. S.; Fischer, A.; Sirlin, C.; Pfeffer, M. *Inorg. Chem.* **2005**, *44*, 1626-1634.
183. Bomben, P. G.; Thériault, K. D.; Berlinguette, C. P. *Eur. J. Inorg. Chem.* **2011**, 1806-1814.
184. Gaussian 09, Revision B.01, Frisch, M. J.; Trucks, G. W.; Schlegel, H. B.; Scuseria, G. E.; Robb, M. A.; Cheeseman, J. R.; Scalmani, G.; Barone, V.; Mennucci, B.; Petersson, G. A.; Nakatsuji, H.; Caricato, M.; Li, X.; Hratchian, H. P.; Izmaylov, A. F.; Bloino, J.; Zheng, G.; Sonnenberg, J. L.; Hada, M.; Ehara, M.; Toyota, K.; Fukuda, R.; Hasegawa, J.; Ishida, M.; Nakajima, T.; Honda, Y.; Kitao, O.; Nakai, H.; Vreven, T.; Montgomery, Jr., J. A.; Peralta, J. E.; Ogliaro, F.; Bearpark, M.; Heyd, J. J.; Brothers, E.; Kudin, K. N.; Staroverov, V. N.; Kobayashi, R.; Normand, J.; Raghavachari, K.; Rendell, A.; Burant, J. C.; Iyengar, S. S.; Tomasi, J.; Cossi, M.; Rega, N.; Millam, N. J.; Klene, M.; Knox, J. E.; Cross, J. B.; Bakken, V.; Adamo, C.; Jaramillo, J.; Gomperts, R.; Stratmann, R. E.; Yazyev, O.; Austin, A. J.; Cammi, R.; Pomelli, C.; Ochterski, J. W.; Martin, R. L.; Morokuma, K.; Zakrzewski, V. G.; Voth, G. A.; Salvador, P.; Dannenberg, J. J.; Dapprich, S.; Daniels, A. D.; Farkas, Ö.; Foresman, J. B.; Ortiz, J. V.; Cioslowski, J.; Fox, D. J. Gaussian, Inc., Wallingford, CT, 2009.
185. Lee, C.; Yang, W.; Parr, R. G. *Phys. Rev. B* **1998**, *37*, 785-789.

186. Becke, A. D. *J. Chem. Phys.* **1993**, *98*, 5648-5652.
187. Andrae, D.; Haussermann, U.; Dolg, M.; Stoll, H.; Preuss, H. *Theor. Chim. Acta* **1990**, *77*, 123-141.
188. Brissard, M.; Gruselle, M.; Malézieux, B.; Thouvenot, R.; Guyard-Duhayon, C.; Convert, O. *Eur. J. Inorg. Chem.* **2001**, 1745-21751.
189. Wachter, E.; Heidary, D. K.; Howerton, B. S.; Parkin, S.; Glazer, E. C. *Chem. Commun.* **2012**, *48*, 9649-9651.
190. Sears, R. B.; Joyce, L. E.; Ojaimi, M.; Gallucci, J. C.; Thummel, R. P.; Turro, C. *J. Inorg. Biochem.* **2013**, *121*, 77-87.
191. Carrington, S. J.; Chakraborty, I.; Mascharak, P. K. *Chem. Commun.* **2013**, *49*, 11254-11256.
192. Boff, B.; Ali, M.; Alexandrova, L.; Espinosa-Jalapa, N. Á.; Saavedra-Díaz, R. O.; Le Lagadec, R.; Pfeffer, M. *Organometallics* **2013**, *32*, 5092-5097.
193. Robson, K. C. D.; Bomben, P. G.; Berlinguette, C. P. *Dalton Trans.* **2012**, *41*, 7814-7829.
194. Bomben, P. G.; Robson, K. C. D.; Koivisto, B. D.; Berlinguette, C. P. *Coord. Chem. Rev.* **2012**, *256*, 1438-1450.
195. Goss, C. A.; Abruña, H. D. *Inorg. Chem.* **1985**, *24*, 4263-4261.
196. (a) Goswami, S.; A.Chakravarty; Chakravorty, A. *Inorg. Chem.* **1981**, *20*, 2246-2250; (b) Krause, R. A.; Krause, K. *Inorg. Chem.* **1982**, *21*, 1714-1720; (c) Goswami, S.; Chakravarty, A. R.; Chakravorty, A. *Inorg. Chem.* **1983**, *22*, 602-

- 609; (d) Goswami, S.; Mukherjee, R.; Chakravorty, A. *Inorg. Chem.* **1983**, *22*, 2825-2832.
197. Zhou, Q.-X.; Lei, W.-H.; Chen, J.-R.; Li, C.; Hou, Y.-J.; Wang, X.-S.; Zhang, B.-W. *Chem. Eur. J.* **2010**, *16*, 3157 - 3165.
198. Sun, Y.; El Ojaimi, M.; Hammitt, R.; Thummel, R. P.; Turro, C. *J. Phys. Chem. B* **2010**, *114*, 14664-14670.
199. (a) Berridge, M. V.; Tan, A. S. *Arch. Biochem. Biophys.* **1993**, *303*, 474-482; (b) Berridge, M. V.; Herst, P. M.; Tan, A. S. Tetrazolium dyes as tools in cell biology: New insights into their cellular reduction, In *Biotechnol. Annu. Rev.* Ed. El-Gewely, M. R. Elsevier, 2005. Vol. 11, 127-152.
200. (a) Fotakis, G.; Timbrell, J. A. *Toxicol. Lett.* **2006**, *160*, 171-177; (b) Mosmann, T. *J. Immunol. Meth.* **1983**, *65*, 55-63.
201. Wilson, A. J.; Liu, A. Y.; Roland, J.; Adebayo, O. B.; Fletcher, S. A.; Slaughter, J. C.; Saskowski, J.; Crispens, M. A.; Jones, H. W.; James, S.; Fadare, O.; Khabele, D. *Cancer Res.* **2013**, *73*, 4758-4769.
202. Ke, W.; Yu, P.; Wang, J.; Wang, R.; Guo, C.; Zhou, L.; Li, C.; Li, K. *Med. Oncol.* **2011**, *28*, 135-141.
203. Liscovitch, M.; Ravid, D. *Cancer Lett.* **2007**, *245*, 350-352.
204. Sangthong, S.; Ha, H.; Teerawattananon, T.; Ngamrojanavanich, N.; Neamati, N.; Muangsin, N. *Bioorg. Med. Chem. Lett.* **2013**, *23*, 6156-6160.
205. Sharma, S. V.; Haber, D. A.; Settleman, J. *Nat. Rev. Cancer* **2010**, *10*, 241-253.
206. Shoemaker, R. H. *Nat. Rev. Cancer* **2006**, *6*, 813-823.

207. Nyst, H. J.; Tan, I. B.; Stewart, F. A.; Balm, A. J. M. *Photodiagn. Photodyn. Ther.* **2009**, *6*, 3-11.
208. Zuluaga, M.-F.; Lange, N. *Curr. Med. Chem.* **2008**, *15*, 1655-1673.
209. Cotton, F. A.; Murillo, C. A.; Walton, R. A. Introduction and Survey, In *Multiple Bonds Between Metal Atoms*. 3rd. ed.; Eds. Cotton, F. A.; Murillo, C. A.; Walton, R. A. New York: Springer Science and Business Media, 2005.
210. Cotton, F. A.; Curtis, N. F.; Harris, C. B.; Johnson, B. F. G.; Lippard, S. J.; Mague, J. T.; Robinson, W. R.; Wood, J. S. *Science* **1964**, *145*, 1305-1307.
211. Cotton, F. A.; Harris, C. B. *Inorg. Chem.* **1965**, *4*, 330-333.
212. Lindsay, V. N. G.; Fiset, D.; Gritsch, P. J.; Azzi, S.; Charette, A. B. *J. Am. Chem. Soc.* **2013**, *135*, 1463-1470.
213. Kornecki, K. P.; Briones, J. F.; Boyarskikh, V.; Fullilove, F.; Autschbach, J.; Schrote, K. E.; Lancaster, K. M.; Davies, H. M. L.; Berry, J. F. *Science* **2013**, *342*, 351-354.
214. Esswein, A. J.; Nocera, D. G. *Chemical Reviews* **2007**, *107*, 4022-4047.
215. Heyduk, A. F.; Nocera, D. G. *Science* **2001**, *293*, 1639-1641.
216. Powers, D. C.; Chambers, M. B.; Teets, T. S.; Elgrishi, N.; Anderson, B. L.; Nocera, D. G. *Chem. Sci.* **2013**, *4*, 2880-2885.
217. Komiya, N.; Nakae, T.; Sato, H.; Naota, T. *Chem. Commun.* **2006**, 4829-4831.
218. Chifotides, H. T.; Dunbar, K. R. *Acc. Chem. Res.* **2005**, *38*, 146-156.
219. Silva, D. d. O. *Anticancer Agents Med. Chem.* **2010**, *10*, 312-323.

220. Miyasaka, H.; Izawa, T.; Takahashi, N.; Yamashita, M.; Dunbar, K. R. *J. Am. Chem. Soc.* **2006**, *128*, 11358-11359.
221. Motokawa, N.; Matsunaga, S.; Takaishi, S.; Miyasaka, H.; Yamashita, M.; Dunbar, K. R. *J. Am. Chem. Soc.* **2010**, *132*, 11943-11951.
222. Chisholm, M. H.; Gustafson, T. L.; Turro, C. *Acc. Chem. Res.* **2012**.
223. Cotton, F. A.; Nocera, D. G. *Acc. Chem. Res.* **2000**, *33*, 483-490.
224. Hughes, R. G.; Bear, J. L.; Kimball, A. P. *Proc. Amer. Ass. Cancer Res.* **1972**, *13*, 120.
225. Erck, A.; Rainen, L.; Whileyman, J.; Chang, I. M.; Kimball, A. P.; Bear, J. *Proc. Soc. Exp. Biol. Med.* **1974**, *145*, 1278-1283.
226. Bear, J. L.; Gray, H. B.; Rainen, L.; Chang, I. M.; Howard, R.; Serio, G.; Kimball, A. P. *Cancer. Chemother. Rep.* **1975**, *59*, 611-620.
227. Erck, A.; Sherwood, E.; Bear, J. L.; Kimball, A. P. *Cancer Res.* **1976**, *36*, 2204-2209.
228. Howard, R. A.; Sherwood, E.; Erck, A.; Kimball, A. P.; Bear, J. L. *J. Med. Chem.* **1977**, *20*, 943-946.
229. Howard, R. A.; Kimball, A. P.; Bear, J. L. *Cancer Res.* **1979**, *39*, 2568-2573.
230. Fimiani, V.; Ainis, T.; Cavallaro, A.; Piraino, P. *J. Chemother.* **1990**, *2*, 319-326.
231. Pruchnik, F.; Dus, D. *J. Inorg. Biochem.* **1996**, *61*, 55-61.
232. Reibschied, E. M.; Zyngier, S. B.; Maria, D. A.; Mistrone, R. J.; Sinisterra, R. D.; Couto, L. G.; Najjar, R. *Braz. J. Med. Biol. Res.* **1994**, *27*, 91-94.



233. Espósito, B. P.; Zyngier, S. B.; Souza, A. R. d.; Najjar, R. *Met. Based Drugs* **1997**, *4*, 333–338.
234. Pruchnik, F. P.; Starosta, R.; Ciunik, Z.; Opolski, A.; Wietrzyk, J.; Wojdat, E.; Dus, D. *Can. J. Chem.* **2001**, *79*, 868–877.
235. Rubin, J. R.; Haromy, T. P.; Sundaralingam, M. *Acta Crystallogr.* **1991**, *C47*, 1712-1714.
236. Aoki, K.; Salam, M. A. *Inorg. Chim. Acta* **2002**, *339*, 427-437.
237. Dunbar, K. R.; Matonic, J. H.; Saharan, V. P.; Crawford, C. A.; Christou, G. *J. Am. Chem. Soc.* **1994**, *116*, 2201-2202.
238. Crawford, C. A.; Day, E. F.; Saharan, V. P.; Folting, K.; Huffman, J. C.; Dunbar, K. R.; Christou, G. *J. Chem. Soc., Chem. Commun.* **1996**, 1113-1114.
239. Catalan, K. V.; Hess, J. S.; Maloney, M. M.; Mindiola, D. J.; Ward, D. L.; Dunbar, K. R. *Inorg. Chem.* **1999**, *38*, 3904-3913.
240. Chifotides, H. T.; Koshlap, K. M.; Pérez, L. M.; Dunbar, K. R. *J. Am. Chem. Soc.* **2003**, *125*, 10714-10724.
241. Chifotides, H. T.; Hess, J. S.; Angeles-Boza, A. M.; Ramon Galan-Mascaros, J.; Sorasaene, K.; Dunbar, K. R. *Dalton Trans.* **2003**, 4426-4430.
242. Catalan, K. V.; Mindiola, D. J.; Ward, D. L.; Dunbar, K. R. *Inorg. Chem.* **1997**, *36*, 2458-2460.
243. Chifotides, H. T.; Koshlap, K. M.; Pérez, L. M.; Dunbar, K. R. *J. Am. Chem. Soc.* **2003**, *125*, 10703-10713.

244. Sherman, S. E.; Gibson, D.; Wang, A. H. J.; Lippard, S. J. *J. Am. Chem. Soc.* **1988**, *110*, 7368-7381.
245. Asara, J. M.; Hess, J. S.; Lozada, E.; Dunbar, K. R.; Allison, J. *J. Am. Chem. Soc.* **1999**, *122*, 8-13.
246. Chifotides, H. T.; Koomen, J. M.; Kang, M.; Tichy, S. E.; Dunbar, K. R.; Russell, D. H. *Inorg. Chem.* **2004**, *43*, 6177-6187.
247. Dunham, S. U.; Chifotides, H. T.; Mikulski, S.; Burr, A. E.; Dunbar, K. R. *Biochemistry* **2005**, *44*, 996-1003.
248. Aguirre, J. D.; Angeles-Boza, A. M.; Chouai, A.; Pellois, J.-P.; Turro, C.; Dunbar, K. R. *J. Am. Chem. Soc.* **2009**, *131*, 11353-11360.
249. Olive, P. L.; Banath, J. P. *Nat. Protocols* **2006**, *1*, 23-29.
250. Aguirre, J. D.; Angeles-Boza, A. M.; Chouai, A.; Turro, C.; Pellois, J.-P.; Dunbar, K. R. *Dalton Trans.* **2009**, 10806-10812.
251. Siu, F.-M.; Lin, I. W.-S.; Yan, K.; Lok, C.-N.; Low, K.-H.; Leung, T. Y.-C.; Lam, T.-L.; Che, C.-M. *Chem. Sci.* **2012**, *3*, 1785-1793.
252. Ribeiro, G.; Benadiba, M.; de Oliveira Silva, D.; Colquhoun, A. *Cell Biochem. Funct.* **2010**, *28*, 15-23.
253. Shtemenko, A. V.; Collery, P.; Shtemenko, N. I.; Domasevitch, K. V.; Zabitskaya, E. D.; Golichenko, A. A. *Dalton Trans.* **2009**, 5132-5136.
254. Shtemenko, N. I.; Chifotides, H. T.; Domasevitch, K. V.; Golichenko, A. A.; Babiy, S. A.; Li, Z.; Paramonova, K. V.; Shtemenko, A. V.; Dunbar, K. R. *J. Inorg. Biochem.* **2013**, *129*, 127-134.

255. Klein, A. V.; Hambley, T. W. *Chem. Rev.* **2009**, *109*, 4911–4920.
256. Molenaar, C.; Teuben, J. M.; Heetebrij, R. J.; Tanke, H. J.; Reedijk, J. *J. Biol. Inorg. Chem.* **2000**, *5*, 655-665.
257. Katano, K.; Safaei, R.; Samimi, G.; Holzer, A.; Tomioka, M.; Goodman, M.; Howell, S. B. *Clin. Cancer. Res.* **2004**, *10*, 4578-4588.
258. Safaei, R.; Katano, K.; Larson, B. J.; Samimi, G.; Holzer, A. K.; Naerdemann, W.; Tomioka, M.; Goodman, M.; Howell, S. B. *Clin. Cancer. Res.* **2005**, *11*, 756-767.
259. Kalayda, G.; Jansen, B. J.; Wielaard, P.; Tanke, H.; Reedijk, J. *J. Biol. Inorg. Chem.* **2005**, *10*, 305-315.
260. Kalayda, G. V.; Zhang, G.; Abraham, T.; Tanke, H. J.; Reedijk, J. *J. Med. Chem.* **2005**, *48*, 5191-5202.
261. Wu, S.; Zhu, C.; Zhang, C.; Yu, Z.; He, W.; He, Y.; Li, Y.; Wang, J.; Guo, Z. *Inorg. Chem.* **2011**, *50*, 11847-11849.
262. Ingram, J. D.; Costa, P. J.; Adams, H.; Ward, M. D.; Félix, V.; Thomas, J. A. *Inorg. Chem.* **2012**, *51*, 10483-10494.
263. Hilderbrand, S. A.; Lim, M. H.; Lippard, S. J. *J. Am. Chem. Soc.* **2004**, *126*, 4972-4978.
264. Hissler, M.; Connick, W. B.; Geiger, D. K.; McGarrah, J. E.; Lipa, D.; Lachicotte, R. J.; Eisenberg, R. *Inorg. Chem.* **2000**, *39*, 447-457.
265. Rempel, G. A.; Legzdins, P.; Smith, H.; Wilkinson, G. *Inorg. Synth.* **1971**, *13*, 90-91.

266. Crawford, C. A.; Matonic, J. H.; Streib, W. E.; Huffman, J. C.; Dunbar, K. R.; Christou, G. *Inorg. Chem.* **1993**, *32*, 3125-3133.
267. Cui, A.; Peng, X.; Fan, J.; Chen, X.; Wu, Y.; Guo, B. *Photochem. Photobiol. A: Chem.* **2007**, *186*, 85-92.
268. Sarkar, B.; Kaim, W.; Klein, A.; Schwederski, B.; Fiedler, J.; Duboc-Toia, C.; Lahiri, G. K. *Inorg. Chem.* **2003**, *42*, 6172-6174.
269. Abry, S.; Lux, F.; Albela, B.; Artigas-Miquel, A.; Nicolas, S.; Jarry, B.; Perriat, P.; Lemerrier, G.; Bonneviot, L. *Chem. Mater.* **2009**, *21*, 2349-2359.
270. Angeles-Boza, A. M.; Bradley, P. M.; Fu, P. K. L.; Wicke, S. E.; Bacsa, J.; Dunbar, K. R.; Turro, C. *Inorg. Chem.* **2004**, *43*, 8510-8519.
271. Angeles-Boza, A. M.; Chifotides, H. T.; Aguirre, J. D.; Chouai, A.; Fu, P. K. L.; Dunbar, K. R.; Turro, C. *J. Med. Chem.* **2006**, *49*, 6841-6847.
272. Crawford, C. A.; Matonic, J. H.; Huffman, J. C.; Folting, K.; Dunbar, K. R.; Christou, G. *Inorg. Chem.* **1997**, *36*, 2361-2371.
273. Joyce, L. E.; Aguirre, J. D.; Angeles-Boza, A. M.; Chouai, A.; Fu, P. K. L.; Dunbar, K. R.; Turro, C. *Inorg. Chem.* **2010**, *49*, 5371-5376.
274. Puckett, C. A.; Barton, J. K. *Bioorg. Med. Chem.* **2010**, *18*, 3564-3569.
275. Puckett, C. A.; Barton, J. K. *J. Am. Chem. Soc.* **2009**, *131*, 8738-8739.
276. Cosgrave, L.; Devocelle, M.; Forster, R. J.; Keyes, T. E. *Chem. Commun.* **2010**, *46*, 103-105.

277. Zhang, J.-X.; Zhou, J.-W.; Chan, C.-F.; Lau, T. C.-K.; Kwong, D. W. J.; Tam, H.-L.; Mak, N.-K.; Wong, K.-L.; Wong, W.-K. *Bioconjugate Chem.* **2012**, *23*, 1623–1638.